APPLIED COMPUTATIONAL ELECTROMAGNETICS SOCIETY JOURNAL

January 2024
Vol. 39 No. 1
ISSN 1054-4887

The ACES Journal is abstracted in INSPEC, in Engineering Index, DTIC, Science Citation Index Expanded, the Research Alert, and to Current Contents/Engineering, Computing & Technology.

The illustrations on the front cover have been obtained from the ARC research group at the Department of Electrical Engineering, Colorado School of Mines

Published, sold and distributed by: River Publishers, Alsbjergvej 10, 9260 Gistrup, Denmark

THE APPLIED COMPUTATIONAL ELECTROMAGNETICS SOCIETY
http://aces-society.org

EDITORS-IN-CHIEF

Atef Elsherbeni
Colorado School of Mines, EE Dept.
Golden, CO 80401, USA

Sami Barmada
University of Pisa, ESE Dept.
56122 Pisa, Italy

ASSOCIATE EDITORS

Maokun Li
Tsinghua University
Beijing 100084, China

Mauro Parise
University Campus Bio-Medico of Rome
00128 Rome, Italy

Yingsong Li
Harbin Engineering University
Harbin 150001, China

Riyadh Mansoor
Al-Muthanna University
Samawa, Al-Muthanna, Iraq

Lijun Jiang
University of Hong Kong, EEE Dept.
Hong, Kong

Shinishiro Ohnuki
Nihon University
Tokyo, Japan

Kubilay Sertel
The Ohio State University
Columbus, OH 43210, USA

Giulio Antonini
University of L Aquila
67040 L Aquila, Italy

Antonio Musolino
University of Pisa
56126 Pisa, Italy

Abdul A. Arkadan
Colorado School of Mines, EE Dept.
Golden, CO 80401, USA

Salvatore Campione
Sandia National Laboratories
Albuquerque, NM 87185, USA

Ibrahim Mahariq
American University of the Middle East
Kuwait and University of
Turkish Aeronautical Association
Turkey

Wei-Chung Weng
National Chi Nan University, EE Dept.
Puli, Nantou 54561, Taiwan

Alessandro Formisano
Seconda Universita di Napoli
81031 CE, Italy

Piotr Gas
AGH University of Science and Technology
30-059 Krakow, Poland

Long Li
Xidian University
Shaanxa, 710071, China

Steve J. Weiss
US Army Research Laboratoy
Adelphi Laboratory Center (RDRL-SER-M)
Adelphi, MD 20783, USA

Jiming Song
Iowa State University, ECE Dept.
Ames, IA 50011, USA

Toni Bjorninen
Tampere University
Tampere, 33100, Finland

Santanu Kumar Behera
National Institute of Technology
Rourkela-769008, India

Daniele Romano
University of L Aquila
67100 L Aquila, Italy

Alireza Baghai-Wadji
University of Cape Town
Cape Town, 7701, South Africa

Marco Arjona López
La Laguna Institute of Technology
Torreon, Coahuila 27266, Mexico

Kaikai Xu
University of Electronic Science
and Technology of China
China

Sheng Sun
University of Electronic Science and
Tech. of China
Sichuan 611731, China

Paolo Mezzanotte
University of Perugia
I-06125 Perugia, Italy

Luca Di Rienzo
Politecnico di Milano
20133 Milano, Italy

Lei Zhao
Jiangsu Normal University
Jiangsu 221116, China

Sima Noghanian
Commscope
Sunnyvale, CA 94089, USA

Nunzia Fontana
University of Pisa
56122 Pisa, Italy

Stefano Selleri
DINFO - University of Florence
50139 Florence, Italy

Yu Mao Wu
Fudan University
Shanghai 200433, China

Fatih Kaburcuk
Sivas Cumhuriyet University
Sivas 58140, Turkey

Huseyin Savci
Istanbul Medipol University
34810 Beykoz, Istanbul

Zhixiang Huang
Anhui University
China

Amin Kargar Behbahani
Florida International University
Miami, FL 33174, USA

Laila Marzall
University of Colorado, Boulder
Boulder, CO 80309, USA

EDITORIAL ASSISTANTS

Matthew J. Inman
University of Mississippi, EE Dept.
University, MS 38677, USA

Shanell Lopez
Colorado School of Mines, EE Dept.
Golden, CO 80401, USA

EMERITUS EDITORS-IN-CHIEF

Duncan C. Baker
EE Dept. U. of Pretoria
0002 Pretoria, South Africa

Allen Glisson
University of Mississippi, EE Dept.
University, MS 38677, USA

Ahmed Kishk
Concordia University, ECS Dept.
Montreal, QC H3G 1M8, Canada

Robert M. Bevensee
Box 812
Alamo, CA 94507-0516

Ozlem Kilic
Catholic University of America
Washington, DC 20064, USA

David E. Stein
USAF Scientific Advisory Board
Washington, DC 20330, USA

EMERITUS ASSOCIATE EDITORS

Yasushi Kanai
Niigata Inst. of Technology
Kashiwazaki, Japan

Mohamed Abouzahra
MIT Lincoln Laboratory
Lexington, MA, USA

Alexander Yakovlev
University of Mississippi, EE Dept.
University, MS 38677, USA

Levent Gurel
Bilkent University
Ankara, Turkey

Sami Barmada
University of Pisa, ESE Dept.
56122 Pisa, Italy

Ozlem Kilic
Catholic University of America
Washington, DC 20064, USA

Erdem Topsakal
Mississippi State University, EE Dept.
Mississippi State, MS 39762, USA

Alistair Duffy
De Montfort University
Leicester, UK

Fan Yang
Tsinghua University, EE Dept.
Beijing 100084, China

Rocco Rizzo
University of Pisa
56123 Pisa, Italy

Atif Shamim
King Abdullah University of Science and
Technology (KAUST)
Thuwal 23955, Saudi Arabia

William O'Keefe Coburn
US Army Research Laboratory
Adelphi, MD 20783, USA

Mohammed Hadi
Kuwait University, EE Dept.
Safat, Kuwait

Amedeo Capozzoli
Univerita di Naoli Federico II, DIETI
I-80125 Napoli, Italy

Wenxing Li
Harbin Engineering University
Harbin 150001, China

Qiang Ren
Beihang University
Beijing 100191, China

EMERITUS EDITORIAL ASSISTANTS

Khaleb ElMaghoub
Trimble Navigation/MIT
Boston, MA 02125, USA

Kyle Patel
Colorado School of Mines, EE Dept.
Golden, CO 80401, USA

Christina Bonnigton
University of Mississippi, EE Dept.
University, MS 38677, USA

Anne Graham
University of Mississippi, EE Dept.
University, MS 38677, USA

Madison Lee
Colorado School of Mines, EE Dept.
Golen, CO 80401, USA

Allison Tanner
Colorado School of Mines, EE Dept.
Golden, CO 80401, USA

Mohamed Al Sharkawy
Arab Academy for Science and Technology, ECE Dept.
Alexandria, Egypt

JANUARY 2024 REVIEWERS

Intan Sorfina Zainal Abidin
Le Chang
Thippesha D.
Chengzhu Du
Alfredo Gomes Neto
Jesus Gonzalez Dominguez
Pankaj Jha
I. Kathir
Mikko Kokkonen
Lihua Li
Matteo Bruno Lodi
Fabrizio Loreto
Enrique Melgoza
Durga Prasad Mishra
Sathishkumar N.
Mahdi Oliaei
Andrew Peterson
Gerardo Ruiz-Ponce
Ajit Kumar Sahoo
Michael Saville
Manthan Shah
M. Mohammadi Shirkolaei
Qiwei Zhan
Xiao Zhang
Wei-Hua Zong

THE APPLIED COMPUTATIONAL ELECTROMAGNETICS SOCIETY JOURNAL

Vol. 39 No. 1 January 2024

TABLE OF CONTENTS

A Rapid Single-view Radar Imaging Method with Window Functions

Wen Ming Yu[1], **Yi Ting Yang**[1], **Xiao Fei Lu**[2], **Chao Yang**[3], **Zai Gao Chen**[3], **and Tie Jun Cui**[1]

[1]School of Information Science and Engineering, Southeast University
Nanjing, 210096, China
wmyu@seu.edu.cn, 230189062@seu.edu.cn, tjcui@seu.edu.cn

[2]Jiuquan Satellite Launch Center
Jiuquan, 732750, China
luxiaofei.2008@tsinghua.org.cn

[3]Northwest Institute of Nuclear Technology
Xi'an, 710024, China
yangchaophy@foxmail.com

Abstract **–** Monostatic rapid single-view radar imaging technology is a technique that employs single incidence angle and single frequency point information to implement rapid monostatic radar imaging within a small angular field. Owing to its analytical expression, this technique can substitute the traditional frequency-angle-scanning imaging in a small angular range, facilitating the rapid generation of highly realistic radar imaging data slices for complex targets and environments. This technology has been significantly applied in scatter hotspot diagnostics and target recognition. In order to achieve the windowing effect equivalent to that of frequency-angle-scanning imaging, and to enhance the scattering feature of monostatic imaging while controlling sidelobes, this paper derives analytic windowed imaging formulas for monostatic radar. It then obtains analytical expressions for various typical monostatic windowing rapid radar imaging scenarios. This enables the monostatic rapid imaging technology to maintain high efficiency in its analytical expressions while achieving the windowing effect equivalent to traditional imaging. The validity and correctness of the analytical formula and software implementation have been confirmed through 1D, 2D, and 3D imaging verifications. This technology can provide a vast amount of training data for modern radars.

Index Terms **–** Radar imaging, single-view, window functions.

I. INTRODUCTION

Radar imaging can reconstruct target geometry and material characteristics through echoes and has a wide range of applications in geographic exploration, ocean observation, disaster prediction and military reconnaissance [1–5], etc. High-resolution one-dimensional distance imaging is often utilized for determining detonation points, while two-dimensional radar imaging is typically used for target recognition and remote sensing data classification [6]. Three-dimensional radar imaging is a crucial basis for radar feature identification in the current field of autonomous driving. How to obtain three-dimensional radar imaging data of the target and the environment is one of the hot research topics in the field of autonomous driving [7].

Traditional radar imaging technology is built upon the Fourier transform relationship between the electromagnetic distribution of the antenna aperture and far-field scattering, typically employing synthetic aperture methods to enhance azimuth resolution. From one dimension to two, and then to three, the utilization rate of imaging information is increasingly high. Superior imaging technologies, such as two-dimensional and three-dimensional, are gradually becoming practical with the advancement of hardware technology. In the field of autonomous driving, due to the all-weather characteristics of millimeter-wave radar, research on target characteristics technology based on three-dimensional millimeter-wave radar imaging is gaining increasing attention.

Radar imaging technology, based on electromagnetic scattering characteristic theory modeling, is a vital means of obtaining data on the radar scattering characteristics of targets and their environments. It has already found applications in military target identification and civilian remote sensing. Monostatic millimeter-wave radar imaging, originating from electromagnetic simulation technology, can significantly reduce the bandwidth and angular sampling expenses required for single-station imaging, enhancing the efficiency of obtaining

Submitted On: October 16, 2023
Accepted On: February 28, 2024

https://doi.org/10.13052/2024.ACES.J.390101

imaging slice data. This technology was first applied to time-domain simulation of radar target scattering characteristics [8], rapidly obtaining time-domain echoes through the convolution of the analytical expression of target partition element time-domain responses with the signal. Subsequently, this technology was used in two-dimensional Inverse Synthetic Aperture Radar (ISAR) imaging [9, 10], and in recent years, applied to automatic target recognition [11–13] and urban remote sensing electromagnetic feature extraction [14].

The windowing operation is a standard procedure within radar imaging algorithms. Imaging represents the comprehensive broadband and angular information from the radar within the time and/or spatial domains. By applying a non-uniform window function prior to the Fourier transform, the spectral leakage effect of the Fast Fourier Transform (FFT) is mitigated. Concurrently, the windowing process is akin to executing a convolution operation in the time or spatial domains, which results in the broadening of the main lobe, thus reducing resolution. Implementing a non-uniform window prior to the Fourier transformation in the imaging of aperture data can effectively lower the sidelobe levels in individual cell imaging and enhance the visibility of target characteristics [15, 16]. Monostatic rapid imaging is mainly used for feature extraction and strong scattering diagnosis of targets. The literature [17] attempted to introduce a window function into the rapid single-view imaging algorithm, but it directly truncated the sinc function in time domain, which could not reproduce the conventional process of obtaining radar images through Fourier transformation after window function weighting.

II. SINGLE–VIEW RADAR IMAGING METHOD

For ease of understanding, this paper describes the imaging principle of single-view millimeter-wave radar using the most representative two-dimensional imaging as an example. The definition of single-view millimeter-wave imaging radar still adheres to the traditional frequency-angle-scanning radar imaging, that is, the received field value of the radar and the radar image constitute a Fourier transform pair [18]:

$$\Gamma(l,d) = \iint E_s e^{-j2\pi(f_l l + f_d d)} df_l df_d. \tag{1}$$

Here, $\Gamma(l,d)$ represents the image or target function in the image domain coordinates (l,d), f_d is the spatial frequency in the radar line of sight direction, and it satisfies $f_d \equiv 2f/c$, so $k_d = \pi f_d$ is the propagation constant of the electromagnetic wave. f_l is the spatial frequency in the direction orthogonal to the line of sight $\hat{l}$, and $k_l = \pi f_l$. $\hat{l}$ can be the direction indicated by azimuth $\hat{\phi}$ or elevation angle $\hat{\theta}$. E_s is the received radar echo electric field value.

The process of sweep-frequency scanning radar imaging is to use FFT to solve the above formula (1). This process requires obtaining the target radar echo field value E_s. In commonly used monostatic radars, it is necessary to implement monostatic wideband small-angle scanning in simulation modeling, especially for two-dimensional and three-dimensional imaging. To cover the entire target or scene, the number of scanning samples can reach the order of 10^4 and 10^6, respectively. Document [9] first gave the monostatic radar distance imaging formula, greatly improving the imaging efficiency. In order to keep the formula consistent with the windowed imaging formula below, the following simple derivation is given using the previous definition: Assume that any complex target is described by a geometric model represented by triangle collection $\{S_i, i \in [0, N-1]\}$. The expression of the far-field scattering field illuminated by a plane wave is as follows [19]:

$$E_s = \frac{e^{-jkr}}{4\pi r} jkE_0 \sum_{i=0}^{N-1} f_i(x,y) I_i. \tag{2}$$

Here, $f_i\ (x,y) \equiv (\hat{k}_i \times E_i + \hat{k}_r \times E_r) \times \hat{n}' + \hat{k}_s \times [(E_i + E_r) \times \hat{n}']$ represents the polarization term, where $\hat{k}_i$ and $\hat{k}_r$ denote the wave vectors of incident and reflected waves for any surface element with the normal vector $\hat{n}'$, respectively, and k is the wave vector constant. E_0 is the amplitude of E_s at source point. r is the distance from observation point to the origin. The term $I_i \equiv \int_S e^{-2jk\hat{k}_i \cdot r'} ds'$ is the phase integral for a unit surface element.

$$\begin{aligned} f_i(x,y) I_i = &\left[f_i(x,y) \iint_S e^{-jk\left(\kappa_{sx}x' + \kappa_{sy}y'\right)} dx'dy' \right] \\ &\cdot e^{-jk\hat{k}_i \cdot R_{i0}} \equiv W_i e^{-jk\hat{k}_i \cdot R_{i0}}, \end{aligned} \tag{3}$$

where R_{i0} represents the position vector of a certain point on the surface element S_i, which serves as a phase reference point. The term $e^{-jk\hat{k}_i \cdot R_{i0}}$ represents the phase shift of this surface element relative to the origin of the coordinate system. $W_i \equiv f_i(x,y) \iint_{S_i} e^{-jk\kappa_{sx}x' + \kappa_{sy}y'} dx'dy'$ represents the scattering shape factor of this surface element. By substituting equation (2) into the imaging formula (1), when $r \to \infty$, the variation of $e^{-jkr}/(4\pi r)$ with k can be ignored.

$$\begin{aligned} \Gamma(l,d) = &\frac{e^{-jkr}}{4\pi r} jkE_0 \sum_{i=0}^{N-1} W_i \\ &\cdot \iint e^{-2jk\hat{k}_i \cdot R_{i0}} e^{-j2\pi(f_l l + f_d d)} df_l df_d. \end{aligned} \tag{4}$$

Under the usual small-angle imaging assumption, ignore the variation of $\hat{k}_d$ with θ or ϕ, $k\hat{k}_i = k\hat{k}_d + k_l\hat{k}_l \approx k\hat{k}_d + k_0\alpha\hat{k}_l$, where k_0 represents the wave number corresponding to the center frequency and α represents θ or ϕ. Let $D \equiv -\hat{k}_d \cdot R_{i0}$ and $L \equiv -\hat{k}_l \cdot R_{i0}$, which represent the line of sight distance and horizontal distance from each triangular reference point to the coordinate origin, respectively.

$$\begin{aligned}\Gamma(l,d) &= \frac{e^{-jkr}}{4\pi r} jkE_0 \sum_{i=0}^{N-1} W_i \int e^{2jkD} e^{-j2\pi f_d d} df_d \\ &\quad \cdot \int e^{2jk_0\alpha L} e^{-j2\pi f_l l} df_l \\ &= \frac{e^{-jkr}}{4\pi r} jkE_0 \sum_{i=0}^{N-1} W_i e^{-2j\pi f_{d0}(d-D/2)} \\ &\quad \cdot B_d \operatorname{sinc}(\pi B_d(d-D/2)) B_l \operatorname{sinc}(\pi B_l(l-L/2)).\end{aligned}$$

When calculating the far field, let the amplitude distance r be 1, and the phase take $r=0$, so:

$$\begin{aligned}\Gamma(l,d) &= \frac{jkE_0}{4\pi} \sum_{i=0}^{N-1} W_i e^{-2j\pi f_{d0}(d-D/2)} \\ &\quad \cdot B_d \operatorname{sinc}(\pi B_d(d-D/2)) B_l \operatorname{sinc}(\pi B_l(l-L/2)).\end{aligned}$$

This equation indicates that the target radar image or target function can be composed of the superposition of sinc functions centered on each triangular element reference point. The terms $\operatorname{sinc}(\pi B_d(d-D/2))$ and $\operatorname{sinc}(\pi B_l(l-L/2))$ are referred to as expansion functions. Because the derivation process assumes a small angle, it's easy to understand: one-dimensional imaging only uses $\operatorname{sinc}(\pi B_d(d-D/2))$ as an expansion function, while three-dimensional imaging requires an additional expansion function similar to $\operatorname{sinc}(\pi B_l(l-L/2))$.

Figure 1 provides a comparison between the three-dimensional imaging of a single-view radar of an aircraft and the three-dimensional imaging of a frequency scanning angle radar. Combined with more experiments, it shows that for complex targets, the rapid single-view imaging, whether in terms of the position of strong scattering points or the intensity of calibrated strong scattering points, is the same as that of frequency scanning angle. However, the former has much higher computational efficiency and is very suitable for strong scatter diagnosis and target feature extraction.

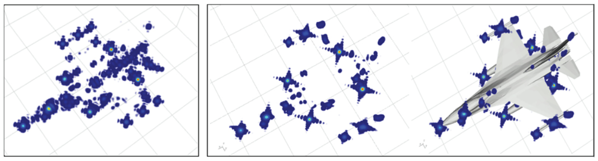
(a) Rapid Single-View Imaging

(b) Frequency-Angle-Scanning Radar Imaging and Its Overlay with Geometric Body

Fig. 1. Comparison of rapid single-view imaging and frequency-angle-scanning imaging.

III. WINDOWED SINGLE-VIEW RADAR IMAGING TECHNIQUE

According to the definition of windowed normalized radar imaging in Cartesian coordinates (l,d) [18], we have:

$$\Gamma(l,d) = \frac{1}{A} \iint SVe^{-j2\pi(f_l l + f_d d)} df_l df_d, \tag{5}$$

where $S \equiv \sqrt{4\pi} RE_s/E_i$ represents the target scattering function, R is the distance from the target center to the observation point (in the far field, it is infinite), and E_s, E_i represent the scattered field and the incident field at the observation point, respectively. V is the window function, and $A \equiv \iint V df l df d$ is the amplitude normalization factor [18]. After changing equation (5) to one-dimensional and three-dimensional integrals, we get the windowed normalized one-dimensional and three-dimensional imaging. For small angle imaging, we have:

$$f_d = \frac{2f}{c}, \quad f_l \equiv f_d \alpha = \frac{2f\alpha}{c}.$$

When V is a rectangular window, we have:

$$A = \iint \frac{4f}{c^2} df d\alpha = \frac{2\Delta_\alpha}{c^2}\left(f_{max}^2 - f_{min}^2\right) = \frac{4f_0}{c^2} B\Delta_\alpha$$

$$\begin{aligned}\Gamma(l,d) &= \frac{1}{A} \iint SVe^{-j4\pi fd/c} \frac{4f}{c^2} df d\alpha \\ &= \frac{1}{B\Delta_\alpha} \iint SVe^{-j4\pi fd/c} df d\alpha.\end{aligned}$$

For traditional frequency-angle-scanning imaging, the aforementioned equation can be calculated through FFT. For rapid single-view imaging, it needs to be transformed into an analytical expression. Referring to the derivation in section II, we can get the single-view radar imaging formula weighted by a rectangular window:

$$\begin{aligned}\Gamma(l,d) &= \frac{1}{2\sqrt{\pi}E_i} \sum_{i=0}^{N-1} (E_{i0}W_i) e^{-j2\pi f_0 \bar{d}} \\ &\quad \cdot B_l \operatorname{sinc}\left[\pi B_l \bar{l}\right] B_d \operatorname{sinc}\left[\pi B_d \bar{d}\right],\end{aligned}$$

where $B_l \equiv 2f_0\Delta_\alpha/c$, $B_d \equiv 2B/c$, f_0 is the center frequency point of bandwidth B, $B \equiv f_{max} - f_{min}$, $\bar{l} = l - L/2$, $\bar{d} = d - D/2$, and L and D are, respectively, the projections of the triangular reference phase vectors that make up the target in the $\hat{l}$ and $\hat{d}$ directions.

After similar derivation, Table 1 gives the key parameters of $\Gamma(l,d)$ corresponding to commonly used window functions. For uniformity, all windowed single-view radar imaging formulas in the table are written in the following mode:

$$\Gamma(l,d) = \frac{1}{A} \frac{1}{2\sqrt{\pi}E_i} \sum_{i=0}^{N-1} (E_{i0}W_i) e^{-j2\pi f_0 \bar{d}} \mathrm{EF}_d \mathrm{EF}_l,$$

where the key variables EF_l and EF_d represent the expansion functions in the l and d directions, respectively, and $1/A$ represents the weighting coefficient, specifics are shown in Table 1. $\Re$ represents real part of a variable. erf is error function. Formulas of EF_l can be obtained by replacing d to l in EF_d.

Table 1: Key quantities for rapid single-view radar imaging with different window functions

Type	**1/A**	$\mathrm{EF}_{\mathbf{d}}$
Rectangle	$\frac{1}{B_d B_l}$	$B_d \operatorname{sinc}\left(\pi B_d \bar{d}\right)$
Triangle	$\frac{4}{B_d B_l}$	$\frac{\left(1-\cos\left(\pi B_d \bar{d}\right)\right)}{\pi^2 B_d \bar{d}^2}$
Welch	$\frac{9}{4B_d B_l}$	$\frac{2\sin\left(\pi B_d \bar{d}\right)-2\pi B_d \bar{d}\cos\left(\pi B_d \bar{d}\right)}{\pi^3 {B_d}^2 \bar{d}^3}$
Sin	$\frac{\pi^2}{4B_d B_l}$	$\frac{2B_d \cos\left(\pi B_d \bar{d}\right)}{\pi\left(1-4B_d^2 \bar{d}^2\right)}$
Hann	$\frac{4}{B_d B_l}$	$\frac{\sin\left(\pi B_d \bar{d}\right)}{2\pi \bar{d}\left(1-B_d^2 \bar{d}^2\right)}$
Hamming	$\frac{46}{25B_d}\frac{46}{25B_l}$	$\frac{\left(\frac{2}{23}B_d^2 \bar{d}^2-\frac{25}{46}\right)\sin\left(\pi B_d \bar{d}\right)}{\pi \bar{d}\left(1-B_d^2 \bar{d}^2\right)}$
Blackman	$\frac{9304}{3919B_d}\frac{9304}{3919B_l}$	$\frac{\left(7B_d^4 \bar{d}^4-915B_d^2 \bar{d}^2+7838\right)\sin\left(\pi B_d \bar{d}\right)}{4652\pi \bar{d}\left(B_d^4 \bar{d}^4-5B_d^2 \bar{d}^2+4\right)}$
Gauss	$\frac{1}{2\pi\sigma^2 \operatorname{erf}^2\left(\frac{1}{2\sqrt{2}\sigma}\right)B_d B_l}$	$\sqrt{\frac{\pi}{2}}\sigma B_d e^{-2\pi^2\sigma^2 B_d^2\ \bar{d}^2}\Re\left\{\operatorname{erf}\left(\frac{1}{2\sqrt{2}\sigma}+j\sqrt{2}\pi\sigma B_d \bar{d}\right)\right\}$

IV. NUMERICAL EXPERIMENTS

To verify the effect of windowed single-view radar imaging, the windowing effect is demonstrated below using the one-dimensional distance image of a dihedral angle and two- and three-dimensional radar imaging of a certain aircraft as examples. The results are shown in Figs. 2, 3, 4, respectively.

For Fig. 2, the radar resolution is 0.01m, the incident pitch angle is 90 degrees, the azimuth angle is 0 degrees, and the center frequency is 13.5GHz. As shown in Fig. 2, when a rectangular window is used, the secondary strong scatterers of the dihedral High Resolution Range Profile (HRRP) are almost drowned out by the sidelobes. After using a non-uniformly distributed window function, all the strong scatterers introduced by the dihedral due to multipath are clearly displayed because the sidelobes are suppressed. To clearly demonstrate the effect, the upper part of Fig. 2 only shows a comparison of the Blackman window and the Rectangular (RECT) window. As can be seen from the figure, the peak positions and peak amplitudes of the two completely overlap where there is no sidelobe obstruction. This validates the correctness of the weight coefficients A and EF in the normalization formula. The main lobe of the Blackman window result shown in the figure is widened, which aligns with the characteristics of windowing in imaging. The lower part of Fig. 2 shows a comparison between all the window functions derived in this paper and the rectangular window. The correctness of the derivation of the weighting coefficients is validated through the degree of overlap of the peak positions and peak amplitudes, as well as the characteristics of the main lobe widening of each window function. Besides, the co-polarized RCS of this dihedral with the same excitation is 46.98 dBsm, which is equivalent to that of the main beam amplitude in HRRP. It also verifies the correctness of the normalized rapid imaging formulations.

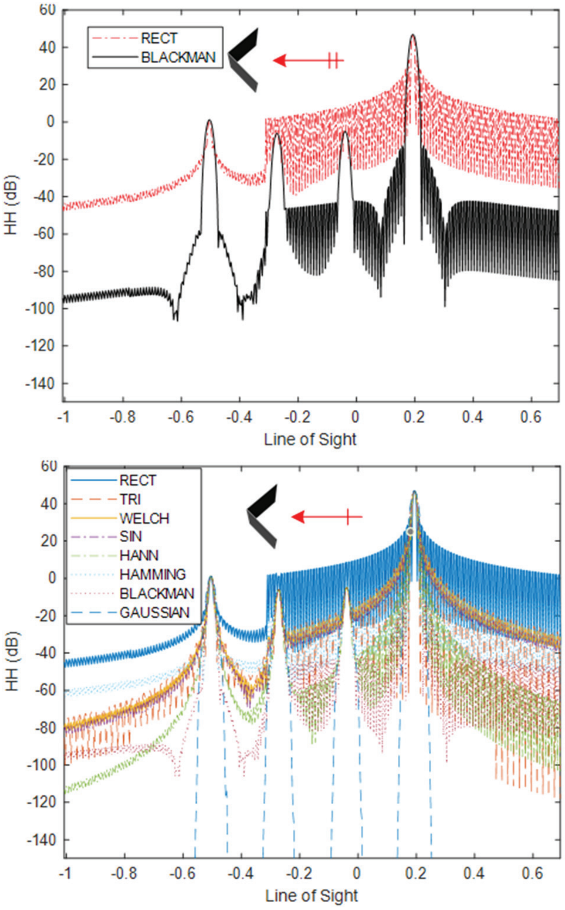

Fig. 2. Comparison of dihedral angle one-dimensional distance images with rectangular and non-rectangular windows.

Figures 3 and 4 give examples of two- and three-dimensional radar images, the radar resolutions are both 0.3 m, the incident pitch angles are 45 degrees, the azimuth angles are 45 degrees, and the center frequencies

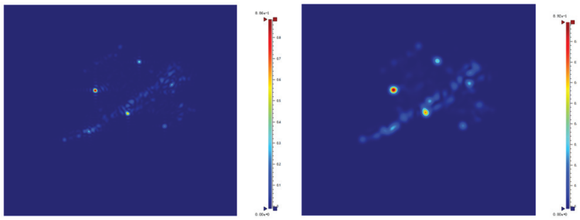

Rectangle Window (abs) Blackman Window (abs)

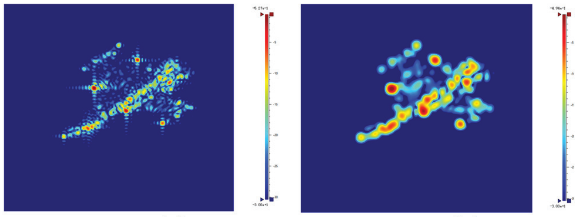

Rectangle Window (dB) Blackman Window (dB)

Fig. 3. Comparison of two-dimensional imaging with rectangular and non-rectangular windows (using the Blackman window as an example).

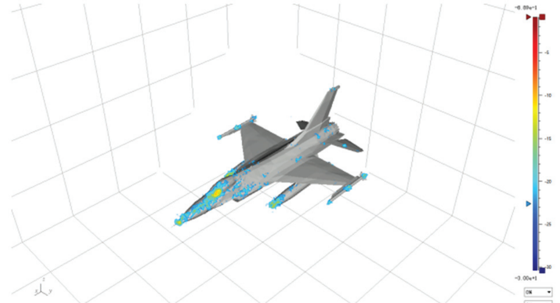

Rectangle Window (dB)

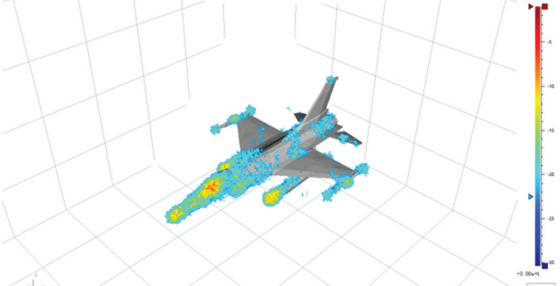

Blackman Window (dB)

Fig. 4. Application of three-dimensional windowed fast imaging.

are 10 GHz. Figures 3 and 4 simultaneously provide the two-dimensional and three-dimensional radar imaging results characterized by absolute (abs) and decibel (dB) values. The dB representation can more clearly display the distribution of the secondary strong scatterers. As can be seen from the figures, the distribution of strong scatterers in the images obtained using non-uniform window functions (taking the Blackman window as an example) and the rectangular window (without windowing) are consistent. Due to the sidelobe suppression, the strong scatterers in non-rectangular window images are clearer, but the resolution is slightly reduced, i.e., the radius of the bright spot is slightly increased.

Owing to certain distinctive aspects of the high-frequency asymptotic algorithm [20, 21], the single-view one-dimensional distance image depicted in Fig. 2 demonstrates a slightly accelerated relative to a traditionally obtained sweep-frequency one-dimensional distance image. To be specific, the former technique procured the image in 0.013 s while the latter required 0.04 s for completion. However, the two-dimensional rapid single-view radar imaging methodology demonstrates markedly increased velocity compared to frequency-angle-scanning approaches. As evidenced by Fig. 3, generating ISAR imagery via RECT and Blackman windowing with the single-view method required approximately 6.7 s and 6.9 s, respectively. In stark contrast, the frequency-angle-scanning technique necessitated 1162.8 s to complete the equivalent imaging task.

Similarly, Fig. 4 provides a comparison before and after three-dimensional windowed imaging. Secondary hotspots become significant after non-rectangle windowed imaging.

To further validate the accuracy of two-dimensional imaging, we deployed the proposed methodology for target radar imaging using MSTAR measurement outcomes as a benchmark standard. Taking the T72 tank as an example, Fig. 5 shows that both target outlines, shadow outlines, and distributions of strong scatters correspond remarkably well, regardless of technique used. Consequently, the method advanced in this paper demonstrates aptitude for generating training datasets well-suited for target recognition algorithms.

Three-dimensional imaging has already become an information perception and utilization method in multiple input multiple output(MIMO) radar technology for autonomous driving [7, 22]. Drawing on perception training technology based on optical imaging, how to quickly obtain massive three-dimensional imaging data of terrestrial targets and environmental elements is one of the key technologies for the development of radar autonomous driving technology. The technology pro-

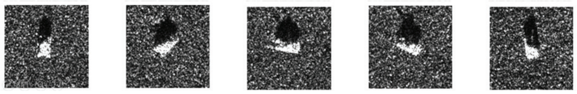

(a) Measured Images

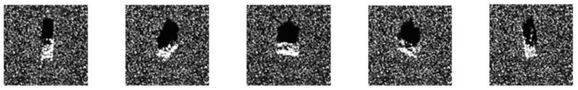

(b) Simulated Images (Proposed Method)

Fig. 5. Two-dimensional imaging comparision between (a) simulated and (b) measured images.

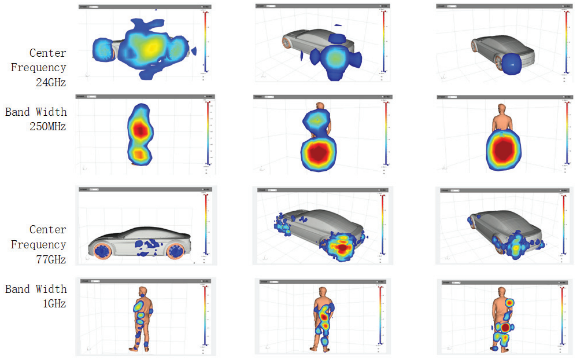

Fig. 6. Three-dimensional imaging of typical vehicles and pedestrians at typical frequency bands.

vided in this paper can help acquire three-dimensional imaging training data for autonomous driving technology.

Figure 6 shows the three-dimensional imaging results of two types of road elements, vehicles and pedestrians, respectively, under 24 GHz (bandwidth 250 MHz) and 77 GHz (bandwidth 1 GHz), demonstrating different radar features from different perspectives. By taking them as typical scenes of panoramic streets and adding various typical elements such as vegetation, street lights, bicycles, etc. (as shown in Fig. 7), setting one of the vehicles with an autonomous driving MIMO radar, and setting the driving lane to constitute a typical autonomous driving scenario, the method proposed in this paper is used. The typical 3D imaging results under a working frequency of 77 GHz (bandwidth 1 GHz) are shown in Fig. 7. The left, middle, and right columns respectively represent the imaging results of beams irradiating to the left, middle, and right directions.

As can be seen from the figure, the method proposed in this paper can provide three-dimensional imaging electromagnetic data under different radar working conditions for typical road elements and panoramic autonomous driving scenarios under different assumed conditions, providing massive training data for autonomous driving machine learning.

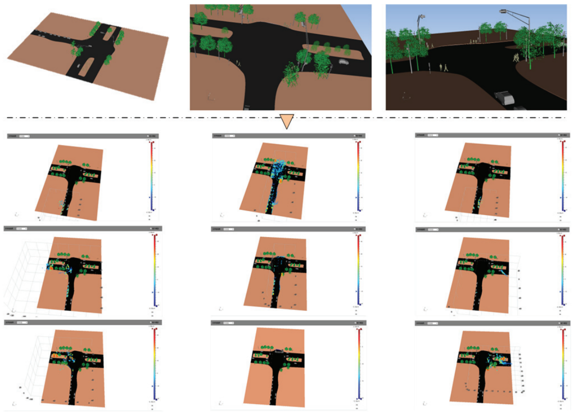

Fig. 7. Scenes and their three-dimensional radar imaging during a vehicle's journey.

V. CONCLUSION

This paper derives and implements a windowed rapid single-view radar imaging technique, providing the analytical extension functions and normalized weighting values when applying typical window functions in single-view imaging. This technique retains the analytical form of rapid single-view radar imaging and, like traditional imaging techniques, can achieve window function filtering and sidelobe suppression effects. Moreover, its imaging efficiency is significantly higher than that of traditional frequency-angle-scanning imaging. It can provide a large number of simulation-based training samples for technologies such as target recognition, remote sensing, and autonomous driving.

ACKNOWLEDGMENT

This work was supported by the sub-project 61890544 of the National Natural Science Foundation of China project 61890540.

REFERENCES

[1] N. Daryasafar, R. A. Sadeghzadeh, and M. Naser-Moghadasi, "A technique for multitarget tracking in synthetic aperture radar spotlight imaging mode based on promoted PHD filtering approach," *Radio Sci.*, vol. 52, no. 2, pp. 248-258, Feb. 2017.

[2] H. Wang, Z. Chen, and S. Zheng, "Preliminary research of low-RCS moving target detection based on Ka-band video SAR," *IEEE Geosci. Remote Sens. Lett.*, vol. 14, no. 6, pp. 811-815, June 2017.

[3] K. D. Singh, "Automated spectral mapping and subpixel classification in the part of thar desert using EO-1 satellite hyperion data," *IEEE Geosci. Remote Sens. Lett.*, vol. 15, no. 9, pp. 1437-1440, Sep. 2018.

[4] C. Hu, L. Wang, Z. Li, and D. Zhu, "Inverse synthetic aperture radar imaging using a fully convolutional neural network," *IEEE Geoscience and Remote Sensing Letters*, vol. 17, no. 7, pp. 1203-1207, Oct. 2019.

[5] G. Xu, B. Zhang, H. Yu, J. Chen, M. Xing, and W. Hong, "Sparse synthetic aperture radar imaging from compressed sensing and machine learning: Theories, applications, and trends," *IEEE Geoscience and Remote Sensing Magazine*, vol. 10, no. 4, pp. 32-69, 2022.

[6] L. Tsang, J. A. Kong, and R. T. Shin, *Theory of Microwave Remote Sensing*, Wiley-Interscience, New York, 1985.

[7] M. Yang, P. López-Dekker, P. Dheenathayalan, F. Biljecki, M. Liao, and R. F. Hanssen, "Linking persistent scatterers to the built environment using ray tracing on urban models," *IEEE Trans. Geosci. Remote Sens.*, vol. 57, no. 8, pp. 5764-5776, Aug. 2019.

[8] S. K. Jeng, R. Bhalla, S. Lee, H. Ling, and D. J. Andersh, "A time-domain SBR technique for range-profile computation," Electromagnetics Lab. Tech. Rep., Univ. of Illinois, Sep. 1993.

[9] R. Bhalla and H. Ling, "A fast algorithm for signature prediction and image formation using the shooting and bouncing ray technique," *IEEE Trans. Antennas Propag.*, vol. 43, no. 7, pp. 727-731, July 1995.

[10] R. Bhalla and H. Ling, "Image domain ray tube integration formula for the shooting and bouncing ray technique," *Radio Sci.*, vol. 30, no. 5, pp. 1435-1446, Sep. 1995.

[11] O. Kechagias-Stamatis and N. Aouf, "Automatic target recognition on synthetic aperture radar imagery: A survey," *IEEE Aerosp. Electron. Syst. Mag.*, vol. 36, no. 3, pp. 56-81, Mar. 2021.

[12] J. H. Cho and C. G. Park, "Multiple feature aggregation using convolutional neural networks for SAR image-based automatic target recognition," *IEEE Geosci. Remote Sens. Lett.*, vol. 15, no. 12, pp. 1882-1886, Dec. 2018.

[13] Y. Sun, L. Du, Y. Wang, Y. Wang, and J. Hu, "SAR automatic target recognition based on dictionary learning and joint dynamic sparse representation," *IEEE Geosci. Remote Sens. Lett.*, vol. 13, no. 12, pp. 1777-1781, Dec. 2016.

[14] X. Dai, X. Wu, B. Wang, and L. Zhang, "Semisupervised scene classification for remote sensing images: A method based on convolutional neural networks and ensemble learning," *IEEE Geosci. Remote Sens. Lett.*, vol. 16, no. 6, pp. 869-873, June 2019.

[15] H. Stankwitz, R. Dallaire, and J. Fienup, "Nonlinear apodization for sidelobe control in SAR imagery," *IEEE Trans. Aerosp. Electron. Syst.*, vol. 31, no. 1, pp. 267-279, Jan. 1995.

[16] F. Harris, "On the use of windows for harmonic analysis with the discrete Fourier transform," *Proc. IEEE*, vol. 66, no. 1, pp. 51-83, Jan. 1978.

[17] N. Gong and X. Xu, "GRECO based fast prediction of 3D radar images for complex targets," *2017 Sensor Signal Processing for Defence Conference*, pp. 1-5, London, UK, Dec. 2017.

[18] X. Xu, "How to understand high resolution radar images and the pixel values of targets," *Chinese Journal of Radio Science*, vol. 34, no. 1, pp. 33-44, Feb. 2019.

[19] J. M. Jin, *The Finite Element Method in Electromagnetics*, Wiley, New York, 2014.

[20] K. Ren and R. J. Burkholder, "A uniform diffraction tomographic imaging algorithm for near-field microwave scanning through stratified media," *IEEE Trans. Antennas Propag.*, vol. 64, no. 12, pp. 5198-5207, Dec. 2016.

[21] Y. Li, J. Zhang, J. Niu, Y. Zhou, and L. Wang, "Computational implementation and asymptotic statistical performance analysis of range frequency autocorrelation function for radar high-speed target detection," *IEEE Trans. Comput. Imaging*, vol. 6, pp. 1297-1308, Aug. 2020.

[22] R. Bhalla, L. Lin, and D. Andersh, "A fast algorithm for 3D SAR simulation of target and terrain using Xpatch," *IEEE International Radar Conference*, pp. 377-382, Arlington, VA, USA, May 2005.

Wen Ming Yu was born in Zhuji, Zhejiang, China, in 1980. He received the B.Sc. and Ph.D. degrees from the Nanjing University of Science and Technology, Nanjing, China, in 2002 and 2007, respectively. He currently serves as a Lecturer at the School of Information Science and Engineering, Southeast University. His research interest is computational electromagnetics.

Yi Ting Yang (1992-) received the B.Sc. and M.Sc. degrees in communication engineering from the School of Electrical Engineering and Optical Technique, Nanjing University of Science and Technology, Nanjing, China, in 2013 and 2016, respectively. She is currently pursuing the Ph.D. degree in State Key Laboratory of Millimeter Waves, Southeast University, Nanjing. Her research interests include the areas of computational electromagnetics and absorbing material design.

Xiao Fei Lu was born in 1981. He received the B.S. and M.S. degrees from the Harbin Institute of Technology (HIT), Harbin, China, in 2002 and 2004, respectively, both in electronic engineering, and the Ph.D. degree in control theory and control engineering from Tsinghua University, Beijing, China, in 2012. He is currently an Engineer with JiuQuan Satellite Launch Center. His main research interests include target recognition, radar signal processing, and their practical application. He has authored or coauthored more than 20 papers.

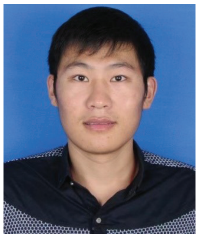

Chao Yang received the B.S. degree in applied physics from Xidian University, Xi'an, China, in 2014, and the Ph.D. degree in electronic science and technology from Zhejiang University, Hangzhou, China, in 2019. He is currently an assistant research fellow with Northwest Institute of Nuclear Technology, Xi'an, China. His research interests include computational electromagnetic, intense electromagnetic pulse environment, and electromagnetic scattering.

Zai Gao Chen was born in China in 1983. He received the B.S. degree in physical electronics from the University of Electronic Science and Technology of China, in 2005, and the M.S. degree in electromagnetic theory and microwave techniques from the Northwest Institute of Nuclear Technology (NINT), Xi'an, China, in 2008, and the Ph.D. degree in physical electronics from Xi'an Jiaotong University, Xi'an. He is currently working with NINT as an Associate Professor. His research interests mainly concentrate on numerical electromagnetic methods and plasma physics.

Tie Jun Cui (M'98-SM'00-F'15) received the B.Sc., M.Sc., and Ph.D. degrees in electrical engineering from Xidian University, Xi'an, China, in 1987, 1990, and 1993, respectively. He became an associate professor there in 1993, then worked in Germany at the University of Karlsruhe until 1997. After that, he joined the University of Illinois at Urbana-Champaign as a postdoc and research scientist. Since 2001, he has been a distinguished professor at Southeast University in China, where he now serves as the main professor and director of a key laboratory in millimeter waves, as well as founding an institute on electromagnetic space.

Dr. Cui's research interests include metamaterials and computational electromagnetics. He proposed the concepts of digital coding and programmable metamaterials, and realized their first prototypes, based on which he founded the new direction of information metamaterials, bridging the physical world and digital world. He has written books on the subject, published over 600 journal articles, and holds more than 150 patents. His work has been widely reported by Nature News, MIT Technology Review, Scientific American, Discover, New Scientists, etc.

Dr. Cui is the Academician of Chinese Academy of Science, and IEEE Fellow. He has held editorial roles for several scientific journals and has delivered over 100 keynote speeches. In 2019-2021, he was ranked in the top 1% for the highly cited papers in the field of Physics by Clarivate Web of Science (Highly Cited Researcher).

A New Miniaturized Double Stop-band Frequency Selective Surface

Qiannan Li^{1,2}, Qing Wang^{2}, Hui Zhang^{1}, Jian-Qiang Hou^{2}, and Jun Zhao^{2}

^{1}College of Physics and Electronic Engineering
Xianyang Normal University, Xianyang, 712000, China
2321887532@qq.com, xdzhxy@163.com

^{2}School of Physics and Electrical Engineering
Xidian University, Xi'an, 710071, China
wangqing@mail.xidian.edu.cn

Abstract – A miniaturized double stop-band FSS for WLAN was proposed based on the structure of a ring patch with internal branches and a cross zigzag loaded line. This construction is obtained by using the multilayer connection method to paint the two layers of the patch that we designed on the top and bottom of the dielectric substrate to simulate the designed construction by using HFSS simulation. Analyzing the frequency response characteristics of the FSS indicates that the construction can generate two transmission band gaps at 1.92-2.17 GHz and 4.94-5.99 GHz in the WLAN wave. This construction has stronger polarization stability and angle stability when the incident electromagnetic wave is 0-60°. It also has a simple construction, small size, and significant engineering application value.

Index Terms – Double stop-band, frequency selective surface (FSS), miniaturization, wireless local area network (WLAN).

I. INTRODUCTION

The typical frequency selective surface (FSS) is either a single layer or multilayer formed by coating a certain shape of metal patch (bandstop) or metal aperture (bandpass) on a dielectric substrate in a two-dimensional periodic array structure [1–5], which is essentially a spatial filter that has frequency selection characteristics for electromagnetic waves with different operating frequencies, polarization states, and incident angles, and does not absorb radio frequency energy [6]. The frequency response of FSS is mainly affected by the shape, size, and arrangement of the unit structure, the dielectric constant, and the thickness of the dielectric substrate. Its filtering characteristics can be controlled by adjusting its structural parameters. According to its filtering performance, FSS is mainly divided into four types: low pass, high pass, bandpass, and bandstop. It has been widely used in communications [7, 8], electromagnetic shielding [9–11], and radar stealth fields [12–14]

A series of studies on frequency selective surfaces originated from Francis Hopkinson [15] in 1785, who observed the diffraction spot phenomenon. Subsequently, American scientists Hopkinson and Rittenhouse [16] found through experiments that white light is decomposed into monochrome light when passed through thin ribbons. Since then, a series of studies on frequency selective surfaces have been developed. In the 19th century, Fraunhofer and Hertz further explained the phenomenon through experiments. In the 1970s, Munk [17] and Luebbrs completed basic theoretical research on typical FSSs. In recent years, with the improvement of channel capacity and communication quality, single frequency FSSs can no longer meet the requirements of high communication capacity, and the multifrequency design of FSSs has become a popular topic of research. At present, the design of a multiband FSS can be realized by multilayer cascade [18, 19], the multiple resonant element method [20], composite technology [21, 22], fractal structure [23, 24], and other methods. Much work has been performed on the design of multiband FSSs. In 2015, Majidzadeh [25] and others devised a combined FSS, based on the angle of the fractal and combined units, which can realize multiband filtering. In 2016, Gao [26] and others, based on the multi-resonance unit method, proposed a double-pass band FSS with a square grid and hybrid resonant structure. In the same year, Palange [27] and others designed a triple bandstop FSS with a fractal structure. In 2017, Zhou Yulong and others designed a windmill-type double stop-band FSS through electric dipole resonance and windmill FSS high-order mode resonance, which can realize -35 dB electromagnetic shielding in the band. In 2018, based on the multilayer cascade method, Malone and others applied a quadrilateral ring dual bandpass FSS for the X-band and K-band. In 2019, based on the square ring

Submitted On: July 13, 2023
Accepted On: February 7, 2024

https://doi.org/10.13052/2024.ACES.J.390102

structure, Zhou Ruicheng and others designed a three-way band FSS by using the multilayer cascade method, with a pass-band reflection coefficient of -30 dB.

There are few reports on the miniaturized band-stop FSS design of the wireless local area network (WLAN) frequency band. Based on previous studies, this paper proposes a new miniaturized dual stop-band frequency selective surface for WLAN. The structure is formed by coating different shapes of metal patches on the upper and lower sides of the dielectric substrate. This proposed structure achieves a strong shielding effect on electromagnetic waves in the WLAN frequency band and has strong polarization, angular stability, a simple structure, and easy processing.

II. STRUCTURE DESIGN

The resonant frequency of any FSS mainly depends on the size of the unit. For a specific structure, when the size and wavelength have a definite relationship, total reflection or total transmission of electromagnetic waves will occur on the FSS structure. Based on this, a dual-band blocking FSS applied to WLAN is proposed. As shown in Fig. 1 (a), this structure is divided into two layers: the ring patch [28] and the zigzag line structure based on the shape of a cross. These shapes are coated separately and are on the upper and lower sides of a square dielectric substrate with a side length *P* and thickness h respectively. The upper and lower structures of the designed FSS are shown in Figs. 1 (b) and (c). The double-band miniaturization design of the FSS is realized by loading branches inside the upper ring and twisting the lower cross-shaped structure. The dielectric substrate is tp-2, the dielectric constant is 6.55, and the loss tangent is 0.001. Table 1 shows the structural parameters of the FSS unit.

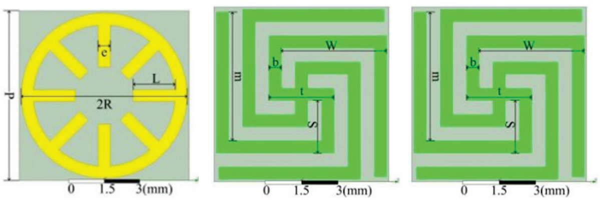

(a) (b) (c)

Fig. 1. Evolution of our FSS design: (a) ring patch structure loaded with internal branches, (b) zigzag line structure based on cross, and (c) evolved final shape of our FSS.

Table 1: FSS unit structure parameters

Parameter	***P***	***R***	***L***	**e**	**T**
Value(mm)	7.3	3.06	1.82	0.5	2.7
Parameter	**S**	**W**	***M***	**b**	***H***
Value (mm)	2.2	4.4	5.39	0.5	1.5

III. SIMULATION ANALYSIS AND OPTIMIZATION

A. FSS design process analysis

The electromagnetic simulation software HFSS is used for simulation calculation. Periodic boundary conditions are set along the x-axis and y-axis, and the Floquet excitation port is set on the z-axis to make the plane electromagnetic wave incident perpendicular to the FSS surface along the z-axis.

Figure 2 shows the frequency response characteristic curve of the single layer ring loaded branch structure. Figures 2 (a) and (b) show the influence that the curves of the ring outer radius *R* and the branch length *L* have on the FSS frequency response S_{21}, respectively. When the value of *R* is increased from 3 mm to 3.2 mm, and *L* is increased from 1.5 mm to 1.9 mm, the resonance points of the single-layer ring-loaded branch structure FSS all move in the low-frequency direction, and the stop-band bandwidth becomes slightly wider. When *R* is 3 mm and *L* is 1.5 mm, the stop-band range of the FSS is 3.37-6.99 GHz, and the in-band resonance point is 5.51 GHz, which can shield the electromagnetic wave in the 5 GHz (5.030-5.835 GHz) frequency band of the WLAN by -68 dB.

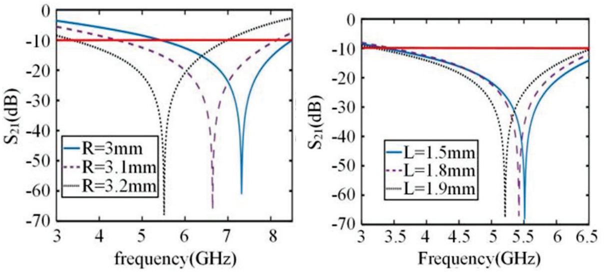

(a) (b)

Fig. 2. Frequency response characteristic curve 3 of the ring-loaded branch structure: (a) the influence of the ring outer radius *R* on the FSS frequency response and (b) the influence of the stub length *L* on the FSS frequency response.

Figure 3 shows the influence curve of the outermost line of the single-layer cross meander line structure (*m*) on the frequency response of the FSS. In the process of increasing *m* from 3.8 mm to 5.4 mm, the resonance point of the cross meander line structure FSS moves in the low-frequency direction from 2.81 GHz to 2.38 GHz, and the stop-band bandwidth is basically unchanged. When *m* is 4.8 mm, the FSS stop-band range of the structure is 1.94-2.87 GHz, and the resonance point is 2.46 GHz, which can shield the electromagnetic wave in the 2.4 GHz (2.4-2.4835 GHz) frequency band of the WLAN with -62 dB.

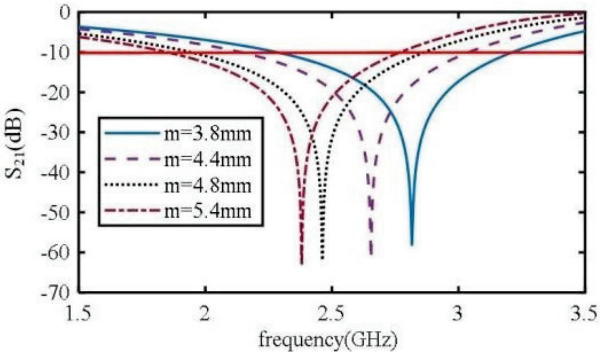

Fig. 3. The influence of the outer line length *m* of the cross zigzag line structure on the frequency response of FSS.

The research shows that the multiband design of FSSs can be realized through the multilayer cascade method. Based on this, this research cascades the ring-loaded branch structure and the cross zigzag structure in Section A and uses the parameter optimization function of HFSS to complete it. The frequency response characteristic curve of the new double-layer FSS after the wave simulation optimization design is shown in Fig. 4, and the optimized structural parameters are shown in Table 1. These show that the new FSS exhibits dual stop-band characteristics. Two transmission bands are formed at 1.92-2.71 GHz and 4.94-5.99 GHz. The resonance frequencies are f_1=2.45 GHz and f_2=5.80 GHz. The working frequency ranges of WLAN are 2.4-2.4835 GHz and 5.030-5.835 GHz. The designed FSS stop-band rejection is -60 dB and -45 dB, respectively. This structure has an excellent ability to suppress electromagnetic waves in the WLAN frequency band. The size of the designed FSS unit is 7.3 mm×7.3 mm. It is known that the resonance frequency in the 2.4 GHz frequency range is f_1=2.45 GHz, $c_0=3\times10^8$ m/s, and the wavelength of the first resonance frequency in vacuum is λ_0 =122.45 mm. Through analysis, it can be seen that the size of the designed FSS unit is $0.0596\lambda_1\times0.0596\lambda_1$, which meets the miniaturization design requirements and can be used in actual projects.

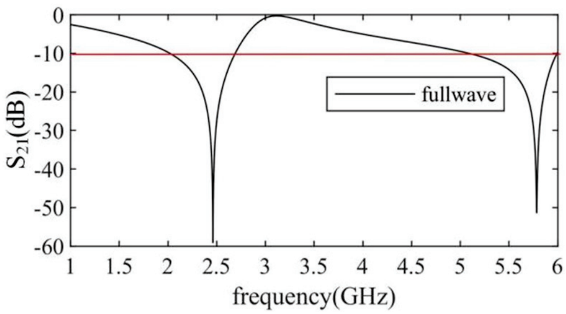

Fig. 4. Frequency response characteristic curve of the dual-frequency FSS.

B. Analysis of the surface current distribution

When the electromagnetic wave is incident on the FSS, the surface of the FSS will excite the surface current, and the scattered field that is generated will affect the transmittance of the electromagnetic wave. The filtering mechanism of the designed structure in the WLAN frequency range can be investigated by analyzing the surface current distribution of the FSS at the transmission zero point. By using the J-Surf function in HFSS to view the surface current distribution of the designed FSS, Figs. 5 (a) and (b) show the surface current distribution of the designed FSS when electromagnetic waves are perpendicular to 2.45 GHz and 5.9 GHz, respectively. Figure 5 (a) shows that the current when electromagnetic waves are incident at 2.45 GHz is mainly distributed in the lower structure of the FSS, which indicates that f_1 is mainly generated by the lower cross zigzag line structure. Figure 5 (b) shows that the current is mainly distributed in the upper structure when electromagnetic waves are incident at 5.6 GHz perpendicularly. It shows that f_2 is mainly produced by the upper ring-loaded branch structure. Obviously, the FSS filter characteristics can be controlled by adjusting the structural parameters of the upper and lower units.

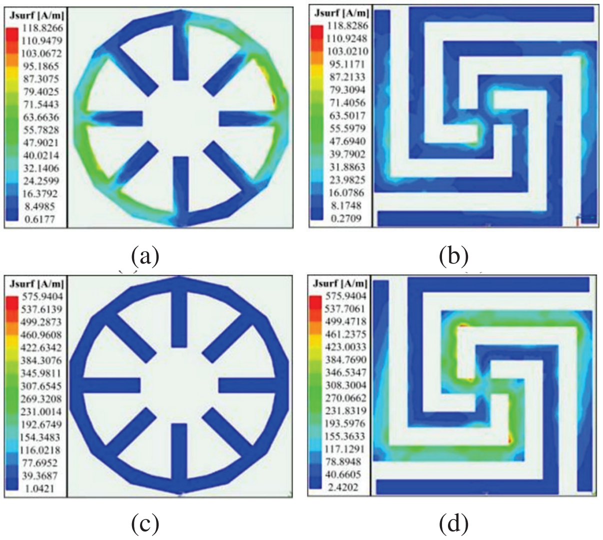

(a) (b)

(c) (d)

Fig. 5. FSS surface current distribution: (a) on the upper surface of the FSS when the frequency is 2.4 GHz, (b) on the lower surface of the FSS when the frequency is 2.4 GHz, (c) on the upper surface of the FSS when the frequency is 5.6 GHz, and (d) on the lower surface of the FSS when the frequency is 5.6 GHz.

C. Analysis of the relationship between the structure size and frequency response characteristics

Figures 6–8 show the influence curves of *m*, *L*, and *R* on the frequency response characteristics of the designed FSS. With increasing *m*, the transmission zero frequency of the 2.45 GHz band of the dual-frequency FSS shifts to the left, and the bandwidth is basically unchanged. The transmission zero frequency of the 5 GHz band is maintained at 5.8 GHz. With increasing *L* and *R*, the 5 GHz transmission zero frequency of the dual-band FSS shifts to the left, and the stop-band bandwidth increases slightly. The transmission zero point of the 2.4 GHz frequency band is basically unchanged. The frequency response in the 2.4 GHz frequency band is only affected by *m*, while *L* and *R* mainly regulate the frequency response in the 5 GHz frequency band.

In engineering applications, most of the time, electromagnetic waves are incident to an FSS at a certain angle, and the polarization modes of incident waves are diverse. To study the influence of the incident angle and polarization mode of the incident wave on the FSS designed in this paper, the FSS is irradiated with 0°, 15°, 30°, 45°, and 60° plane electromagnetic waves. The relationship between its frequency response curve and incident angle is obtained through an HFSS simulation calculation. Figure 9 (a) shows the S_{21} curve of the FSS under transverse electric (TE) polarizations, transverse magnetic (TM) polarizations, and full wave simulation. Figures 9 (b), (c), and (d) show the S_{21} curve of the full

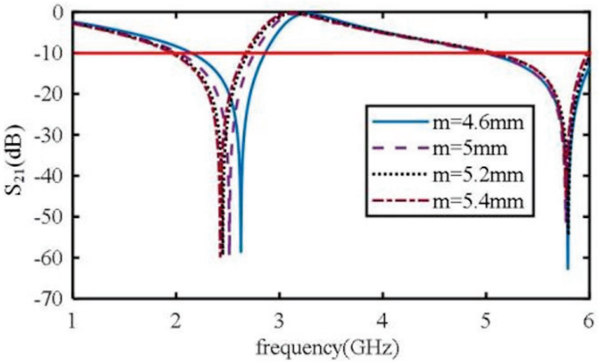

Fig. 6. The influence of *m* on the frequency response of the dual-band FSS.

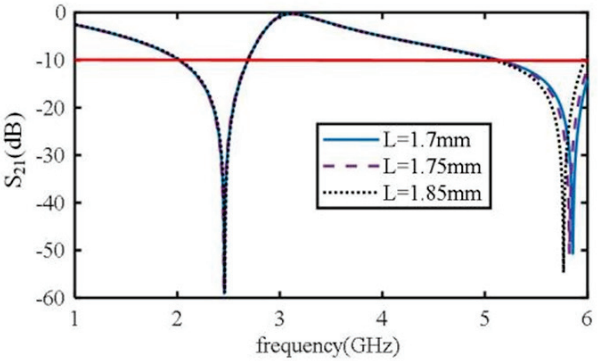

Fig. 7. The influence of *L* on the frequency response of the dual-band FSS.

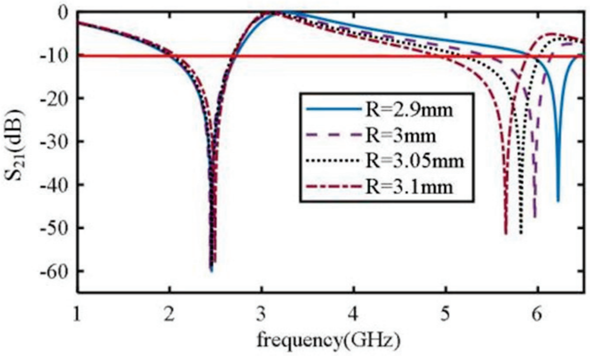

Fig. 8. The influence of *R* on the frequency response of the dual-band FSS.

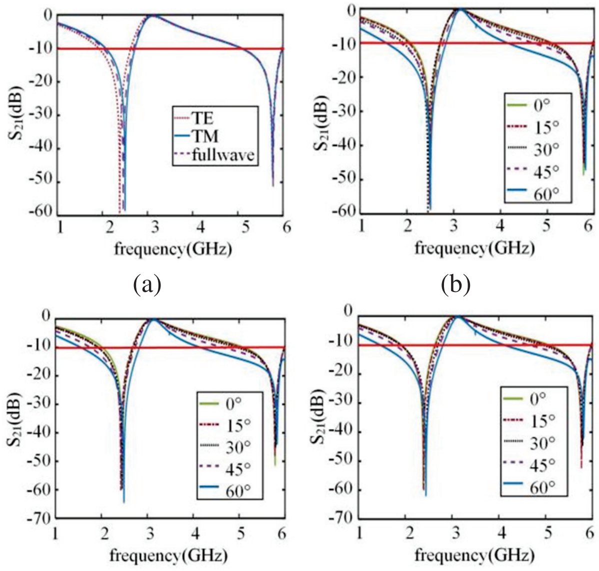

(a) (b)

(c) (d)

Fig. 9. Frequency response characteristic curve of the FSS when different polarized waves are incident at different angles: (a) polarization characteristics of the dual-band FSS, (b) S_{21} curve of FSS when the electromagnetic wave is incident at different angles in full wave mode, (c) S_{21} curve of FSS when the electromagnetic wave is incident at different angles in transverse electric (TE) polarizations wave mode, and (d) S_{21} curve of the FSS when the electromagnetic wave is incident at different angles in the transverse magnetic (TM) polarizations wave mode.

wave mode, transverse electric (TE) polarizations wave mode, and transverse magnetic (TM) polarizations wave mode when the electromagnetic wave is incident on the FSS at 0-60°. We find that the polarization mode of the incident wave does not affect the frequency response of the FSS in the 5 GHz frequency band. The transmission zero point within the 2.4 GHz frequency band is offset to the low frequency by 0.06 GHz when the transverse electric (TE) polarizations wave is incident. When the transverse magnetic (TM) polarizations wave is incident, it is offset to high frequency by 0.04 GHz, and the offset is small. Under different incident wave modes, when the incident angle of the designed FSS increases from 0-60°, the bandwidth of the two transmission stop-bands in the WLAN frequency band increases, the transmission zero point is basically maintained at approximately 2.45 GHz and 5.8 GHz, and the offset is very small. It shows that when different polarization waves are incident on the FSS at different angles, the FSS can show a better double stop-band function, and the structure has strong polarization stability and angle stability.

IV. EXPERIMENTAL VERIFICATION

To better verify the performance of the proposed FSS, a 190×190 mm FSS model was machined on tp-2 substrate with a thickness of 1.5 mm using printed circuit board technology, which is composed of 26×26 small unit structures, as shown in Fig. 10. The material of the medium substrate is tp-2 and its relative dielectric constant is 6.55 with the loss tangent of 0.001.

The frequency responses of the proposed FSS are measured by the free-space method [29], and its measurement environment is given in Fig. 11. There are two horn antennas (operating from 2 to 8 GHz), the FSS prototype, and turntable (can be used to adjust the angle of the incident wave). The FSS prototype is placed on the turntable for measurement of incident stability. A pair of horn antennas are located about 0.35 m apart from each side of the centered rotatable screen, so that a uniform plane wave striking upon the FSS. The two horn antennas are connected by the vector network analyzer.

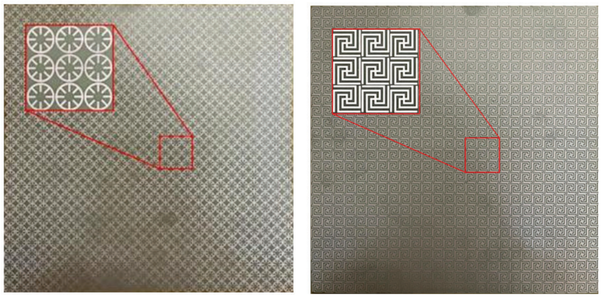
(a) (b)

Fig. 10. Photographs of the fabricated prototypes: (a) upper surface and (b) lower surface.


Fig. 11. Measurement setup.

The measured results under different polarizations are demonstrated in Fig. 12 compared with the simulated ones. The measurement results under different incident angles are shown in Fig. 13. It is clear that the transmission coefficients keep very stable for transverse electric (TE) and transverse magnetic (TM) polarizations. It is clear from the Fig. 13 that the proposed double layer FSS provides closely spaced dual stop-band response with highly stable angular independency. The frequency response characteristic curve of the FSS tested very closely resembles the simulation results. The operating frequency bands are 2-2.8 GHz and 4.9-6 GHz.

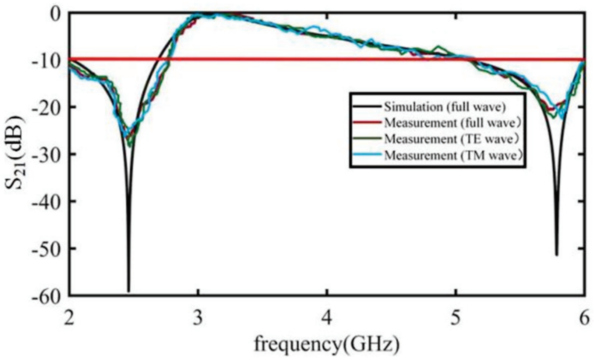

Fig. 12. Frequency response characteristic curve comparison between full-wave simulation and the transverse electric (TE) and transverse magnetic (TM) polarizations measurement data.

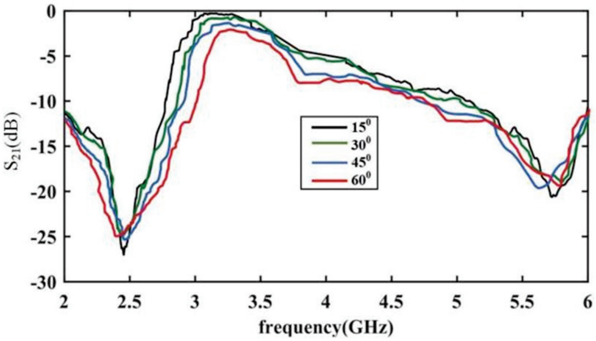

Fig. 13. Measurement results at different incident angles conditions.

V. CONCLUSION

Based on the traditional cross and ring structures, this paper proposes a miniaturized dual stop-band FSS applied to WLAN using the multilayer cascade method. In this structure, the designed two layers of patches are coated on the upper and lower layers of the dielectric substrate, and independent control of the transmission zero point can be realized by adjusting the geometric parameters of the upper and lower patch units. This structure produces two transmission band gaps in the WLAN frequency band, and the structure has better polarization stability and angle stability in the working frequency band. Both the simulation results and the measured results show that the FSS has good performance and can be applied to practical projects.

ACKNOWLEDGMENT

This study was partially supported by Provincial Science Foundation of Shaanxi (2021JM-128).

REFERENCES

[1] Y. Li, P. Ren, Z. Xiang, and B Xu, “Design of dual-stopband FSS with tightly spaced frequency response characteristics,” *IEEE Microwave and Wireless Components Letters*, vol. 32, no. 8, pp. 1011-1014, Apr. 2022.

[2] X.-J. Sheng, J.-J. Fan, N. Liu, and C.-B. Zhang, “A miniaturized dual-band FSS with controllable frequency resonances,” *IEEE Microw. Wireless Compon. Lett*, vol. 27, no. 10, pp. 915-917, Oct. 2017.

[3] S. Dey, “Conformal miniaturized angular stable triband frequency selective surface for EMI shielding,” *IEEE Transactions on Electromagnetic Compatibility*, vol. 64, no. 4, pp. 1031-1041, Mar. 2022.

[4] X. Zhou, B. Yuan, S. Chen, and G. Wang, “A novel design of a compact frequency-selective surface with high selectivity and angular stability,” *IEEE Microwave and Wireless Components Letters*, vol. 32, no. 7, pp. 931-934, Mar. 2022.

[5] P. Jiang, W. Jiang, W. Hu, and S. Gong, “An interlaced grid dual-band dual-polarized bandpass FSS with a large band ratio,” *IEEE Antennas and Wireless Propagation Letters*, vol. 21, no. 5, pp. 1027-1031, Mar. 2022.

[6] L. Zhao, X. Liang, Z.-M. Chen, Y. Lee, S. Zhang, H. Ma, and X. Shen, “An ultraminiaturized dual-stopband frequency selective surface for ultra high frequency,” *IEEE Access*, vol. 8, pp. 44830-44835, Mar. 2020.

[7] G. D. Catton, H. G. Espinosa, A. A. Dewani, and S. G. O’Keefe, “Miniature convoluted FSS for gain enhancement of a multiband antenna,” *IEEE Access*, vol. 9, pp. 36898-36907, Feb. 2021.

[8] A. J. A. Al Gburi, I. B. M. Ibrahim, M. Y. Zeain, and Z. Zakaria, “Compact size and high gain of CPW-fed UWB strawberry artistic shaped printed monopole antennas using FSS single layer reflector,” *IEEE Access*, vol. 8, pp. 92697-92707, May 2020.

[9] N. Liu, X. Sheng, C. Zhang, and D. Guo, “Design of frequency selective surface structure with high angular stability for radome application,” *IEEE Antennas and Wireless Propagation Letters*, vol. 17, no. 1, pp. 138-141, Jan. 2018.

[10] H. Huang and Z. Shen, “Low-RCS reflectarray with phase controllable absorptive frequency-selective reflector,” *IEEE Transactions on Antennas and Propagation*, vol. 67, no. 1, pp. 190-198, Jan. 2019.

[11] M. Koohestani, R. Perdriau, M. Ramdani, and J. Carlsson, “Frequency selective surfaces for electromagnetic shielding of pocket-sized transceivers,” *IEEE Transactions on Electromagnetic Compatibility*, vol. 62, no. 6, pp. 2785-2792, Dec. 2020.

[12] S. Narayan, G. Gulati, B. Sangeetha, and R. U. Nair, “Novel metamaterial-element-based FSS for airborne radome applications,” *IEEE Trans. Antennas Propag*, vol. 66, no. 9, pp. 4695-4707, Sep. 2018.

[13] B. Gao, S. Huang, Z. Ren, Y. Chen, and X. Wang, “Design and verification of an integrated free-standing thick-screen FSS radome,” *IEEE Antennas and Wireless Propagation Letters*, vol. 17, no. 9, pp. 1630-1634, Sep. 2018.

[14] J. Jiao, N. Xu, and J. Gao, “Complementary frequency selective surface with polarization selective responses,” *Applied Computational Electromagnetics Society (ACES) Journal*, vol. 37, no. 4, pp. 382-387, Apr. 2022.

[15] R. Mittra, C. H. Chan, and T. Cwik, “Techniques for analyzing frequency selective surfaces-A review,” *Proceedings of the IEEE*, vol. 76, no. 12, pp. 1593-1615, Dec. 1988.

[16] F. Hopkinson and D. Rittenhouse, "An optical problem, proposed by Mr. Hopkinson, and solved by Mr. Rittenhouse," *Trans. Amer. Phil. Soc*, vol. 2, pp. 201-206, 1786.

[17] B. Munk, R. Kouyoumjian, and L. Peters, "Reflection properties of periodic surfaces of loaded dipoles," *IEEE Transactions on Antennas and Propagation*, vol. 19, no. 5, pp. 612-617, Sep. 1971.

[18] M. Yan, J. Wang, H. Ma, M. Feng, Y. Pang, S. Qu, J. Zhang, and L. Zheng, "A tri-band, highly selective, bandpass FSS using cascaded multilayer loop arrays," *IEEE Transactions on Antennas and Propagation*, vol. 64, no. 5, pp. 2046-2049, May 2016.

[19] S. Vegesna, Y. Zhu, A. Bernussi, and M. Saed, "Terahertz two-layer frequency selective surfaces with improved transmission characteristics," *IEEE Transactions on Terahertz Science and Technology*, vol. 2, no. 4, pp. 441-448, July 2012.

[20] M. Gao, S. M. A. Momeni Hasan Abadi, and N. Behdad, "A dual-band, inductively coupled miniaturized-element frequency selective surface with higher order bandpass response," *IEEE Transactions on Antennas and Propagation*, vol. 64, no. 8, pp. 3729-3734, Aug. 2016.

[21] W. Wan, Y. Li, H. Wang, Y. Cheng, Z. Zhu, H. Chen, W. Wang, L. Zheng, J. Wang, and S. Qu, "Composite frequency selective structure with the integrated functionality of transmission, absorption, and scattering," *IEEE Antennas and Wireless Propagation Letters*, vol. 20, no. 9, pp. 1819-1823, Sep. 2021.

[22] Y. Ma, X. Zhang, S. Wu, Y. Yuan, and N. Yuan, "A hybrid 2-d-3-d miniaturized multiorder wide bandpass FSS," *IEEE Antennas and Wireless Propagation Letters*, vol. 21, no. 2, pp. 307-311, Feb. 2022.

[23] L. Murugasamy and R. Sivasamy, "A novel fractal inspired iterated four-legged loaded loop elements based 2.5-D miniaturized frequency selective surface," *IEEE Transactions on Electromagnetic Compatibility*, vol. 63, no. 6, pp. 2164-2167, Dec. 2021.

[24] V. Chaudhary and R. Panwar, "Neural network topology-based terahertz absorber using fractal frequency selective surface," *IEEE Sensors Journal*, vol. 21, no. 21, pp. 24028-24037, Sep. 2021.

[25] M. Majidzadeh, C. Ghobadi, and J. Nourinia, "Novel single layer reconfigurable frequency selective surface with UWB and multi-band modes of operation," *AEU-International Journal of Electronics and Communications*, vol. 70, no. 2, pp. 151-161, Feb. 2015.

[26] M. Gao, S. M. A. Momeni Hasan Abadi, and N. Behdad, "A dual-band, inductively coupled miniaturized-element frequency selective surface with higher order bandpass response," *IEEE Transactions on Antennas and Propagation*, vol. 64, no. 8, pp. 3729-3734, Aug. 2016.

[27] A. K. Palange, A. Sonker, and S. S. Yadav, "Designing of multiband frequency selective surfaces," in *2016 International Conference on Communication and Signal Processing (ICCSP)*, Melmaruvathur, India, pp. 0491-0494, Apr. 2016.

[28] S. U. Rahman, H. Deng, and M. Sajjad, "Angularly stable frequency selective surface for the gain enhancement of isolated multiple input multiple output antenna," *Microwave and Optical Technology Letters*, vol. 63, no. 11, pp. 2803-2810, Mar. 2021.

[29] Z. Yu and W. Tang, "A third-order bandpass three-dimensional frequency selective surface with multiple transmission zeros," *Applied Computational Electromagnetics Society (ACES) Journal*, vol. 35, no. 12, pp. 1548-1555, Dec. 2020.

Qiannan Li was born Shaanxi, China, in 1994. She received the B.S. degree in Physics from Xianyang Normal University, in 2019 and M.S. degree in optics from Xi'an Technological University, in 2022. She is currently an Assistant Experimenter with the School of College of Physics & Electronic Engineering, Xianyang Normal University, Xianyang. Her research interests include bioelectromagnetics and microwave antenna.

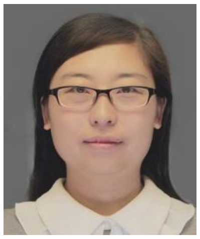

Qing Wang was born Shaanxi, China, in 1984. She received the B.Eng. degree in Measuring and Control Technology and Instrumentations from Xidian University, China, in 2006 and Ph.D. degree in Electromagnetic Field and Microwave Technology from Xidian University, China, in 2012. From 2009 to 2011, she was a visiting student in Clemson University, USA. She is currently an Assistant Professor with the School of Electronic Engineering, Xidian University, Xi'an. Her research interests include computational electromagnetics and millimeter wave technology.

Hui Zhang was born Shaanxi, China, in 1965. He received the M.E. degree in Biomedical Engineering from Xi'an University of Electronic Science and Technology, China, in 2000 and Ph.D. degree in Circuit and Systems from Northwestern Polytechnical University, China, in 2005. He is currently an Professor with the School of college of physics & electronic engineering, Xianyang Normal University, Xianyang. His research interest contains bioelectromagnetics and computational electromagnetics.

Jian-Qiang Hou received the B.Eng. degree in electromagnetic field and microwave technology from Xidian University, China, in 1999, M.E. degree in electromagnetic field and microwave technology from Xidian University, China, in 2004 and Ph.D. degree in electromagnetic field and microwave technology from Xidian University, China, in 2012. He is currently an associate Professor with the School of Electronic Engineering, Xidian University, Xi'an. His research interest contains microwave millimeter-wave circuits and systems and modeling and design of microwave devices and optoelectronic devices.

Jun Zhao was born in DaLian, Liaoning, China, in 1997. He received the B.S. degree from the Dalian Maritime University, Dalian, China, in 2020, and the M.E. degree in electronics and communication engineering from Xidian University, Xi'an, China, in 2023. His research interests include electromagnetic metasurface and lens antenna.

ACES JOURNAL, Vol. 39, No. 01, January 2024

A Dual-Polarization Broadband Coupling Feed Dipole Antenna Based on Artificial Magnetic Conductor

Z. N. Jiang[1,2], Z. W. Li[1], and Z. X. Wang[1]

[1]School of Electronic Science and Applied Physics
Hefei University of Technology, Hefei, China
jiangzhaoneng@hfut.edu.cn, 1335677546@qq.com, 1364665074@qq.com

[2]National Mobile Communications Research Laboratory
Southeast University, Jiangsu, China

Abstract – A dual-polarized broadband coupled feed dipole antenna loaded with artificial magnetic conductor (AMC) structure is proposed. The proposed AMC structure with 4×4 elements shown in this paper consists of four perfect electrical conductor (PEC) rectangular strips and a ring to reduce the profile height of the dual-polarized dipole antenna. In addition, the dual-polarization antenna adopts coupling feed microstrip to excite two pairs of bow-tie patch. The overall size of the coupling feed dipole antenna is $1.1\lambda_0 \times 1.1\lambda_0 \times 0.09\lambda_0$ at 5.5 GHz. Measured results shows that the proposed dual-polarization antenna loaded AMC exhibit a 25.2% common working bandwidth (4.75-6.12 GHz). The isolation is less than -14 dB, and the peak gain is 10.6 dBi. This dipole antenna with AMC structure has the virtues of low profile, wide band, and good radiation performance and it has the potential to be used in C-band communication.

Index Terms – artificial magnetic conductor, coupled feed, dual-polarization, low profile.

I. INTRODUCTION

With the evolution of wireless technology in the field of personal communications and military applications, under the limited spectrum resources, there are increasingly more requirements for the design of antennas in communication systems. In order to reduce the influence of multipath effect on wireless communication system, dual-polarized antennas are designed and have been widely used [1–3]. So as to achieve directional radiation and maximum gain, the patch of a traditional dipole is kept away from the metal floor about $\lambda_0/4$ [4]. This results in a higher profile of the antenna, but the AMC structure solves this problem well.

Two independent ports are often used to feed across dipole antenna to obtain vertical and horizontal polarization [5–7]. Reference [8] designed a dual-polarized cross slot antenna using two orthogonal slot radiators. The common impedance bandwidth of the antenna at Ports 1 and 2 is 1.56-2.73 GHz (54.5%), the isolation is greater than -26 dB, and the profile height is about $0.27\lambda_0$. In [9], there is a pair of printed dipoles with a reflective ground to obtain two linear polarizations. The cross polarization of the dual-polarized dipole antenna is less than -30 dB within 575-722 MHz (22.7%), the port isolation is more than -35 dB, and the profile height is about $0.27\lambda_0$ at 575 MHz. Although the antenna in [8] and [9] has good performance, it is difficult to integrate with microwave circuit due to its complex structure and high profile.

In this paper, a broadband dual-polarized coupled feed dipole antenna loaded with AMC is presented. The antenna adopts coupling feed to excite two pairs of bow-tie patch, which realizes horizontal polarization and vertical polarization, respectively. The measured results show that the common impedance bandwidth of this antenna is 4.75-6.12 GHz (25.2%). The coupling feed structure adopted in this paper provides a new design idea for the double polarized dipole antenna loaded with the AMC structure.

II. DUAL-POLARIZATION DIPOLE DESIGN

The geometry of the bow-tie dual-polarized cross dipole antenna is shown in Fig. 1. The antenna is composed of a pair of bow-tie radiation structures, strip coupling microstrip line, coaxial feed structure, dielectric cylinder and PEC reflector plate. The patch is printed on a square Rogers 5880 substrate with a thickness of 1.016 mm. The bow-tie shaped radiation structure is printed on the lower surface of the dielectric substrate as a dual-polarized radiator. Port 1 is connected to a 0° dipole to induce 0° polarization, and Port 2 is connected to a 90° dipole to induce 90° polarization. At the center frequency of 5.5 GHz, the theoretical value should be a quarter wavelength, that is, 13.6 mm. After simulation and optimization, the overall design of the dipole is W1+W2+W3=10.1 mm, which is slightly different from the theoretical value. The width of the microstrip line

Submitted On: April 18, 2023
Accepted On: February 8, 2024

https://doi.org/10.13052/2024.ACES.J.390103

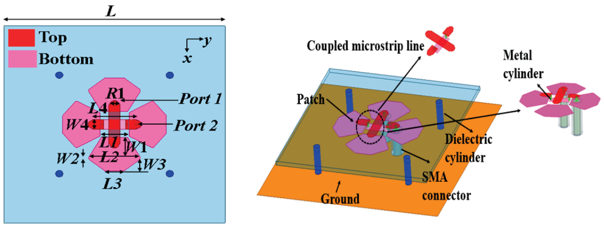

(a) (b)

Fig. 1. Geometry of the proposed dipole antenna: (a) top view and (b) side view.

is calculated according to 50 ohms, and the calculated result is 3.1 mm, and the actual value is 3 mm. Commercial simulation software High Frequency Structural Simulator (HFSS) was used for simulation calculation. The optimization algorithm is a quasi-Newton method, whose basic idea is to find the estimated value of the minimum point by quadratic expansion of the objective function near the minimum point. Figure 2 shows the simulation results of the reflection coefficients for the dual-polarized antenna. Due to the difference between the two strip coupled microstrip lines, the reflection coefficients of Port 1 and Port 2 are slightly different. The working bandwidths of Port 1 and Port 2 are 5.36-5.67 GHz and 5.25-5.52 GHz, respectively. The common bandwidth is 5.36-5.52 GHz. The port isolation within the working bandwidth is less than -11 dB.

By introducing an AMC structure instead of a PEC reflector, we can improve the performance of crossed dipole dual-polarization antennas, such as reducing the profile, increasing the operating bandwidth, increasing the isolation, and improving the radiation characteristics. Figure 3 shows the designed AMC structure and the corresponding simulation of reflection coefficient curve. The patch unit is printed on the Arlon 880 dielectric substrate, with a thickness of 2 mm. The bottom of the dielectric substrate is a PEC layer. The optimized dimensions of AMC are as follows: *S*=15 mm, *Ra*=5.5 mm, *Rb*=7.4 mm, *a*=1.7 mm, and *hamc*=2 mm.

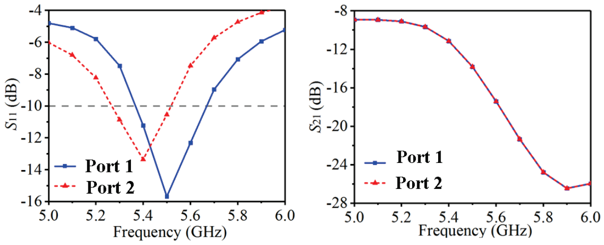

(a) (b)

Fig. 2. Simulation results of reflection coefficient (a) S_{11} and (b) S_{21}.

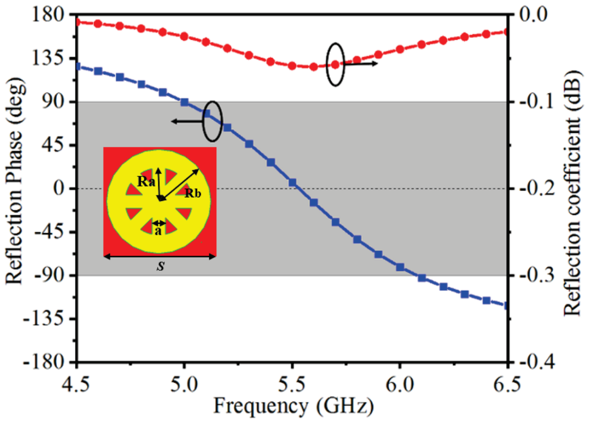

Fig. 3. Geometry of the proposed AMC and simulation results of reflection coefficient.

III. AMC UNIT DESIGN

It can be seen from Fig. 3 that the in-phase reflection bandwidth of AMC proposed in this section is 5-6.08 GHz, and the relative bandwidth is 19.5%. The frequency corresponding to the 0° reflection phase is close to the central frequency of 5.5 GHz, and the reflection coefficient modulus curve is above -0.06 dB, which basically shows the characteristics of total reflection.

In order to more intuitively explain the design idea of the AMC structure, Fig. 4 shows the two different AMC structures and the corresponding reflection characteristic curves. The initial AMC is a ring structure, and the in-phase reflection bandwidth is 4.16-4.6 GHz (10%). The reflection coefficient modulus is greater than -0.12 dB. In order to adjust the offset 0° reflection phase to the designed center frequency point of 5.5 GHz, it is necessary to move the reflection phase curve to the high frequency. Therefore, four rectangular structures are loaded on the initial AMC. It can be seen that the ring AMC loaded with rectangular branches not only has larger in-phase reflection bandwidth, but also has lower reflection loss, which proves the effectiveness of the design structure.

Figure 5 establishes the simple circuit model of the proposed AMC [10]. The gap between adjacent periodic patches and the slot gap in the patch together provide a slot capacitance C_a, the radius *Ra* of each circular patch and the width *a* of the rectangular branch will produce an inductance L_a, and C_d represents the capacitance between the dielectric substrate and the metal ground. The resonant frequency can be calculated by the following formula [11]:

$$f_r = \frac{1}{2\pi}\sqrt{\frac{1}{L_a}\left(\frac{1}{C_a}+\frac{1}{C_d}\right)}. \tag{1}$$

Obviously, the resonant frequency points of the designed AMC structure are mainly related to the equiv-

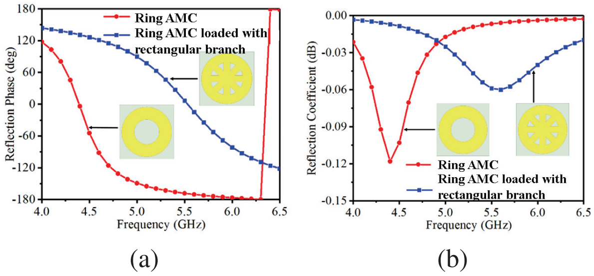

(a) (b)

Fig. 4. Reflection phase results of the proposed two AMC structures: (a) reflection phase and (b) reflection coefficient.

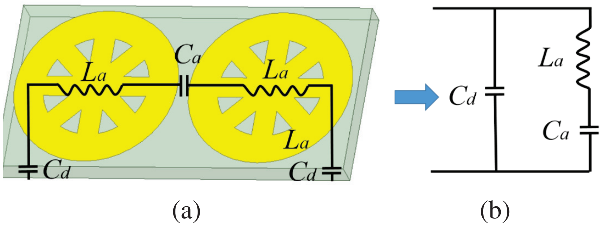

(a) (b)

Fig. 5. Circuit model of the AMC.

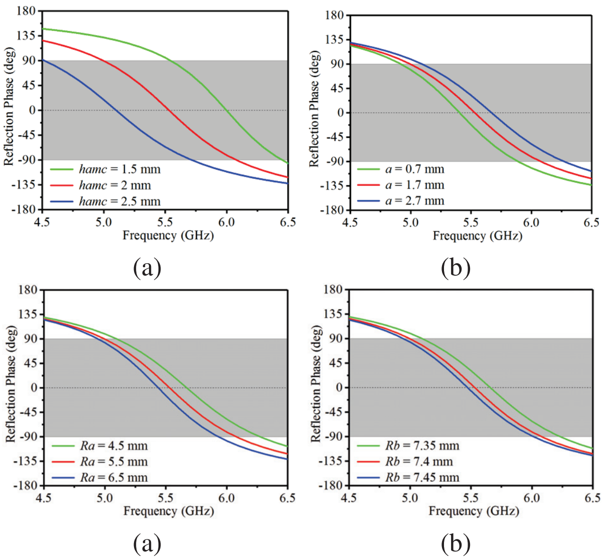

(a) (b)

(a) (b)

Fig. 6. The influence of different parameters on AMC reflection phase.

alent inductance of the patch, the capacitance by the patch slot and the parallel capacitance generated between the dielectric substrate and the ground. By adjusting the parameters of AMC, the ideal in-phase reflection bandwidth can be generated.

Figure 6 (a) shows the curve of AMC reflection phase changing with the thickness of medium layer *hamc*. It can be seen that with the increase of the dielectric plate height, the slope of the reflection phase curve becomes smaller, and the central resonant frequency moves to the low frequency. This is because the height of the dielectric plate increases, and the equivalent capacitance increases, that is, C_d becomes larger, so the resonant frequency decreases. Figure 6 (b) shows the curve of AMC reflection phase changing with rectangular branch width parameter *a*. With the increase of *a*, the resonant frequency point moves to high frequency, and the slope of the reflection phase curve slowly increases. Figure 6 (c) shows the variation curve of the AMC reflection phase with the radius *Ra* of the small ring. With the increase of *Ra*, the equivalent inductance L_a of the patch itself increases, the resonant frequency decreases, and the slope decreases slowly. When *Ra*=5.5 mm, the resonant frequency is closest to the center frequency, and the reflection phase bandwidth is larger. Figure 6 (d) shows the curve of the AMC reflection phase with the radius *Rb* of the large ring. With the increase of *Rb*, the equivalent gap capacitance C_a increases, the resonant frequency decreases and the in-phase reflection phase bandwidth decreases. When *Rb*=7.4 mm, the frequency corresponding to the 0° reflection phase appears at 5.5 GHz, so the value of the parameter *Rb* is finally chosen to be 7.4 mm. Thus, the resonant frequency of this AMC can be adjusted by changing the values of *hamc, Ra, Rb,* and *a*.

Figure 7 shows the overall structure of the dipole antenna loaded with AMC. The AMC is located 2 mm below the crossed dipole antenna, the total height of the antenna is 5.016 mm, and it is about $0.09\lambda_0$ at 5.5 GHz. After simulation and optimization, the final dimensions of the proposed dipole antenna are listed in Table 1.

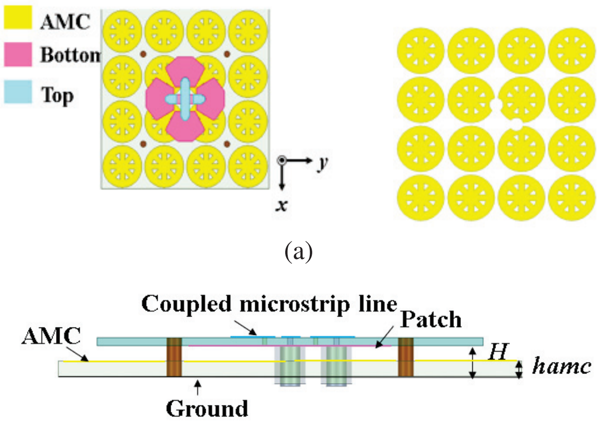

(a)

(b)

Fig. 7. The overall structure of the antenna: (a) top view and (b) side view.

Table 1: Dimension of the proposed dipole antenna (unit: mm)

Parameter	Value	Parameter	Value	Parameter	Value
L	50	$R1$	2.4	S	15
$W1$	6	$L1$	7.2	Ra	4.5
$W2$	0.6	$L2$	14	Rb	7
$W3$	3.5	$L3$	5.4	a	1.8
$W4$	3	$L4$	3	H	4
$hamc$	2				

IV. CROSS DIPOLE ANTENNA WITH AMC

In order to verify the performance of the antenna, a low profile dual-polarized antenna loaded with AMC is fabricated, as shown in Fig. 8. Figure 9 is the simulation and measured S-parameter diagram, and the measured results are in good agreement with the simulation results. The common impedance bandwidth is 4.75-6.12 GHz (25.2%), and the isolation is less than -14 dB. Figure 10 shows the simulation and measured gain and radiation efficiency of the antenna. The radiation efficiency exceeds 83% in the frequency band, and the maximum peak gain reaches 10.6 dB. At the central frequency, the gain of 5.5 GHz reaches 9.46 dBi. Good radiation characteristics are maintained in the whole frequency.

In order to verify the effectiveness of the AMC structure, the cross dipole antenna Ant-AMC loaded with AMC is compared with the cross dipole antenna Ant-PEC loaded with PEC. PEC reflector and AMC reflector have the same size, both of which are 60 × 60 mm, and the distance from both to the cross dipole radiator is 2 mm. The vertical and horizontal polarized radiation patterns of this antenna at 4.8 GHz, 5.5 GHz and 6 GHz are given in Fig. 11. From the figure, it can be seen that the antenna achieves good forward radiation with both the back lobe less than -10 dB and the cross-polarisation less than -20 dB. The spatial radiation patterns are slightly asymmetric, which is mainly due to the asymmetric placement of the feed position and the current imbalance between the two arms of the dipole caused by the coaxial feed. Figure 12 shows the comparison results of different antennas in S_{11}, S_{22}, gain and radiation efficiency (Port 1). The specific values are listed in Table 2.

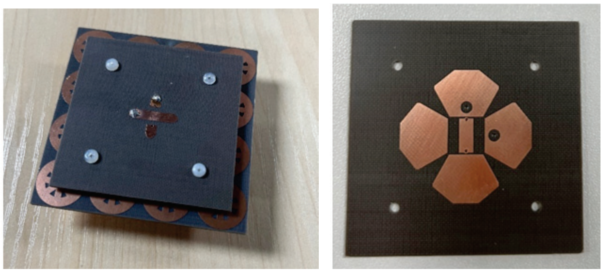
(a) (b)

Fig. 8. Fabricated antenna loaded with AMC: (a) overall structure drawing and (b) dipole patch layer.

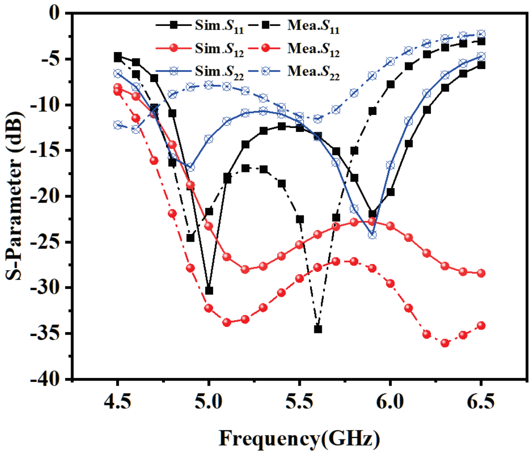

Fig. 9. Simulated and measured result of S-parameters.

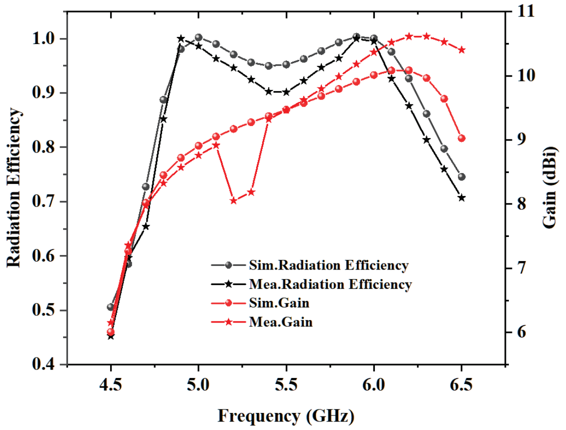

Fig. 10. Simulated and measured result of gain and radiation efficiency.

At the central frequency point, the antenna is improved from PEC loaded structure to AMC loaded structure, and the section size of the antenna is reduced from 0.13 to 0.09. With the profile height is reduced to $0.09\lambda_0$, the S-parameter curve deteriorates sharply in the required frequency band, and the gain and radiation efficiency under horizontal polarization mode also decrease accordingly.

It can be seen from Table 2 that the peak gain of the three antennas when excited at Port 1 has little change. After the introduction of AMC structure, it can be seen from Fig. 12 (c) that the antenna gain is significantly improved in the whole operating frequency band. At the

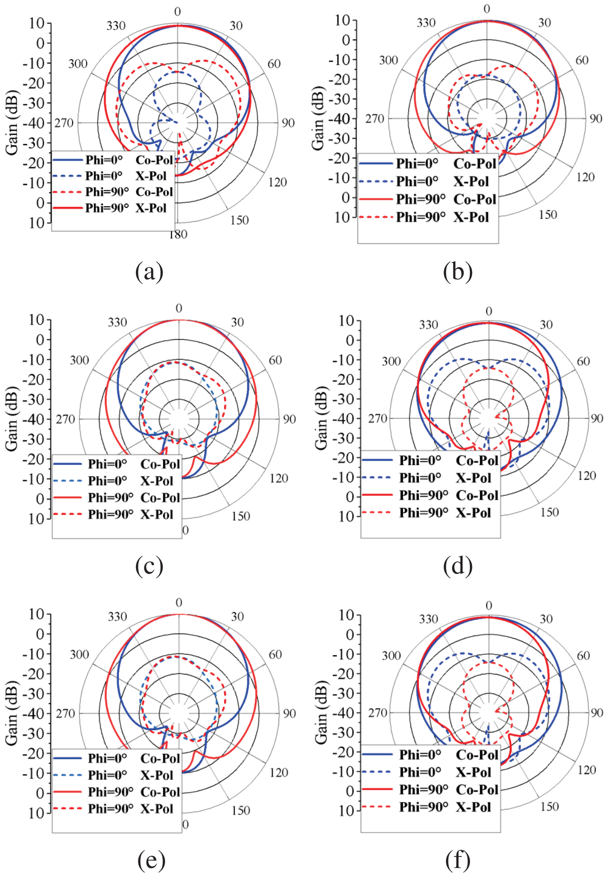

Fig. 11. Measured radiation patterns: (a) Port 1 -4.8 GHz, (b) Port 1 -5.5 GHz, (c) Port 1 -6 GHz, (d) Port 2 -4.8 GHz, (e) Port 2 -5.5 GHz, and (f) Port 2 -6 GHz.

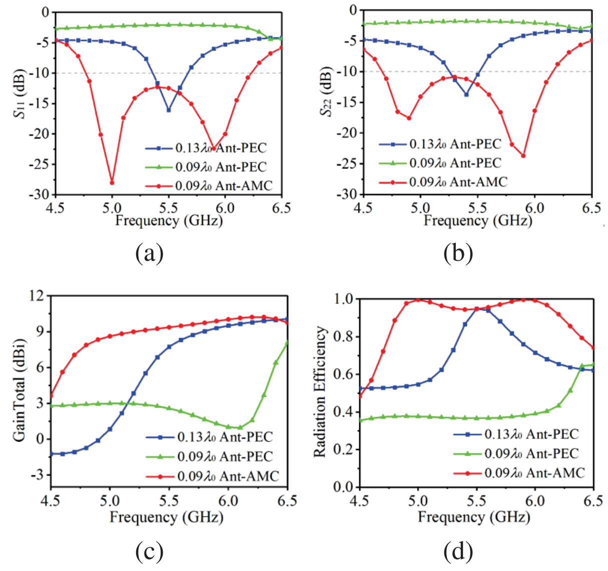

Fig. 12. Performance comparison results: (a) S_{11}, (b) S_{22}, (c) gain total, and (d) radiation efficiency.

Table 2: Comparison results of different antennas

Antenna	Port 1 BW/GHz	Port 1 BW/GHz	Port 1 Peak Gain/dBi	Efficiency (%)
$0.13\lambda_0$ Ant-PEC	5.36-5.67	5.25-5.52	10	60-94
$0.09\lambda_0$ Ant-PEC	-	-	8	35-65
$0.09\lambda_0$ Ant-AMC	4.77-6.23	4.66-6.16	10.3	80-99

same time, the radiation efficiency curve of the antenna loaded with AMC is also above the others. Through performance comparison, it is found that the AMC structure proposed in this paper can significantly reduce the profile height of the antenna, improve the working bandwidth of the antenna, and enhance the gain and radiation efficiency of the antenna.

Table 3 shows the comparison results of the working bandwidth and profile height between the antenna designed in this paper and the existing AMC based dual-polarized antenna. Compared with [6], [12] and [13], the proposed dual-polarized antenna has wider bandwidth, but the profile is higher than that of [13]. Compared with [6], [12], [13], and [14], the dual-polarized antenna proposed in this paper has higher gain.

Table 3: Comparison of the antenna with some existing work

Ref.	Bandwidth	Height (λ_0)	Peak Gain (dBi)
[6]	11.4%	0.21	7
[12]	15.6%	0.09	7.2
[13]	11.7%	0.06	7.2
[14]	20.5%	0.056	4.25
Pro.	25.2%	0.09	10.6

V. CONCLUSION

In this paper, a broadband dual-polarized coupling feed dipole antenna based on artificial magnetic conductor is designed, optimized and analyzed. The profile height of the proposed dual-polarized dipole antenna is $0.09\lambda_0$, and the antenna uses coupling feed to excite the dipole radiation patch, and the impedance bandwidth reaches 25.2%. The proposed antenna has the advantages of dual-polarization, low profile, broadband. It has great application potential in C-band radar communication and satellite communication.

ACKNOWLEDGMENT

This work was supported by fund of Nationa Mobile Communications Research Laboratory, Southeast University (No. 2023D05), Enterprise entrusted project (W2021JSKF0153, W2020JSFW0112), HeFei University of Technology teacher program (JZ2019-HGTB0093), Anhui Natural Science Foundation (2208085MF161), the Fundamental Research Funds for the Central Universities (JZ2021HGTA0144), and the Natural Science Foundation of Anhui Province (No. JZ2022AKZR0453).

REFERENCES

[1] Y. Li, Z. Zhang, W. Chen, Z. Feng, and M. F. Iskander, "A dual-polarization slot antenna using a compact CPW feeding structure," *IEEE Antennas and Wireless Propagation Letters*, vol. 9, pp. 191-194, 2010.

[2] Z. Wang, G.-X. Zhang, Y. Yin, and J. Wu, "Design of a dual-band high-gain antenna array for WLAN and WiMAX base station," *IEEE Antennas and Wireless Propagation Letters*, vol. 13, pp. 1721-1724, 2014.

[3] P. Kumar, S. Dwari, R. K. Saini, and M. K. Mandal, "Dual-band dual-sense polarization reconfigurable circularly polarized antenna," *IEEE Antennas and Wireless Propagation Letters*, vol. 18, no. 1, pp. 64-68, Jan. 2019.

[4] A. P. Feresidis, G. Goussetis, Shenhong Wang, and J. C. Vardaxoglou, "Artificial magnetic conductor surfaces and their application to low-profile high-gain planar antennas," *IEEE Transactions on Antennas and Propagation*, vol. 53, no. 1, pp. 209-215, Jan. 2005.

[5] D.-Z. Zheng and Q.-X. Chu, "A wideband dual-polarized antenna with two independently controllable resonant modes and its array for base-station applications," *IEEE Antennas and Wireless Propagation Letters*, vol. 16, pp. 2014-2017, 2017.

[6] Z.-Y. Zhang and K.-L. Wu, "A wideband dual-polarized dielectric magnetoelectric dipole antenna," *IEEE Transactions on Antennas and Propagation*, vol. 66, no. 10, pp. 5590-5595, Oct. 2018.

[7] L.-H. Wen, S. Gao, Q. Luo, Q. Yang, W. Hu, Y. Yin, X. Ren, and J. Wu, "A compact wideband dual-polarized antenna with enhanced upper out-of-band suppression," *IEEE Transactions on Antennas and Propagation*, vol. 67, no. 8, pp. 5194-5202, 2019.

[8] C. Zhou, H. Wong, and L. K. Yeung, "A wideband dual-polarized inductor-end slot antenna with stable beamwidth," *IEEE Antennas and Wireless Propagation Letters*, vol. 17, no. 4, pp. 608-612, Apr. 2018.

[9] S.-G. Zhou, P.-K. Tan, and T.-H. Chio, "Low-profile, wideband dual-polarized antenna with high isolation and low cross polarization," *IEEE Antennas and Wireless Propagation Letters*, vol. 11, pp. 1032-1035, 2012.

[10] M. Li, M. Y. Jamal, C. Zhou, L. Jiang, and L. K. Yeung, "A novel dipole configuration with improved out-of-band rejection and its applications in low-profile dual-band dual-polarized stacked antenna arrays," *IEEE Transactions on Antennas and Propagation,* vol. 69, no. 6, pp. 3517–3522, June 2021.

[11] H. R. Raad, A. I. Abbosh, H. M. Al-Rizzo, and D. G. Rucker, "Flexible and compact AMC based antenna for telemedicine applications," *IEEE Transactions on Antennas and Propagation*, vol. 61, no. 2, pp. 524-531, Feb. 2013.

[12] H. Zhai, K. Zhang, S. Yang, and D. Feng, "A low-profile dual-band dual-polarized antenna with an AMC surface for WLAN applications," *IEEE Antennas and Wireless Propagation Letters*, vol. 16, pp. 2692-2695, 2017.

[13] H. Yang, X. Liu, Y. Fan, and L. Xiong, "Dual-band textile antenna with dual circular polarizations using polarization rotation AMC for off-body communications," *IEEE Transactions on Antennas and Propagation*, vol. 70, no. 6, pp. 4189-4199, June 2022.

[14] W. Yang, W. Che, H. Jin, W. Feng, and Q. Xue, "A polarization-reconfigurable dipole antenna using polarization rotation AMC structure," *IEEE Transactions on Antennas and Propagation*, vol. 63, no. 12, pp. 5305-5315, Dec. 2015.

Zhaoneng Jiang was born in Xuancheng, China. He received the Ph.D. degree from Nangjing University of Science and Technology, Nanjing, China, in 2012. Since 2013, he has worked on the numerical method of computational electromagnetism. He is currently a Professor with the Hefei University of Technology, Hefei, China. He has authored or coauthored more than 90 papers in refereed international conferences and journals and has served as Program Committee Member in several international conferences. Currently, he is focusing on antenna and microwave device.

Zhiwei Li was born in Xuancheng, China. He received his master's degree from Hefei University of Technology, Hefei, China, in 2023. Since 2020, he has worked on electromagnetic metasurfaces and vortex electromagnetic waves.

Zhixin Wang was born in Anhui, China. She received her master's degree in electronic communication from Hefei University of Technology in 2022. Currently, she is focusing on antenna and microwave device.

A High-gain Low-sidelobe Dual-polarized Broadband Array Antenna

Qi-Lei Zhou, Bo-Wen Zhang, Neng-Wu Liu, and Guang Fu

National Key Laboratory of Antennas and Microwave Technology
Xidian University, Xian, 710075, China
20021110068@stu.xidian.edu.cn, zhangbowenjp@gmail.com, nwliu@xidian.edu.cn, gfu@mail.xidian.edu.cn

Abstract **–** In this paper, we present a dual-polarized broadband low side lobe array designed for operation in the Ku-band. The antenna array operates within the frequency range of 14.0 GHz to 15.2 GHz, covering a bandwidth of over 8%. To realize this wide operational frequency, we have selected broadband microstrip antenna elements as the units of the array. In order to fulfill the demanding criteria of broadband performance and low sidelobe characteristics, we introduce a broadband low-sidelobe feeding network based on a directional coupler design. This feeding network ensures connectivity with the antenna units, resulting in a voltage standing wave ratio (VSWR) <2 within the 14.0 GHz to 15.2 GHz frequency range. Furthermore, our antenna array achieves an array gain exceeding 21 dBi and keeps array sidelobes below -20 dB across the entire operating frequency band. Our research breakthrough addresses the critical design challenge of creating large-scale array antennas that combine broadband capabilities with high gain and minimal sidelobe interference.

Index Terms **–** broadband low sidelobe, dual-polarization, high-isolation, multi-layer.

I. INTRODUCTION

In recent years, the rapid advancement of electronic information technology has ushered in a compelling demand for enhanced antenna performance. Conventional single antennas are often inadequate in meeting the evolving requirements of modern electronic systems, which necessitate higher gain and broader bandwidth coverage. To address these challenges, array antennas have emerged as a prominent solution due to their ability to deliver increased gain. In addition to heightened gain, array antennas possess the distinct advantage of offering reduced sidelobes. The reduction in sidelobe radiation is of paramount importance in contemporary electronic systems, especially in the face of ever-growing electromagnetic complexity. Lower sidelobes equate to improved anti-interference capabilities, which are increasingly critical in ensuring the reliable operation of electronic systems within our intricate and crowded electromagnetic environment.

In the realm of synthetic array networks, there exist two predominant feeding configurations: series feed and parallel feed. Both configurations can achieve low sidelobe distributions through differential amplitude power divisions [1–2]. Arrays that utilize a series feed configuration present notable advantages such as high efficiency and structural simplicity. Nonetheless, intrinsic limitations in their feed structures typically confine them to a working bandwidth of less than 3% [3–7]. For applications necessitating broader bandwidths, it becomes imperative to employ a composite network that utilizes parallel feeding mechanisms [8–12]. Yet, as the scale of the array expands and sidelobe constraints become more stringent, the imperative to meet specified power ratios demands the use of T-type power dividers with larger power divisions. Notably, these T-type power dividers, when designed for larger power ratios, inherently possess wider microstrip line widths. This presents a significant design challenge and often results in compromised stability. Consequently, the realization of a wideband, high-gain, low-sidelobe array remains an intricate task.

Aside from the synthesis network with low side lobes for broadband, the broadband antenna unit has also become a key device. As resonant antennas, microstrip antennas inherently lack broadband characteristics due to their physical features. Traditional methods to widen the bandwidth, such as increasing thickness, coupling feed, and adding parasitic units, have proven effective. However, with the recent in-depth research on the resonant technology of microstrip antennas, multi-mode has emerged as a new method to effectively widen the bandwidth [12–18]. This approach can achieve various novel effects, such as achieving broader characteristics at a lower profile and manipulating radiation patterns.

In this paper, we introduce a high-power specific power divider designed around a directional coupler. This novel design attains a directional bandwidth exceeding 8%, maintains a sidelobe suppression of less than -25 dB within the operational frequency range, and exhibits an array gain surpassing 21 dB. Consequently, it enables the realization of a wideband, low-sidelobe, high-gain array, holding significant importance.

Submitted On: May 27, 2023
Accepted On: December 13, 2023

https://doi.org/10.13052/2024.ACES.J.390104

II. GEOMETRY AND WORING PRINCIPLE

The schematic representation of the antenna's overall structure is presented in Fig. 1. This high-gain, wideband, and low-sidelobe antenna array comprises a dual-polarized antenna array integrated with a wideband, low-sidelobe synthesis network. The inter-element separation in the array is set at 14 mm, resulting in a compact array with overall dimensions measuring 220×62 mm.

In order to extend the operational bandwidth of the microstrip antenna, a coupling feeding technique is employed within the antenna's radiation layer. Fabrication of the antenna, as well as the dual-polarization wideband, low-sidelobe array feed network, is achieved through the utilization of multilayer media printing technology. The antenna is printed on two layers of Rogers 4350B substrate, each with distinct thicknesses of 0.724 mm and 0.508 mm, respectively. Additionally, two layers of Rogers 4450F substrate, each 0.1 mm thick, are utilized for adhesion purposes.

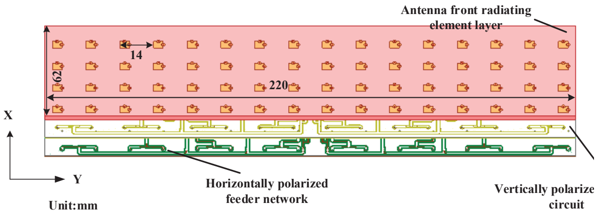

Fig. 1. Configuration of the proposed dual-polarized broadband low-sidelobe array antenna.

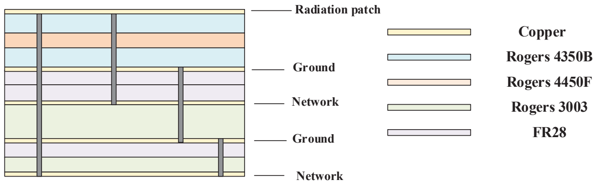

Fig. 2. Schematic diagram of multilayer laminated structure.

To optimize gain performance, the vertically polarized wideband low sidelobe feed network is fabricated on a 0.254 mm Rogers 3003 substrate, securely affixed between two layers of 0.1 mm FR28 substrate. In addition, the horizontally polarized wideband network is manufactured on a 0.127 mm Rogers's 3003 substrate, firmly attached to a single layer of 0.1 mm FR28 substrate.

In line with this construction methodology, the overall configuration of the wideband, high-gain, and low-sidelobe antenna, as proposed in this paper, can be segmented from top to bottom into distinct layers: the antenna radiation layer, a metallic base plate, the vertically polarized feed network, another metallic base plate, and the horizontally polarized feed network. The stratified composition of this multilayer board is visually depicted in Fig. 2.

A. Analysis of wideband antenna unit

Square patches serve as radiators, and their overall side length is illustrated in Fig. 3. Coupled feeders are employed to expand the operational bandwidth, and feed probes are utilized to connect the antenna radiation elements with the feed network. In order to validate the antenna element design, simulations are conducted on the wideband array antenna element. The simulated S-parameters and the radiation pattern of the broadband antenna unit are depicted in Figs. 4 and 5, respectively.

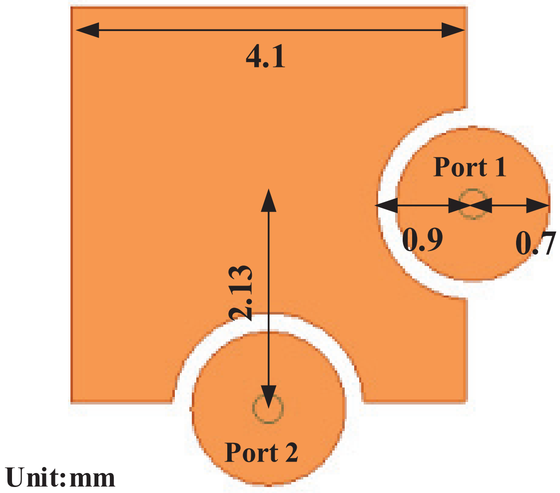

Fig. 3. Schematic diagram of the 2D structure antenna unit.

B. Analysis of wideband low sidelobe network

The wideband low sidelobe synthesis network is configured for parallel feeding, employing the Taylor

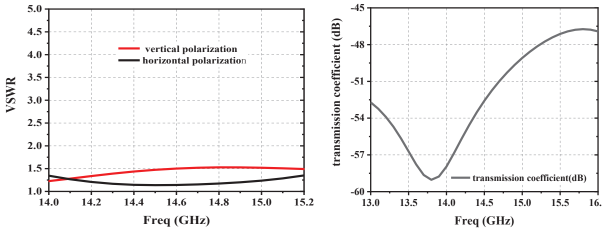

(a) (b)

Fig. 4. (a) Antenna unit VSWR and (b) isolation between the dual-polarized ports.

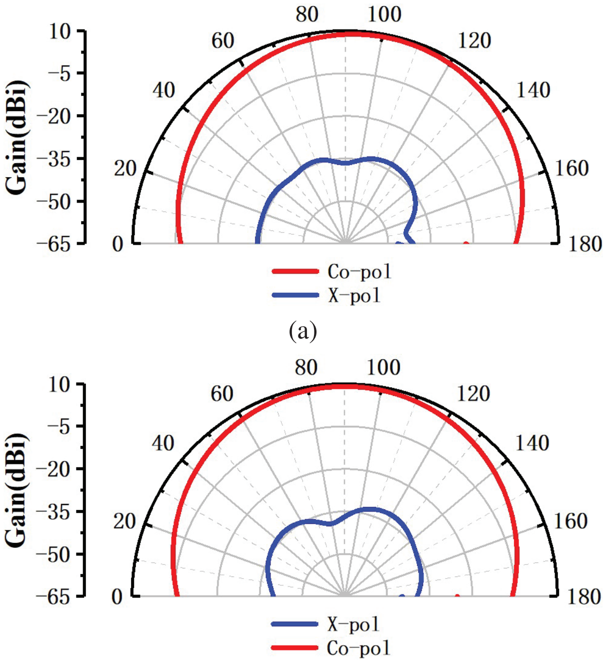

(a)

(b)

Fig. 5. The radiation patterns of the antenna unit at the center frequency points: (a) Vertical polarization 14.0 GHz E plan antenna pattern and (b) horizontal polarization 14.0 GHz E plan antenna pattern.

low sidelobe distribution. To attain ultra-low sidelobes and a heightened power ratio, the conventional T-junction power splitter's impedance conversion section necessitates an exceedingly fine high-impedance microstrip line, which may pose practical challenges. As delineated in Fig. 6, we introduce a novel 16-unit wideband low-sidelobe synthesis network based on a two-stage directional coupler.

To further optimize the performance of the wideband low sidelobe feed network and mitigate coupling effects between transmission lines, we implement a coupling elimination strategy using metal holes. The interface diagram for the feed network, catering to both vertical and horizontal polarizations, is presented below. Short-circuit pins are precisely positioned at a distance of 0.31 mm from the signal transmission lines, and the surrounding dimensions around the feed position are also provided.

Additionally, due to spatial constraints, feed synthesis networks with differing polarizations are segregated into distinct layers. Concurrently, the vertical polarization wideband low sidelobe feed network is positioned as a strip line beneath the antenna array radiation layer, while the horizontal polarization wideband low sidelobe feed network is located as a microstrip line at the lowermost layer.

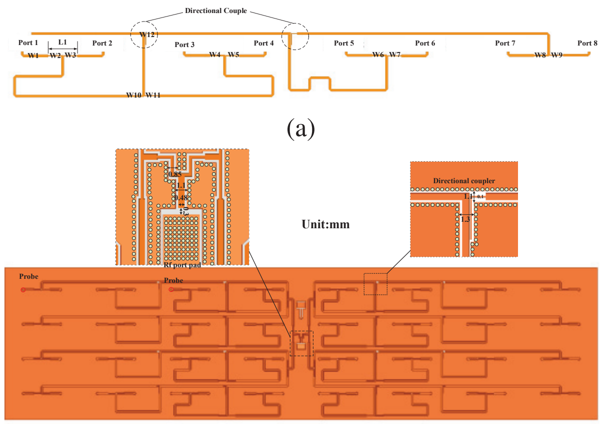

(a)

(b)

Fig. 6. Schematic diagram of half of a 16-unit synthetic horizontal polarization network based on directional coupler.

Drawing upon the principles of unequal amplitude power splitting and directional coupling, we have devised a wideband low sidelobe feed network tailored for horizontal and vertical polarization. The specific dimensional parameters are meticulously documented in Tables 1 and 2. It's noteworthy that the vertical polarization feed network exhibits a comparable topology to its horizontal polarization counterpart, albeit with distinct width specifications, meticulously delineated in Table 2

Table 1: Value of the corresponding parameter in the horizontal polarization feed network

Parameter	Value (mm)	Parameter	Value (mm)
L1	6.28	W7	0.16
W1	0.48	W8	0.29
W2	0.27	W9	0.18
W3	0.21	W10	0.28
W4	0.29	W11	0.18
W5	0.19	W12	0.1
W6	0.31		

Table 2: Value of the corresponding parameter in the horizontal polarization feed network

Parameter	Value (mm)	Parameter	Value (mm)
L1	6.28	W7	0.16
W1	0.48	W8	0.29
W2	0.27	W9	0.18
W3	0.21	W10	0.28
W4	0.29	W11	0.18
W5	0.19	W12	0.1
W6	0.31		

In pursuit of the design's validation for the comprehensive low sidelobe feed network, we have undertaken simulation and verification efforts, focusing on half of the 16-unit low sidelobe composite network. The resulting S-parameter data is visually represented in Figs. 7 and 8.

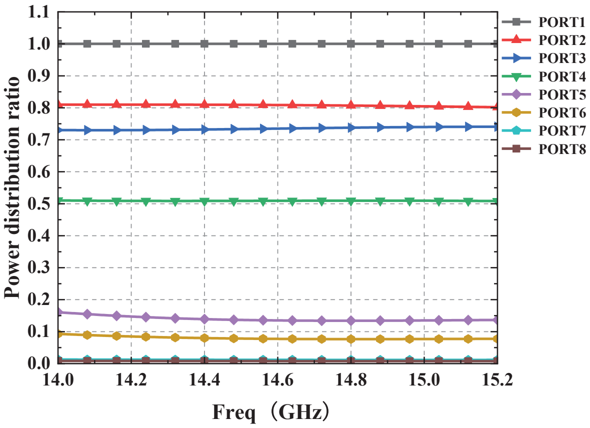

Fig. 7. Power distribution ratio of half of a 16-unit synthetic horizontal polarization network based on directional coupler.

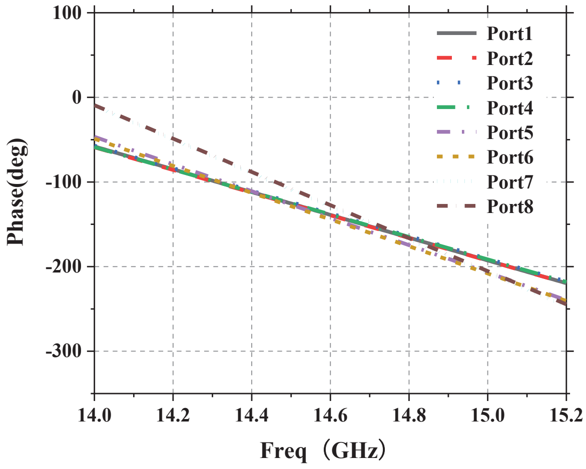

Fig. 8. Power distribution ratio of half of a 16-unit synthetic horizontal polarization network based on directional coupler.

The wideband low sidelobe feed network, utilizing a directional coupler, exhibits consistent and stable power distribution ratios across a broad bandwidth. This facilitates the realization of high-gain, wideband, low sidelobe technology. Notably, the achieved power distribution ratio effectively adheres to the amplitude distribution specifications prescribed by the Taylor distribution. Moreover, it maintains consistent phase characteristics over the wide frequency spectrum, highlighting its potential for broadband low sidelobe performance. It's worth noting that the design principles governing the vertical polarization wideband feed network closely parallel those of the horizontal polarization network.

C. Analysis of wideband low sidelobe network

By analyzing both the microstrip radiation unit and the broadband low sidelobe feed network, the combined effect of the distributed amplitude-phase characteristics of the broadband low sidelobe feed network enables the microstrip radiation unit to exhibit high-gain, broadband, low sidelobe characteristics within the specified frequency band.

III. RESULTS AND EXPERIMENTAL VALIDATION

Based on the operational principles of the antenna unit and the low sidelobe feed synthesis network, the connection of the antenna to the feed network via the feed probe yields a synthesized beam for the array. This beam exhibits a low sidelobe direction pattern across a broad spectrum. To rigorously validate the aforementioned design, comprehensive simulations and processing of the array antenna are performed.

Figure 9 shows a photograph of the prepared antenna, while Fig. 10 illustrates the measurement environment utilized during the antenna testing process. The initial evaluation of the proposed antenna involves both simulation and voltage standing wave measurements, as presented in Fig. 11. Notably, the simulation results closely align with the measured data, demonstrating good agreement.

Fig. 9. Photograph of the fabricated antenna in Fig. 1.

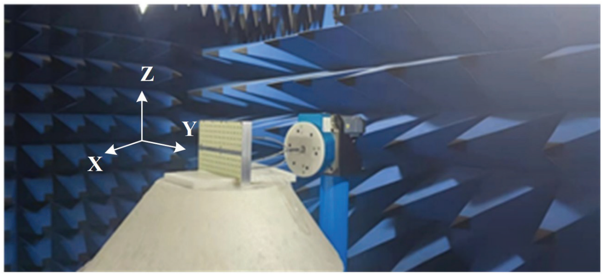

Fig. 10. Photograph of measuring the fabricated antenna in Fig. 1.

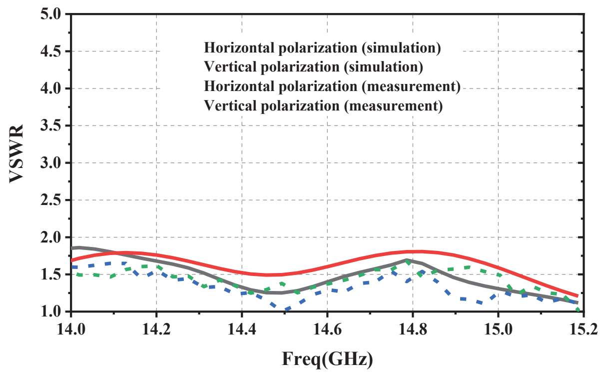

Fig. 11. Simulation and measurement of wideband low side lobe array antenna voltage standing wave ratio.

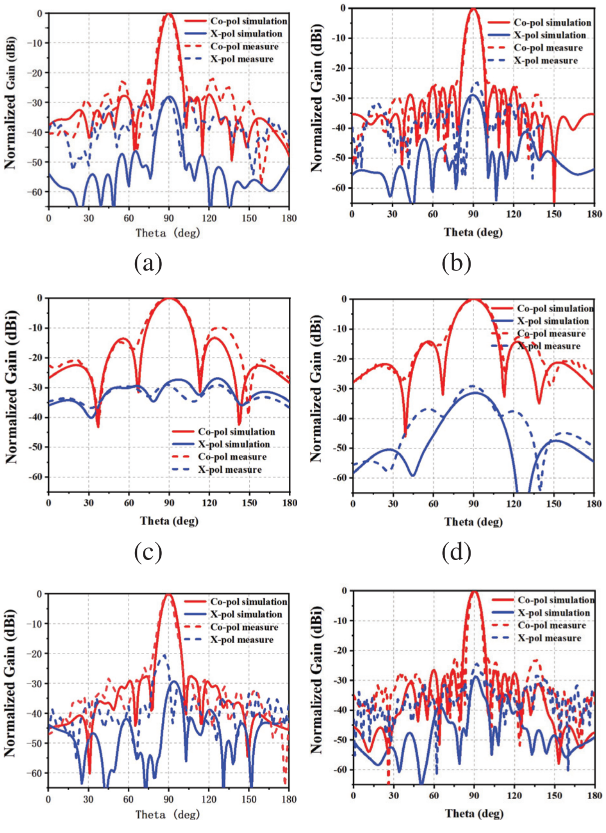

(a) (b) (c) (d) (e) (f)

Fig. 12. *Continued*.

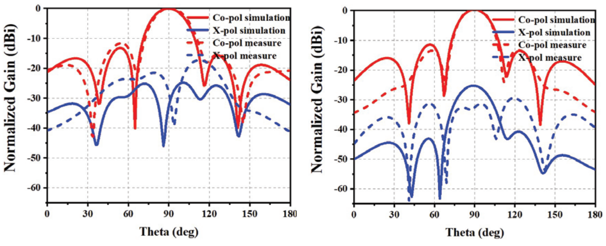

(g) (h)

Fig. 12. (a) horizontal polarization radiation pattern of the antenna array at 14.0 GHz in XOY plane, (b) horizontal polarization radiation pattern of the antenna array at 15.2 GHz in XOY plane, (c) horizontal polarization radiation pattern of the antenna array at 14.0 GHz in XOZ plane, (d) horizontal polarization radiation pattern of the antenna array at 15.2 GHz in XOZ plane, (e) vertical polarization radiation pattern of the antenna array at 14.0 GHz in XOY plane, (f) polarization the radiation patterns of the antenna array at 15.2 GHz in XOY plane, (g) vertical polarization radiation pattern of the antenna array at 14.0 GHz in XOZ plane, and (h) vertical polarization radiation pattern of the antenna array at 15.2 GHz in XOZ plane.

Furthermore, the measured results indicate that the antenna possesses an impedance bandwidth (VSWR <2) of approximately 8%, spanning the frequency range from 14 GHz to 15.2 GHz. Within this frequency band, sidelobes are effectively suppressed to levels lower than -25 dB. The radiation patterns of the proposed wideband, low sidelobe array antenna are visualized in Fig. 12. In this figure, subfigures (a) and (b) depict the 14 GHz vertical polarization YOZ-plane radiation pattern, (c) and (d) illustrate the 14GHz vertical polarization XOZ-plane radiation pattern, while (e) and (f) portray the horizontal polarization YOZ-plane radiation pattern at 15.2 GHz. Additionally, (g) and (h) exhibit the horizontal polarization XOZ-plane radiation pattern. These visualizations underscore the antenna array's capacity to maintain ultra-low sidelobes over a broad bandwidth, with high consistency observed between antenna testing and simulation results.

Moreover, it's important to note that the antenna achieves a maximum gain exceeding 21 dB within this

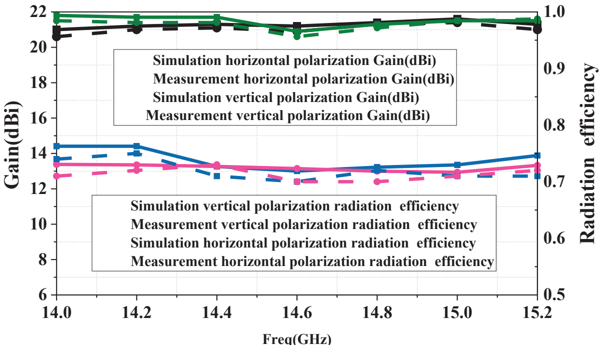

Fig. 13. Simulation and measurement gain of proposed array antenna.

operational frequency band, and this gain behavior in both simulation and testing is depicted in Fig. 12.

In addition, the array antenna exhibits a gain of over 20 dB within the 14 GHz-15.2 GHz frequency range. The measurement results closely align with the simulation outcomes, demonstrating a strong correspondence between them.

Finally, Table 3 presents a comprehensive summary of performance metrics for various antenna arrays. The data reveals that this antenna configuration attains a broader bandwidth while operating at a high-gain condition compared to previous research efforts.

Table 3: Comparison with previous

Ref.	**Gain (dB)**	**Sidelobe Level (dB)**	**Bandwidth**	**Feed Network Mode**	**Radiation Efficiency**	**Array Size**
[1]	16.0	-24.2	1%	Series	67.0%	1×26
[2]	9.0	-26.0	13%	Parallel	Less than 50%	1×6
[3]	20.0	-28.0	1%	Series	Unknown	16×8
[4]	13.0	-28.0	< 1%	Series	75%	3×3
[5]	19.0	-23.0	< 1%	Series	Unknown	8×8
[6]	23.0	-20.0	< 1%	Series	85%	2×24
[7]	22.0	-20.0	2%	Series	Unknown	6×8
[8]	14.0	-20.0	22%	Parallel	45.1%	1×8
[9]	15.4	-18.0	23%	Parallel	50.0%	1×8
[10]	15.5	-18.6	18%	Parallel	Unknown	1×8
[11]	15.3	-30.0	14%	Parallel	Unknown	4×4
[12]	15.2	-19.2	46%	Parallel	Unknown	1×8
Prop.	21.0	-25.0	8%	Parallel	>72%	16×4

IV. CONCLUSION

In this paper, a novel dual-polarized broadband low-sidelobe array antenna is proposed, in which the antenna elements are integrated with a novel directional coupler-based broadband low-sidelobe synthesis network through a multilayer board process. Over 21 dB of gain and less than 25 dB of side lobes can be achieved in over 8% of the bandwidth.

ACKNOWLEDGMENT

This work is supported by the National Natural Science Foundation of China under General Program (62271364), Key Research and Development Program of Shaanxi (Program No. 2023-GHZD-45), Fundamental Research Funds for the Central Universities (ZYTS23145), University of Macau (0080/2021/A2), and Special Grant CPG2023-00020-FST. (Corresponding author: Guang Fu)

REFERENCES

[1] H. Khalili, K. Mohammadpour-Aghdam, S. Alamdar, and M. Mohammad-Taheri, “Low-cost series-fed microstrip antenna arrays with extremely low sidelobe levels,” *IEEE Transactions on Antennas and Propagation*, vol. 66, no. 9, pp. 4606-4612, Sep. 2018.

[2] A. Falahati, M. NaghshvarianJahromi, and R. M. Edwards, “Wideband fan-beam low-sidelobe array antenna using grounded reflector for DECT, 3G, and ultra-wideband wireless applications,” *IEEE Transactions on Antennas and Propagation*, vol. 61, no. 2, pp. 700-706, Feb. 2013.

[3] J. Qian, H. Zhu, M. Tang, and J. Mao, “A 24 GHz microstrip comb array antenna with high sidelobe suppression for radar sensor,” *IEEE Antennas and Wireless Propagation Letters*, vol. 20, no. 7, pp. 1220-1224, July 2021.

[4] R. Chopra and G. Kumar, “Series-fed binomial microstrip arrays for extremely low sidelobe level,” *IEEE Transactions on Antennas and Propagation*, vol. 67, no. 6, pp. 4275-4279, June 2019.

[5] Y. Chang, Y.-C. Jiao, L. Zhang, G. Chen, and X. Qiu, “A K-band series-fed microstip array antenna with low sidelobe for anticollision radar application,” *2017 Sixth Asia-Pacific Conference on Antennas and Propagation (APCAP)*, Xi’an, China, pp. 1-3, 2017.

[6] J. Yue, C. Zhou, K. Xiao, L. Ding, and S. Chai, “W-band low-sidelobe series-fed slot array antenna based on groove gap waveguide,” *IEEE Antennas and Wireless Propagation Letters*, vol. 22, no. 4, pp. 908-912, Apr. 2023.

[7] Y. Liu, G. Bai, and M. C. E. Yagoub, “A 79GHz series fed microstrip patch antenna array with bandwidth enhancement and sidelobe suppression,” *2020 International Conference on Radar, Antenna, Microwave, Electronics, and Telecommunications (ICRAMET)*, Tangerang, Indonesia, pp. 155-158, 2020.

[8] W. Ma, W. Cao, R. Hong, J. Jin, and B. Zhang, “Planar broadband higher-order mode millimeter-wave microstrip patch antenna array with low sidelobe level,” *IEEE Antennas and Wireless Propagation Letters*, vol. 20, no. 12, pp. 2225-2229, Dec. 2021.

[9] J. Wang, Y. Li, and J. Wang, “A low-profile dual-mode slot-patch antenna for 5G millimeter-wave applications,” *IEEE Antennas and Wireless Propagation Letters*, vol. 21, no. 3, pp. 625-629, Mar. 2022.

[10] C. Chen, J. Chen, and X. Zhu, “Design of a low profile and low sidelobe metasurface antenna array for millimeter-wave application,” *2022 Asia-Pacific Microwave Conference (APMC)*, Yokohama, Japan, 2022.

[11] Y. Dong, X. Cai, and G. Wen, “Circularly polarized antenna array with suppressed sidelobes for electronic toll collection,” *IEEE Antennas and Wireless Propagation Letters*, vol. 21, no. 5, pp. 988-992, May 2022.

[12] G. Bai, Y. Liu, and C. Liao, “A broadband high gain microstrip yagi antenna array for mm-wave communication systems,” *2020 International Conference on Radar, Antenna, Microwave, Electronics, and Telecommunications (ICRAMET)*, Tangerang, Indonesia, pp. 180-183, 2020.

[13] L. Zhu and N. Liu, “Multimode resonator technique in antennas: A review,” *Electromagnetic Science*, vol. 1, no. 1, article no. 0010041, 2023.

[14] N.-W. Liu, L. Zhu, and W.-W. Choi, “Differential-fed microstrip patch antenna with bandwidth enhancement under operation of TM10 and TM30 modes,” *IEEE Transactions on Antennas and Propagation*, vol. 65, no. 4, pp. 1607-1614, 2017.

[15] N.-W. Liu, L. Zhu, W.-W. Choi, and X. Zhang, “A low-profile aperture-coupled microstrip antenna with enhanced bandwidth under dual resonance,” *IEEE Transactions on Antennas and Propagation*, vol. 65, no. 3, pp. 1055-1062, 2017.

[16] N.-W. Liu, L. Zhu, W.-W. Choi, and J.-D. Zhang, “A novel differential-fed patch antenna on stepped-impedance resonator with enhanced bandwidth under dual-resonance,” *IEEE Transactions on Antennas and Propagation*, vol. 64, no. 11, pp. 4618-4625, 2016.

[17] N.-W. Liu, L. Zhu, W.-W. Choi, and X. Zhang, “Wideband shorted patch antenna under radiation of dual-resonant modes,” *IEEE Transactions on Antennas and Propagation*, vol. 65, no. 6, pp. 2789-2796, June 2017.

[18] N.-W. Liu, L. Zhu, W.-W. Choi, and X. Zhang, “A low-profile differential-fed patch antenna with bandwidth enhancement and sidelobe reduction under operation of TM10 and TM12 modes,” *IEEE Transactions on Antennas and Propagation*, vol. 66, no. 9, pp. 4854-4859, 2018.

Qi-lei Zhou was born in Shaanxi, China, in September 1996. He received the B.S. degree in electronic information Technology from Xidian University, Xi’an, China, in 2019, where he is currently pursuing the Ph.D. degree. His current research interests include broadband miniaturized circularly polarized antenna and millimeter wave phased array.

Bo-Wen Zhang was born in Xi’an, China. He received the B.S. degree in electronic information Technology from Xidian University, Xi’an, China, in 2012. After that he received the M.E. in science and engineering from Toyo University, Tokyo, Japan. Since 2019, he is currently pursuing the Ph.D. degree from Xidian University. His current research interests include corrugated horn antenna beam-shaped array antenna and metamaterial applications in antenna

Neng-Wu Liu (Senior Member, IEEE) was born in Changde, China. He received the B.S. and M.E. degrees in electrical engineering from Xidian University, Xi’an, China, in 2012 and 2015, respectively, and the Ph.D. degree from the University of Macau, Macau, in 2017. Since 2018, he has been an Associate Professor with Xidian University. From 2019 to 2021, he was the UM Macao Post-Doctoral Research Fellow under the UM Macao Talent Program. His current research interests include designs of antenna theory, low-profile antenna, multimode antenna, wideband antenna, patch antenna, dielectric resonator antenna, circularly polarized antennas, filtering antenna, slot antenna, and phased array. Dr. Liu was a recipient of several academic awards, which includes the Best Student Paper Award in the 17th IEEE Macau/HK AP/MTT Postgraduate Conference and the Best Student Paper Award in 2017 National Conference on Antennas. He was also a recipient of the Outstanding Reviewer Award from the IEEE Transactions on Antennas and Propagation in 2020, 2021, and 2022; and the 2022 Macao Natural Science Awards (Second Prize) from the Science and Technology Development Fund (FDCT), Macau. He serves as an Associate Editor for IET Microwaves, Antennas and Propagation, IEEE Access, and Electronics Letters (IET).

Guang Fu received the B.S. and M.S. degrees in electromagnetic field and microwave technology from Xidian University, Xi’an, China, in 1984 and 1991, respectively.

He became a Professor with Xidian University, in 2001. His current research interests include theory and engineering of antenna and antenna array.

Diplexer Antenna for 5G Full-duplex Application

Hong Quang Nguyen[1], Trong Toan Do[2], Dinh Hai Truyen Hoang[2], Quoc Cuong Nguyen[1], and Minh Thuy Le[1*]

[1]School of Electrical and Electronic Engineering
Hanoi University of Science and Technology, 100000, Vietnam

[2]Viettel High Technology Industries Corporation
Viettel Group, 10000, Vietnam
thuy.leminh@hust.edu.vn
*Corresponding Author

***Abstract* –** This work proposes a spiral filter-based diplexer antenna for dual-band full-duplex 5G application in C-band. The shared radiator is formed by a cross-shape Yagi-Uda antenna. The dual-band full-duplex characteristic is obtained by applying a diplexer with two different band-stop filters (BSFs) based on a high-order rectangular spiral-shaped open-stub filter. The proposed diplexer antenna is suitable for modern 5G full-duplex communication system applications with a small frequency ratio and high isolation between two ports by applying a Wilkinson power divider. The diplexer antenna is designed, fabricated, and measured, showing good performance of channel isolations of 27 dB/23 dB and the antenna gain of 4.7 dBi/4.2 dBi at two operation bands from 3.56 GHz to 3.68 GHz and from 3.72 GHz to 3.83 GHz covering the required 100 MHz maximum bandwidth in C-band while its frequency ratio is only 1.04.

***Index Terms* –** Bandstop filter, diplexer antenna, dual-band antenna, full duplex, small frequency ratio.

I. INTRODUCTION

Full-duplex communication allows a device to transmit and receive signals at the same time. It can potentially increase capacity of the system and contribute to minimize the latency [1]. In the terminal devices, the full-duplex antenna enables transmitting and receiving signals using a shared radiator-based antenna. However, the main challenge in the full-duplex antenna is the interference between the transmitter (Tx) and receiver (Rx) when they operate at the same time on the same frequency band or close frequency bands [2, 3]. It has been receiving many studies to solve this problem [4–9]. In [4], a duplexing antenna is developed and denoted based on a dual-band slot antenna. The bandwidths are 6.2% and 11%, with a frequency ratio of 1.48, defined by the high band's center frequency divided by the low band's center frequency. The isolation between Tx and Rx is higher than 20 dB. A dual-port dual-band antenna with an integrated duplexer and filter working at 4.3 GHz and 6 GHz was proposed in [5]. The proposed antenna showed a high isolation of 30 dB with a frequency ratio of 1.39. However, it required three substrates, leading to a complex design process. In [6], the dual-band patch antenna is achieved by coupling a square patch with a hairpin resonator through a slot in the ground, and the frequency ratio is just 1.14. However, these structures are complex, with high insertion loss because they used the resonators for higher-order filters. In addition, multi-substrates lead to high-cost fabrication processes. In [8], a highly integrated dual-band duplex antenna for the base station was proposed using a cross-dipole antenna. The diplexer with a band-pass filter was integrated with a balun, which coupled a quarter-wavelength resonator operating at 3.5 GHz and 4.9 GHz, respectively. However, the isolation between two frequency bands is just 20 dB with a frequency ratio of 1.4. In [9], a low-profile single-layer duplex-filter antenna using a SIW-based cavity resonator was presented. Dual-band characteristics can be controlled by the slot-cum-loaded vias that half-mode SIW realized. Although it realized a small frequency ratio of 1.08, the isolation is just 21 dB. In most existing literature, the antenna and diplexer are integrated into a single inseparable module, namely a duplex antenna for more compact with small dimensions and high selectivity [5, 6, 10, 11]. However, they use high-cost substrates and multi-layers. Besides, these structures are more suitable for patch antenna applications.

One band that has proven particularly highly contested is the C-band, parts of which have been identified by the International Telecommunications Union for International Mobile Telecommunications (IMT)

Submitted On: October 9, 2023
Accepted On: February 7, 2024

https://doi.org/10.13052/2024.ACES.J.390105

services, more commonly called 5G in the 3.6 GHz band and fixed satellite service (FSS) earth stations operating in an adjacent frequency band of 3.8 GHz [12]. These two close bands may cause significant interference in designing a dual-band antenna for C-band full-duplex applications.

To overcome all these limitations, in this work, we propose a novel planar diplexer antenna with a minimal frequency ratio of 1.04 for dual-band full-duplex application in C-band. The diplexer antenna combines a diplexer and a wideband antenna element in a single layer for low-cost fabrication. Firstly, we design a wideband dipole antenna. Then, a diplexer is proposed using a Wilkinson power divider with two high-order spiral open stub filters to obtain high isolation between two close frequency bands. Note that using a diplexer will decrease the operating bandwidth, but the proposed antenna still covers the required 100 MHz bandwidth in C-band [13]. The contribution of the proposed work is as follows: (i) The Tx and Rx channels share a single Yagi-Uda antenna structure, making them more compact and flatter than separate radiation parts. (ii) The bent diplexer is presented with a compact size, adjustable frequency ratio by changing the stub length, and high Tx/Rx isolation. To the best of our knowledge, no dual-band antenna structure for complete duplex application in the open literature has a smaller frequency ratio than this work.

II. DIPLEXER ANTENNA DESIGN

A. Antenna element design

The initial dipole antenna is designed at the central frequency of 3.7 GHz, as antenna 1 in Fig. 1. The antenna evolution using V-arms dipole is shown in Fig. 1. To extend the bandwidth, the second dipole is added and rotated at an angle of 90° with the first two arms of the initial dipole, namely V-arms. The proposed V-arms-shaped dipole antenna uses an integrated J-shaped balun. The gap between the two lines and the length of the balun's shorted line are critical factors in adjusting impedance matching between a V-arms-shaped dipole and a J-shaped balun as antenna 3.

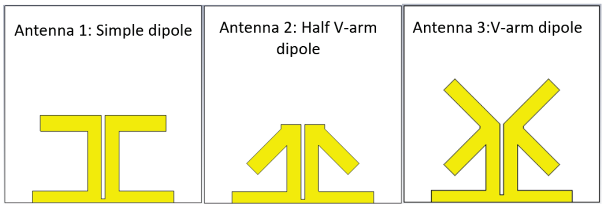

Fig. 1. Evaluation process of the antenna design.

The bandwidth expansion ability of the proposed structure is described through the reflection coefficient in Fig. 2. As can be seen, the bandwidth increases 10% from 13.2% to 23.2%.

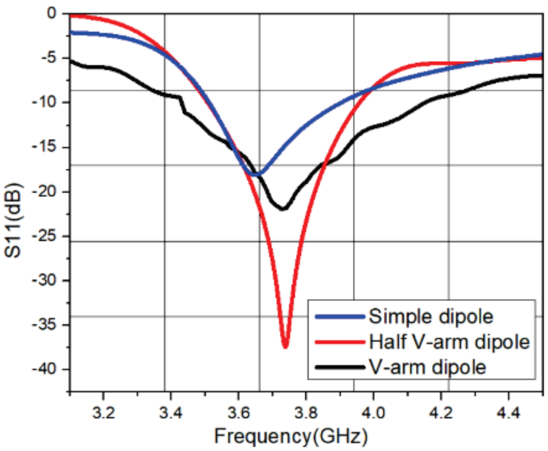

Fig. 2. Simulated S11 of three design steps.

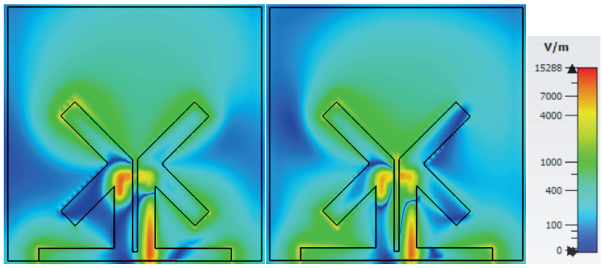

(a) (b)

Fig. 3. Electric field distribution of the proposed antenna at the metal-dielectric interface: (a) 3.5 GHz and (b) 3.9 GHz.

As shown in Fig. 3, the E-Field of the lower band is mostly determined by the two upper arms and the lower right arm. On the other hand, the E-Field distribution of higher frequencies is mainly created by the left V-arm and the gap between two V-arms.

To enhance the antenna's gain up to 6 dBi, two directors are placed above the V-arms according to the Yagi-Uda antenna principle. The geometry of the printed dipole antenna using Roger 4003C substrate (h= 0.8 mm, ε_r= 3.55, and tanδ = 0.0027) is shown in Fig. 4. Figure 5 (a) shows the simulated and measured results of the proposed printed V-arms dipole antenna and the gain simulation and measured result. It was found that there is an agreement between the simulated and the measured reflection coefficient. The simulated bandwidth of the proposed V-arms shaped dipole is 17.7% (3.45-4.12 GHz), and the measured result is 19% (3.41-4.13 GHz), respectively, fully cover the sub-6 5G frequencies band. The simulated gain of the proposed

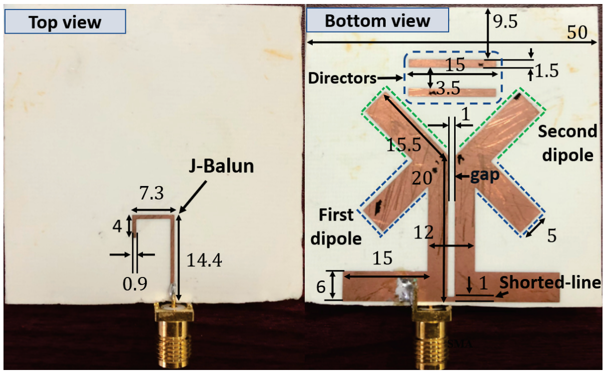

Fig. 4. Proposed antenna element (all dimensions are in mm).

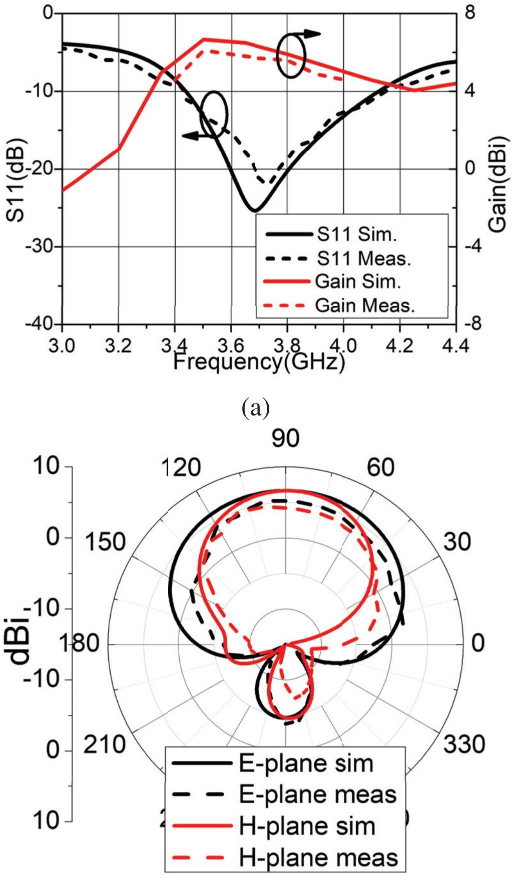

(a)

(b)

Fig. 5. (a) The simulated and measured S11 result of a V-arms dipole antenna and antenna gain and (b) radiation pattern at 3.7 GHz.

antenna is 5.64-6.64 dBi, while the measured value is 4.9-6 dBi over the operating bandwidth. The simulated radiation pattern is well matched with the measured one at the center frequency of 3.7 GHz, which indicates a directional radiation like a traditional Yagi Uda antenna, as in Fig. 5 (b). The half-power beam widths (HPBWs) are 122° and 75° in the E- and H-plane, respectively.

B. Diplexer design

A diplexer typically comprises two microwave bandpass filters (BPFs) at distinct center frequencies, and it was studied in the early 1960s by Matthaei et al. [14]. The desired diplexers are compact, low-cost, high isolation, planar and easily integrated into transceiver circuits [15–19]. In [15], a hairpin line diplexer with two wideband band-pass filters and high isolation was proposed. It comprises a T-junction connecting with two 5th-order hairpin line wideband band-pass filters operating at two bands of 3.1-4.9 GHz and 6.2-9.7 GHz. However, the isolation between the two channels is just 20 dB and poor S11 of -10 dB in the lower band. The hairpin line diplexer has considerable size and complexity limitations in design. In [17], a novel diplexer was proposed, which comprises two pairs of open-loop ring resonators with different resonant frequencies to couple with three microstrip lines of different lengths. However, its insertion loss is 2.73/3.68 dB, leading to low diplexer efficiency. Although numerous diplexers have been proposed, most focus on a large frequency ratio. However, for most modern 5G terminal devices, the TX and RX bands are incredibly close to each other. Thus, high isolation is challenging. This section proposes a compact, simple, high isolation design with a frequency ratio of nearly 1.0.

The proposed diplexer consists of two spiral-shaped filters working at two center frequencies of 3.6 GHz and 3.8 GHz, as shown in Fig. 6 (a). Because these two frequencies are close, applying BSFs instead of band-pass filters is more appropriate. The desired diplexer requires two narrow-operating bands to let the 3.6 GHz center frequency pass through and block the 3.8 GHz frequency and vice versa to other ports. Therefore, we use two high-order rectangular spiral-shaped open stubs for BSFs. The equivalent circuit of BSFs is shown in Fig. 6 (b). The open stub is equivalent to a serial $L_s{-}C_s$ circuit. L_s and C_s represent the inductance and the capacitance of the open stub, respectively. The ohmic loss is represented by a serial resistor R_s that is inserted next to the inductor since the conductive material is non-ideal. The center stop-band frequencies f_g are calculated by the inductor and the capacitor of the open stub, which can be adjusted by stub length. When the size of the open stub increases, the inductance L_s and the capacitance C_s become larger, resulting in a decrease in f_g. The stub width is an essential factor to adjust the impedance matching of Port 3’ to Port 3.

BSF is formed by $L_{sp}= (2n+1)\lambda_s/4$ open stub having narrow bandwidth and excellent selectivity (L_{sp} is

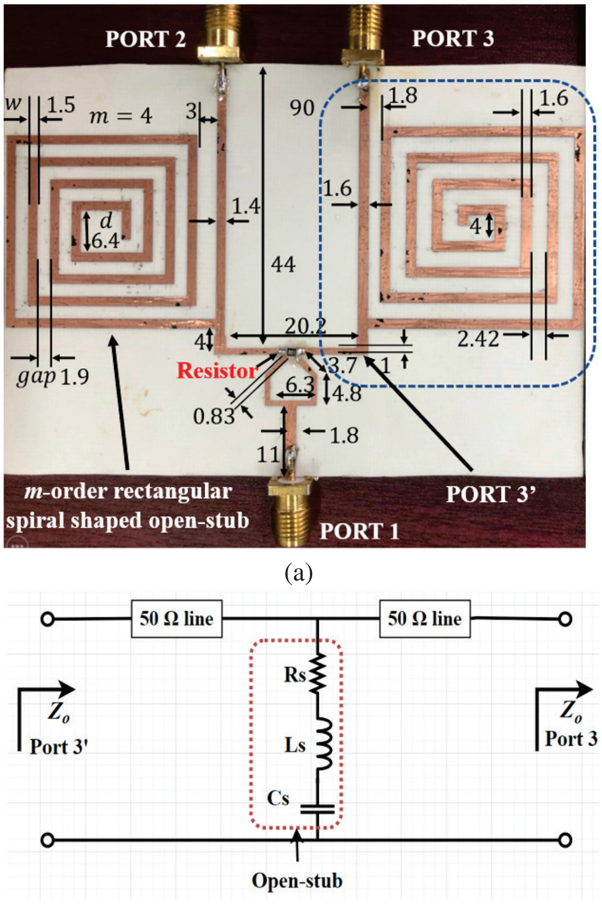

(a)

(b)

Fig. 6. (a) Proposed diplexer (all dimensions are in mm) and (b) equivalent circuit of an m-order rectangular spiral shape open-stub.

the stub length). The filter's bandwidth can be obtained as follows [20]:

$$\mathrm{BW} = \frac{\Delta f}{f_s} = \frac{1}{2n+1}, \tag{1}$$

where λ_s is the wavelength of the stopband f_s in the dielectric substrate. n is a natural number representing the filter level. When n gets higher, the bandwidth becomes narrower. The stub length is carefully chosen depending on n and λ_s. To the best transmittance of f_t, the desired transmission frequency, and the best reflection of the stopband f_s, the best chosen n is calculated as follows:

$$n = \frac{1}{4}\left(\frac{f_s + f_t}{|f_s - f_t|} - 1\right). \tag{2}$$

The operating frequency of the diplexer depends on n, as shown in Fig. 7. For instance, if the blocked frequency is 3.6 GHz and the desired transmission frequency is 3.2 GHz, n and the stub length, according to (2) will be 4 and $9\lambda_s/4$ for the best performance (as shown in Fig. 4, solid black line). This type of diplexer can control the frequency ratio between f_t and f_s, even if the frequency ratio is very close to 1, and it can be suitable for controllable dual-band transceiver or dual-band antenna applications and full-duplex applications. In this work, the diplexer operates at 3.6 GHz and 3.8 GHz, so n is selected as 9 and each stub length is chosen $L_{sp} = 19\lambda_s/4$ for the best selectivity and rejection. With two long stubs, the overall size of the diplexer is bulky. It is crucial to miniaturize the stub size for a more compact diplexer.

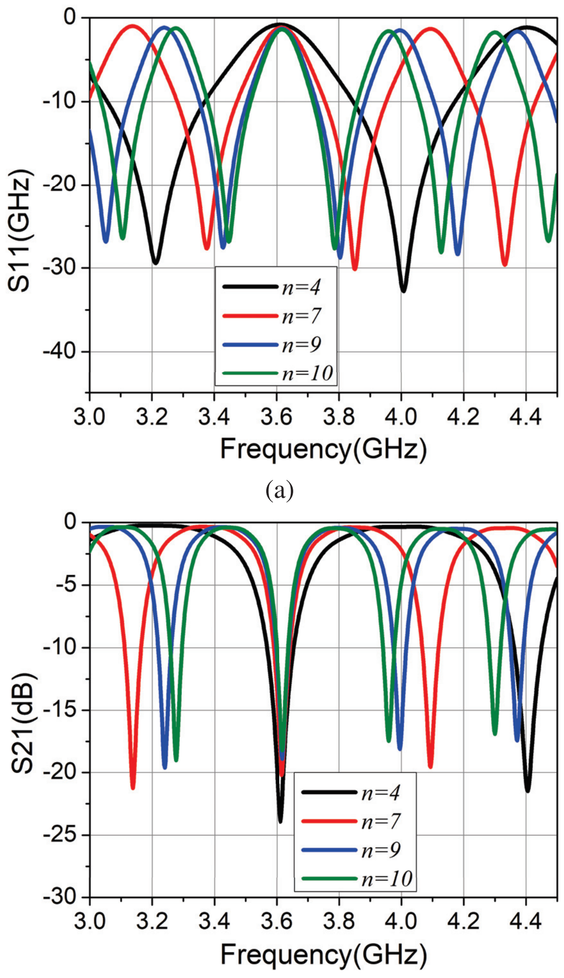

(a)

(b)

Fig. 7. Simulated S-parameters of diplexer at different values of n: (a) S11 and (b) S21.

Many previous works proposed various methods to miniaturize the size of the RF circuit [21, 22]. In this work, to reduce the total size, we proposed a bending method to turn the stubs into a rectangular spiral shape, as shown in Fig. 3 (a). The length of the rectangular spiral stub is calculated based on the arithmetic progression as follows:

$$L_{sp} = 8md + 4m^2 w + 4m(m-1)gap, \tag{3}$$

where *m* is the number of turns, *w* is the width of the stub, and *gap* is the distance of two turns. *d* is the length of starting coil as shown in Fig. 6 (a).

The dimensions of the rectangular stub are chosen with $m = 4$ for compactness and good matching. *w*, *d*, and *gap* are optimized by numerical optimization. After completing the design of two filters based on 4-order open spiral stubs, they are connected to the V-arms dipole antenna through a Wilkinson power divider to form a diplexer. A Wilkinson power divider whose resistor is 100Ω is used to enhance the isolation between two ports. As shown in Fig. 6 (a), a diplexer prototype is fabricated with the dimension of $1.3\lambda_0 \times 1.9\lambda_0$ which is 19 times smaller than the original stubs, where λ_0 is the wavelength of the center frequency in the substrate.

Figure 8 illustrates the simulated and measured S-parameters of the proposed diplexer. The diplexer shows a good filtering performance in the operating frequency bands. Port 2 shows the S21 at 3.6 GHz with -20 dB and 3.8 GHz with -1.9 dB of insertion loss, whereas Port 3 shows the S31 at 3.8 GHz with -21 dB and 3.6 GHz with -1.75 dB of insertion loss, respectively. The agreement of the simulation and measurement indicates that the diplexer has good band rejection and in-band transmission, except for a little frequency shift due to the fabrication tolerances and soldering technique. It also has good isolation of less than -20 dB in the 3.6-3.8 GHz band. The highest isolation reaches -30 dB at 3.64 GHz and -27 dB at 3.78 GHz. To our knowledge, this is the first time a diplexer with a frequency ratio below 1.05 has been proposed. The above results prove that the diplexer has a good performance and is suitable for full-duplex applications with two close frequency bands. The diplexer and antenna are then integrated to form the diplexer antenna. Because the bandwidth of the V-arms dipole antenna fully covers the bandwidth of the proposed diplexer, the proposed antenna has no extra 50 Ω connector or transmission line, which avoids additional insertion loss due to the imperfect connection, as shown in Fig. 9.

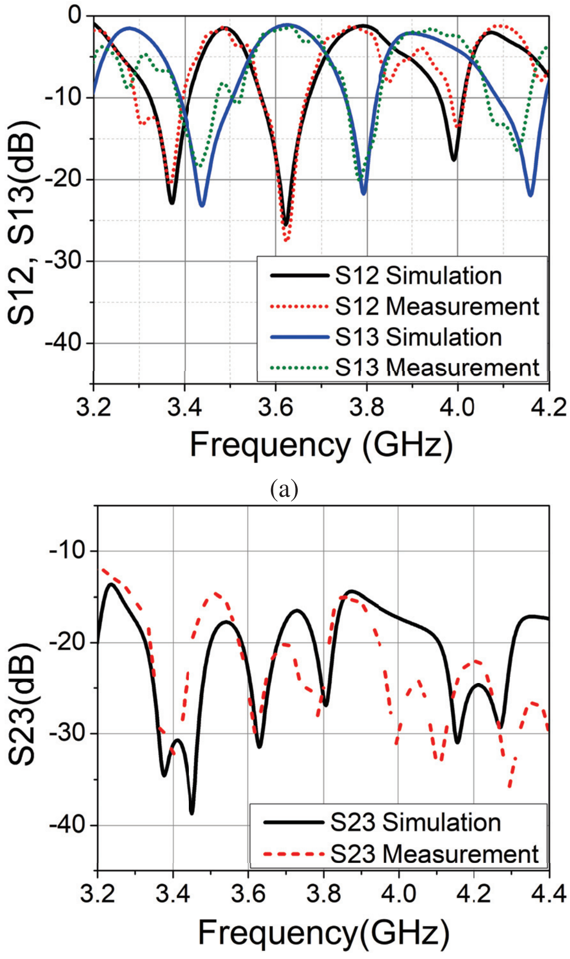

(a)

(b)

Fig. 8. Simulated and measured S-parameters of the proposed diplexer: (a) S12 and S13 and (b) S23.

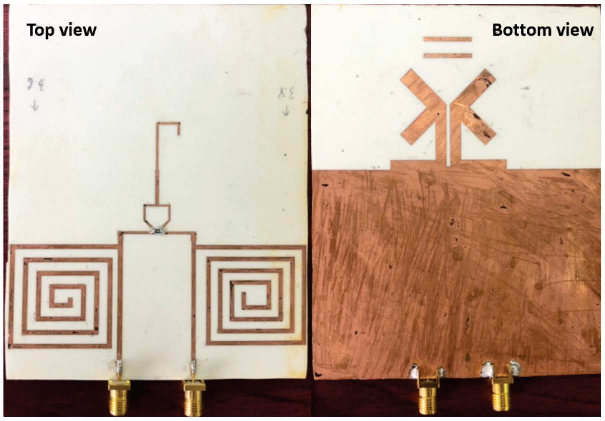

Fig. 9. Fabricated proposed antenna.

III. RESULTS AND DISCUSSION

Figure 10 presents the simulated and measured S-parameter of the proposed diplexer antenna. The antenna has two operating bands excited by two corresponding ports (or two channels). The measured results agree well with the simulated results showing a bandwidth of 3% (3.72-3.83 GHz) in measurement and 3.3% (3.78-3.86 GHz) in simulation for channel-1 and a bandwidth of 3.3% (3.563.68 GHz) in measurement and 3.3% (3.57-3.7 GHz) in simulation for channel-2, covering the C-band for 5G and satellites, respectively. The achieved frequency ratio is 1.04. The two operating bandwidths are narrow because of two BSFs with higher order mode according to equation (1).

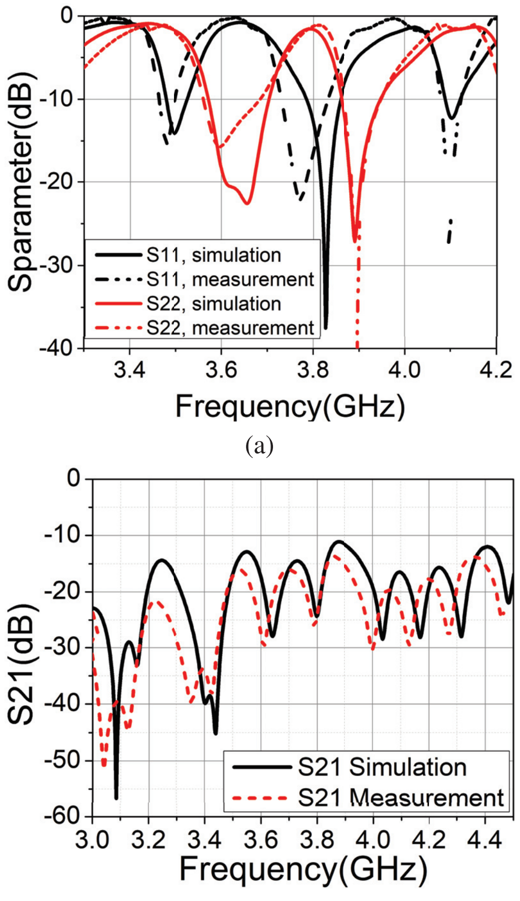

(a)

(b)

Fig. 10. Simulated and measured S-parameter of the diplexer antenna: (a) S11 and S22 and (b) S21.

As shown in Fig. 10 (b), the antenna exhibits high isolation with the measured S21 up to -27 dB at 3.61 GHz and -23 dB at 3.8 GHz. It also has good isolation of less than -20 dB in the operation band. Figure 11 shows the radiation patterns at 3.6 GHz and 3.8 GHz with a good agreement between simulation and measurement. At 3.6 GHz, the half-power beam widths (HPBWs) are 125° and 55° in the E-plane and H-plane, respectively. The patterns also maintain slightly similar shapes within the operating bandwidth, when HPBWs of 72° and 65° are yielded at 3.8 GHz.

To provide a clearer understanding of the ability of frequency selectivity in two adjacent frequency bands of the antenna, the antenna gain is simulated and measured, as shown in Fig. 12. The results show that the antenna maintains high gains in the transmission bands and achieves near-null radiation at the stopbands. Although the gain of the diplexer antenna decreases compared to the antenna element, it maintains a small difference between the measured gain of 4.2-4.7 dBi and the simulated gain of 4.6–5.7 dBi.

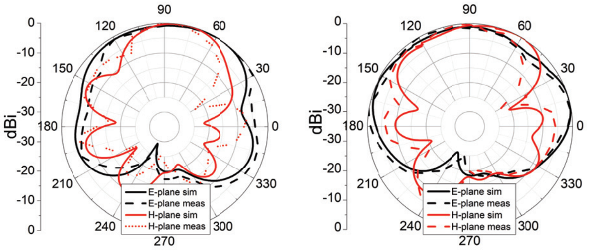

(a)

(b)

Fig. 11. Simulated and measured radiation pattern of diplexer antenna: (a) 3.6 GHz and (b) 3.8 GHz..

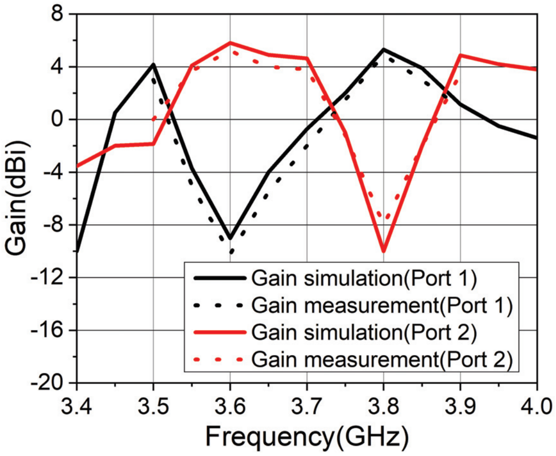

Fig. 12. Simulated and measured gain of proposed diplexer antenna.

The related diplexer antennas are summarized in Table 1. In [4], the proposed duplexing antenna has high gain and compact compared to other works, but a high frequency ratio (FR) and lower isolation are reported. [6, 7] proposed a compact duplexing antenna and low frequency ratio, but using a two-layer substrate can lead to a high-cost and complex fabrication process. In addition, the proposed antenna in [6] can change the frequency ratio by modifying the foam thickness between two substrates, which results in a bulky system if the frequency ratio comes to 1. In [9], a low-profile single-layered duplex-filtenna scheme was proposed by using two feeds, and a common substrate integrated waveguide (SIW) cavity. Although the antenna used a high-cost substrate and SIW technique, the proposed antenna has the same results as our proposed antenna. Compared with the related works, the proposed solution is significant in terms of high isolation at the lowest frequency ratio (1.04). Note that the smaller the frequency ratio, the more challenged the high isolation level. Our diplexer antenna uses a single layer of Roger 4003C substrate, which is low-cost for fabrication, while all related works

Table 1: Comparison between this work and related works

Ref.	Freq./FR	Subs.	Gain	Iso.
[4]	3.5/5.2, 1.48	RT/Duroid 5880 single	4.67/6.3	20.3
[6]	1.8/2.045, 1.14	Roger 4003C double	7/7.2	21/35
[7]	4.1/4.9, 1.19	RT/Duroid 5880 double	4.3/4.8	25/23
[9]	8.75/9.4, 1.08	RT/Duroid 5880 single	4.48/4.6	21.5/29.7
This work	3.6/3.8, 1.04	Roger 4003C Single	4.6/4.1	27/23

use double layers or a high-cost substrate of Duroid 5880. Moreover, the proposed diplexer can easily change the frequency ratio by modifying the stub length. In addition, the two ports are close to each other and enable easy connection to the transceiver in most terminal devices.

IV. CONCLUSION

In this paper, we propose a spiral filter-based diplexer antenna with low-cost, small frequency ratio, high isolation, and high selectivity advantages. The dual-band characteristics with a frequency ratio of 1.04 are achieved using a single printed V-arms dipole antenna integrated with the diplexer based on high-order rectangular spiral-shaped open-stub filters. The proposed diplexer exhibits good filtering performance, which could be used in an integrated RF front-end with reduced complexity, cost, and size with a small and flexible frequency ratio. By changing the length of the stub, the frequency ratio of the diplexer and the proposed antenna is easily adjustable, and the bandwidth of the in-band frequency selectivity and out-of-band rejection is adjusted. In addition, our proposed model may find potential uses in C-band full-duplex applications for 5G and satellites.

REFERENCES

[1] A. Sabharwal, P. Schniter, D. Guo, D. W. Bliss, S. Rangarajan, and R. Wichman, "In-band full-duplex wireless: Challenges and opportunities," *IEEE J. Sel. Areas Commun.*, vol. 32, no. 9, pp. 1637-1652, Sep. 2014.

[2] Z. Zhang, K. Long, A. V. Vasilakos, and L. Hanzo, "Full-duplex wireless communications: Challenges, solutions, and future research directions," *Proc. IEEE*, vol. 104, no. 7, pp. 1369-1409, July 2016.

[3] K. E. Kolodziej, B. T. Perry, and J. S. Herd, "In-band full-duplex technology: Techniques and systems survey," *IEEE Trans. Microw. Theory Tech.*, vol. 67, no. 7, pp. 3025-3041, July 2019.

[4] Y. Xie, F.-C. Chen, and J.-F. Qian, "Design of integrated duplexing and multi-band filtering slot antennas," *IEEE Access*, vol. 8, pp. 126119-126126, 2020.

[5] C.-X. Mao, S. Gao, Y. Wang, Y. Liu, X.-X. Yang, Z.-Q. Cheng, and Y.-L. Geng, "Integrated dual-band filtering/duplexing antennas," *IEEE Access*, vol. 6, pp. 8403-8411, 2018.

[6] J.-F. Li, D.-L. Wu, G. Zhang, Y.-J. Wu, and C.-X. Mao, "Compact dual-polarized antenna for dual-band full-duplex base station applications," *IEEE Access*, vol. 7, pp. 72761-72769, 2019.

[7] K.-Z. Hu, M.-C. Tang, Y. Wang, D. Li, and M. Li, "Compact, vertically integrated duplex filtenna with common feeding and radiating SIW cavities," *IEEE Trans. Antennas Propag.*, vol. 69, no. 1, pp. 502-507, Jan. 2021.

[8] J. Li, P. Hu, J. Chen, K.-D. Xu, C.-X. Mao, and X. Y. Zhang, "Dual-polarized duplex base-station antenna with a duplexer-integrated balun," *IEEE Antennas Wirel. Propag. Lett.*, vol. 21, no. 2, pp. 317-321, Feb. 2022.

[9] A. Kumar and A. A. Althuwayb, "SIW resonator-based duplex filtenna," *IEEE Antennas Wirel. Propag. Lett.*, vol. 20, no. 12, pp. 2544-2548, Oct. 2021.

[10] C.-X. Mao, S. Gao, Y. Wang, F. Qin, and Q.-X. Chu, "Compact highly integrated planar duplex antenna for wireless communications," *IEEE Trans. Microw. Theory Tech.*, vol. 64, no. 7, pp. 2006-2013, July 2016.

[11] C.-X. Mao, S. Gao, and Y. Wang, "dual-band full-duplex tx/rx antennas for vehicular communications," *IEEE Trans. Veh. Technol.*, vol. 67, no. 5, pp. 4059-4070, May 2018.

[12] J. R. Parker, I. D. Flood, and G. D. Carter, "Adjacent channel compatibility between IMT and ubiquitous FSS earth stations in the 3.4-3.8 GHz frequency band," *Wirel. Netw.*, vol. 27, no. 2, pp. 1103-1110, Feb. 2021.

[13] "5G frequency bands & spectrum allocations," CableFree.

[14] G. L. Matthaei and E. G. Cristal, "Multiplexer channel-separating units using interdigital and parallel-coupled filters," *IEEE Trans. Microw. Theory Tech.*, vol. 13, no. 3, pp. 328-334, May 1965.

[15] M.-H. Weng, C.-Y. Hung, and Y.-K. Su, "A hairpin line diplexer for direct sequence ultra-wideband wireless communications," *IEEE Microw. Wirel. Compon. Lett.*, vol. 17, no. 7, pp. 519-521, July 2007.

[16] M.-L. Chuang and M.-T. Wu, "Microstrip diplexer design using common t-shaped resonator," *IEEE*

Microw. Wirel. Compon. Lett., vol. 21, no. 11, pp. 583-585, Oct. 2011.

[17] C.-M. Chen, S.-J. Chang, C.-F. Yang, and C.-Y. Chen, "A simple and effective method for designing frequency adjustable balun diplexer with high common-mode suppression," *IEEE Microw. Wirel. Compon. Lett.*, vol. 25, no. 7, pp. 433-435, July 2015.

[18] C.-F. Chen, K.-W. Zhou, R.-Y. Chen, H.-Y. Tseng, Y.-H. He, W.-J. Li, and J.-H. Weng, "Design of microstrip multifunction integrated diplexers with frequency division, frequency selection, and power division functions," *IEEE Access*, vol. 9, pp. 53232-53242, 2021.

[19] Y. Wu, L. Hao, W. Wang, and Y. Yang, "Miniaturized and low insertion loss diplexer using novel inter-digital capacitors and microstrip section inductors," *IEEE Trans. Circuits Syst. II Express Briefs*, vol. 69, no. 11, pp. 4303-4307, Oct. 2022.

[20] M. Q. Dinh and M. T. Le, "Triplexer-based multi-band rectenna for RF energy harvesting from 3G/4G and Wi-Fi," *IEEE Microw. Wirel. Compon. Lett.*, pp. 1-1, 2021.

[21] R. O. Ouedraogo, E. J. Rothwell, A. R. Diaz, K. Fuchi, and A. Temme, "Miniaturization of patch antennas using a metamaterial-inspired technique," *IEEE Trans. Antennas Propag.*, vol. 60, no. 5, pp. 2175-2182, May 2012.

[22] C. Sharma and D. K. Vishwakarma, "Miniaturization of spiral antenna based on fibonacci sequence using modified Koch curve," *IEEE Antennas Wirel. Propag. Lett.*, vol. 16, pp. 932-935, 2017.

Hong Quang Nguyen was born in Hai Duong, Vietnam, in 1999. He received his B.Eng. degree in electrical engineering from Hanoi University of Science and Technology (HUST), Hanoi, Vietnam. He is currently a second year master student, major in electrical engineering, Hanoi University of Science and Technology. His current interests include millimeter-wave antennas, bio-based material microwave circuits, and RF energy harvesting.

Trong Toan Do was born in Hai Duong, Vietnam, in 1991. He received his Degree of Engineer in electronics and communication engineering from HUST, Hanoi, Vietnam. He has been working for Viettel High Tech RnD from 2014. He is currently a group leader of antenna team in 5G project in Viettel. His current research interests include wideband antennas, array antennas, and 5G beamforming.

Dinh Hai Truyen Hoang was born in Ha Tinh, Vietnam, in 1984. He received his Degree of Engineer in electronics and communications engineering from HUST, Hanoi, Vietnam. He has been working for Viettel High Tech RnD from 2010. He is currently a chief technology officer who takes care of 5G projects in Viettel. His current research interests include high speed circuits, RF high power and frequency amplifiers, antennas, array antennas, and 5G beamforming.

Quoc Cuong Nguyen received the engineer (1996) and M.S. (1998) degrees in electrical engineering from HUST, and the Ph.D. degree in Signal - Image - Speech - Telecoms from INP Grenoble, France, in 2002. He is a professor at the Department of Automation, School of Electrical and Electronic Engineering (SEEE). His research interests include signal processing, speech recognition, beamforming, smart sensors, and RF communications.

Minh Thuy Le was born in Vietnam. She received the B.E. and M.S. degrees in electrical engineering from the Hanoi University of Science and Technology (HUST), in 2006 and 2008, respectively, and the Ph.D. degree in optics and radio frequency from the Grenoble Institute of Technology, France, in 2013. She is currently a professor and a group leader of the Radio Frequency Group, School of Electrical Engineering and Electronic (SEEE), HUST. Her current research interests include built-in antennas, antenna arrays, beamforming, metamaterials, indoor localization and RF energy harvesting, wireless power transfer, and autonomous wireless sensors.

A New Type of Reflective Reconfigurable Electronic Beam Squinting Feed

Bo-Wen Zhang, Liang-Xin Xia, Neng-Wu Liu, and Guang Fu

National Key Laboratory of Antennas and Microwave Technology
Xidian University, Xian, 710065, China
zhangbowenjp@stu.xidian.edu.cn, Liangxinxia@stu.xidian.edu.cn, nwliu@xidian.edu.cn, gfu@mail.xidian.edu.cn

Abstract – With the development of highly integrated technology, a large number of satellites have been launched into synchronous orbit, saturating the number of satellites in these orbits. As a result, there has been a substantial increase in demand for near-Earth orbit satellites. However, due to their proximity to Earth, the location of these satellites rapidly drifts in free space. To maintain the received and transmitted signals within range, the ground antenna must track the satellites immediately. Therefore, near-Earth orbit satellite tracking has become a key technology in satellite communication research. In order to further improvement, we propose a new type of electronic beam squinting (EBS) tracking feed. In this paper, we will conduct both theoretical and experimental analyses of this EBS feed.

Index Terms – electronic beam squinting(EBS) system, near earth orbit satellites tracking technology, reconfigurable EBS feed.

I. INTRODUCTION

The electronic beam squinting (EBS) technique [1] was investigated in the 1980s. By applying electronic switching technology, the EBS tracking system [2] could effectively perform real-time spatial measurements of the tracking signal [3]. This pseudo-real-time amplitude sensing system enables almost real-time derivation of the tracking error, and its accuracy is comparable to that of a single-pulse system. Additionally, only a simple single-channel tracking receiver is required to receive the signal.

In this work, we propose a reflective reconfigurable EBS feed to replace the traditional feed in the EBS system. The reflective EBS feed is a type of TE_{21} mode coupler typically employed in precision tracking [4-10]. To ensure the tracking sensitivity and accuracy, it is essential to extract the TE_{21} mode signal as efficiently as possible while suppressing the TE_{11} mode by at least 40 dB. A common design for achieving this is the application of a 48-holes or 32-holes Bessel distribution coupler. In our work, we select the 32-holes coupler to excite a porous coupling in the reflective reconfigurable EBS feed.

The theory of waveguide coupling was extensively researched by Miller in the 1950s [11, 12]. Choung and colleagues [13] analyzed the TE_{21} mode using the loose and tight coupling mode coupler theory, providing an empirical determination of the coupling aperture in the Ku band equation. In the original EBS system, a slot coupling technique was applied to excite the TE_{21} mode in the primary waveguide. This slot was positioned perpendicular to the primary waveguide, between the primary and secondary waveguides. By adjusting the width of the slot, the TE_{21} mode could be coupled from the secondary waveguide to the primary waveguide. However, in the reflective reconfigurable EBS feed, the slot coupler is replaced by a porous coupler, which allows for stronger coupling while minimizing the coupling of higher order modes. This adjustment simplifies the filter design and improves port isolation. In consideration of structure, the secondary waveguide is located along the primary waveguide, effectively reducing the feed's horizontal size. This miniaturization greatly simplifies the system.

The reflective reconfigurable EBS feed utilizes a reconfigurable secondary waveguide at the reflective surface to control the phase of the transmitted TE_{10} mode in the secondary waveguide [14, 15]. As a result, the phase of the TE_{21} mode in the primary waveguide changes, thus modifying the phase distribution over the aperture. So, beam direction could be changed in both the azimuth and elevation directions, meeting the requirements of the EBS system.

II. DESIGN OF REFLECTIVE RECONFIGURABLE EBS FEED

In the reflective reconfigurable EBS feed, a circular waveguide is applied as the primary waveguide, while four rectangular waveguides are applied as the secondary waveguides (shown in Fig. 1). By selecting appropriate dimensions for the primary and secondary waveguides, the equivalent phase constants of the TE_{21} mode in primary waveguide and the TE_{10} mode in the secondary waveguide are equal. The phases of the two modes are precisely aligned, resulting in wave superposition and achieving strong coupling as close as possible

Submitted On: June 29, 2023
Accepted On: November 12, 2023

https://doi.org/10.13052/2024.ACES.J.390106

to 0 dB. For other modes in primary waveguide which have different equivalent phase constants compared to the TE_{10} mode, the energy cancels each other out when coupled to the secondary waveguide. However, there is a slight difference in the reflection coefficients between these two modes. This is because the TE_{21} mode in the circular waveguide is reflected by a smaller diameter, while the TE_{10} mode in the rectangular waveguide is reflected by reflective surface. To reduce these differences, it is necessary to adjust the size of each circular and rectangular waveguide. Additionally, if curved fading or step transformation is used for the circular waveguide aperture transformation, the length of the transformation section can be further reduced.

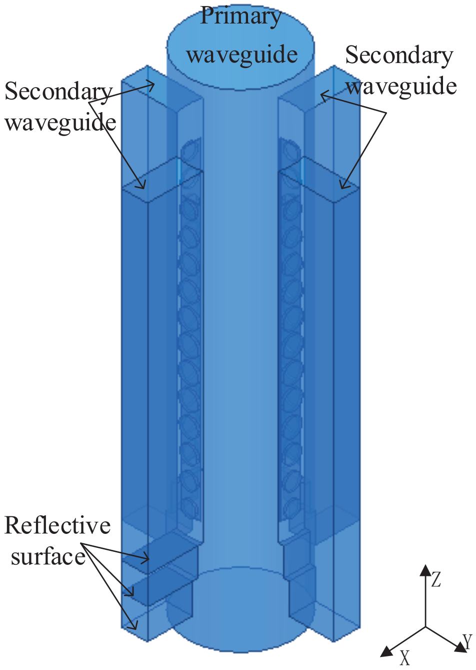

Fig. 1. Structure of feed.

Under the reciprocity theorem of transmission and reception, the feed can be considered as a transmission antenna. To generate phase differences for the purpose of shifting the phase center, a pair of coupling waveguides and primary waveguides can be utilized. The phase distributions of the TE_{11} mode and the TE_{21} mode along the Y-axis play a crucial role in achieving the desired phase center shifting. In Fig. 2, a pair of coupling waveguides and primary waveguides are applied to demonstrate how phase differences are generated to make phase center shifting.

When observing the phase distribution along the Y-axis for the TE_{11} mode (shown in Fig. 3), there is no difference in phase along the Y-axis. On the other hand, when observing the phase distribution along the Y-axis for the TE_{21} mode (shown in Fig. 4), it becomes apparent that the phase is exactly opposite along the Y-axis. This characteristic of the TE_{21} mode plays a critical role in achieving the necessary phase differences required for the phase center shifting. By using these phase differences in the TE_{21} mode, the phase center shifting can be effectively realized.

In primary waveguide, the mode is mixed with TE_{11} and TE_{21} which are from port 1 and port 2/3, respectively. In this hybrid mode, the direction of the beam

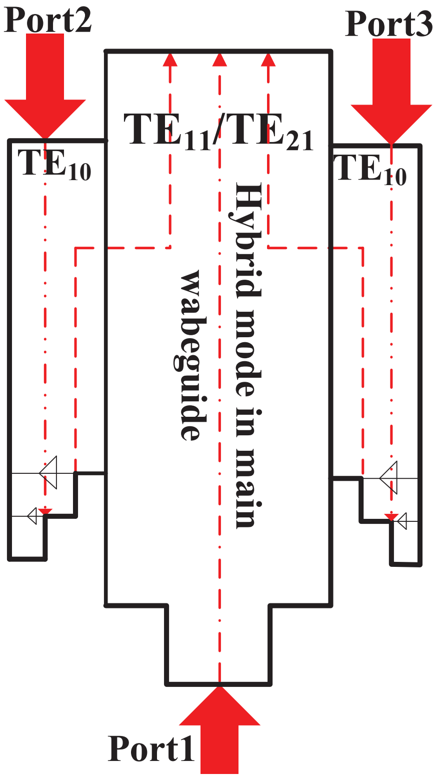

Fig. 2. Workflow of EBS feed.

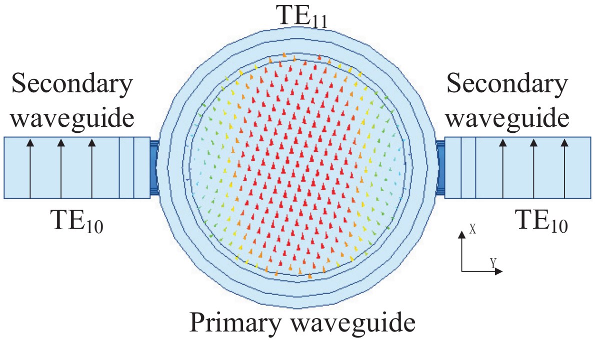

Fig. 3. Schematic of fields in both main/secondary waveguide (TE_{11}).

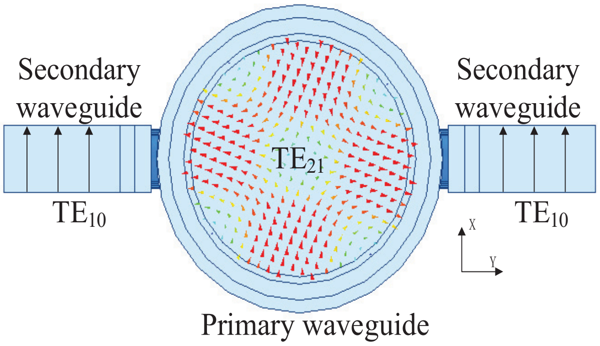

Fig. 4. Schematic of fields in both main/secondary waveguide (TE_{21}).

corresponds to the phase center. Therefore, if the phase center squints, the beam direction will also squint proportionally.

To control the phase differences between the TE_{10} modes in a pair of secondary coupling waveguides, different reflective surfaces are applied in each secondary waveguide. By adjusting the reflective surfaces, the phase distribution over the aperture can be adjusted to achieve desired phase center. After applying diodes in different reflective surfaces, the position of these reflective surfaces is reconfigurable, allowing for precise control of the phase differences. When the phase difference between the two secondary waveguides is 0°, the phase center over the aperture will be located at its geometric center, and the TE_{21} modes from both secondary coupling waveguides will cancel each other out. However, when the phase difference is ±180°, the phase center will be located at the maximum offset position, thus generating the desired beam squinting.

In 2010, Satish K. Sharma and Ashish Tuteja designed a 3-mode feed using slot coupling. This feed achieved a gain of about 14 dBi at the center frequency of 7.73 GHz, a maximum beam shift of ±24° in the azimuth and elevation direction, and a bandwidth of about 7.48-8 GHz for $S_{11} \leqq -10$ dB. However, in this work, a porous coupling is applied to replace the slot coupling. In this way, we could improve the isolation between each port and accuracy of phase center control. S-parameters are shown in Fig. 5.

From Fig. 5 we observed that significant improvements have been achieved compared to the 3-mode feed developed by Satish K. Sharma in terms of S_{11} and port isolation. The S_{11} parameter being less than -20 dB over the bandwidth range indicates good matching, while the port isolation exceeding 45 dB around the center frequency of 12.5 GHz demonstrates strong suppression of the reflected TE_{11} mode. The port isolation improvement is attributed to the strong coupling utilized in this antenna.

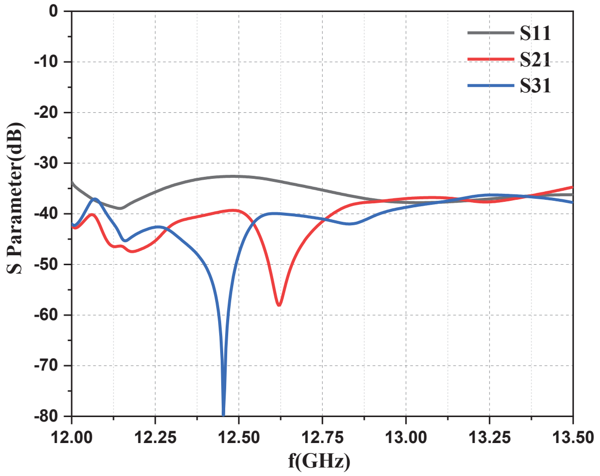

Fig. 5. Simulated S-parameter.

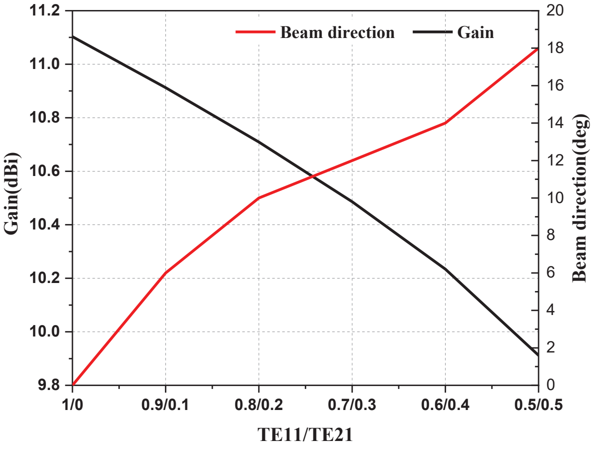

Fig. 6. Gain and beam direction.

For a comprehensive analysis of the hybrid mode in the transmission antenna, it is essential to quantitatively analyse the magnitudes in both coupling waveguides. By ensuring that the magnitudes in both coupling waveguides are the same, the beam direction and gain can be calculated separately for different hybrid mode ratios. The beam direction and gain are calculated separately in different hybrid mode ratios (shown in Fig. 6). By systematically evaluating the influence of varying hybrid mode ratios on these parameters, a thorough understanding of the antenna's performance under different configurations can be obtained.

As shown in Fig. 6, there is a direct relationship between the difference in mode ratio, beam direction, and gain. Specifically, the greater the difference in mode ratio, the greater the beam direction and the greater the drop in gain. This accentuates the importance of selecting an appropriate mode ratio to achieve a desirable balance between beam direction and gain. Since the beam

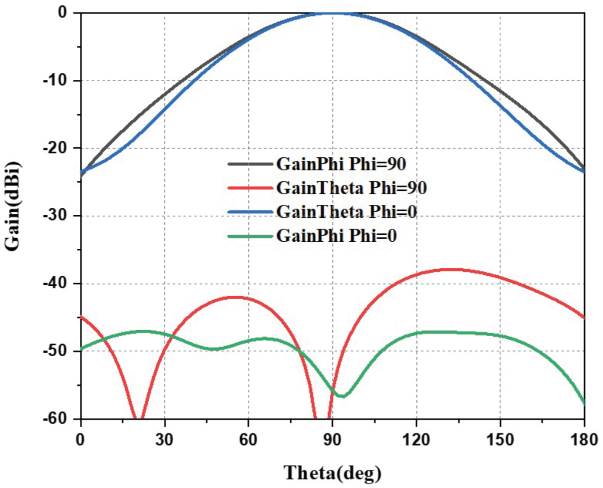

Fig. 7. Simulated radiation pattern in 0° phase difference.

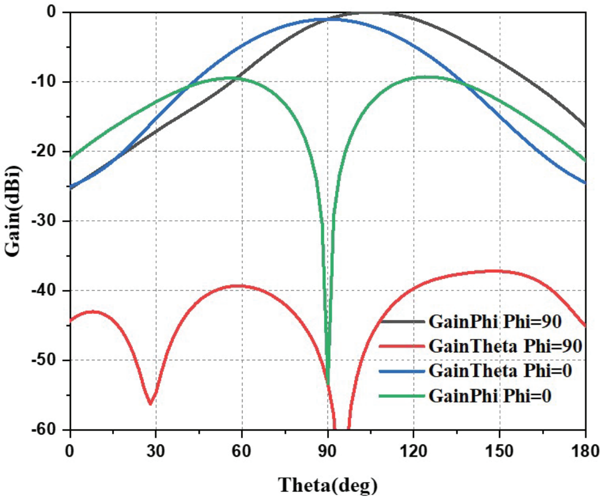

Fig. 8. Simulated radiation pattern in 180° phase difference.

direction corresponds to the phase center, when the beam direction is at its maximum degree, the phase center shifts to the maximum position. Therefore, it is critical to carefully consider the impact of different mode ratios on the phase center to avoid undesirable beam squinting.

In this work, in case the gain is too low, it is advisable to select a mode ratio of 6:4. Additionally, the simulated radiation patterns in different phases are shown in Figs. 7–9 in the horizontal plane.

Figure 7 shows the results of 0° phase difference in both E and H plane with cross-polarization. It can be observed from Fig. 7, E plane and H are equalized well. Figure 8 also shows the results of 180° phase difference in E and H plane with cross-polarization. The main beam in H plane is 14°. Figure 9 shows the results of -180° phase difference in E and H plane with cross-polarization. The main beam in H plane is $-14°$.

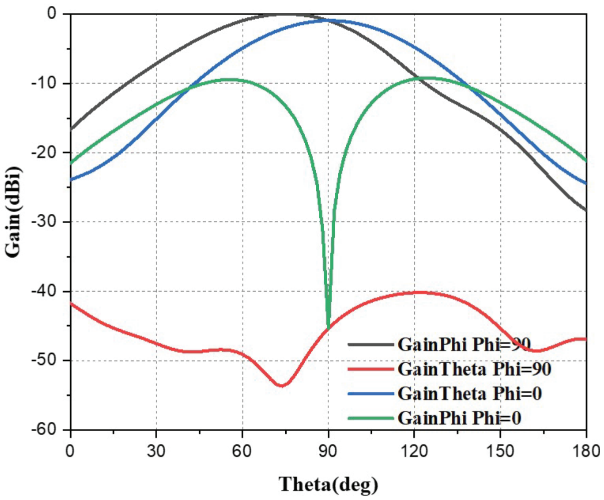

Fig. 9. Simulated radiation pattern in -180° phase difference.

The cross-polarization isolation is greater than 40 dB in all three radiation patterns shown in Figs. 7–9, indicating that cross-polarization has minimal influence on tracking accuracy.

Furthermore, it is evident from the results that by controlling the phase of the reflective reconfigurable EBS feed, electronic beam shifting within ±14° can be achieved. However, to achieve a larger beam shift degree, a larger aperture may be needed, which could lead to a decrease in aperture efficiency.

Under the reciprocity theorem of transmission and reception, if the transmission antenna can achieve a certain angle of beam squinting, it can also receive signals within ±14°. Table 1 provides information on other phase differences that result in beam squinting.

Table 1: Phase difference and beam squinting

Phase Difference	Beam Squinting	Phase Difference	Beam Squinting
30°	4°	30°	−4°
60°	8°	60°	−8°
90°	12°	90°	−12°
180°	14°	180°	−14°

III. RESULTS AND EXPERIMENTAL VALIDATION OF REFLECTIVE RECONFIGURABLE EBS FEED

After the simulation, it is necessary to validate the performance of the reflective reconfigurable EBS feed. To accomplish this, the Voltage Standing Wave Ratio (VSWR) of the antenna is measured using a vector network analyzer. Additionally, the radiation patterns of the antenna at ±180° phase differences are measured in a microwave measurement darkroom at Xi'an University of Electronic Science and Technology. The antenna far field measurement system used for this purpose was XD-2. For reference, a photograph of the reflective reconfigurable EBS feed is shown below. The photograph of the processed antenna and the measurement environment are shown in Figs. 10 and 11, respectively.

The results shown in Fig. 12 indicate that the S-parameter measurements of the feed are close to the simulation results. The reflection coefficient for port 1 (S_{11}) is less than -20 dB across the bandwidth. Moreover, the port isolation (S_{21} and S_{31}) is measured to be greater than -40 dB, indicating effective isolation between port 1 and port 2, as well as between port 1 and port 3. It is noted that the porous coupler has a positive impact on improving the port isolation, which is an important factor in ensuring minimal interference and efficient functioning of the feed. These results validated the effectiveness of the feed design and its ability to maintain good matching and isolation characteristics, as verified through the S-parameter measurements.

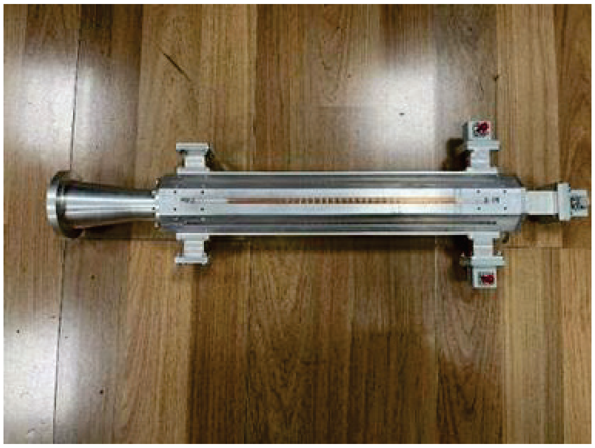

Fig. 10. Photograph of processed antenna.

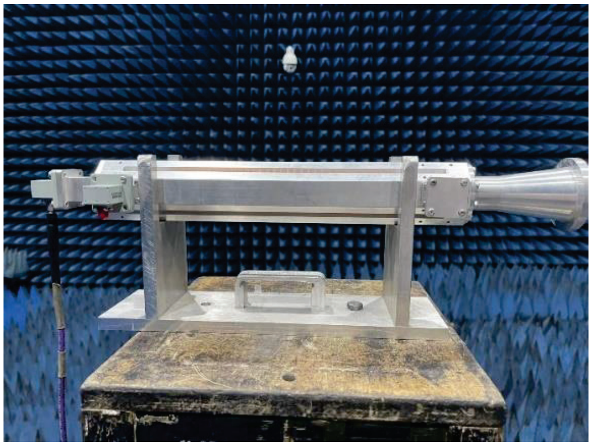

Fig. 11. Photograph of measuring the processed antenna.

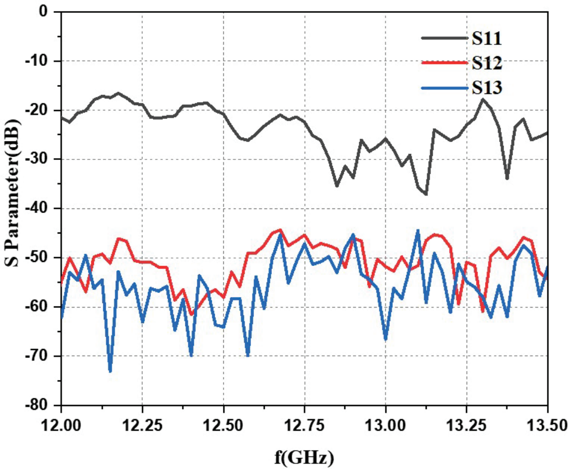

Fig. 12. Measured S-parameter.

For the accuracy of the main and cross-polarization, phase center of both measure and measured antenna should be aligned. The measured radiation patterns of reflective reconfigurable EBS feed are shown in Figs. 13 and 14.

In Fig. 13, with a 180° phase difference, the results show the cross-polarization and beam squinting in both the E and H planes. The maximum beam squinting is 13°. Similarly, Fig. 14 shows -180° phase difference results in both planes. Notably, the main beam is -13°.

In this case, the beam squint is from -13° to 13° and the cross-polarization isolation is larger than 30 dB. Table 2 provides further details on the measured radiation patterns under various phase differences.

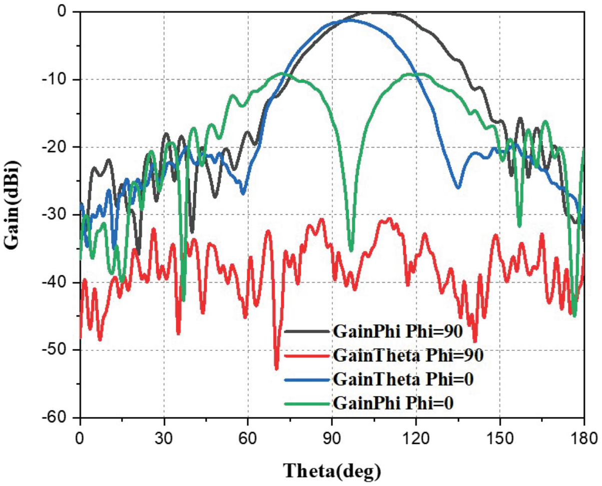

Fig. 13. Measured radiation pattern in 180° phase difference.

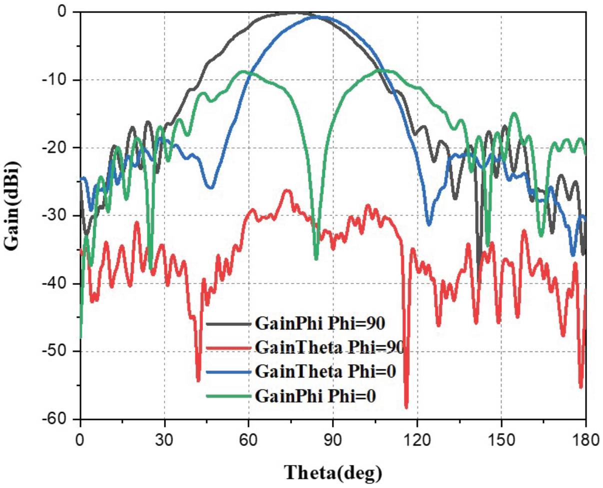

Fig. 14. Measured radiation pattern in -180° phase difference.

Table 2: Experiment result of phase difference and beam squinting

Phase Difference	Beam Squinting	Phase Difference	Beam Squinting
30°	3°	30°	-3°
60°	6°	60°	-6°
90°	9°	90°	-9°
180°	13°	180°	-13°

Considering the measurement errors, when compared with the simulation results, the experiment results are close to simulation results. This agreement between the measured and simulated results further strengthens the dependability of the experimental results.

By validating the experiment against the simulation, it verifies that the antenna's performance matches the anticipated performance. This enhances our confidence in the reliability and accuracy of the experimentally obtained radiation patterns and the overall performance evaluation of the reflective reconfigurable EBS feed.

IV. CONCLUSION

In this paper, reflective reconfigurable EBS feed is proposed. The application of porous coupling improves the port isolation, demonstrating an effective way to improve the antenna's performance. Furthermore, the separation of the primary and secondary waveguides enables control of the phase and manipulation of the main beam direction.

To ensure accurate phase control in the secondary waveguide, minimizing the leakage from the primary waveguide is crucial. As such, the authors have simplified the structure by removing corrugations or chokes and applying the porous coupler to increase port isolation.

This EBS feed could achieve beam squinting in horizontal plane within ±14° without reflector and higher aperture efficiency (85%). By adjusting reflective surface with diodes, the reaction time is reduced, enabling faster adjustments to meet changing requirements. Moreover, the application of the secondary waveguide located along the main waveguide enables miniaturization of the feed, making it more compact and easier to integrate into various systems.

Overall, the proposed reflective reconfigurable EBS feed offers several advantages over traditional designs, including improved port isolation, accurate phase control, and high aperture efficiency. These characteristics make it a valuable addition to satellite communication that require accurate tracking and rapid response.

ACKNOWLEDGMENT

This work is supported by the National Natural Science Foundation of China under General Program (62271364), Key Research and Development Program of Shaanxi (Program No. 2023-GHZD-45), Fundamental Research Funds for the Central Universities (ZYTS23145).

REFERENCES

[1] G. J. Hawkins, D. J. Edwards, and J. P. McGeehan, “Tracking system for satellite communications,” *IEE Proceedings*, vol. 135, no. 5, pp. 393-407, Oct. 1988.

[2] G. J. Hawkins and D. J. Edwards, “Operational analysis of electronic tracking schemes,” *IEE Proceedings,* vol. 136, no. 3, pp. 181-188, June 1989.

[3] P. B. Kenington, D. J. Edwards, and J. P. McGeehan, “Receivers for an electronic ‘beam-squint’ tracking system,” *IEEE Proceedings. Part I: Communications, Speech and Vision*, vol. 136, no. 4, pp. 305-311, Aug. 1989.

[4] L. Solymar, “Waveguide tapers, transitions and couplers,” *Electronics and Power*, vol. 26, no. 10, p. 823, Oct. 1980.

[5] J. S. Cook and R. Lowell, “The autotrack system,” *The Bell System Tech,* vol. 42, no. 4, pp. 1283-1307, July 1963.

[6] R. E. Collin, *Field Theory of Guided Waves*. New York: Wiley, 1991.

[7] N. Marcuvitz, *Waveguide Handbook*. Stevenage: Institution of Electrical Engineers, 1986.

[8] Jin Au Kong, *Electromagnetic Wave Theory*. Cambridge, MA: EMW Publishing, 2008.

[9] Y. Rahmat-Samii, *The Handbook of Antenna Design: Volume I*. Antennas and Propagation Society Newsletter, IEEE, 1983.

[10] L. Zhu and N. Liu, “Multimode resonator technique in antennas: A review,” *Electromagnetic Science*, vol. 1, no. 1, pp. 1-17, 2023.

[11] S. E. Miller “Coupled wave theory and waveguide applications,” *Bell System Technical Journal*, vol. 33, no. 3, pp. 661-719, May 1954.

[12] S. E. Miller, “On solutions for two waves with periodic coupling,” *Bell System Technical Journal*, vol. 47, no. 8, pp. 1801-1822, Oct. 1968.

[13] Y. H. Choung, K. R. Goudey, and L. G. Bryans, Theory and design of a Ku-band TE/sub21/-mode coupler, *IEEE Transactions on Microwave Theory and Techniques*, vol. 30, no. 11, pp. 1862-1866, Nov. 1982.

[14] E. H. Lenzing and H. F. Lenzing, “Characteristics of the TE_{21} mode in circular apertures as used for satellite tracking,” *IEEE Transactions on Aerospace and Electronic Systems*, vol. 37, no. 3, pp. 1113-1117, July 2001.

[15] S. K. Sharma and A. Tuteja, “Investigations on a triple mode waveguide horn capable of providing scanned radiation patterns,” *2010 IEEE Antennas and Propagation Society International Symposium*, Toronto, July 2010.

Bo-Wen Zhang was born in Xi’an, China. He received the B.S. degree in electronic information Technology from Xidian University, Xi’an, China, in 2012. After that he received the M.E. in science and engineering from Toyo University, Tokyo, Japan. Since 2019, he is currently pursuing the Ph.D. degree from Xidian University. His current research interests include corrugated horn antenna, beam-shaped array antenna and metamaterial applications in antenna.

Liang-Xin Xia was born in Anhui, China, in February 1997. He received the B.S. degree in electronic information Technology from Xidian University, Xi’an, China, in 2019, where he is currently pursuing the Ph.D. degree. His current research interests include Fabry-Perot cavity antenna, wide-beam antenna and beam-shaped array antenna.

Neng-Wu Liu (Senior Member, IEEE) was born in Changde, China. He received the B.S. and M.E. degrees in electrical engineering from Xidian University, Xi’an, China, in 2012 and 2015, respectively, and the Ph.D. degree from the University of Macau, Macau, in 2017, Since 2018, he has been an Associate Professor with Xidian University. From 2019 to 2021, he was the UM Macao Post-Doctoral Research Fellow under the UM Macao Talent Program. His current research interests include designs of antenna theory, low-profile antenna, multimode antenna, wideband antenna, patch antenna, dielectric resonator antenna, circularly polarized antennas, filtering antenna, slot antenna, and phased array. Dr. Liu was a recipient of several academic awards, which includes the Best Student Paper Award in the 17th IEEE Macau/HK AP/MTT Postgraduate Conference and the Best Student Paper Award in 2017 National Conference on Antennas. He was also a recipient of the Outstanding Reviewer Award from the IEEE Transactions on Antennas and Propagation in 2020, 2021, and 2022; and the 2022 Macao Natural Science Awards (Second Prize) from the Science and Technology Development Fund (FDCT), Macau. He serves as an Associate Editor for IET Microwaves, Antennas and Propagation, IEEE Access, and Electronics Letters (IET).

Guang Fu received the B.S. and M.S. degrees in electromagnetic field and microwave technology from Xidian University, Xi’an, China, in 1984 and 1991, respectively.

He became a Professor with Xidian University in 2001. His current research interests include theory and engineering of antenna and antenna array.

Optimized Ferromagnetic Core Magnetorquer Design and Testing for LEO Nanosatellite Attitude Control

Gabriel Villalba-Alumbreros[1], Diego Lopez-Pascual[2], and Efren Diez-Jimenez[1]

[1]Mechanical Engineering Area, Signal Theory and Communications Department
Universidad de Alcalá, 28805, Madrid, Spain
gabriel.villalba@uah.es, efren.diez@uah.es

[2]Electrical Engineering Area, Signal Theory and Communications Department
Universidad de Alcalá, 28805, Madrid, Spain
d.lopezp@uah.es

***Abstract* –** Magnetorquers are a very suitable solution for the nanosatellite's attitude and orbital control of low Earth orbit (LEO) given its constraints: small available volume, limited power consumption, and maximum weight limitation. In this work, an optimized ferromagnetic core magnetorquer is designed for LEO nanosatellites, considering the geometrical, electrical, and magnetic parameters in an electromagnetic finite element analysis (FEA). The final design dimensions are 10.9 mm diameter and 100 mm in length, with a ferromagnetic core made of high performance soft magnetic alloy Vacoflux50 measuring 5 mm diameter and 100 mm in length. Magnetorquer geometry has been optimized to achieve a very high compactness, reaching an optimal combination of high specific magnetic moment and magnetic moment-input power ratio at the same time. It shows a maximum magnetic moment of 1.42 Am^2, a magnetic moment-input power ratio of 2.52 Am^2/W, and a specific magnetic moment of 22.5 Am^2/kg, with a power consumption of 0.565 W and 0.5 A. Such a combination of high-performance values has not been previously found. Furthermore, it has displayed higher magnetic moment and specific magnetic moment than previous prototypes in literature. The simulated model is validated with the experimental testing of a manufactured prototype, by measuring the magnetic and electric variables.

***Index Terms* –** attitude control, magnetic devices, magnetic rod, magnetorquer.

I. INTRODUCTION

Attitude control, stabilization and detumbling are some problems related to the position of any spacecraft in space around Earth [1]–[3]. For space applications, mechanical components with active moving parts can be used for attitude and vibration control [4]–[11]. However, they may suffer from reduced reliability as friction and wear may appear. On the other hand, magnetorquers are cheap, compact, reliable, and lightweight mechanical actuators without moving parts to control the orientation of the spacecraft [12].

Nanosatellites are constructed by only a 10 cm cube module or the junction of several cube modules, never exceeding 10 kg of total mass. In recent years, the development of this type of satellite has been increasing for commercial and military applications [13], including small satellite constellations [14]–[15]. This is due to plenty of new applications achievable with lower budgets and shorter development periods than those required for larger satellites.

A magnetorquer mainly consists of an electromagnet which produces a dipolar magnetic moment m when an electrical current flows through the winding. The magnitude of magnetic moment generated is mainly determined by the geometry, the magnetic properties of the materials and the circulating current. The square of the circulating current multiplied by the electrical resistance of the coil gives the power consumption of a magnetorquer, which is a significant performance parameter of this type of device. Depending on the size of the satellite, larger or smaller magnetic moment amounts are desired, and the smaller and lighter the magnetorquer is, the better for its integration in the satellite [16].

Magnetorquers interact with the Earth's magnetic field B producing a magnetic torque τ (Nm). It allows the satellite to rotate around its own center of mass. This relation is a vectorial product between B (T) and m (Am^2), as defined in equation (1):

$$\vec{\tau} = \vec{m} \times \vec{B} = |\vec{m}| \cdot |\vec{B}| \cdot \sin\theta. \tag{1}$$

Satellites located in low Earth orbit are subject to a more intense and uniform magnetic field compared to further away orbits. This is a requirement for the proper working of the magnetorquer, and it limits the use of

Submitted On: December 12, 2023
Accepted On: March 1, 2024

https://doi.org/10.13052/2024.ACES.J.390107

magnetorquers to LEO missions where the orbit has an altitude ranging from 200-300 km and up to 1600 km [17]. Hence, a magnetorquer designed for bigger satellites on further away orbits would have a lower torque-power ratio, given that the magnetic torque achievable with the same power consumption is lower.

The winding is made of low electrical resistivity materials such as copper or aluminum. Different coils can be manufactured depending on the size of the winding, from macro to micro size [18]–[19]. Its shape can vary from planar coreless square coils [20] to slender round iron-cored coils [21]. PCB printed planar coils are also used. The volume occupied by this kind of magnetorquer is very small and it also benefits the integration with its electronics [22]–[23]. Typically, different types of magnetorquer actuators are combined in an attitude control system for a suitable coordinated operation. In addition, systems like Helmholtz cages are used to test the mentioned system under controlled magnetic fields [24].

Iron-cored magnetorquers are especially interesting. The presence of a soft magnetic material core with a very high magnetic permeability increases the amount of magnetic moment generated [25]. Moreover, its low coercivity allows it to reduce the remanent magnetic moment when the coils are off. With these characteristics, more efficient designs are achievable. Nevertheless, the cylinder of the core tends to be very thin to minimize the demagnetization factor effects. The exact relation between the length of the core and its radius depends on the total size, and it can also be optimized.

The proposed iron-core magnetorquer in this work must fit in the nanosatellites volume, therefore, a maximum length of 100 mm for the magnetorquer is defined. The proposed design in this work, as it is optimized, reaches a combination of both high specific moment and magnetic moment-input power ratio, while maintaining a high magnetic moment and low power consumption. This combination of high values is not found in any previous magnetorquers found in literature.

In Table 1, some commercial and research magnetorquers with similar sizes are listed and compared. The total magnetic moment and relative specific and input power ratios are shown, giving some values of the goal performance.

In this paper an optimized iron-cored magnetorquer design is presented. In the following sections the theoretical model and its equations are defined. An electromagnetic parametric model in FEA software used for optimization is displayed. After the optimization, a detailed design is presented.

Finally, a prototype is manufactured, and a test setup is assembled to validate the FEA model with the present measurements.

Table 1: State-of-the-art of small magnetorquers

Length x Ø (mm x mm)	***m* (Am^2)**	***m*/Power (Am^2/W)**	***m*/I (Am^2/A)**	***m*/Mass (Am^2/kg)**	**Ref**
40x10.6	0.018	0.267	0.360	1.200	**[26]-[27]**
70x9	0.200	1.000	5.000	6.667	[28]
94x13	1.190	1.488	7.438	22.453	[29]
140x16	1.000	2.5	-	5	[30]
75x10	0.394	3.71	9.38	11.588	[31]

II. MAGNETORQUER DESIGN

The design of the magnetorquer is shown in Fig. 1. It consists of an inner cylindrical ferromagnetic core, fully winded with several overlapped layers of copper wire. The geometrical, electrical, and magnetic parameters are shown in Table 2. These parameters will be modified to find the optimal solution.

The materials properties also affect the performance, since the electrical power depends on the electrical resistivity of conductor, and the magnetic moment depends on the relative magnetic permeability of the core. In ferromagnetic materials, the desired properties are low coercivity (opposition to external field), high relative mag-

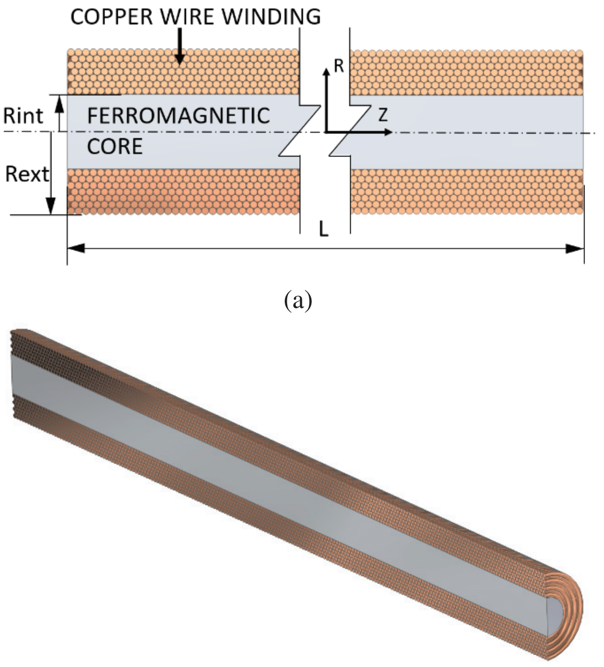

(a)

(b)

Fig. 1. (a) Magnetorquer elements and dimensional parameters and (b) 3D cross-section of the magnetorquer.

Table 2: Magnetorquer parameters

Symbol	Quantity
R_{int}	Core radius
R_{ext}	External winding radius
L	Length of the magnetorquer
D_{cable}	Wire diameter
mass	Device mass
I	Current
j	Current density
R	Electrical resistance
P	Power consumption
m	Magnetic moment

netic permeability (multiplication of external field), and high magnetic saturation (maximum field that can be stored inside the material). Among ferromagnetic materials, Fe-Co alloys present higher magnetic saturation than other alloys like Fe-Si or Ni-Fe. This means that a higher magnetic moment in less material is possible.

The material selected for the inner core is Vacoflux50® from the company VACUUM-SCHMELZE GmbH & Co, Hanau, Germany. Vacoflux50 showed one of the highest magnetic saturations on a machinable bar shape. According to the manufacturer, this material is composed of 49% Fe, 49% Co, 2% V + Nb. This material has been selected for its low coercivity (H_C = 100 A/m), high permeability (μ_r = 7000) and high saturation (B_{sat} = 2.3 T) [32].

To simplify the variable sweeping for the optimization in the design process, a solid copper body is considered instead of the series of layers of winding wire, as shown in Fig. 2. This simplification is possible, due to the fact that the magnetic field contribution to the core of a bare copper cylinder and a compact winding of wire copper is almost the same, because the conductor cross-section is nearly the same.

This simplification drives to equation 2, which correlates the total consumed power with the geometrical design parameters, the material conductivity and the current density applied. Equation 3 is included in the parametric FEA model to change the amount of copper of the magnetorquer depending on the electrical parameters (current density and power) and geometrical parameters of the core (radius and length). The mass is calculated by using the density and the bulk of copper and iron core:

$$\begin{aligned} P &= I^2 \cdot R = j^2 \cdot S^2 \cdot \rho \cdot \frac{L}{S} \\ &= j^2 \cdot (R_{\text{ext}} - R_{\text{int}}) \cdot L \cdot \rho \cdot \pi \cdot (R_{\text{ext}} + R_{\text{int}}), \end{aligned} \tag{2}$$

$$R_{ext} = \sqrt{\frac{P}{L \cdot \rho \cdot \pi \cdot j^2} + R_{int}{}^2}, \tag{3}$$

$$mass = L \cdot \pi \cdot \left(\rho_{copper} \cdot \left(R_{ext}{}^2 - R_{int}{}^2\right) + \rho_{alloy49} \cdot R_{int}{}^2\right). \tag{4}$$

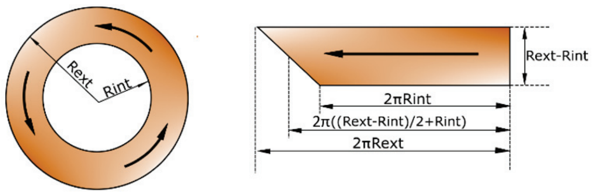

Fig. 2. Magnetorquer simplified parametric model.

III. FINITE ELEMENT MODEL AND MAGNETIC MODEL CALCULATION

All calculations have been done using Ansys Electronics, a finite element model (FEM) software for simulation of electromagnetic fields. The magnetostatic field solution verifies Maxwell's equations:

$$\nabla \times \vec{H} = \vec{J}, \tag{5}$$

$$\nabla \cdot \vec{B} = 0, \tag{6}$$

with the following relationship applicable to each material:

$$\vec{B} = \mu_0(\vec{H} + \vec{M}) = \mu_0 \cdot \mu_r \cdot \vec{H} + \mu_0 \cdot \vec{M}_p, \tag{7}$$

where H is the magnetic field intensity, B is the magnetic field density, J is the conduction current density, M_p is the permanent magnetization, μ_0 is the permeability of vacuum, and μ_r is the relative permeability of the core material [33].

The magnetostatic solver calculates the magnetic field distribution produced by combination of a known DC current density vector distribution and a spatial distribution of objects with magnetic properties. It is also needed to apply boundary conditions to the model, defining the limits of the environment of the simulation.

The design of the preliminary model for the FEM is shown in Fig. 3. It is an axisymmetric 2D model where the Z-axis is the axial symmetry axis. In this model, the geometrical parameters L and R_{int} can be modified

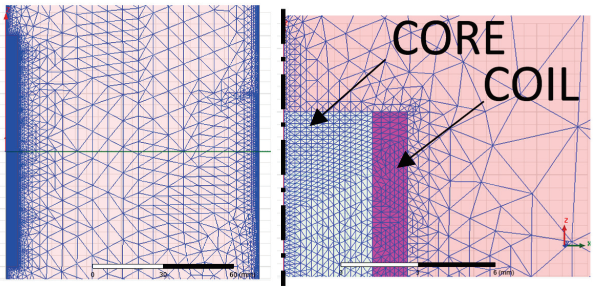

(a) (b)

Fig. 3. (a) 2D axil-symmetrical model of the magnetorquer and (b) detail of the inner core and coil mesh.

parametrized. Mesh model size is proportional to the main geometrical parameters R_{int}, being finer in the surrounding interfaces. Triangular 2D elements have been considered.

A “Balloon” type boundary condition has been applied in the external edges. The Balloon condition models the region outside of the model space as being “infinitely” large. Moreover, an axisymmetric condition on the Z-axis has been imposed.

The external excitation of the model is a constant current density uniformly distributed in the copper coil cross-section, pointing perpendicularly towards the outside of the XZ plane. The value for this current density is j = 4 A/mm^2, common value for copper wires. The cross-section area corresponding with the coils is automatically modified by parametric modelling to adjust the specific power consumption. This is calculated using equation 3.

Materials considered in the simulation are the following: Vacoflux50, vacuum and copper. The defined properties for each of these materials are: magnetic permeability of vacuum, $\mu_0 = 4\pi \cdot 10^{-7}\mathrm{H/m}$; relative permeability of copper, μ_{rCu} = 0.99991; conductivity of copper at 20°C, $\sigma_{\mathrm{Cu}} = 5.8 \cdot 10^7$ S/m; saturation of Vacoflux50 = 2.3 T; magnetic permeability of Vacoflux50 = 15000; and finally the B-H curve retrieved from the datasheet.

The main electromagnetic parameter that defines the behavior of the magnetorquer is the magnetic moment, m. The term magnetic moment normally refers to a system’s magnetic dipole moment [34], the component of the magnetic moment that can be represented by an equivalent magnetic dipole: a magnetic north and south pole separated by a very small distance. In this article, we obtain the magnetic moment by postprocessing of the field density B measured in the axis of the magnetorquer at a certain distance from its center.

Two theoretical approximations have been used: uniformly magnetized core expression and magnetic dipole approximation. The expression to describe the magnetic field generated along the rotation axis by an uniformly magnetized core of length L is [25]:

$$B_z = \frac{m\,\mu_0}{4\pi}\left[\frac{\frac{z}{L}-\frac{1}{2}}{\left(z^2-zL+\frac{L^2}{4}\right)^{3/2}}-\frac{\frac{z}{L}+\frac{1}{2}}{\left(z^2+zL+\frac{L^2}{4}\right)^{3/2}}\right], \tag{8}$$

where z is the distance from the center of the core along the longitudinal Z-axis and m is the magnetic moment. Therefore, by using this expression, the magnetic moment can be determined if the simulation calculates the magnetic field B_z. This expression is useful since it does not require simulating and/or measuring the magnetic field far from the source. However, it assumes that the cylinder is uniformly magnetized which is not the case where the core is not fully saturated.

The magnetic dipole approximation correlates the generated magnetic field with the magnetic moment as:

$$B_z = \frac{\mu_0}{4\pi}\left[\frac{2m}{z^3}\right]. \tag{9}$$

The magnetic dipole approximation is valid, provided that the considered magnetic field is far from the magnetic field source. As a rule of thumb, it is required to measure/simulate magnetic field at a distance more than 10 times the length of the magnetorquer.

In post-processing, we have calculated the magnetic moment simultaneously at different distances and with two different methods. The value of the magnetic moment used for the study is the average between the two methods at z = 0.75 m. This distance is enough to consider that the average value is stabilized for the maximum length of 10 cm with a tolerable error.

IV. GEOMETRY OPTIMIZATION FOR MAXIMUM PERFORMANCE

A geometry optimization process to define the best performing geometric combination has been carried out. The electromagnetic simulation is performed for steady state conditions. Dynamic behavior is not considered, nevertheless, non-linearities on Earth’s magnetic field, changes on orientation commands, and detumbling problems need to be considered during operation. Several techniques have been developed using inertial measurement units [35].

The objective of the optimization is to maximize specific magnetic moment and magnetic moment-input power ratio at the same time. The output variables are total magnetic moment, specific magnetic moment (magnetic moment/mass) and magnetic moment-input power ratio (magnetic moment/power). In the first optimization step, input variables are length L and radius of the core R_{int}.

The dimensions have been limited to ranges from 10 to 100 mm in length and from 1 to 15 mm in radius, which are typical values of commercial magnetorquers. We have performed the simulation for 0.3 and 3 W, typical available power levels in satellites. Having the power as a constraint, and fixing a maximum current density, equation (3) returns a value of R_{ext} by selecting L and R_{int}.

Figure 4 shows the total magnetic moment for different combinations of length and core radius applying a power of 0.3 W. It can be observed that the total magnetic moment is larger for longer magnetorquers and for smaller core radius. This makes sense since demagnetizing factors are more severe for larger R/L ratios, i.e., thicker cylinders, than for slim cylinders. In any case, the longer the cylinder is, the larger its total magnetized

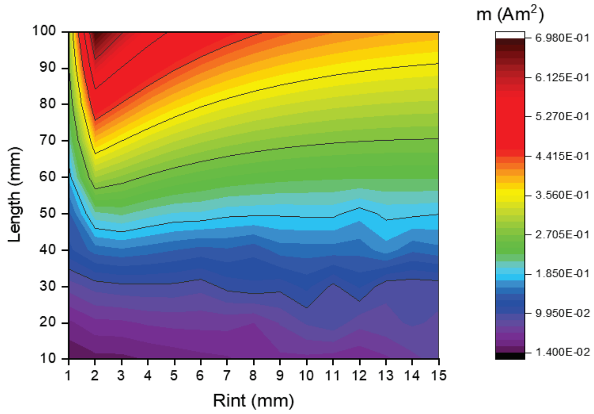

Fig. 4. Magnetic moment for different length and core radius, power P=0.3 W.

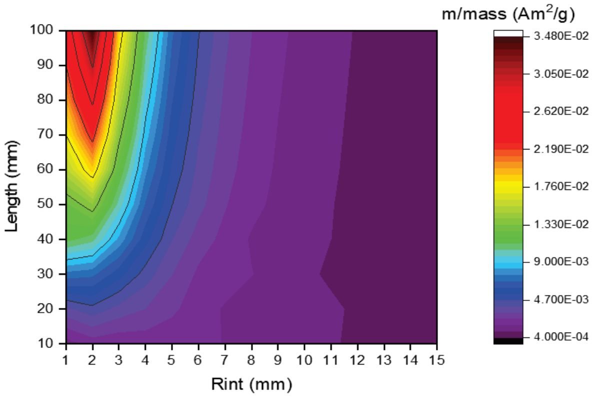

Fig. 5. Specific magnetic moment for different length and core radius, power P=0.3 W.

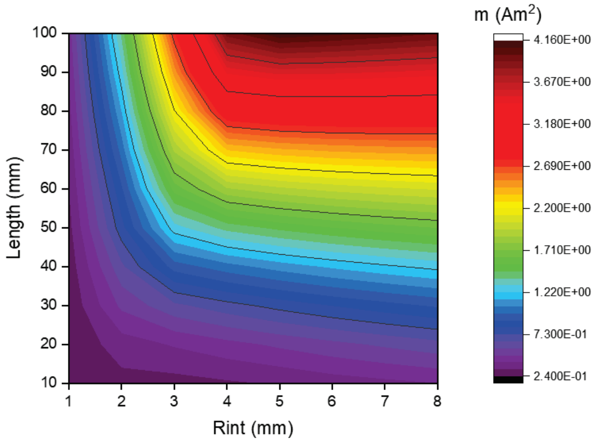

Fig. 6. Magnetic moment for different length and core radius, power P=3 W.

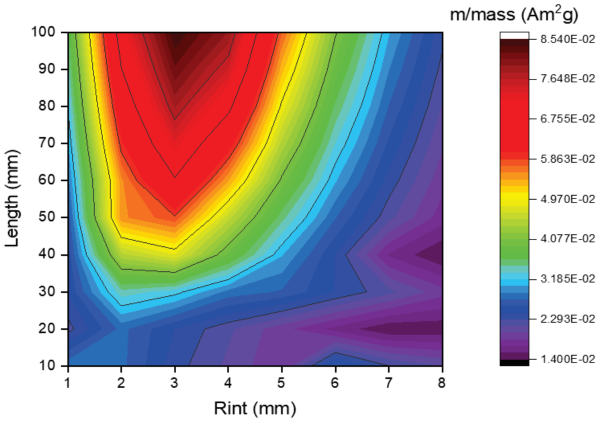

Fig. 7. Specific magnetic moment for different length and core radius, power P=3 W.

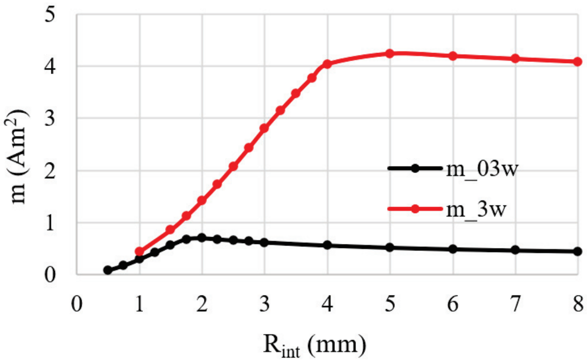

Fig. 8. Magnetic moment comparison for power 0.3 and 3 W with a fixed length of 100 mm.

mass will be, and thus the larger its magnetic moment, even for the same power applied.

Figure 5 shows the specific magnetic moment for different combinations of length and core radius. The effect of the demagnetizing factor is even more pronounced for this parameter. The longer and thinner the magnetorquer, the more optimized in compactness (m/mass) it is.

The same analysis has been done for a power of 3 W, with similar results, as shown in Figs. 6 and 7. After this first optimization analysis, we determined that L = 100 mm is the optimal length in terms of specific magnetic moment for both levels of power.

To fix the core radius, different comparisons have been done from previous simulation results for L = 100 mm. Figure 8 shows a comparison of the total magnetic moment values for the two levels of power.

As expected, the magnetic moment is larger for a higher power, since more power also implies a larger current, and thus more magnetization is achieved in the volume. But it can be observed that the maximum of the magnetic moment is achieved in different core radius values for each power level. More specifically, for a power of 0.3 W, the maximum is achieved at around

2 mm of radius; for 3 W, this maximum is achieved at 4 mm.

Regarding the compactness of the magnetorquer, the behavior reverses. As shown in Fig. 9, the magnetorquer provides a larger specific magnetic moment for a lower level of power. This can be explained by the fact that, for larger power, there are some areas of the magnetorquer that get saturated, so they do not proportionally contribute for larger magnetic fields. Again, maximums are found at between 2 and 4 mm.

The last analyzed parameter is the ratio between the magnetic moment and the corresponding power consumption to obtain it. Figure 10 shows the ratio for both levels of power and for different core radius. It is more efficient when operating at 0.3 W than at 3 W, getting the maximum value again at 2 mm for 0.3 W and at 4 mm for 3 W. It shows that maximum achievable magnetic moment-input power ratio is reduced when the applied electric power increases for any size of core diameter in the evaluated range of 0.3-3 W, contrary to the magnetic moment generation.

Therefore, for an operation ranging between 0.3 and 3 W, an optimal value for the core radius will be located between 2 and 4 mm. From this optimization analysis, we have set the core radius to be R_{int} = 2.5 mm, as a tradeoff between 0.3 and 3 W of power. This value optimizes both specific moment (m/mass) and magnetic moment/power ratio (m/power) giving a unique combination of high compactness never found previously in literature.

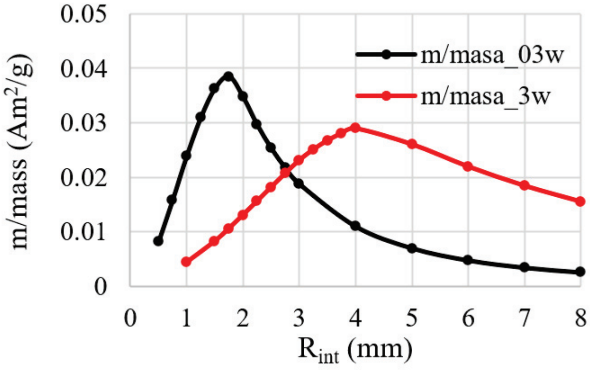

Fig. 9. Specific magnetic moment comparison for power 0.3 and 3 W with a fixed length of 100 mm.

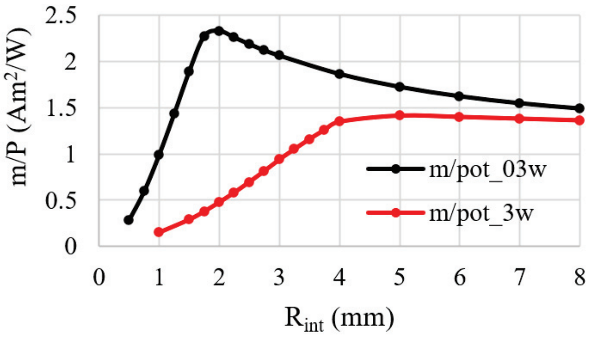

Fig. 10. Magnetic moment/power ratio comparison for power 0.3 and 3 W with a fixed length of 100 mm.

Table 3: Magnetorquer design for several power levels

Power (W)	R_{ext} (mm)	m (Am^2)	m/Power (Am^2/W)	m/Mass (Am^2/kg)
0.1	2.72	0.24	2.35	12.00
0.3	3.12	0.65	2.18	25.24
0.75	3.87	1.44	1.92	35.55
1	4.23	1.81	1.81	37.16
3	6.42	2.97	0.99	25.97
10	11.07	3.75	0.38	10.92

The value of the external radius R_{ext} is related to the amount of power that the magnetorquer is thought to handle. Table 3 shows the different values of external radius needed to handle several levels of power, maintaining a current density value of 4 A/mm^2, and the specific and magnetic moment-input power ratio performance variables obtained. Between 3.87 mm and 6.42 mm of external radius high magnetic moment and maximum specific moment in mass and power have been found. Finally, a value of 5 mm has been selected since it allows higher levels of moment while reaching maximum values of specific magnetic moment.

V. FINAL DESIGN DESCRIPTION AND FEM ANALYSIS

Once the dimensional parameters of the simplified model are fixed, several wire diameter configurations have been simulated for a constant current density of 4 A/mm^2. An analytical expression has been used to predict the total length of the wire considering an overlapping configuration between layers. This led to a more realistic resistance calculus, which depends on wire geometry:

$$\begin{aligned} L_{\text{Cable}} &= f\left(L, n, D_{\text{Cable}}\right) = \frac{L}{D_{\text{Cable}}} 2\pi \cdot n_i \cdot \\ &\quad \left(R_{\text{int}} + D_{\text{Cable}}\left(0.866 \cdot n_i - 0.366\right)\right) \\ &\quad + \left(\frac{L}{D_{\text{Cable}}} - 1\right) 2\pi \cdot n_p \cdot \\ &\quad \left(R_{\text{int}} + D_{\text{Cable}}\left(0.866 \cdot n_p + 0.5\right)\right)). \end{aligned} \tag{10}$$

In terms of total consumed power, generated magnetic moment, and transient time constant, there are no significant changes when the diameter of the wire varies. In Fig. 11, a comparative of the simulation for different wire diameters is shown, where the impact of the filling factor of the winding is visible. Nevertheless, the

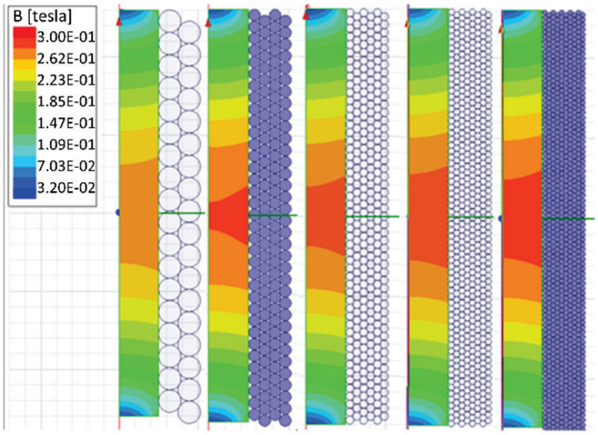

Fig. 11. Simulation of field density in the core for different bare wire diameters.

resistance and the voltage increase as the wire gets thinner, as well as the flowing current decreases. Another consideration that must be taken account is the dynamic behavior of the device. It is adjustable by varying the number of layers and wire diameter, without altering the steady state value. Calculations show that the inductance and resistance of the design ranges from 0.94 uH and 0.0092 Ω (for 2 layers) to 440 uH and 4.865 Ω (for 6 layers). Electronic elements as resistors, inductors or capacitors can be added to adjust the dynamic response too.

The selection of the wire is a compromise between manufacturing feasibility and electrical compatibility. Use of larger wires results in an easier manufacturing process, since for very small wires the control of the layers is more complex. In addition, the electronic systems mounted on the satellite are cheaper and easier to integrate when lower levels of current are needed.

The selected diameter has been a compromise between appropriate levels of current and feasibility on manufacturing, choosing 6 layers for 0.5 mm of wire diameter and 200 turns per layer. Considering the protecting varnish of the real cable the number of turns is corrected to 180, and the external radius to 5.45 mm. In Table 4, the configuration and the operation ranges of the detailed final design are shown.

The detailed model has been simulated varying the input current. The results show the average magnetic saturation level inside the ferromagnetic core. In Fig. 12 it can be observed that, between 0.75 A and 1 A, there is a value of current from which the core starts saturating. It means that the magnetic moment gained from that point is mostly due to vacuum magnetic permeability rather than the permeability of the core material, the moment-current ratio drops from a constant value and stars decreasing, as Fig. 13 shows.

Table 4: Magnetorquer final design parameters

R_{int} (mm)	2.5
R_{ext} (mm)	5.45
L (mm)	100
D_{cable} (mm)	0.5
Mass (g)	63.26
R (ohm)	2.26
I (A)	1.15
P (W)	0.3-3
R_{int} (mm)	2.5

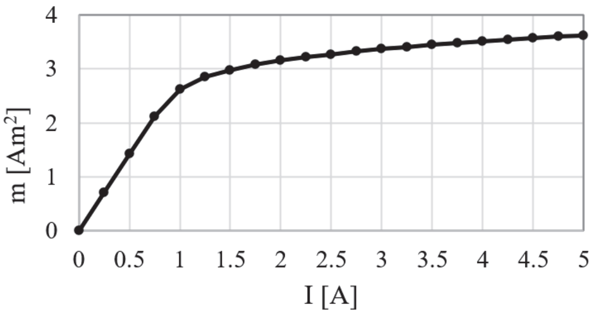

Fig. 12. Magnetic moment as function of the applied current.

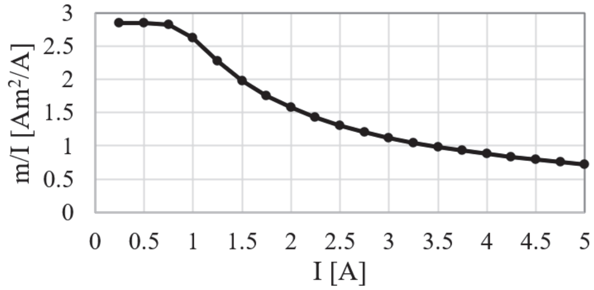

Fig. 13. Magnetic moment sensitivity with current as function of the applied current.

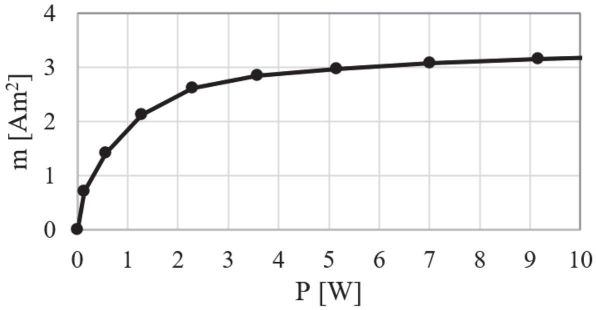

Fig. 14. Magnetic moment as function of the applied power.

In the case of the power, rapidly the saturation point is reached near to 4 W, as shown in Fig. 14, because power is function to the square of the current. The best operation range for the device in terms of magnetic moment-input power ratio is the 0.3-3 W range. However, increasing the power when the core is close to saturation worsens this ratio, but it still gives more absolute magnetic moment.

Table 5: Magnetorquer operation working points

P (w)	0.3	0.565	3
I (A)	0.36	0.5	1.15
m (Am^2)	1.02	1.42	2.76
m/Power (Am^2/W)	3.4	2.52	0.92
m/I (Am^2/A)	2.83	2.85	2.4
m/Mass (Am^2/kg)	16.12	22.5	43.63

In Table 5, values of magnetic moment, magnetic moment-input power ratio, and specific moment are shown for various operation working points, including operation limits. Compared with Table 1, for the lower power limit of operation, the magnetic moment-input power ratio is higher than commercial products, but the specific moment is low. In contrast, the upper power limit of operation presents a higher specific moment than the commercial products, but the magnetic moment-input power ratio is low. A trade-off operation point of 0.565 W and 0.5 A is selected. It presents higher values of magnetic moment and specific moment than all the state-of-the-art (SOA) magnetorquers presented in Section I. If the input power is reduced to 0.3 the magnetic moment-power ratio reaches more than 91% of the maximum power found in literature. The comparison between SOA and this work is shown in Table 6.

Electromagnetic contamination of the magnetorquer at any point in space can be directly obtained by using the magnetic dipolar moment approximation once it is known the effective magnetic moment. Requirements for EMC shielding can be designed from these calculations.

Table 6: Comparison between magnetorquers of SOA and this work

Length x Ø (mm x mm)	***m* (Am^2)**	***m*/Power (Am^2/W)**	***m*/I (Am^2/A)**	***m*/Mass (Am^2/kg)**	**Ref.**
40x10.6	0.018	0.267	0.360	1.200	[26]-[27]
70x9	0.200	1.000	5.000	6.667	[28]
94x13	1.190	1.488	7.438	22.453	[29]
140x16	1.000	2.5	-	5	[30]
75x10	0.394	3.71	9.38	11.588	[31]
100x10.9	1.42	2.52	2.85	22.5	This work

VI. PROTOTYPE MANUFACTURING AND EXPERIMENTAL SET-UP

A prototype has been manufactured to validate the FEA electromagnetic model of the design. A 5 mm diameter and 100 mm long core of Vacoflux50 was machined in a lathe. The rod was made with small holes on its ends for assembling the retainers. These removable glued support parts allow a correct axial alignment between the Hall-effect probe and the magnetorquer in the measurements. In addition, it helps to ensure a correct compactness between turns during the winding process.

A 0.5 mm diameter enameled copper wire has been used for making the windings. Due to the thickness of the protective layer of wires, the filling factor has been reduced from 200 turns per layer to 180 turns per layer as predicted. Through the length of wire used and the unitary resistance of the wire, the resistance of the winding can be predicted. Furthermore, the resistance of the final winding was measured with an LRC impedance measuring device, showing a value of 2.291 Ω. This ensures that the number of turns in the winding, its disposition and resistance accomplish the predicted values. The final prototype is shown in Fig. 15.

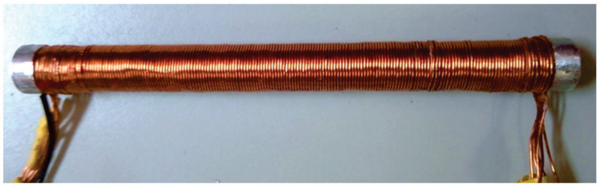

Fig. 15. Manufactured prototype.

The connections between layers were made in series so that it was possible to apply the same current through all the layers. For that purpose, a connection PCB board with neglectable resistance was made through micro-CNC machining process. Afterwards, the terminals were welded to the board.

The experimental set up assembled for the measurements consists of a voltage supply (EX355P-USB from AIM-TTI INSTRUMENTS) and a magnetic field Hall-effect sensor (GM08 from Hirst Magnetics) which measures the axial magnetic field density with an axial probe. The voltage source also measures consumed current.

The magnetorquer is fixed to an aluminum base through aluminum brackets, keeping it away from any magnetic material so as to not contaminate the measurement space. The probe is set in the aluminum retainer and fixed with another backet. The final assembly is shown in Fig. 16. The probe the magnetorquer keeps aligned, with a controlled distance of 5 mm to the end of the magnetorquer.

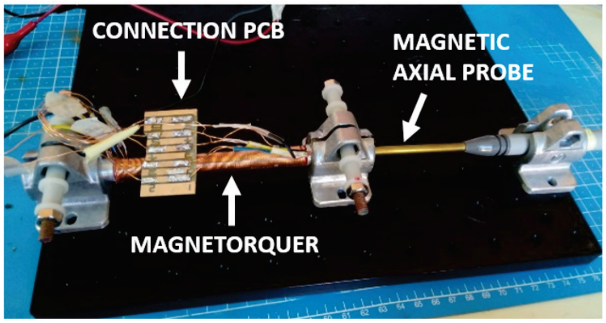

Fig. 16. Magnetorquer and probe assembly set up.

Once the setup is mounted, several measurements at different voltage points have been done. The comparison has been made through the magnetic field-current curve, considering the measurement distance. The distance between the center of the magnetorquer to the Hall-effect transducer of the probe is 55.5 mm. That is the distance to be considered for the validation of the prototype and the later calculation of the magnetic moment.

The measurement must be done as close as possible to the end of the magnetorquer, since with increasing distances the field intensity gets lower, and misalignment or distance errors are more likely to occur.

VII. TEST RESULTS AND DISCUSSION

The validation of the prototype has been achieved through the magnetic field density measurement in the FEA electromagnetic model, measured at the same axial distance. After validation, the magnetic moment can be calculated at a further distance measuring the field in the simulation model.

In Fig. 17, the comparison between testing measurements and simulation for two configurations is presented. At lower magnetic field levels, such as a 3-layer configuration, in the mostly linear behavior, the simulation curve perfectly fits the experimental measures. The difference between the two curves in the 6-layer case is caused by a change in the magnetic properties of the ferromagnetic material. This change at higher magnetic field levels can be produced by the effect of the heat generation during operation while measuring. However, the model is validated and it is demonstrated that the prototype has the expected specifications of the design and the electromagnetic model.

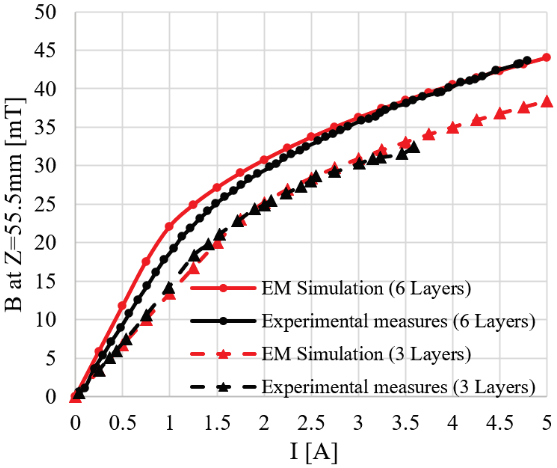

Fig. 17. Generated magnetic field as function of current.

VIII. CONCLUSION

A magnetorquer, as any other spacecraft subsystem, has very strict constraints in terms of mass, volume, and power consumption. An optimized iron-core magnetorquer prototype for LEO nanosatellites is presented in this work.

The design process starts with the definition of a conceptual design with its own variables. A simplified design, with a context of parameters, equations and limitations, is established. Through an electromagnetic finite element analysis (FEA) model, the parametric optimization has been done. Using both the electrical and geometrical parameters, the optimization had the objective of achieving values as high as possible of magnetic moment, specific moment, and moment.

After the simplified model is optimized, a detailed design is presented. The design achieves a combination of magnetic moment, magnetic moment-input power ratio and specific moment values not found in the state of the art. The magnetorquer proposed in this work has 100 mm length and 10.9 mm diameter, with a ferromagnetic core made of Vacoflux50 with 5 mm diameter. The wire is an enameled copper wire with 0.5 mm bare copper diameter.

The operation condition range studied for the device is from 0.3 W (0.36 A) to 3 W (1.15 A). The optimized working point has been found to be at 0.565 W (0.5 A). At this point the values reached are: 1.42 Am^2, 2.52 Am^2/W, and 22.5 Am^2/kg. Magnetorquer geometry has been optimized to achieve a very high compactness, reaching an optimal combination of high magnetic moment, specific magnetic moment, and magnetic moment-input power ratio at the same time. Such a combination of high-performance values has not been found in the literature before with iron-cored magnetorquers. The value of magnetic moment and specific magnetic moment is higher than found on earlier prototypes in the literature.

Finally, to validate the model, a prototype has been manufactured, as well as a test setup. In the test setup, measurements of magnetic field density, voltage, current and resistance have been done without considering thermal effects, which will have to be evaluated in a relevant environment in future work. As the simulated and experimental values were in good agreement, the FE model of the prototype is validated.

REFERENCES

[1] Y. Gu, Q. Liang, S. Wang, A. Zhou, and C. Liu, "Shape optimization of the momentum ring cross section for satellite attitude control based on magnetohydrodynamics," *Applied Computational Electromagnetics Society (ACES) Journal*, vol. 37, no. 3, pp. 348-353, 2022.

[2] F. Mesch, "Magnetic components for the attitude control of space vehicles," *IEEE Trans. Magn.*, vol. 5, no. 3, pp. 586-592, 1969.

[3] K. R. Rajagopal, "Design and development of a permanent magnet torquer for a gyroscope," *IEEE Trans. Magn.*, vol. 37, no. 4, pp. 2630-2633, 2001.

[4] M. Tang, J. Zhou, C. Jin, and Y. Xu, "Vibration isolation of magnetic suspended platform with double closed-loop PID control," *Applied Computational Electromagnetics Society (ACES) Journal*, vol. 32, no. 8, pp. 712-719, 2017.

[5] R. Alcover-Sanchez, J. M. Soria, J. Pérez-Aracil, E. Pereira, and E. Diez-Jimenez, "Design and experimental characterization of a novel passive magnetic levitating platform," *Smart Struct. Syst.*, vol. 29, no. 3, pp. 499-512, 2022.

[6] E. Diez-Jimenez, C. Alén-Cordero, R. Alcover-Sánchez, and E. Corral-Abad, "Modelling and test of an integrated magnetic spring-eddy current damper for space applications," *Actuators*, vol. 10, no. 1, 2021.

[7] M. Muñoz-Martínez, E. Diez-Jimenez, M. J. Gómez-García, R. Rizzo, and A. Musolino, "Torque and bearing reaction forces simulation of micro-magnetic gears," *Applied Computational Electromagnetics Society (ACES) Journal*, vol. 34, no. 4, pp. 541-546, 2019.

[8] E. Diez-Jimenez, R. Sanchez-Montero, and M. Martinez-Muñoz, "Towards miniaturization of magnetic gears: Torque performance assessment," *Micromachines*, vol. 9, no. 1, p. 16, Dec. 2017.

[9] F. Fiorillo, F. Santoni, E. Ferrara, M. L. Battagliere, O. Bottauscio, and F. Graziani, "Soft magnets for passive attitude stabilization of small satellites," *IEEE Trans. Magn.*, vol. 46, no. 2, pp. 670-673, Feb. 2010.

[10] J. Esnoz-Larraya, I. Valiente-Blanco, C. Cristache, J. Sanchez-Garcia, F. Celis, E. Diez-Jimenez, and J. L. Perez-Diaz. "OPTIMAGDRIVE: High performance magnetic gears development for space applications," in *17th European Space Mechanisms and Tribology Symposium*, pp. 1-5, 2017.

[11] J. Perez-Diaz, E. Diez-Jimenez, I. Valiente-Blanco, C. Cristache, and J. Sanchez-Garcia-Casarrubios, "Contactless mechanical components: Gears, torque limiters and bearings," *Machines*, vol. 2, no. 3, pp. 312-324, 2014.

[12] D. S. Ivanov, M. Y. Ovchinnikov, V. I. Penkov, D. S. Roldugin, D. M. Doronin, and A. V. Ovchinnikov, "Advanced numerical study of the three-axis magnetic attitude control and determination with uncertainties," *Acta Astronaut.*, vol. 132, pp. 103-110, Mar. 2017.

[13] T. Wekerle, J. B. P. Filho, L. E. V. L. da Costa, and L. G. Trabasso, "Status and trends of smallsats and their launch vehicles - An up-to-date review," *J. Aerosp. Technol. Manag.*, vol. 9, no. 3, pp. 269-286, 2017.

[14] T. Inamori, R. Kawashima, P. Saisutjarit, N. Sako, and H. Ohsaki, "Magnetic plasma deorbit system for nano- and micro-satellites using magnetic torquer interference with space plasma in low Earth orbit," *Acta Astronaut.*, vol. 112, pp. 192-199, 2015.

[15] J. H. Park, S. Matsuzawa, T. Inamori, and I. S. Jeung, "Nanosatellite constellation deployment using on-board magnetic torquer interaction with space plasma," *Adv. Sp. Res.*, vol. 61, no. 8, pp. 2010-2021, 2018.

[16] A. Ali, M. R. Mughal, H. Ali, L. M. Reyneri, and M. N. Aman, "Design, implementation, and thermal modeling of embedded reconfigurable magnetorquer system for nanosatellites," *IEEE Trans. Aerosp. Electron. Syst.*, vol. 51, no. 4, pp. 2666-2679, 2015.

[17] C. S. Allen, M. Giraudo, C. Moratto, and N. Yamaguchi, "Spaceflight environment," in *Space Safety and Human Performance*, T. Sgobba, B. Kanki, J.-F. Clervoy, and G. M. Sandal, Eds. Amsterdam: Elsevier, pp. 87-138, 2017.

[18] M. Martinez-Muñoz, E. Diez-Jimenez, G. V. Villalba-Alumbreros, M. Michalowski, and A. Lastra-Sedano, "Geometrical dependence in fixtures for 2D multipole micromagnets magnetization pattering," *Applied Computational Electromagnetics Society (ACES) Journal*, vol. 34, no. 7, 2019.

[19] M. Martinez-Muñoz, E. Diez-Jimenez, R. Sanchez-Montero, P. L. Lopez-Espi, and J. A. Martinez-Rojas, "Analysis of the geometric parameters influence in PCB fixtures for 2D multipole magnetization patterning of thin layer micro-magnets," *Int. J. Appl. Electromagn. Mech.*, vol. 61, no. 1, 2019.

[20] G. Cervettini, S. Pastorelli, H. Park, D. Y. Lee, and M. Romano, "Development and experimentation of a CubeSat magnetic attitude control system testbed," *IEEE Trans. Aerosp. Electron. Syst.*, vol. 57, no. 2, pp. 1345-1350, 2021.

[21] M. Fakhari Mehrjardi and M. Mirshams, "Design and manufacturing of a research magnetic torquer rod," *Fourth Int. Conf. Exp. Mech.*, vol. 7522, no. 5, p. 75221W, 2009.

[22] M. R. Mughal, H. Ali, A. Ali, J. Praks, and L. M. Reyneri, "Optimized design and thermal analysis of printed magnetorquer for attitude control of reconfigurable nanosatellites," *IEEE Trans. Aerosp. Electron. Syst.*, vol. 56, no. 1, pp. 736-747, 2020.

[23] N. J. Sorensen, "Efficiency-optimized design of PCB-integrated magnetorquers for CubeSats," *IEEE Trans. Aerosp. Electron. Syst.*, vol. 57, no. 6, pp. 3623-3632, 2021.

[24] R. C. Da Silva, I. S. K. Ishioka, C. Cappelletti, S. Battistini, and R. A. Borges, "Helmholtz cage design and validation for nanosatellites HWIL testing," *IEEE Trans. Aerosp. Electron. Syst.*, vol. 55, no. 6, pp. 3050-3061, 2019.

[25] J. Lee, A. Ng, and R. Jobanputra, "On determining dipole moments of a magnetic torquer rod - Experiments and discussions," *Can. Aeronaut. Sp. J.*, vol. 48, no. 1, pp. 61-67, 2002.

[26] G. P. Candini, F. Piergentili, and F. Santoni, "Designing, manufacturing, and testing a self-contained and autonomous nanospacecraft attitude control system," *J. Aerosp. Eng.*, vol. 27, no. 6, p. 04014033, 2014.

[27] G. P. Candinia, F. Piergentilib, and F. Santoni, "Miniaturized attitude control system for nanosatellites," *Acta Astronaut.*, vol. 81, no. 1, pp. 325-334, 2012.

[28] "CubeSatShop Cubesat NCTR-M002 magnetic rod," Datasheet.

[29] "CubeSatShop Cubesat NCTR-M012 magnetic rod," Datasheet.

[30] "Sputnix SX-MT Magnetic Torquers," Datasheet.

[31] H. Ali, M. R. Mughal, Q. ul Islam, M. R. Anjum, S. Ishaq, and L. M. Reyneri, "Parametric optimization and analysis of power efficient magnetorquer rod actuator for nanosatellite," *IEEE J. Miniaturization Air Sp. Syst.*, vol. 3, no. 2, pp. 30-35, 2022.

[32] "Vaccumshmeltze: Iron-cobalt alloys," Datasheet.

[33] "Ansoft Ansys Maxwell v15 - Help assistant," Datasheet, 2018.

[34] Y. Yu, H. Yue, F. Yang, H. Zhao, and Y. Lu, "Electromagnetic interaction between a slowly rotating conducting shell and magnetic dipoles: A theoretical and numerical study," *IEEE Trans. Magn.*, vol. 57, no. 8, 2021.

[35] D. M. Torczynski, R. Amini, and P. Massioni, "Magnetorquer based attitude control for a nanosatellite testplatform," *American Institute of Aeronautics and Astronautics*, 2010.

Gabriel Villalba-Alumbreros received his M.Sc. in Industrial Engineering in 2022 and B.Sc. in Electronics and Industrial Automation Engineering in 2019. Currently he is working in UWIPOM2 project under Horizon 2020 EU funding programme for research and innovation at University of Alcalá.His research interests are focused in electromagnetic actuators, mechatronic systems, MEMS and control systems.

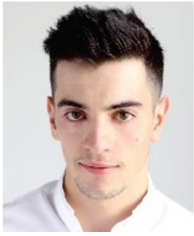

Diego López-Pascual is an Assistant Professor at the Electrical Engineering area of Universidad de Alcalá. He obtained his Ph.D. on Industrial Engineering in 2023. He joined the Mechanical, Electric & Thermal Technologies research group at Universidad de Alcalá at the beginning of 2020, where he is working on the UWIPOM2 project under EU funding. His main research interests are industrial design, thermal characterization of systems, and renewable energy systems modelling, subject on which his Ph.D. was developed.

Efrén Díez-Jiménez is a Professor at the Mechanical Engineering area of Universidad de Alcalá. He obtained his Ph.D. on Mechanical Engineering and Industrial Organization in 2012, M.Sc. on Machines and Transport Engineering in 2010 and Bachelor on Industrial Engineering in 2008 from Universidad Carlos III de Madrid, Spain. In 2013, he received the Extraordinary Award for the Best Thesis in Mechanical Engineering. He has participated as coordinator into different ESA-H2020-FP7 projects with successful results. Currently, he is coordinator of H2020 European project UWIPOM2, where micro-robotic rotary actuators are being developed. Author of more than 35 articles and 5 patents granted, he also collaborates as reviewer in mechanical engineering journals. His main research interests are mechanisms and machine design, electromagnetic actuators and MEMS.

Polarization Agile Reconfigurable Rectangular Patch Antenna for Biomedical Applications

Saravanan Manavalan[1*], Balraj Shankarlal[2], Veeraswamy Radhakrishnan Prakash[3], Sathish Eswaramoorthy[4], and Madasamy Rajmohan[5]

[1]Department of ECE, Vel Tech Rangarajan Dr. Sagunthala R&D Institute of Science and Technology
Chennai, India
msarawins@ieee.org
*Corresponding Author

[2]Department of ECE, Perunthalaivar Kamarajar Institute of Engineering and Technology
Karaikal, India
shankarlal.pkiet@gmail.com

[3]Department of ECE, Hindustan Institute of Technology and Science
Chennai, India
vrprakash@hindustanuniv.ac.in, mrajmohan@hindustanuniv.ac.in

[4]School of Electronics Engineering, Vellore Institute of Technology
Chennai, India
sathish.e@vit.ac.in

Abstract – A polarization agile patch antenna resonating at 2.4 GHz ISM band is presented. The antenna is based on a rectangular radiating element along with reconfigurable parasitic patches located at its periphery of the radiating element. Two switching diodes are used to reconfigure the geometry of the radiating element. Upon proper biasing of the switching diodes the antenna attains linear or circular (LHCP/RHCP) polarization states. The entire antenna is modelled using a high-frequency structure simulator and is validated using an Agilent network analyser (N9925A) and antenna test systems for measuring impedance and radiation characteristics. Over the entire operating band, the antenna shows better impedance matching and achieves −10 dB impedance bandwidth of 100 MHz (2.40-2.5 GHz) in linear state and 85 MHz (2.41-2.495 GHz) in the circularly polarization states along with peak gain of 5.61 dBi for LP state and 4.98 dBi for CP state in the operating range.

Index Terms – impedance matching, microstrip patch, polarization reconfiguration, radiation pattern.

I. INTRODUCTION

Patch antennas play a crucial role in biomedical communications with external devices for monitoring patients due to their miniaturization and low weight. These antennas come with various geometries and materials according to the requirement of monitoring patients. In order to have a better signal link, orientation between transmitter and receiver antenna must be maintained. However, it is always possible for both the antennas to maintain line of sight orientation. Hence the need for circular polarized antennas replacing traditional antennas becomes important [1–2]. These on-body wearable antennas for monitoring patients health issues must have low back radiation with reduced specific absorption rate (SAR) values and also must perform well on moving bodies [3]. A wideband circularly polarized patch antenna for bio telemetric application is presented in [4]. The antenna utilizes 2×2 multiple-input multiple-output (MIMO) radiating patches with defected ground structures which leads to back radiation towards patients tissue. Moreover, these MIMO antennas are densely packed which increases the mutual coupling between the antenna elements. The isolation can be improved by placing adjacent radiating elements perpendicular to each other [5]. In order to improve the antenna performances, different structures, including electromagnetic band-gap (EBG) and high impedance surfaces, are utilized. A compact monopole based on EBG structure for wearable applications [6] and a high impedance surface-based patch [7] are presented. However, these structures

Submitted On: June 22, 2022
Accepted On: December 7, 2023

https://doi.org/10.13052/2024.ACES.J.390108

require complexity of the antenna design and also a number of substrate layers required for the antenna. In order to reduce cross talks between the antenna, a filtering antenna is incorporated along with traditional circularly polarized antennas [8], which requires additional design space for a filtering antenna and also increases the complexity of the design. A 3D printed ultrawideband antenna system with stable impedance matching has been proposed in [9]. Polarization reconfigurable antennas are widely used due to their ability to switch polarization in real time [10]. The reconfigurable antennas have better cross polarization isolation and mitigate the multipath reception of signals, which improves signal quality. This reconfiguration can also be achieved by means of MEMS switches [11] with better miniaturization.

Most of the literature utilizes fixed circularly polarized state patch antennas with increased number of switching elements for switching polarization states. This reduces efficiency of the antenna greatly. In this paper, a polarization agile patch with reduced number of switching elements modelled on single layer substrate is designed. The bottom side of the antenna is fully grounded to arrest the undesired back radiation. The antenna is operating at 2.4 GHz ISM band, and its impedance and radiation characteristics are validated through measured results.

II. GEOMETRY OF THE PROPOSED ANTENNA

The geometry of the proposed patch is shown in Fig. 1. The rectangular patch is taken for its simplicity and better control over its dimensions on design performances. Moreover, the geometry is symmetrical and hence avoids undesired frequency shifts between the frequencies between polarizations states, which makes it ideal for biomedical applications. The antenna is modelled on low-cost fire-retardant substrate with permittivity of 4.4 and loss tangent of 0.02. The overall antenna is modelled on single lay substrate having a dimension of 50×50 mm with thickness of 1.6 mm. Two parasitic patches are placed on either side of the antenna geometry in order to reconfigure the antenna structure, thereby modifying the surface current distribution over the antenna radiating element. A shorting via is made in the parasitic patch to complete the DC bias path. Two switching diodes are placed between the parasitic element and the radiating element. Upon proper biasing, the diodes bridge the parasitic element with radiating patch and thereby makes the path for the surface current to flow through parasitic elements, which leads to additional phases for achieving different polarization reconfiguration.

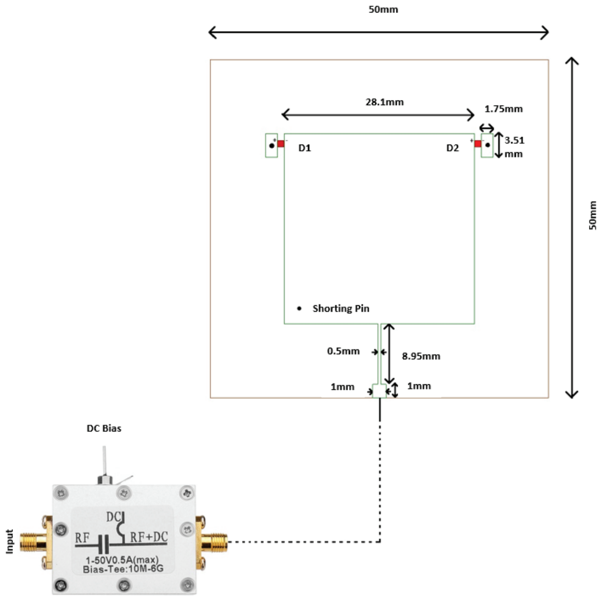

Fig. 1. Antenna geometry.

The feed position is chosen in such a way that it matches the impedance of the radiating element by means of using a quarter-wave transformer between the radiating elements and the feed point.

III. PRINCIPLE OF OPERATION

Polarization reconfiguration is achieved by properly biasing the pin diodes (NXP BAP50-03, 50 mA, 50 V). The resistance of the diodes during its operation plays a crucial role in the radiation efficiency of the antenna. The pin diodes are chosen in such a way that it must have a minimum forward resistance during ON condition. The pin diodes used in the model will have a series resistance and inductance of 5 Ω and 1.8 nH during ON state and shunt capacitance 0.35 pF with the reverse resistance of 500 kΩ during OFF state. The equivalent circuit model of the pin diode used is given in Fig. 2. Figures 2 (a), (b) show the diode equivalent circuit model during ON and OFF state. Figure 2 (c) shows the equivalent circuit corresponding to the biasing circuit. It comprises a DC block capacitor and RF choke inductor for isolating the bias network from the antenna elements and hence avoids direct coupling.

The diodes are placed in such a way that the cathode of the diode D1 points towards the radiating patch while the anode points towards the parasitic patch, which has shorting vias with the ground for the DC path. Similarly, the anode of the diode D2 points towards the radiating patch while the cathode points towards the parasitic patch, which has shorting vias with the ground for the DC path. A Tee- Bias network is used for properly biasing the pin diodes to achieve polarization

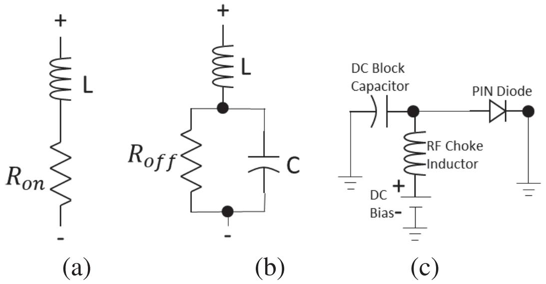

(a) (b) (c)

Fig. 2. Equivalent circuit model of the pin diode and biasing circuit.

reconfiguration. Table 1 shows the different operating modes of the proposed antenna model.

Table 1: Different operating modes

S. No.	DC Bias Voltage	Diode D1	Diode D2	Polarization State
1	0 V	OFF	OFF	LP
2	+2 V	OFF	ON	RHCP
3	-2 V	ON	OFF	LHCP

When no bias voltage (0 V) is given, both diodes are in OFF state, and the geometry resembles a simple rectangular patch antenna and gives a linear polarization state that resonates at center frequency. When DC bias voltage of +2 V is given, diode D2 turns into ON state as the anode of the diode D2 points towards the radiating patch while the cathode points towards the parasitic patch, which has shorting vias with the ground and hence closes the DC path. Thus, the length of the patch in the right symmetry increases slightly, which introduces additional phase shift between the electric currents $(E_x \text{ and } E_y)$. This generates two orthogonal modes with same amplitude with -90^0 phase difference and hence attains right-hand circular polarization.

Similarly, when DC bias voltage of -2 V is given, diode D1 turns into ON state as the cathode of the diode D2 points towards the radiating patch while the cathode points towards the parasitic patch, which has shorting vias with the ground and hence closes the DC path. Thus, the length of the patch in the left symmetry increases slightly, which introduces additional phase shift between the electric currents $(E_x \text{ and } E_y)$. This generates two orthogonal modes with the same amplitude with $+90^\circ$ phase difference and hence attains left-hand circular polarization. The surface current distribution corresponding to different polarization states are shown in Fig. 3.

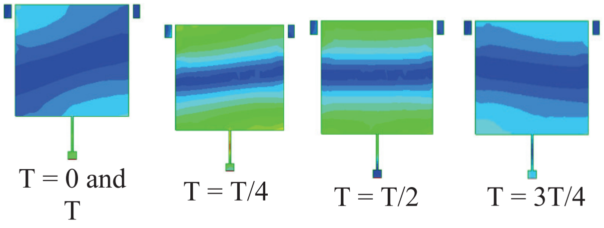

(a) Linearly polarized

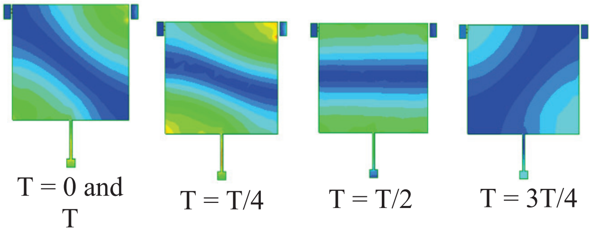

(b) Circularly polarized (RHCP)

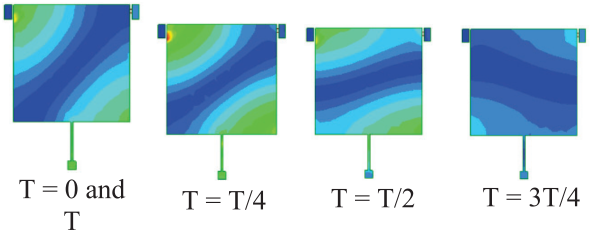

(c) Circularly polarized (LHCP)

Fig. 3. Surface current distribution.

IV. RESULTS AND DISCUSSION

The performance of the proposed antenna is validated by measuring its impedance and its radiation characteristics. The antennas are fabricated on FR4 substrate and are connected with 50 ω SMA connector, as shown in Fig. 4. The diodes are placed to bridge the radiating patch with the outer parasitic elements. A standard T bias switch is coupled with SMA connector input for biasing the RF switch to switch its polarization characteristics. The shorting pin is punched at its radiating patch center for providing a DC path during biasing of the diodes.

The impedance characteristics are measured with Agilent network analyzer (N9925A) and are compared with simulated results, as shown in Fig. 5. From Fig. 5 it is inferred that the antenna attains a -10 dB impedance bandwidth of 100 MHz (2.40-2.5 GHz) in linear state and 85 MHz (2.41-2.495 GHz) in the circularly polarization states respectively.

The radiation measurement setup used to analyze the radiation characteristics of the antenna is shown in Fig. 6.

Figure 7 shows the radiation characteristics of the antenna, which are measured using an antenna test system that comprises a pyramidal horn antenna having a standard gain of 9 dB placed inside the anechoic

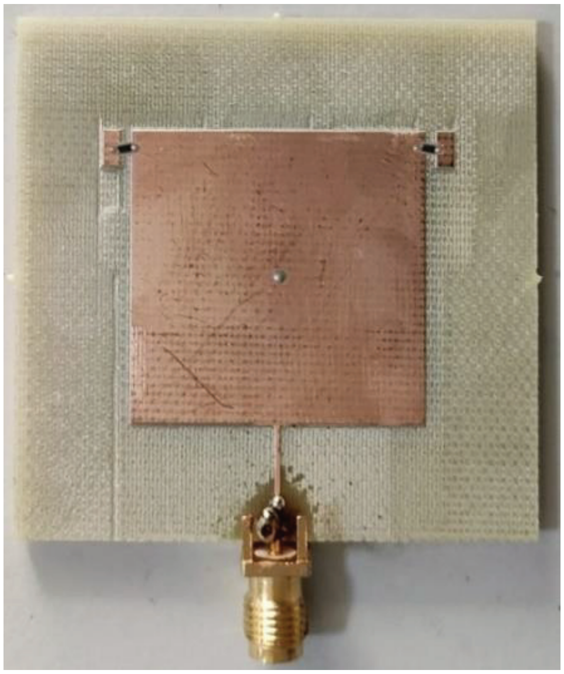

Fig. 4. Fabricated prototype.

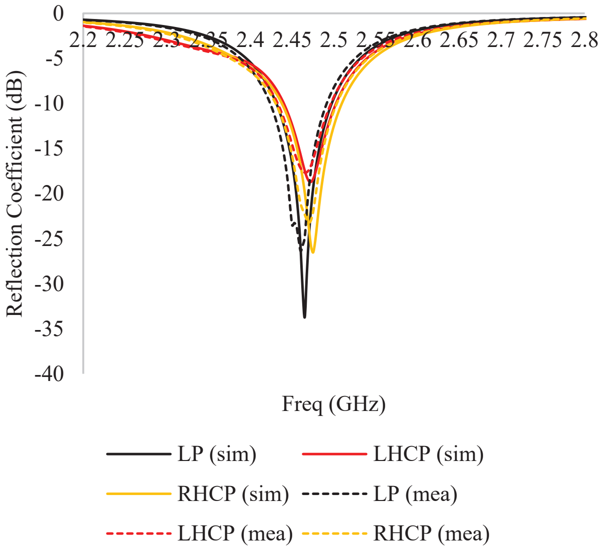

Fig. 5. Reflection Coefficient (dB).

chamber. The test antenna is placed at a far-field distance of $2D^2/\lambda$ from the transmitter antenna, and the gain of the test is calculated based on the Friis transmission equation:

$$P_r = P_t G_r G_t \left(\frac{\lambda}{4\pi R}\right)^2. \tag{1}$$

The relative gain corresponding to the fabricated prototype is measured for both the planes. The antenna

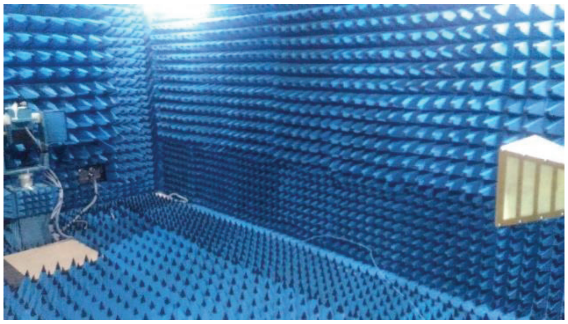

Fig. 6. Measurement setup environment for test antenna.

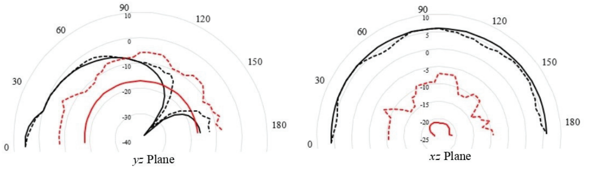

(a) Linear polarized state

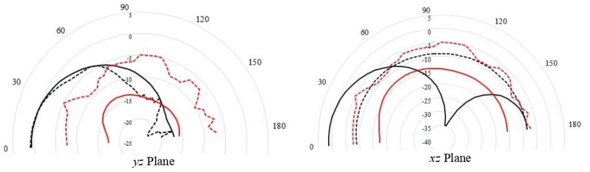

(b) Circularly Polarized (RHCP) State

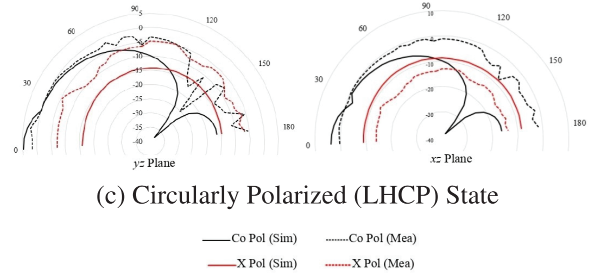

(c) Circularly Polarized (LHCP) State

Fig. 7. Radiation characteristics of the proposed antenna.

attains symmetrical radiation pattern in the direction of propagation. The antenna attains maximum gain of 5.61 dBi for the LP state and 4.98 dBi for the LHCP/RHCP state.

The axial ratio bandwidth corresponding to the proposed model for LHCP and RHCP modes is given Fig. 8. It is inferred that compared to impedance bandwidth, the axial ratio bandwidth is lesser, since the tangential components of the electric fields are attenuated closed to the ground surface. The model attains axial ratio bandwidth of 2.42-2.51 GHz in the operating band.

Specific absorption rate (SAR) is used to quantify the electromagnetic radiation over human tissues, and SAR is calculated by

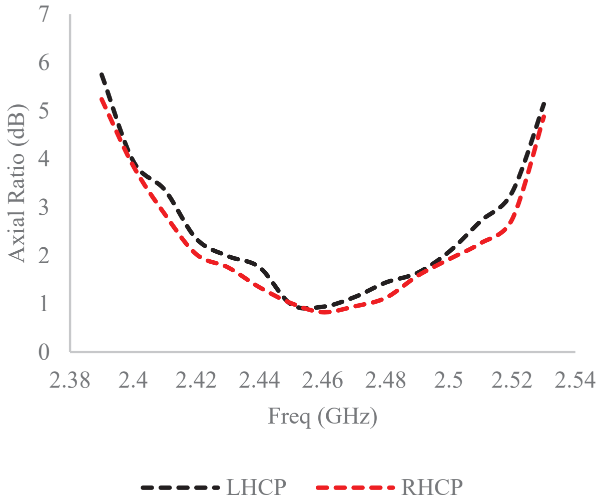

Fig. 8. Axial ratio bandwidth of the proposed antenna.

$$\mathrm{SAR} = \frac{\sigma\left|E^2\right|}{\rho}, \tag{2}$$

where σ and ρ are thermal conductivity, $(\mathrm{S/m})$ mass density $(\mathrm{kg/m^3})$ of the tissue medium, and E is the electric field intensity $(\mathrm{V/m})$, which is calculated from the power input using the relation given here:

$$Power\left(\mathrm{W/m^2}\right) = \frac{\left(E\,(\mathrm{V/m})\right)^2}{377}. \tag{3}$$

An agar based homogenous tissue model is prepared to mimic human tissue (palm) having a permittivity of 26.47 [12] to measure the SAR value of the proposed model. The model achieves a minimum SAR value of 0.385 W/kg at its operating bands.

Performance comparison of the proposed model with other conventional models is given in Table 2. Most of the traditional antennas utilize linear polarization or fixed circular polarization techniques, which limits their application. The proposed model utilizes reconfigurable polarization characteristics with a minimum number of electronically controlled switching diodes without sacrificing the impedance and radiation characteristics of the antenna in its operating band. In addition to that, the antenna attains minimum SAR value at the operating band, which makes it suitable for biomedical applications.

Table 2: Performance comparison of the proposed antenna

Ref	**Size** $(\mathrm{mm^3})$	**Operating Freq.**	**Polarization**	**Axial Ratio Bandwidth**	**SAR (W/kg)**
[13]	25 × 20 × 0.07	2.45 GHz	Linear	1.22%	1.0
[14]	14 × 14 × 05	2.45 GHz	Circular	6.93%	0.494
[15]	24 × 22 × 0.7	2.45 GHz	Linear	24.4%	0.719
[16]	21 × 13.5 × 0.254	2.45 GHz	Circular	53.8%	0.78
Proposed	50 × 50 × 1.6	2.45 GHz	Circular	44.8%	0.385

V. CONCLUSION

A polarization reconfigurable antenna based on switching pin diodes is presented. The antenna is designed at the 2.45 GHZ ISM band and attains three different polarization states upon proper biasing of the switching diodes. The model is validated by fabricating on single FR4 substrate, and the measured results are compared with simulated results. The antenna achieves -10 dB impedance bandwidth of 100 MHz (2.40-2.5 GHz) in linear state and 85 MHz (2.41-2.495 GHz) in the circularly polarization states along with a peak gain of 5.61 dBi for LP state and 4.98 dBi for CP state in the operating range. The antenna attains maximum axial ratio bandwidth of 44.8% in the operating band with a SAR value of 0.385 W/kg.

ACKNOWLEDGMENT

The work is funded under SEED Grant No.: VTU SEED (FY 22-23) -18 provided by Vel Tech Rangarajan Dr. Sagunthala R&D Institute of Science and Technology, Chennai, India.

REFERENCES

[1] Z. Xia, H. Li, Z. Lee, S. Xiao, W. Shao, X. Ding, and X. Yang, "A Wideband circularly polarized implantable patch antenna for ISM band biomedical applications," *IEEE Transactions on Antennas and Propagation*, vol. 68, no. 3, pp. 2399-2404, Mar. 2020. doi: 10.1109/TAP.2019.2944538.

[2] C. Liu, Y. Guo, and S. Xiao, "Capacitively loaded circularly polarized implantable patch antenna for ISM band biomedical applications," *IEEE Transactions on Antennas and Propagation*, vol. 62, no. 5, pp. 2407-2417, May 2014. doi: 10.1109/TAP.2014.2307341.

[3] Z. H. Jiang and D. H. Werner, "A compact, wideband circularly polarized co-designed filtering antenna and its application for wearable devices with low SAR," *IEEE Transactions on Antennas and Propagation*, vol. 63, no. 9, pp. 3808-3818, Sep. 2015. doi: 10.1109/TAP.2015.2452942.

[4] A. Iqbal, A. Smida, A. J. Alazemi, M. I. Waly, N. Khaddaj Mallat, and S. Kim, "Wideband circularly polarized MIMO antenna for high data wearable biotelemetric devices," *IEEE*

Access, vol. 8, pp. 17935-17944, 2020. doi: 10.1109/ACCESS.2020.2967397.

[5] K. Kaboutari and V. Hosseini, "A compact 4-element printed planar MIMO antenna system with isolation enhancement for ISM band operation," *AEU - International Journal of Electronics and Communications*, vol. 134, ID: 153687, 2021. doi: 10.1016/j.aeue.2021.153687.

[6] M. A. B. Abbasi, S. S. Nikolaou, M. A. Antoniades, M. Nikolić Stevanović, and P. Vryonides, "Compact EBG-backed planar monopole for BAN wearable applications," *IEEE Transactions on Antennas and Propagation*, vol. 65, no. 2, pp. 453-463, Feb. 2017. doi: 10.1109/TAP.2016.2635588.

[7] Y. Chen and T. Ku, "A low-profile wearable antenna using a miniature high impedance surface for smartwatch applications," *IEEE Antennas and Wireless Propagation Letters*, vol. 15, pp. 1144-1147, 2016. doi: 10.1109/LAWP.2015.2496366.

[8] Z. H. Jiang, M. D. Gregory, and D. H. Werner, "Design and experimental investigation of a compact circularly polarized integrated filtering antenna for wearable biotelemetric devices," *IEEE Transactions on Biomedical Circuits and Systems*, vol. 10, no. 2, pp. 328-338, Apr. 2016. doi: 10.1109/TBCAS.2015.2438551.

[9] A. Basir and H. Yoo, "A stable impedance-matched ultrawideband antenna system mitigating detuning effects for multiple biotelemetric applications," *IEEE Transactions on Antennas and Propagation*, vol. 67, no. 5, pp. 3416-3421, May 2019. doi: 10.1109/TAP.2019.2905891.

[10] M. Saravanan and M. J. S. Rangachar, "Circular ring-shaped polarization reconfigurable antenna for wireless communications," *Progress In Electromagnetics Research M*, vol. 74, pp. 105-113, 2018. doi:10.2528/PIERM18081608.

[11] A. Priya, S. K. Mohideen, and M. Saravanan, "Design of polarization reconfigurable patch antenna for wireless communications," *Applied Computational Electromagnetics Society (ACES) Journal*, vol. 35, no. 8, pp. 893-893, 2020.

[12] D. K. Ghodgaonkar, O. P. Gandhi, and M. F. Iskander, "Complex permittivity of human skin in vivo in the frequency band 26.5-60 GHz," *IEEE Antennas and Propagation Society International Symposium. Transmitting Waves of Progress to the Next Millennium. 2000 Digest*, vol. 2, pp. 1100-1103, 2002.

[13] K. Kumar Naik, S. Chaithanya Teja, B. V. Sailaja, and P. Amala Sri, "Design of flexible parasitic element patch antenna for biomedical application," *Progress in Electromagnetics Research M*, vol. 94, pp. 143-153, 2020.

[14] G. V. Kumar and T. Deepali, "Design and performance analysis of a CPW-fed circularly polarized implantable antenna for 2.45 GHz ISM band," *Microwave and Optical Technology Letters*, vol. 62, no. 12, pp. 3952-3959, 2020.

[15] K. Kumar Naik, G. Dattatreya, and S. Sandhya Rani, "In-vitro test of miniaturized CPW fed implantable conformal patch antenna at ISM band for biomedical applications," *IEEE Access*, vol. 7, pp. 43547-43554, 2019.

[16] A. D. Butt, J. Khan, S. Ahmad, A. Ghaffar, A. J. Abdullah Al-Gburi, and M. Hussein, "Single-fed broadband CPW-fed circularly polarized implantable antenna for sensing medical applications," *PLoS ONE*, vol. 18, no. 4, e0280042, 2023.

Saravanan Manavalan received his master of engineering degree (comm. system) from Anna Univ., Coimbatore, India in 2012. He did his Ph.D. degree in electronics and comm. engineering at the Hindustan University, India. He had 2 years of teaching experience and more than 5 years of research experience in the field of antennas. Currently he is working as assistant professor at Vel tech University. His area of research includes reconfigurable antennas, metamaterials, and SIW based antennas.

Balraj Shankarlal received his Ph.D. degree in electronics and comm. engineering at Annamalai University, Chidambaram, India. His area of research includes digital image processing.

Veeraswamy Radhakrishnan Prakash faculty in the Department of Electronics and Comm. Engineering, in Hindustan Institute of Technology and science, Chennai, India. His major research work is on video processing and real time image processing. He is an active IEEE member and has published papers in Scopus and Web of science.

Sathish Eswaramoorthy received Ph.D. degree in electronics and comm. engineering at National Institute of Technology, Tiruchirappalli. Currently he is working as assistant professor at Vellore Institute of Technology, India.

Rajmohan Madasamy received his B.E. degree in electronics and comm. engineering from Govt. College of Engineering, Tirunelveli, in 2001. He obtained his M.Tech. degree in VLSI from Dr. M.G.R. Educational and Research Institute, Chennai, in 2005. He obtained his Ph.D. in software defined radio from Hindustan Institute of Technology and Science, Chennai, in 2021. He has around 2 years of industry experience and 14 years of teaching experience. Currently he is an assistant professor in the department of Electronics and Communication Engineering at Hindustan Institute of Technology and Science, Chennai. His research interests include digital circuits and logic design, reversible logic and synthesis, and software defined radio.

Optimization of PMSM for EV based on Vibration and Noise Suppression

Mingwei Zhao[1,2], Xiangyu Wang[2], Lijun Liu[1,2*], Xiaowei Tu[1], and Qinghua Yang[1*]

[1]School of Electromechanical Engineering and Automation
Shanghai University, Shanghai, 200444, China
xznu_zmw@163.com, xznu_llj@163.com, yqh_lw@163.com

[2]School of Electrical Engineering and Automation
Jiangsu Normal University, Xuzhou, 221116, China
wxyinjsnu@163.com, tuxiaowei@shu.edu.cn
*Corresponding Author

***Abstract* –** The key to the suppression of vibration and noise for PMSM is the optimization of electromagnetic excitation force. The method of motor body optimization can effectively reduce the radial excitation force of the motor, so as to suppress the vibration and noise of the motor. Firstly, the stator structure of the motor is optimized with V-shape skew slot based on the analytical modeling of the radial electromagnetic excitation force of the motor. Then, the structural parameters of the motor that affect the electromagnetic excitation force of the motor are determined, and the average torque, torque ripple and radial electromagnetic excitation force generated by tangential electromagnetic excitation force are taken as the optimization objectives. The sensitivity analysis and classification of the structural parameters of the motor are carried out. The multi-objective genetic algorithm and response surface method are combined to optimize the structural parameters of the motor. Finally, the finite element analysis, modal analysis, multi-speed vibration and noise analysis of the optimized motor are done. The performance comparisons before and after optimization have proved that the peak of equivalent sound power level have decreased by 8.65% after the optimization of V-shaped skewed slot structure. After the optimization of structural parameters, the power level of permanent magnet synchronous motor has been reduced by 9.22%. For the vibration noise caused by resonance and the main frequency of vibration noise harmonics, the suppression effects are also better than those of V-shape skewed slots optimization, and the ERPL values are reduced by 9.22% and 10.12%, respectively, in two cases. The results show that the vibration and noise of permanent magnet synchronous motor are effectively suppressed.

***Index Terms* –** genetic optimization algorithm, multi-objective hierarchical optimization, PMSM, skewed slots optimization, vibration and noise suppression.

I. INTRODUCTION

The problem of Noise, Vibration, Harshness (NVH) of vehicles is one of the issues of great concern to major new energy vehicle manufacturers. The NVH problem involves all parts of the vehicle, but as a new energy electric vehicle, the motor is the core component of the power system and the most important incentive source of NVH. The interior permanent magnet synchronous motor (IPMSM) has the advantages of small size, light weight, high efficiency and high power density, and the electric drive system with it as the core has the characteristics of excellent comprehensive performance indicators. Therefore, vibration and noise suppression of the IPMSM is one of the hot spots in the field of electric vehicle research at present [1].

Electromagnetic stress and modal parameters are two key factors affecting electromagnetic vibration noise of motor. Electromagnetic waves include tangential and radial electromagnetic waves, and tangential force waves can cause torque pulsation, resulting in vibration noise [2]. The radial electromagnetic wave will cause periodic deformation of the motor core and cause vibration, which is the main source of vibration noise [3]. The influence of motor mode and radial electromagnetic force on noise was studied in [4–5], showing that larger vibration noise would be caused when the frequency of radial electromagnetic wave was close to the mode frequency.

The main method to suppress the electromagnetic vibration noise of PMSM is to optimize the motor body at present. It can be divided into two categories. One is to suppress the noise by optimizing the air gap shape, permanent magnet structure and structure of stator and rotor. In [6], segmented skew pole optimization was carried out for the motor, but only for a step skew pole optimization, and no further optimization was carried out. The IPMSM using single and double permanent magnet rotors was analyzed, which showed that the

Submitted On: September 18, 2023
Accepted On: February 4, 2024

https://doi.org/10.13052/2024.ACES.J.390109

electromagnetic noise performance of double permanent magnet yoke was better in [7]. In [8], a virtual tooth structure between poles was used to weaken the six frequency vibration noise of the surface mounted permanent magnet motor, and the third, fifth and seventh harmonics were weakened at the same time, but the weakening effect on other harmonics was missing. NVH could be optimized by means of stator tooth chamfering [9]. In [10], a method was proposed to cut auxiliary slots in the top of the stator teeth and to optimize the parameters of the slots. In [11], the magnetic amplitude was reduced to near the resonant frequency by optimizing the slot width. However, only the optimization of radial electromagnetic excitation force was considered, and the tangential electromagnetic torque was not analyzed in [7–11].

The other is to reduce the vibration noise of PMSM from the structural parameters. In [12], a three-dimensional finite element analysis method was proposed to analyze the influence of parameters of stator and rotor on the resonant frequencies of reducing the total sound power, so as to avoid the occurrence of resonance phenomenon. However, only single-stage optimization of structural parameters was carried out, which was inferior to hierarchical optimization in terms of optimization efficiency and optimization fitness. In [13], the electromagnetic force density of the air gap is analyzed and derived, and the minimum peak value of the electromagnetic force density distributed along the air gap circumference of the motor was taken as the optimization objective, and the optimization values of the stator skew-slot shape, magnetic steel size and air gap size were determined based on the sensitivity analysis results, but only a single objective optimization was carried out without comprehensive analysis of multiple objectives. As the complexity of motor structure increases, it is proposed that the randomness and global nature of multiple samples in optimization have a great impact on the global nature of optimization results, so a multi-objective optimization algorithm is adopted to comprehensively consider the optimization effect of multiple objectives [14]. In [15], the multi-objective optimization of the torque ripple and the peak value of radial electromagnetic force distributed along the circumference of the air gap was carried out for the structural parameters of the motor, and the parameters were graded according to the sensitivity analysis results, so as to obtain a better optimization effect. However, only the angle of the step skewed slots was optimized as a structural parameter.

A 40 kW 48-slot 8-pole IPMSM are taken as an example in this paper. Two aspects of optimization are adopted at the same time based on the analytical modeling of the radial electromagnetic force of the motor. On the one hand, the skewed slot structure optimization is carried out, and the effects of various skewed slot optimization structures are compared and analyzed, and the best skewed slots structure scheme is selected. On the other hand, multi-objective optimization of motor structure parameters affecting electromagnetic vibration noise is carried out with the objectives of minimum radial electromagnetic force peak, minimum torque ripple and maximum average torque. Based on the sensitivity analysis of motor structure parameters, the motor structure parameters are divided into three levels: high sensitivity parameters, low sensitivity parameters and irrelevant parameters. The multi-objective genetic algorithm and response surface method are combined to optimize the high and low structural parameters of the motor. The effectiveness of the proposed method is verified by comparing the radial electromagnetic force space harmonics, torque pulsation and equivalent radiated power level (ERPL) of the IPMSM before and after optimization.

II. RADIAL ELECTROMAGNETIC FORCE THEORY OF IPMSM

A. Radial electromagnetic excitation stress model of IPMSM

The radial electromagnetic force, the main source of electromagnetic vibration and noise, is mainly generated by a series of stator and rotor magnetic field harmonics [16]. The magnetic field established by synchronous motor armature reaction magnetomotive force is:

$$b_1(\theta,t)=\sum_{\upsilon}B_{\upsilon}\cos[\omega_1 t-\upsilon\theta-(\psi+90^{\circ})], \quad (1)$$

where $\psi+90^{\circ}$ is the initial phase, ω_1 is the frequency of three-phase current in the stator winding, and B_{υ} is the υ-order harmonic magnetic density amplitude of the armature reaction magnetic field, and can be expressed as:

$$B_{\upsilon}=\frac{p}{\upsilon}\left|\frac{k_{\mathrm{dp}\upsilon}}{k_{\mathrm{dp}1}}\right|X_{\mathrm{ad}}^{*}B_{\delta}I^{*}, \quad (2)$$

where B_{δ} is the air gap magnetic density for no load, considering the salient pole effect of the rotor, X_{ad}^{*} is the per-unit value of direct axis armature reaction reactance, I^{*} is per-unit value of load current, p is the number of pole pairs of the fundamental wave of the stator magnetomotive force (number of motor rotor pole pairs), and the order of harmonics $\upsilon=(6k+1)p$, $k=0,\pm1,\pm2\cdots$.

The magnetic field established by the rotor magnetomotive force of the synchronous motor, that is, the no-load airgap magnetic field is:

$$\begin{aligned}b_2(\theta,t)&=\textstyle\sum_{\mu}B_{\mu}\overline{\Lambda}_0\cos[\mu\frac{\omega_1}{p}t-\mu\theta]\\&+\textstyle\sum_{\mu}\sum_{\mathrm{k}}(-1)^{\mathrm{k}+1}\frac{1}{2}B_{\mu}\overline{\Lambda}_{\mathrm{k}}\cos[\mu\frac{\omega_1}{p}t-(\mu\pm kZ_1)\theta]\end{aligned}, \quad (3)$$

where B_{μ} is the magnetic density amplitude of the μ-order harmonic of the main pole magnetic field under load.

$$B_{\mu}=\frac{\mu_0F_{\mu}}{\delta}=\frac{p}{\upsilon}\left|\frac{\sin\frac{\mu}{p}\bullet\frac{\alpha\pi}{2}}{\sin\frac{\alpha\pi}{2}}\right|B_1, \quad (4)$$

where B_1 is the magnetic density amplitude of the fundamental wave, α is the polar arc coefficient, and Z_1 is the number of stator slots. The first term in (3) is the magnetic field generated by the rotor magnetomotive force in the uniform air gap, the second term is the additional magnetic field caused by the stator slots.

When the synchronous motor is running under load, the air gap magnetic field is the sum of the armature reaction magnetic field and the rotor magnetomotive force magnetic field, that is:

$$\begin{aligned} b(\theta,t) &= b_1(\theta,t)+b_2(\theta,t) \\ &= \sum_{v} B_v \cos\left[\omega_1 t - v\theta - (\psi+90^\circ)\right] \\ &\quad + \sum_{\mu} B_\mu \bar{\Lambda}_0 \cos\left[\mu \frac{\omega_1}{p} t - \mu\theta\right] \\ &\quad + \sum_{\mu}\sum_{\mathrm{k}} (-1)^{\mathrm{k}+1} \frac{1}{2} B_\mu \bar{\Lambda}_{\mathrm{k}} \cos\begin{bmatrix} \mu \frac{\omega_1}{p} t \\ -(\mu \pm kZ_1)\,\theta \end{bmatrix}. \end{aligned} \tag{5}$$

According to Maxwell stress tensor, the radial force under load is:

$$\begin{aligned} p_n &\approx \frac{1}{2\mu_0} b^2(\theta,t) \\ &= \frac{1}{2\mu_0} \left\{ \begin{array}{l} \sum_v B_v \cos\left[\omega_1 t - v\theta - (\psi+90^\circ)\right] \\ \\ +\sum_\mu B_\mu \bar{\Lambda}_0 \cos\left[\mu \frac{\omega_1}{p} t - \mu\theta\right] \\ \\ +\sum_{\mu\mathrm{k}} (-1)^{\mathrm{k}+1} \frac{1}{2} B_\mu \bar{\Lambda}_{\mathrm{k}} \cos\left[\mu \frac{\omega_1}{p} t - (\mu \pm kZ_1)\,\theta\right] \end{array} \right]^2. \end{aligned} \tag{6}$$

After expansion of (6), the term that has a greater impact on electromagnetic noise is retained, so (6) can be simplified as:

$$p_n \approx \frac{1}{2\mu_0} \left\{ \begin{array}{l} \sum_\mu \frac{1}{2} {B_\mu}^2 {\bar{\Lambda}_0}^2 \cos\left[2\mu \frac{\omega_1}{p} t - 2\mu\theta\right] \\ +\sum_{\mu_1}\sum_{\mu_2}\sum_{\mathrm{k}} \frac{1}{2} B_{\mu_1} B_{\mu_2} \bar{\Lambda}_0 \bar{\Lambda}_{\mathrm{k}} \cos\left\{(\mu_2 \pm \mu_1) \frac{\omega_1}{p} t - \left[(\mu_2 \pm \mu_1) \pm kZ_1\right]\theta\right\} \\ +\sum_v \sum_\mu B_v B_\mu \bar{\Lambda}_0 \cos\left[(\mu \pm p)\frac{\omega_1}{p} t - (\mu \pm v)\theta - (\pm\psi \pm 90^\circ)\right] \\ +\sum_v \sum_\mu \sum_{\mathrm{k}} (-1)^{\mathrm{k}+1} \frac{1}{2} B_v B_\mu \bar{\Lambda}_{\mathrm{k}} \cos\left\{(\mu \pm p)\frac{\omega_1}{p} t - \left[(\mu \pm kZ_1) \pm v\right]\theta - (\pm\psi \pm 90^\circ)\right\} \end{array} \right\}. \tag{7}$$

The orders of each force wave are 2μ, $(\mu_2 \pm \mu_1) \pm kZ_1$, $(\mu \pm \upsilon)$ and $(\mu \pm kZ_1) \pm \upsilon$. μ, μ_1 and μ_2 can be expressed as:

$$\left.\begin{array}{l} \mu = (2r+1)\,p \\ \mu_1 = (2r_1+1)\,p \\ \mu_2 = (2r_2+1)\,p \end{array}\right\}, \tag{8}$$

where $r,\ r_1,\ r_2\ = 0,1,2,3\cdots$.

The first item in (7) is the force waves generated by the alone action of the same order harmonics of the rotor magnetic field itself. The second term is the force waves generated by the combined modulation of different order harmonics of the rotor magnetic field itself. The third and fourth terms are the force waves generated by the interaction between the stator and rotor harmonic magnetic fields.

B. Force waves that may cause strong vibration noise of the motor

When the motor is running under load, whether a series of force waves included by radial force can cause strong vibration and noise of the motor depends on the three elements of force wave, including size, order and change frequency [17]. It can be seen from (8) that the frequency of radial force wave during load operation of synchronous motor is an integer multiple of twice the frequency of power supply, that is:

$$f = 2rf_1, \tag{9}$$

where f_1 is the power supply frequency, and $r = 1,2,3\cdots$.

Accordingly, the vibration frequency caused by radial force wave is also an integer multiple of twice the power supply frequency f_1. Relative to the rotor rotation frequency, the frequency of the radial force wave is the $2rp$ times the rotor rotation frequency, that is, the time order of the radial force wave is $2rp$ order, namely, the number of vibrations of the rotor rotating a full circle is an integer multiple of the number of poles. In addition, according to each order of radial force wave in (6), the lowest non-zero order of spatial force wave of synchronous motor is $2p$ during load operation.

The radial force waves that need to be paid attention to when the synchronous motor is loaded are as follows:

(1) Radial force waves with frequency $2f_1$ produced by the main wave magnetic field

Namely, the first force wave in (7), when $r = 1$, corresponds to the radial force wave caused by the main wave magnetic field (harmonic order p) with the pole pairs p.

(2) Lower order force wave generated by the interaction between the first order tooth-harmonic magnetic field of stator and the μ-order harmonic magnetic field of rotor

When the synchronous motor is running without load, the radial force wave generated by the interaction between the μ-order harmonic of the rotor main pole magnetic field with the pole number μ and frequency $\mu \bullet \omega_1/p$ and the first order tooth-harmonic of the rotor main wave with the pole number $p \pm Z_1$ and frequency ω_1, is the main source of electromagnetic vibration noise which corresponds to the radial force wave of the 2nd term of (7) when $\mu_2 = \mu\mu_1 = pk = 1$.

When r or $r+1$ is the integer closest to $Z_1/2p$, the number of slots per pole, the orders of two lower order dangerous force waves, i.e., $n = 2rp - Z_1$ or $n = 2(r+1)p - Z_1$, appears as a minimum.

In the case of the synchronous motor load operation, the radial force wave generated by the interaction between the stator first order teeth harmonic magnetic field of the armature winding and the μ-order harmonic magnetic field of the rotor is the 3rd term of (7) when $\upsilon = p \pm Z_1$.

When r or $r+1$ is the integer closest to $Z_1/2p$, the number of slots per pole, the 3rd term in (7) contains two low-order dangerous force waves. The minimum value of the orders of these two force waves, i.e., $n = 2rp - Z_1$ or $n = 2(r+1)p - Z_1$, is most likely to cause electromagnetic vibration noise of synchronous motor load.

(3) Radial force wave generated by the interaction between the stator and the rotor harmonic magnetic field

When the synchronous motor is running under load, the radial force wave generated by the interaction between the stator υ-order harmonic magnetic field and the rotor μ-order harmonic magnetic field is the 3rd term of (7), and the orders of dangerous force waves with lower order are:

$$\mathrm{n} = \mu - \upsilon = \begin{cases} (2\mathrm{r}-6\mathrm{k})\ \mathrm{p} & \text{Integer slot winding} \\ (2\mathrm{r}-\frac{6\mathrm{k}}{\mathrm{d}})\mathrm{p} & \text{Fractional slot winding} \end{cases}, \tag{10}$$

where d is the denominator of the number of slots of per pole per phase.

When r is closest to $3k$ or $3k/d$, the minimum value of n appears, and the generated force wave is most likely to cause electromagnetic vibration noise of the synchronous motor load.

(4) Radial force waves generated by interaction between stator tooth-harmonic magnetic field and permanent magnet rotor field

The 4th term of (7) contains the lower order dangerous force waves generated by interaction between stator tooth-harmonic magnetic field and permanent magnet rotor field and the orders of dangerous force waves are, respectively:

$$n = \begin{cases} (2r-6k)p + kZ_1 & \text{Integer slot winding} \\ (2r-\frac{6k}{d})p + kZ_1 & \text{Fractional slot winding} \end{cases}, \tag{11}$$

and

$$n = \begin{cases} (2r+6k+2)p - kZ_1 & \text{Integer slot winding} \\ (2r+\frac{6k}{d}+2)p - kZ_1 & \text{Fractional slot winding} \end{cases}. \tag{12}$$

For the integer slot winding, when r and $-kZ_1/2p + 3k$ are closest, or r and $kZ_1/2p - 3k - 1$ are closest, n appears the minimum value, and the generated force wave is most likely to cause the electromagnetic vibration noise of the synchronous motor load.

III. NUMERICAL ANALYSIS OF RADIAL ELECTROMAGNETIC FORCE

A. Initialization design of IPMSM

In order to reduce the electromagnetic noise of the motor, a 48-slot 8-pole IPMSM is selected. The working parameters of the motor are shown in Table 1, including rated power, rated speed and rated voltage. Motor structure parameters are shown in Table 2. They are stator outer diameter Dso, stator inner diameter Dsi, slot Angle Ske, slot height Hs_0, slot shoulder height Hs_1, slot width height Hs_2, slot width Bs_0, slot center width Bs_1, slot bottom width Bs_2, rotor outer diameterDro, rotor inner diameter Dri, pole arc coefficient Emb, magnetic bridge thickness $Bridge$, cross axis magnetic path width rib, cross axis magnetic path height $Hrib$, magnetic steel thickness Thi, core length $Length$, and the distance between rotating shaft and magnetic steel o_2, respectively. The motor model is established based on the parameters above, and the cross section and main structural parameters of the motor are shown in Fig. 1.

Table 1: Operating parameters of motor

Parameters	Value	Parameters	Value
Rated power /kW	40	Rated speed/ Maximum speed/ rpm	3000/6000
Rated torque/ Maximum torque/N.m	127.3/318.3	Efficiency (at rated speed)	>85%
Rated voltage/V	126	Operating temperature /cel	120
Material of iron core	DW310_35	Material of magnetic steel	NdFe35

Table 2: Structure parameter of motor

Parameters	Value	Parameters	Value
Dso/mm	220	Dro/mm	142
Dsi/mm	144	Dri/mm	48
Ske/deg	7.5	Emb	0.73
$\mathrm{Hs_0}$/mm	0.5	Bridge/mm	1.5
$\mathrm{Hs_1}$/mm	0.5	Rib/mm	10
$\mathrm{Hs_2}$/mm	23	Thi/mm	5
$\mathrm{Bs_0}$/mm	2.5	Length/mm	149
$\mathrm{Bs_1}$/mm	5.2	Hrib/mm	4.6466
$\mathrm{Bs_2}$/mm	7.5	$\mathrm{o_2}$/mm	37.6638

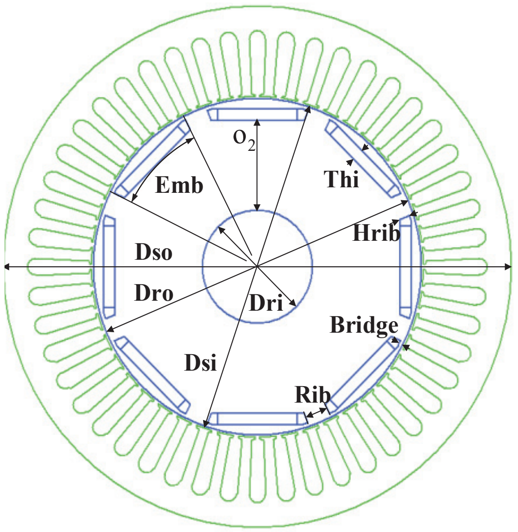

Fig. 1. Cross-section of the motor model.

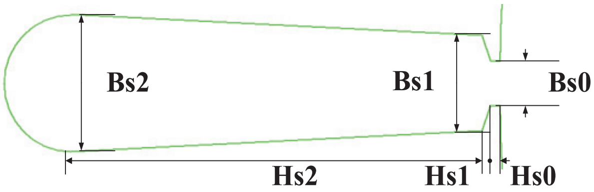

Fig. 2. Stator groove structure of motor.

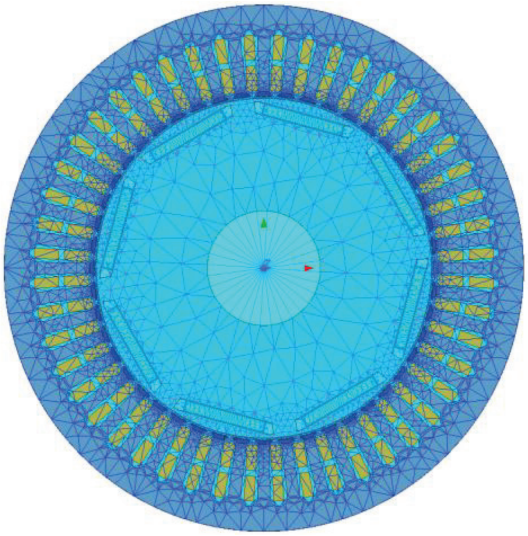

Fig. 3. Maxwell 2D finite element model of motor with mesh division.

The stator slot adopts a pear-shaped slot, and its structure and main parameters are shown in Fig. 2.

The 2D finite element model of the motor is shown in Fig. 3. The rotation region and boundary of the model are set, respectively. In order to improve the running accuracy of the model, the model is discretized by mesh generation and the finite element solution is carried out. The current source excitation of the motor finite element model is $275.0076\sin(2\pi\times 200t)$.

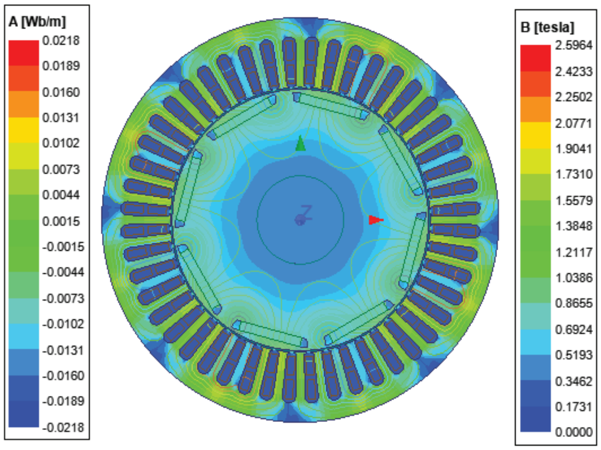

Fig. 4. Distribution of magnetic induction intensity and field line of motor.

The distribution of magnetic induction intensity and magnetic field line of the motor are shown in Fig. 4, which shows the density of magnetic field line A at each position of the stator and rotor and the magnetic induction intensity B at different positions at a certain time. It can be seen more intuitively that the magnetic field line always passes along the path with small magnetoresistance.

B. Calculation and analysis of radial excitation force

The Cartesian coordinate system is used to simulate and solve the motor, and then the field calculator is adopted to post-process the results. The radial magnetic induction intensity B_r is converted according to the following formula:

$$B_r = B_x \cos\varphi + B_y \sin\varphi, \qquad (13)$$

where φ is the angle between the x axis and the column coordinate, B_x and B_y are the components of the magnetic induction intensity B in the direction of x axis and y axis, respectively.

The variation of radial electromagnetic waves along the air gap circumference of the motor model with time and space is shown in Fig. 5. Due to the influence of stator teeth and slots, the radial electromagnetic force changes periodically with the space position, and it is also a periodic function of time. Therefore, the harmonic response analysis of the radial electromagnetic force can further analyze its influence on electromagnetic vibration.

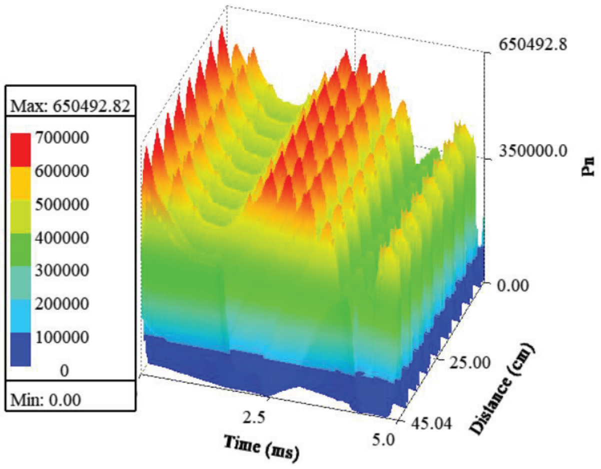

Fig. 5. 3D diagram of radial electromagnetic stress with time and space.

IV. OPTIMIZATION OF SKEWED SLOTS STRUCTURE OF IPMSM

A. Skewed slots optimization method

(1) Step skewed slots

When the stator slots are skewed, the tooth-harmonics of the stator and rotor magnetic fields are weakened, and the radial force wave has phase displacement along the axial direction. Therefore, the average radial force along the axial direction is reduced, reducing the electromagnetic vibration and noise of the motor effectively [18]. The skewed slots structure of stator is shown in Fig. 6. The relevant parameters are identified in the figure, where Z is the identification of the stator axial direction, $b_{\mathrm{sk}} = \theta_{\mathrm{sk}} \cdot R$ is the skewed slots distance, i.e., arc length, R is the outer radius of the stator, θ_{sk} is the angle of the skewed slots, and l is the length of stator core.

When the stator slots are skewed, and the rotor slots are straight, the radial exciting force p_{n} generated by the interaction between the stator υ-order harmonic magnetic field and the μ-order harmonic magnetic field generated by the fundamental wave current of the rotor is integrated along the direction of core length l and then the average radial force, that is, the axial zero-order vibration radial force p_{n0}, can be expressed as:

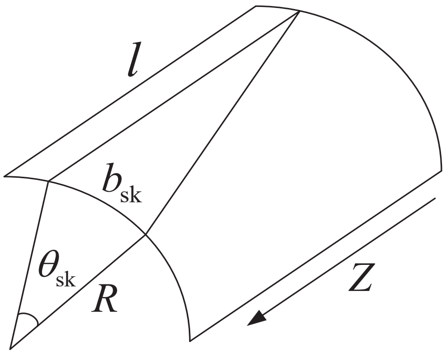

Fig. 6. Schematic diagram of skewed slot structure of stator.

$$\begin{aligned} p_{\mathrm{n0}} &= \frac{1}{l}\int_{-1/2}^{1/2} p_{\mathrm{n}} dZ \\ &= \frac{1}{l}\int_{-1/2}^{1/2} P_{\mathrm{nm}} \cos\left(\omega_{\mathrm{n}} t - n\theta - \varphi_{\mathrm{n}} - v\frac{b_{\mathrm{sk}}}{R}\frac{Z}{l}\right) dZ, \quad (14) \\ &= P_{\mathrm{nm}} \frac{\sin\left(v b_{\mathrm{sk}}/2R\right)}{v b_{\mathrm{sk}}/2R} \cos\left(\omega_{\mathrm{n}} t - n\theta - \varphi_{\mathrm{n}}\right) \end{aligned}$$

where P_{nm} refers to the amplitude of 0-order radial force when no skewed slots.

The skewed slots coefficient is defined as:

$$K_{\mathrm{sk}} = \frac{\sin(\upsilon b_{\mathrm{sk}}/2R)}{\upsilon b_{\mathrm{sk}}/2R} = \frac{\sin(\upsilon \pi b_{\mathrm{sk}}/Z_1 t_1)}{\upsilon \pi b_{\mathrm{sk}}/Z_1 t_1}, \quad (15)$$

where t_1 is the slot distance of stator.

The theoretical analysis shows that the average amplitude of the 0-order radial force wave along the axial direction is:

$$P_{\mathrm{n0}} = P_{\mathrm{nm}} \cdot K_{\mathrm{sk}}. \quad (16)$$

In addition, due to the role of the skewed slots, the skewed slots coefficient of the tooth-harmonics, that is, the most important magnetic field harmonics in the motor, is very small or even 0, which greatly reduces the vibration noise caused by tooth-harmonics.

(2) V-shape skewed slot

Although the unidirectional skewed slots can reduce the vibration noise caused by tooth-harmonics, it will cause transverse current and torsional moment, thus increasing the additional loss, generating additional axial force and torsional vibration [18]. In order to avoid the above side effects, V-shape skewed slots measures can also be used. Its structure is characterized by dividing the stator into two halves along the axial length, each half is equivalent to a skewed slots stator, and two parts are twisted in the opposite directions, forming a ”V” shape, as shown in Fig. 7. The relative tooth-harmonics of the two parts of the stator are just in reverse phase, and the harmonic torque generated by the first-order and odd-order tooth-harmonics in the two stator segments cancels each other, which is more conducive to reducing the vibration and noise of the motor.

B. Motor skewed slots optimization design

The skewed slots are set based on the initial design of motor model. The structure of the segment skewed slots are adopted, the motor stator is divided into five sections, and two skewed slots schemes of step and

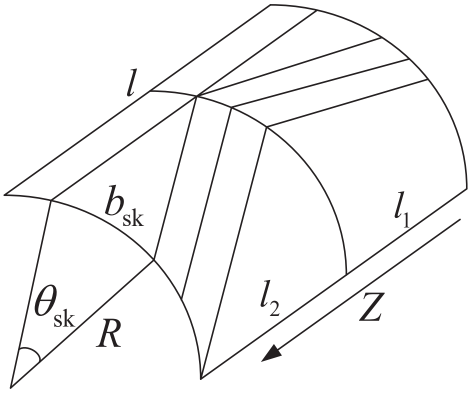

Fig. 7. Diagram of V-shape skewed slots structure.

V-shape are used, respectively. The parameter settings of each scheme are shown in Table 3.

Table 3: Parameters settings of skewed slots

Mode of Skewed Slots	Step Skewed Slots	V-shape Skewed Slots
Number of segments	5	5
Best equivalent skewed slots angle	7.5	7.5
Angle set actually	6	5
Twist angle of segment 1	- 3	2
Twist angle of segment 2	1.5	0.5
Twist angle of segment 3	0	- 3
Twist angle of segment 4	1.5	0.5
Twist angle of segment 5	3	2

C. Evaluation index of motor skewed slots optimization scheme

The peak value P_{nm} of radial electromagnetic stress p_{n} distributed along the circumference of air gap under different skewed slots schemes is taken as the evaluation index. The smaller P_{nm} is, the smaller vibration noise caused by the radial force is, and the better the optimization effect.

The expression of radial electromagnetic stress distribution P_{n} along the arc of the center of the air gap is:

$$P_{\mathrm{n}} = \int_{2\pi \mathrm{R}_{\mathrm{airgap}}} p_{\mathrm{n}} dr, \tag{17}$$

where R_{airgap} is the arc radius of the center of the air gap, which can be expressed as:

$$R_{\mathrm{airgap}} = \frac{Dis - dr}{2}, \tag{18}$$

where Dis is the inner diameter of the stator and dr is the length of the air gap.

So the peak value of P_{n} can be denoted by:

$$P_{\mathrm{nm}} = \max\{P_{\mathrm{n}}\}. \tag{19}$$

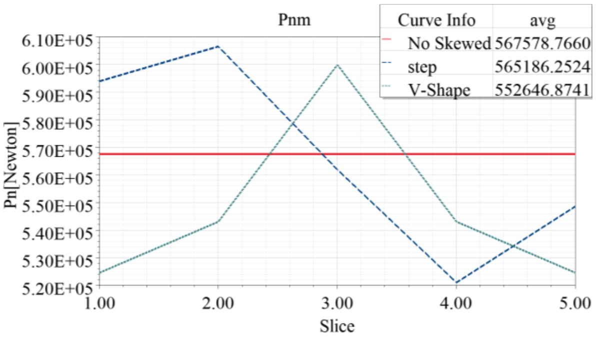

Fig. 8. Distribution diagram of radial force peak P_{nm} under different schemes.

D. Optimization effect comparison of different skewed slots schemes

Figure 8 shows the P_{nm} distribution of stator in different segments of the motor under different skewed slots schemes. When the stator has no skewed slots, P_{nm} is 567578.7660N, and the average P_{nm} of the five-segment stator with step slots is 565186.2524N, which decreases 2392.5136N compared with that without skewed slots. The average P_{nm} of the five-segment stator with a V-shaped skewed slots is 552646.8741N, which decreases 14931.8919N compared with that without skewed slots. Therefore, the improvement degree of electromagnetic noise of IPMSM with stator V-shaped skewed slots structure is higher than that of the step skewed slots.

V. MULTI-OBJECTIVE HIERARCHICAL OPTIMIZATION OF IPMSM STRUCTURE PARAMETERS

The optimization principle of this paper is as follows: on the premise of not changing the external structure of the motor and not affecting other performance of the motor, the structural parameters of the motor are optimized based on V-shaped skewed slots optimization to reduce the radial electromagnetic force and electromagnetic torque ripple of the motor, so as to suppress the electromagnetic noise.

A. Determination of optimization objectives

The basis of optimization objectives selection is:

(i) The peak value of radial electromagnetic force and tangential electromagnetic torque ripple are related to the magnitude of vibration and noise directly, and the suppression of these two targets can produce better results;

(ii) Since the direct suppression process of vibration noise is coupled to multiple physical fields, there is a high demand for computer processors and hard disks, so the indirect suppression process of independent magnetic field calculation with higher efficiency under the same computing power is adopted.

Therefore, the indirect suppression of electromagnetic noise method has been adopted in this paper, and tangential electromagnetic torque has been taken into account to suppress electromagnetic noise. The optimization objective has been determined as follows.

(i) The peak value P_{nm} of radial electromagnetic stress distribution along the circumference of the air gap is the smallest, that is:

$$obj_1 = min(P_{\mathrm{nm}}). \tag{20}$$

(ii) The torque ripple T_{ripple} is minimal, that is:

$$obj_2 = min(T_{\mathrm{ripple}}). \tag{21}$$

T_{ripple} is indicated as:

$$T_{\mathrm{ripple}} = \frac{T_{\mathrm{max}} - T_{\mathrm{min}}}{T_{\mathrm{avg}}} \times 100\%, \tag{22}$$

where T_{max}, T_{min} and T_{avg} are the maximum, the minimum and the average of the output torque, respectively.

(iii) The average of tangential electromagnetic torque is maximal, that is:

$$obj_3 = \max(T_{\mathrm{avg}}). \tag{23}$$

T_{avg} is denoted by:

$$T_{\mathrm{avg}} = \frac{1}{\tau}\int_0^{\tau} T(t)dt, \tag{24}$$

where τ is the time of one cycle of the output torque waveform of the motor. $T(t)$ is the output electromagnetic torque of the motor.

B. Determination of optimization variables

The magnitude of the radial excitation force harmonics (especially tooth-harmonics) is closely related to the size and shape of the pole arc, the length of the air gap and the size of the magnetic permeability wave caused by the slot of the stator and rotor. Therefore, these effective methods, i.e., optimizing the size and shape of the pole arc of IPMSM to make the radial excitation force density waveform close to sine as much as possible and optimizing the size of the stator and rotor slots (especially the notch), so as to reduce the electromagnetic vibration noise caused by the tooth and slot, can be used to reduce the electromagnetic noise of the motor. Table 4 shows the selected optimization variables and their corresponding value ranges.

C. Sensitivity analysis and parameter classification

OptiSLang software is used to analyze the sensitivity of structural parameters, and screen and grade structural parameters based on the prediction coefficient. IPMSM is analyzed and optimized under the V-shaped skewed slots scheme, and Advanced Latin Hypercube Sampling (ALHS) based on Monte Carlo sampling is adopted for sampling. A total of 100 samples were collected for the sample space composed of 10 structural parameters and their variation ranges. This method can not only ensure the accuracy of sensitivity analysis but also reduce the amount of calculation, and is suitable for sensitivity analysis when the number of parameters is less than 50. Furthermore, the influence of the irrelevant relationship between parameters on the subsequent sensitivity analysis results is minimized by introducing a random evolutionary strategy, so that relatively accurate results can still be obtained in the case of small samples [15].

Table 4: Initial value and variation range of optimization parameters

Optimization Parameters	**Initial Value**	**Value Range**
$\mathrm{Hs}_0/\mathrm{mm}$	0.5	$0.35 \sim 0.7$
$\mathrm{Hs}_1/\mathrm{mm}$	0.5	$0.35 \sim 0.7$
$\mathrm{Hs}_2/\mathrm{mm}$	23	$20 \sim 25$
$\mathrm{Bs}_0/\mathrm{mm}$	2.5	$1.9 \sim 4.1$
$\mathrm{Bs}_1/\mathrm{mm}$	5.2	$4 \sim 6$
$\mathrm{Bs}_2/\mathrm{mm}$	7.5	6-8.6
dr/mm	1	$0.7 \sim 1.3$
Thi/mm	5	$2 \sim 8$
o_2/mm	37.6638	$37.0136 \sim 38.1787$
$\mathrm{Hrib}/\mathrm{mm}$	4.6466	$4.0892 \sim 5.3504$

In order to calculate more efficiently, the Coefficient of Prognosis (CoP), based on polynomial fitting, is used to evaluate the sensitivity of the target. Based on the collected samples and the corresponding solution results, the polynomial regression equation fitting the objective function $y(X_{\mathrm{i}})$ to the analysis parameter X_{i} is:

$$y(X_{\mathrm{i}}) = p^{\mathrm{T}}(X_{\mathrm{i}})\beta + \varepsilon_{\mathrm{i}}, \tag{25}$$

where β is the determinant of the polynomial coefficient, ε_{i} is the fitting error, and $p^{\mathrm{T}}(X_{\mathrm{i}})$ is the polynomial about the structural parameters, which can be denoted by:

$$p^{\mathrm{T}}(X_{\mathrm{i}}) = [1\ X_1\ X_2\ X_3 \cdots X_1^2\ X_2^2\ X_3^2\ \cdots\ X_1X_2\ X_1X_3\ \cdots]^{\mathrm{T}}. \tag{26}$$

We define the total variation of the output as:

$$SS_{\mathrm{T}} = \sum_{\mathrm{i}=1}^{\mathrm{M}} (y_{\mathrm{i}} - \mu_{\mathrm{y}})^2, \tag{27}$$

where y_{i} is the actual value of the sample target, μ_{y} is the average of the sample target, and M is the number of samples.

We define the sum of squares of all prediction errors as:

$$SS_{\mathrm{E}} = \sum_{\mathrm{i}=1}^{\mathrm{M}} (y_{\mathrm{i}} - \hat{y}_{\mathrm{i}})^2, \tag{28}$$

where $\hat{y}_{\mathrm{i}}$ is the corresponding calculated value for the $y(X_{\mathrm{i}})$.

The prediction quality evaluation index CoP is:

$$CoP = 1 - \frac{SS_{\mathrm{E}}}{SS_{\mathrm{T}}}. \tag{29}$$

The larger the value of CoP, the greater the influence of structural parameters X_{i} on optimization objective y_{i}, and the higher the sensitivity.

Table 5: Sensitivity analysis results of structural parameters

Objectives Sensitivity Parameters		$min(P_{nm})$	$\max(T_{avg})$	$min(T_{ripple})$
CoP (%) of a single structural parameter	Hs$_0$/mm	/	/	/
	Hs$_1$/mm	/	/	/
	Hs$_2$/mm	/	2.6	27.7
	Bs$_0$/mm	30.0	/	17.4
	Bs$_1$/mm	30.6	2.2	10.2
	Bs$_2$/mm	8.9	3.8	5.7
	dr/mm	17.0	/	9.9
	Thi/mm	1.0	83.9	32.8
	o$_2$/mm	/	7.9	17.4
	hrib/mm	/	/	/
CoP (%) of the overall structural parameters		85	98.7	77.6

The optimization design of IPMSM can be simplified to the multi-stage and multi-physical field optimization through sensitivity analysis [19]. The sensitivity of each parameter to each optimization target and the overall sensitivity results are shown in Table 5 after the sensitivity calculation of structural parameters. The following conclusions can be drawn from Table 5:

(i) The values of CoP of overall structural parameters of the three optimization objectives are all above 75%, indicating that the determined structural parameters have high sensitivity to the three optimization objectives;

(ii) High sensitivity parameters: Bs$_0$, Bs$_1$, Hs$_2$ and Thi have a high influence on one or more of the three optimization objectives. The values of CoP of them are bigger than 20%, so they are set as high sensitivity parameters.

(iii) Low sensitivity parameters: o$_2$ and dr only affect two objectives and the values of CoP are below 20%, and the sensitivity of Bs_2 to the three optimization objectives is all below 20%, so these three structural parameters are set as low sensitivity parameters.

(iv) Irrelevant parameters: Hs$_0$, Hs$_1$and Hrib don't have corresponding CoP value, so they do not participate in the optimization in the next stage. The number of structural parameters to be optimized is reduced to 7.

D. Process of hierarchical optimization

The appropriate optimization method is adopted for each level of parameters to reduce the calculation amount and to improve the accuracy of optimization for each parameter based on the results of sensitivity classification [20]. The process of hierarchical optimization of structural parameters is shown in Fig. 9.

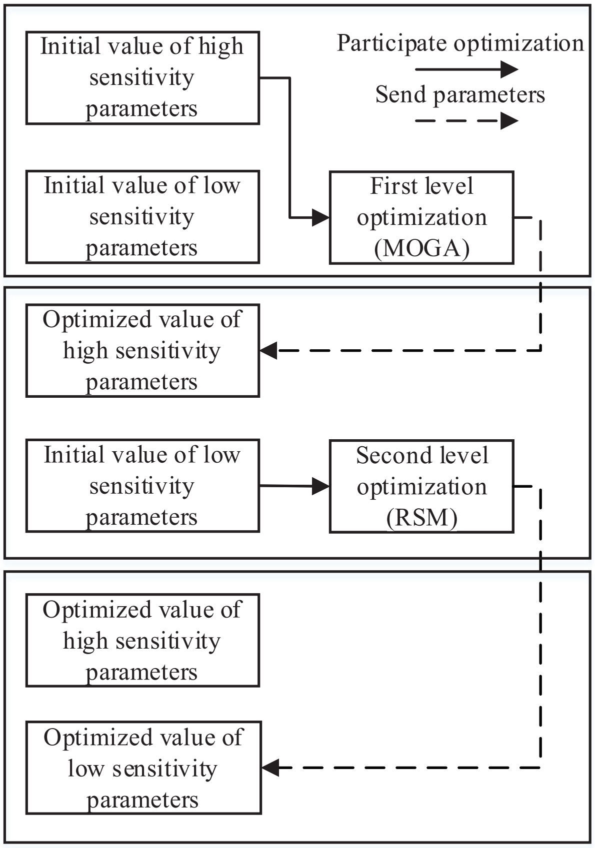

Fig. 9. Optimization flow of structure parameter hierarchical optimization.

ALHS is used to sample in the optimization space and determine the initial samples of all levels of optimization, and an adaptive strategy is introduced to determine the samples of each iteration, so as to improve the randomness and global character of the initial samples and iterations and reduce their global influence on the optimization results [15].

After a round of hierarchical optimization being completed, the global nature of the optimization results under a given optimization environment is judged, and the optimized structural parameters are imported into the optimization process as initial values for the second round of optimization. If the difference between the value of the multi-objective optimization function $W_{\max}(x_i)$ after the second round optimization and the result of the first round is less than 2%, the first round result is judged to meet the global requirements, and the first round result is output as the final optimization result of the structural parameters. Otherwise, the next round of optimization is carried out based on the results of the sec-

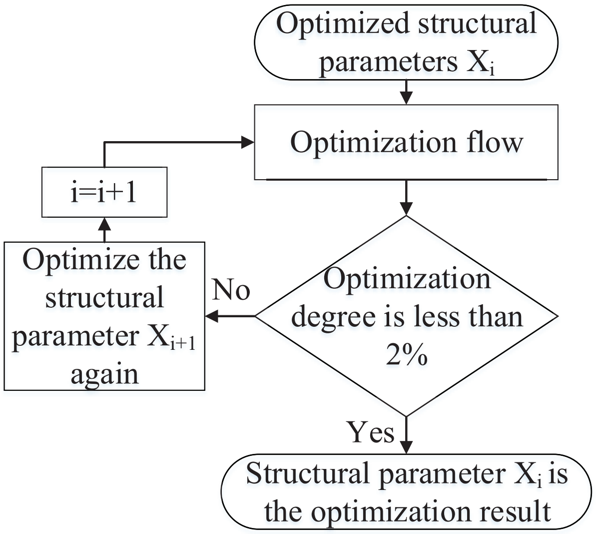

Fig. 10. Global judgment process of optimization.

ond round of hierarchical optimization until the global demand is met. The overall judgment process of hierarchical optimization results is shown in Fig. 10.

The optimal solution of Pareto solution set obtained by all levels of optimization in the optimization process can be selected by normalized weighting function, and the weighting function can be expressed as:

$$W_{\max}(x_i) = \lambda_1 \frac{T_{\mathrm{avg}}(x_\mathrm{i})}{T^{\mathrm{o}}_{\mathrm{avg}}(x_\mathrm{i})} + \lambda_2 \frac{P^{\mathrm{o}}_{\mathrm{nm}}(x_\mathrm{i})}{P_{\mathrm{nm}}(x_\mathrm{i})} + \lambda_3 \frac{T^{\mathrm{o}}_{\mathrm{ripple}}(x_\mathrm{i})}{T_{\mathrm{ripple}}(x_\mathrm{i})}, \quad \lambda_1+\lambda_2+\lambda_3=1 \tag{30}$$

where $T^{\mathrm{o}}_{\mathrm{avg}}(x_\mathrm{i})$, $P^{\mathrm{o}}_{\mathrm{nm}}(x_\mathrm{i})$ and $T^{\mathrm{o}}_{\mathrm{ripple}}(x_\mathrm{i})$ are the maximum value of the optimized tangential electromagnetic torque mean value, the optimized radial electromagnetic force peak value and the minimum value of torque ripple, respectively. x_i is the ith solution in the Pareto solution set. $T_{\mathrm{avg}}(x_\mathrm{i})$, $P_{\mathrm{nm}}(x_\mathrm{i})$ and $T_{\mathrm{ripple}}(x_\mathrm{i})$ are result of each optimization scheme. λ_1, λ_2 and λ_3 are the weight coefficients of three optimization objectives [21]. Because the main purpose of this optimization is to suppress electromagnetic noise, the radial electromagnetic force density and torque ripple weight coefficient are higher, and the values of λ_1, $\lambda_2$andλ_3 are set to 0.2, 0.4 and 0.4, respectively.

E. First round optimization of highly sensitive parameters

The highly sensitive parameter optimization includes four structural parameters and three optimization objectives, which belongs to multi-parameter and multi-objective optimization, and it is difficult to construct a direct functional relationship between structural parameters and optimization objectives. The four structural parameters have a great influence on the optimization objectives, which requires deep optimization and a large amount of calculation. The three optimization objectives of P_{nm}, T_{ripple} and T_{avg} are contradictory and need to be considered in a compromise. Multi-objective genetic algorithm (MOGA) is used for global optimization. For multi-objective optimization and tradeoff among optimization objectives, the optimal solution set is given by using Pareto frontier.

The sample size is set to 200, the initial population is 20, the crossover probability is 50%, and the mutation probability is 14%. The generated Pareto frontier is shown in Fig. 11. The first round of optimization results obtained after selecting Pareto solution sets of high sensitivity parameters by using the normalized weighting function is shown in Table 6.

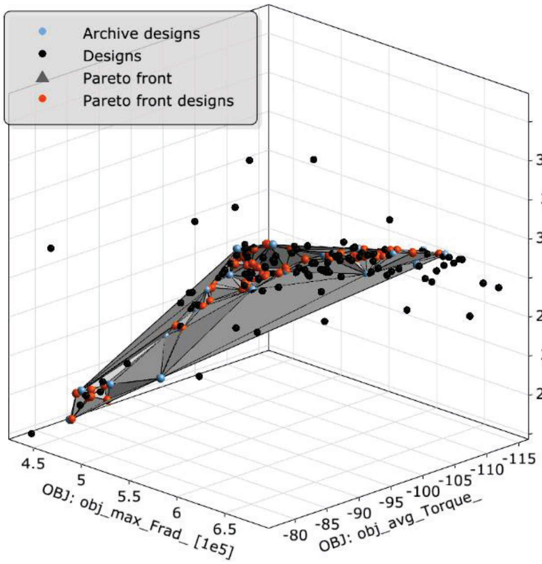

Fig. 11. Pareto front surface of multi-objective optimization.

Table 6: Results of high sensitivity optimization

Parameters/ Objectives	Pre-optimization Value	Post-optimization Value
Bs_0/mm	2.5	2.012727
Bs_1/mm	5.2	5.851049
Hs_2/mm	23	21.34658
Thi/mm	5	5.49087
P_{nm}	552646.9	433154.7
T_{ripple}	2.8476	2.424988
T_{avg}	103.83	104.3193

It can be seen from Table 6 that each optimization index of high sensitivity parameters has improved to some extent after optimization by *MOGA*. The peak P_{nm} of radial electromagnetic force density has decreased by 27.59%, the mean T_{avg} of tangential electromagnetic torque has increased by 0.47%, and the torque ripple T_{ripple} has decreased by 17.43%. The values of the four highly sensitive parameters are modified to the optimized values after the optimization is completed, which are used as fixed values to participate in the subsequent optimization.

F. First round of optimization of low sensitivity parameters

The low sensitivity parameter optimization includes three structural parameters and three optimization objectives, which belongs to multi-parameter multi-objective optimization. The influence of the three parameters on the optimization objectives is smaller than that of the highly sensitive parameters, so it is unnecessary to collect many samples. Therefore, the response surface method is used to optimize the low sensitivity parameters. The low sensitivity optimization results can also be evaluated based on the multi-objective normalized optimization function $W_{\max}(x_i)$ in the optimization process. Table 7 shows the changes of parameters and target values after optimization of low sensitivity parameters.

It can be seen that after the low sensitivity parameters optimization, the peak P_{nm} of radial electromagnetic density has been reduced by 13.45%, the torque ripple T_{ripple} has been reduced by 7.37%, but the mean T_{avg} of tangential electromagnetic torque has been reduced by 8.1%. The comprehensive optimization index has been improved to some extent.

Table 7: Results of low sensitivity optimization

Parameters/ Objectives	First Level Optimization Value	Second Level Optimization Value
o_2/mm	37.6638	37.016
Bs_2/mm	7.5	8.4408
dr/mm	1	1.2984
P_{nm}	433154.7	374870
T_{ripple}	2.424988	2.6218
T_{avg}	104.3193	96.634

G. Global judgement of hierarchical optimization results

The optimized results of Tables 6 and 7 are imported into the hierarchical optimization process again as the results of the first round of optimization, and the second round of hierarchical optimization is carried out. The comparison of the two rounds of optimization results is shown in Table 8. The multi-objective optimization function $W_{\max}(x_i)$ is reduced by 0.29%, and the improvement degree is less than 2% after the second round of optimization. According to the global judgment process, the final output is the optimization result of the first round.

Table 8: Comparison of two rounds of hierarchical optimization results

Parameters/ Objectives	First Round Results	Second Round Results
Bs_0/mm	2.012727	2.169249
Bs_1/mm	5.851049	5.838322
Bs_2/mm	8.4408	8.5995
Hs_2/mm	21.34658	21.94714
Thi/mm	5.49087	5.596182
dr/mm	1.2984	1.2988
o_2/mm	37.016	37.67575
P_{nm}	374870	373730
T_{ripple}	2.6218	2.6313
T_{avg}	96.634	96.411

This shows that the results obtained by hierarchical optimization of the seven structural parameters have better global performance in the optimization space composed of the given initial optimization value and optimization range [15].

VI. VERIFICATION OF OPTIMIZATION EFFECT OF IPMSM

A. Finite element verification of hierarchical optimization results

Figure 12 shows the comparison of the distribution of electromagnetic excited force before and after the optimization of structural parameters. It can be seen that the peak value of radial force P_{nm} is 373534.2742N after the optimization of structural parameters, which decreases by 34.19% compared with that without skewed slots and 28.79% compared with the V-shaped skewed slots.

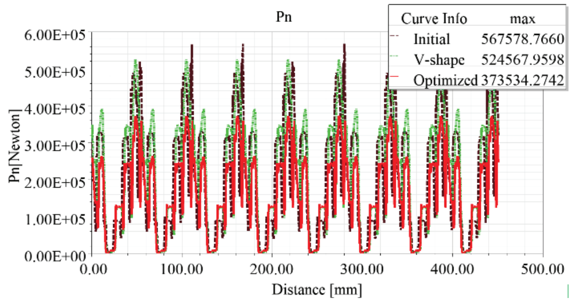

Fig. 12. Comparison of radial force distribution before and after optimization of structural parameters.

Many radial electromagnetic force harmonics of different orders and frequencies will be generated in the air gap of PMSM when the electromagnetic fields of the stator and rotor interact, which are the main factors leading to radial vibration of the stator core of the motor. The harmonic optimization of the radial electromagnetic force

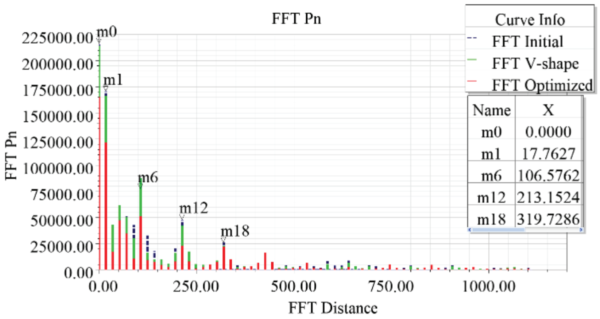

Fig. 13. Harmonic optimization of radial electromagnetic waves.

wave is shown in Fig. 13. $m0 \sim m18$ list the spatial distance X and amplitude Y of force waves with different orders, and the relationship between force wave order n and spatial distance X is expressed as:

$$n = \frac{2\pi R_a X}{1000}, \tag{31}$$

where R_a is the radius of the air gap circumference.

The major orders of space harmonics of radial electromagnetic waves converted by (31) are shown in Table 9. The 8th order force wave is the radial force wave with frequency $2f_1$, which is mainly generated by the magnetic field of the main wave. The 0th and 8th order force waves are also lower order force waves modulated by the first order tooth-harmonic magnetic field of the stator and the harmonic magnetic field of the rotor. The 48th, 96th and 144th order force waves are the radial force waves generated by the interaction between the stator and the rotor harmonic magnetic field, and also the radial force waves generated by the interaction between the stator tooth-harmonic magnetic field and the permanent magnet rotor magnetic field.

Table 9: Optimization of the main spatial harmonic order of radial electromagnetic waves

Point	X/mm	r	**Initial Force /N**	**V-shape Force /N**	**Optimized Force /N**
m0	0.0000	0	216912.80	214192.01	165369.22
m1	17.7627	8	170873.21	166385.01	121907.56
m6	106.5762	48	77168.65	87619.53	51467.84
m12	213.1524	96	47800.92	42057.04	23221.42
m18	319.7286	144	25985.30	22815.83	21879.61

From Fig. 13 and Table 9, it can be seen that the fundamental, the 8th, 48th, and 96th order harmonics after the optimization of structural parameters are further reduced on the basis of the V-shaped skewed slots optimization, indicating that the electromagnetic vibration noise is effectively suppressed.

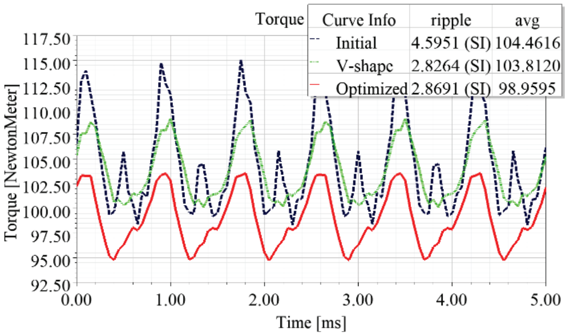

Fig. 14. Ripple torque before and after optimization.

The comparison between torque ripple T_{ripple} and average torque T_{avg} before and after optimization of structural parameters is shown in Fig. 14. After the compromise of multiple optimization objectives, the torque ripple after optimization is 2.8691, which is 41.44% lower than that before optimization and basically equivalent to the effect of V-shape skewed slots optimization. The average torque after optimization is significantly lower than the initial value and the V-shaped skewed slots, but the average torque in the V-shaped skewed slots is basically the same as the initial value.

B. Modal optimization analysis of IPMSM stator structure

Motor vibration not only depends on the stress of exciting vibration of motor, but also relates to the natural vibration characteristics of the motor structure, including the natural vibration mode and natural frequency of the motor structure itself. The motor stator is a circular structure, and the radial electromagnetic force directly acts on the teeth and magnetic poles of the stator. The natural vibration modes of this stator ring model are mainly the radial modes of different orders, and the order r of the vibration mode of corresponding shape of the stator is usually defined by the order n of the force wave, that is, $r = n$ [22].

The resonance effect will occur, making the motor produce larger vibration and noise, when the frequency and order of the radial electromagnetic excited force wave are close to or consistent with the corresponding natural frequency and natural vibration mode order of the motor stator.

The specific relationship between the natural frequency of each vibration mode and the motor structure can be summarized as follows:

(i) The natural frequency is closely related to the average radius R_c of the stator yoke. The natural frequency is approximately inversely proportional to R_c for breathing mode $(r = 0)$. The natural frequency is approximately inversely proportional to the square of R_c and, the larger the radius, the lower the natural frequency for the other mode ($r \neq 0$).

(ii) The natural frequency is also closely related to the order r of the mode and is approximately proportional to the square of r.

(iii) The natural frequency is also related to the yoke thickness h, mainly the ratio of the thickness of the stator yoke to its average radius, i.e., h/R_c. A large h/R_c indicates that the stiffness of stator is large, and the natural frequency will be high. Small h/R_c indicates that the stiffness of stator is small, and the natural frequency will be low.

The inherent modes of a certain order can be understood and the actual modes of each order can be predicted through modal analysis of IPMSM [7]. The natural vibration modes of the stator model corresponding to the 1st to 4th order are shown in Fig. 15.

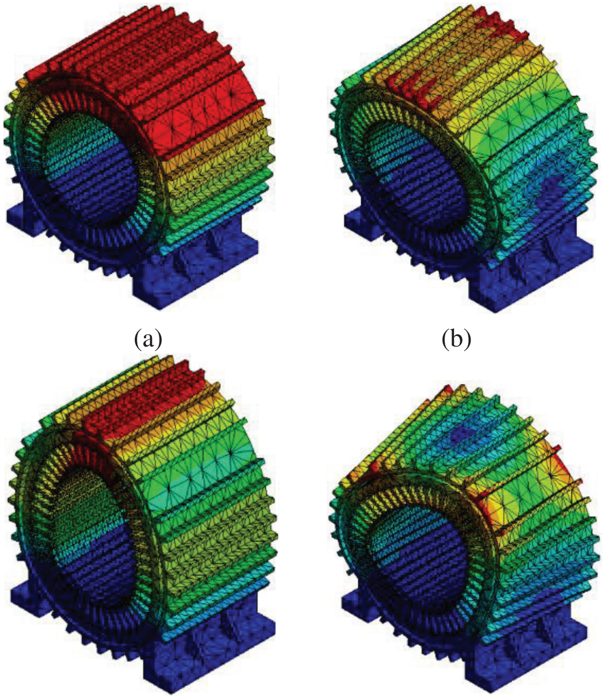
(a) (b)

(c) (d)

Fig. 15. Stator natural vibration modes of each order: (a) $r = 1$, (b) $r = 2$, (c) $r = 3$, and (d) $r = 4$.

The comparison of natural frequencies of each order for stator skew slots optimization and structural parameter optimization is shown in Table 10. After the stator skew slots is used, the natural frequency is improved, and the natural frequency is slightly reduced after the structural parameter optimization, which proves that the optimization of motor body structure parameters can improve the natural frequency of motor stator structure and effectively reduce the resonance risk.

Table 10: Comparison of motor natural frequency before and after optimization

Orders Frequency/Hz Optimization	$r = 1$	$r = 2$	$r = 3$	$r = 4$
Initial	397.78	676.12	978.05	1503.9
V-shaped	404.29	706.49	992.45	1557.5
Optimized	403.64	705.9	992.09	1558.4

C. Optimization verification of vibration and noise suppression of IPMSM

The stator will produce a continuous steady state harmonic response when the periodic electromagnetic excitation force is applied to the stator of the motor, and the dynamic balance equation of the stator is expressed as:

$$m\ddot{x}(t) + r_m\dot{x}(t) + kx(t) = F(t), \tag{32}$$

where m, r_m, and k are the mass, mechanical damping coefficient, and stiffness of the stator vibration system, respectively, $F(t)$ is simple harmonic exciting force, and $F(t) = P_{nm}\cos\omega t$. $\ddot{x}(t)$ is the vibration acceleration of the stator vibration system, $\dot{x}(t)$ is vibration speed and $x(t)$ is vibration displacement.

Let the solution of (32) be:

$$x(t) = X_m\cos(\omega t - \varphi). \tag{33}$$

Substitute (33) into (32) to get:

$$X_m = \frac{P_{nm}}{\omega\sqrt{{r_m}^2 + (\omega m - \frac{k}{\omega})^2}}. \tag{34}$$

According to equation (34), when $\omega m - \frac{1}{\omega\lambda} = 0$, the system will resonate, and the square of the resonant frequency is:

$${\omega_0}^2 = \frac{1}{m\lambda}. \tag{35}$$

When the excitation frequency is far away from the resonance frequency, the damping coefficient r_m is much less than $(\omega m - k/\omega)$, which is ignored, and (35) substituted into (34) obtains:

$$X_m = \frac{P_{nm}}{\omega(\frac{k}{\omega} - \omega m)} = \frac{P_{nm}}{k(1 - \frac{\omega^2}{{\omega_0}^2})}. \tag{36}$$

For the r-order vibration mode ($r \geq 2$), the equivalent distributed stiffness of the stator core is approximately proportional to $(r^2 - 1)^2$, that is:

$$k \propto (r^2 - 1)^2. \tag{37}$$

Substitute (37) into (36) and take into account $\omega = 2\pi f$ to get:

$$X_m \propto \frac{P_{nm}}{1 - \frac{f^2}{{f_0}^2}}\frac{1}{(r^2 - 1)^2}. \tag{38}$$

According to (38), the response of motor vibration system under simple harmonic excitation is still harmonic. The vibration amplitude X_m is directly proportional to the excitation force P_{nm}. The response frequency is equal to the excitation force frequency. The system will resonate and produce a large amplitude when the exciting frequency f of the exciting force is close to the natural frequency f_0 of the motor vibration system. In addition, X_m is approximately inversely proportional to $(r^2-1)^2$, so the smaller order r should be focused on.

(1) Vibration and noise evaluation criteria

Since the vibration frequency of the motor is mostly in the mid-frequency band (f=10∼1000 Hz), the harm of mid-frequency vibration is mainly reflected in the transmission scale of vibration energy, such as the noise generated by vibration and fatigue damage of vibration components, and the vibration energy is proportional to the square of the vibration speed, so the vibration speed is used as the characteristic quantity in the vibration test.

The motor is regarded as a spherical radiator, and the radiation sound intensity is:

$$I = 2\rho C\pi^2 f^2 {X_\mathrm{m}}^2 \cdot I^*, \tag{39}$$

where $I^*$is the relative radiated sound intensity of the spherical radiator, which can be obtained by the curve shown in Fig. 16, sound velocity C is an inherent parameter of the medium, which depends on the density ρ and elastic modulus E of the medium, and can be expressed as:

$$C = \sqrt{\frac{E}{\rho}}. \tag{40}$$

The sound power W radiated by the motor housing is:

$$\begin{aligned} W &= I \cdot 2\pi DL \\ &= 2\rho C\pi^2 f^2 {Y_\mathrm{m}}^2 \cdot 2\pi DL \cdot I^* \end{aligned}, \tag{41}$$

where D is the radius of the housing and L is the length of the housing.

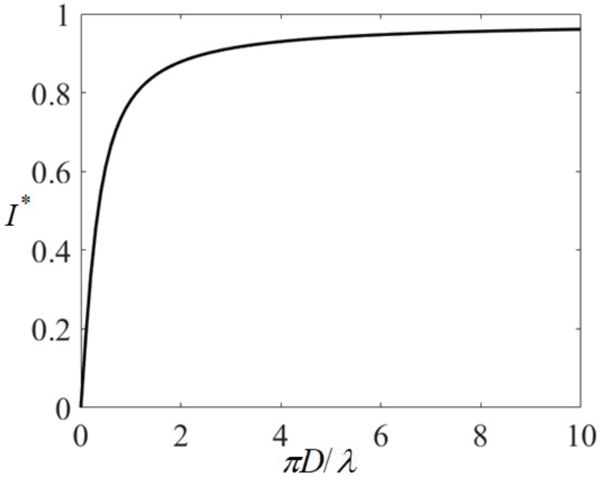

Fig. 16. Relative radiated sound intensity of a spherical radiator.

According to (41), the equivalent radiated power of the motor is proportional to the square of the amplitude of vibration velocity of the motor stator housing. The amplitude of the vibration density can be expressed as the product of the vibration displacement amplitude and vibration frequency. ERPL is used to characterize the harmonic response of the motor [23], and the expression is:

$$ERPL = 10\lg\frac{W}{W_0}, \tag{42}$$

where W_0 is the reference equivalent radiated power, generally taken as $10^{-12}W$.

(2) Vibration and noise suppression optimization results

The air-gap electromagnetic stress of the stator housing after the structural parameter optimization is shown in Fig. 17. The red part is the imported electromagnetic excitation force, including radial electromagnetic force and tangential torque.

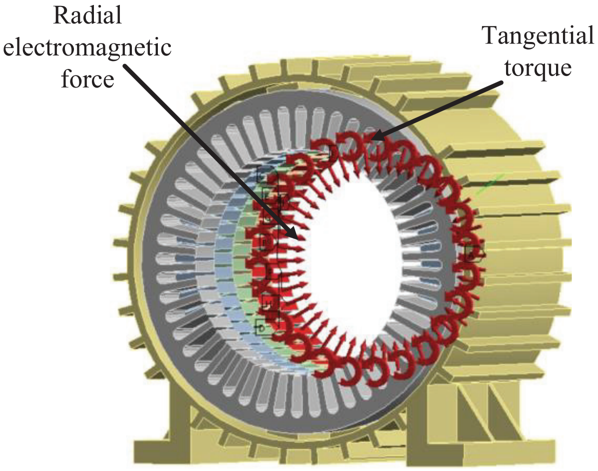

Fig. 17. Radial electromagnetic force and torsional force model after optimization of structural parameters.

The chassis base is set as a fixed constraint, and the frequency band is considered as 601 segments. The modal superposition method is used to solve the multi-speed EPRL waterfall diagram of IPMSM, and the speed range is from 1000 rpm to 6000 rpm. The ERPL waterfall diagram of IPMSM is obtained in Fig. 18 after harmonic response analysis.

As can be seen from Fig. 18 corresponding to 6000 rpm, that is, at mark point 1, the color is the darkest and the ERPL value is the largest, reaching 129.16 dB. According to the electromagnetic force theory, this is because the vibration frequency of the motor housing is close to the natural frequency, it causes a large vibration noise. Another darker point corresponding to 3000 rpm, namely, mark point 2, has an ERPL value of 117.4 dB, which is generated by the interaction of the stator magnetomotive force harmonics themselves,

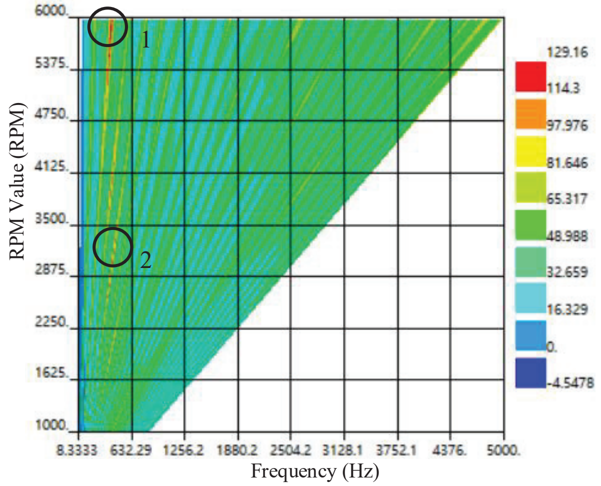

Fig. 18. ERPL waterfall diagram of the initial motor model.

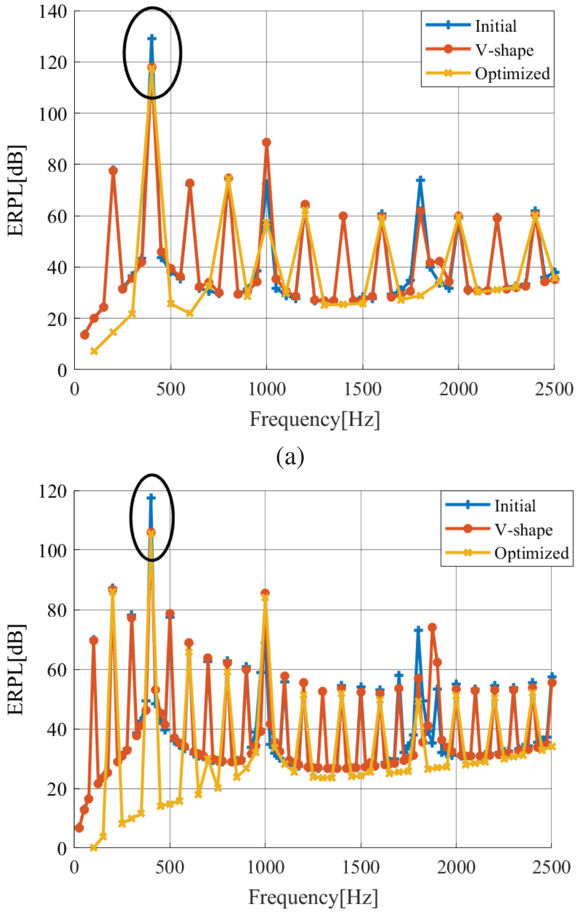

(a)

(b)

Fig. 19. Line diagram comparison of ERPL before and after optimization: (a) line diagram comparison of ERPL on 6000 rpm and (b) line diagram comparison of ERPL on 3000 rpm

and the vibration frequency is twice the fundamental frequency.

Figure 19 shows the ERPL line chart comparison of the motor before and after optimization. It can be seen from Fig. 19 (a) that the maximum value of ERPL is at the vibration frequency of 400 Hz at 6000 rpm, which is equal to the natural frequency at the vibration order. Moreover, the ERPL value is reduced from 129.16 dB to 117.98 dB to 117.25 dB from initial model to V-shaped skewed slots to structural parameter optimization. Compared with that of initial model, the optimized ERPL is reduced by 8.65% and 9.22%, respectively, indicating that the natural frequency of the stator housing of the motor can be changed through structural optimization and structural parameter optimization, so that the vibration and noise suppression caused by resonance is better. Figure 19 (b) shows that the maximum value of ERPL corresponding to 3000 rpm is also at the vibration frequency of 400 Hz, and the ERPL value decreases from 117.40 dB to 106.03 dB and then to 105.52 dB from initial model to V-shaped skewed slots and then to structural parameter optimization. After optimization, the ERPL is reduced by 9.68% and 10.12%, respectively, which proves that the harmonic components in the vibration response of the motor can be effectively reduced by optimization, so as to obtain better vibration noise suppression effect.

VII. CONCLUSION

The vibration and noise of 48-slot 8-pole IPMSM suitable for new energy vehicles are suppressed by combining structural optimization and structural parameter optimization, and the following conclusions are drawn:

(1) The radial force wave causing electromagnetic vibration noise is a spatiotemporal harmonic function, the main orders of the space harmonics are an integer multiple of the order 8 of main wave magnetic field, and the frequency of the time harmonics are an integer multiple of the power supply frequency twice.

(2) Compared with the step skewed slots optimization, the V-shape stator skewed slots structure is a better scheme for skewed slots structure optimization, and the radial force is reduced by 2.62%.

(3) The sensitivity of the motor structure parameters to the optimization objective has been calculated by the evaluation index of CoP, and the structure parameters have been classified into high sensitive parameters, including Bs$_0$, Bs$_1$, Hs$_2$ and Thi, and low sensitive parameters, covering o$_2$, dr, and Bs$_2$, and irrelevant parameters, involving Hs$_0$, Hs$_1$ and Hrib.

(4) MOGA and RSM have been integrated to optimize the structural parameters of the motor hierarchically, and global verification has been carried out. Considering the compromise of the three optimization

objectives, the torque ripple increases slightly on the basis of the V-shaped skewed slots optimization, but decreases 41.44% compared with the initial value. The continuous reduction of the average torque results in the reduction of the peak value of the radial electromagnetic force by 28.79% on the basis of V-shaped skewed slots optimization, and significant reduction of the peak value of the major orders spatial harmonics of the electromagnetic force, which is in line with the expected optimization goal.

(5) The results of vibration and noise suppression optimization show that the optimization method proposed has obvious suppression effect on the larger amplitude of the vibration noise caused by resonance and the main order vibration and noise harmonics, and the ERPL values in the two cases are reduced by 9.22% and 10.12%, respectively, which is better than the vibration and noise suppression effect of V-shaped skewed slots optimization.

ACKNOWLEDGMENT

The authors would like to thank the National Natural Science Foundation of China (Grant no. 62173165) and the Modern Education Technology Research Project of Jiangsu Province (Grant no. 2021-R-91852), Jiangsu Normal University Graduate Research and Practice Innovation Project (2022XKT0162) for providing funds and equipment for this research.

REFERENCES

[1] R. Fu, “Design and parameter research of permanent magnet synchronous motor for electric bus,” Ph.D. thesis, Northwestern Polytechnical University, 2015.

[2] K. Luo, S. L. Wu, C. Ren, and Y. Liu, “Analysis and control of electromagnetic noise of permanent magnet synchronous motor for electric vehicle,” *Electric Drive*, vol. 52, no. 10, pp. 15-20, 2022.

[3] Z. Qian, T. X. Liu, W. Z. Deng, and Q. J. Wang, “Vibration and noise suppression of vehicle permanent magnet synchronous drive motor with current harmonic injection,” *Electric Machines and Control*, vol. 26, no. 07, pp. 115-124, 2022.

[4] D. Wang, C. Peng, J. Li, and C. Wang, “Comparison and experimental verification of different approaches to suppress torque ripple and vibrations of interior permanent magnet synchronous motor for EV,” *IEEE Transactions on Industrial Electronics*, vol. 70, no. 3, pp. 2209-2220, 2023.

[5] X. Li, W. He, and R. Zhao, “Modal analysis of the stator system of a permanent magnet synchronous motor with integer slot multi-pole pair for electric vehicles,” *IET Electric Power Applications*, vol. 16, no. 1, pp. 1-14, 2022.

[6] X. Y. Wang, X. Y. Luo, and P. Gao, “Rotor structure design based on optimization of vibration and noise of electric vehicle drive motor,” *Proceedings of the CSU-EPSA*, vol. 35, no. 1, pp. 44-50, 77, 2023.

[7] Y. Xie, W. Xin, W. Cai, and Y. J. Fan, “Electromagnetic performance and electromagnetic vibration noise analysis of different rotor topologies of interior permanent magnet synchronous motor,” *Electric Machines and Control,* vol. 27, no. 1, pp. 110-119, 2023.

[8] Z. X. Li, J. K. Xia, T. Liu, and Z. Y. Guo, “Reduction of sixfold frequency vibration and noise of surface mounted permanent magnet motors based on virtual tooth structure between poles,” *Transactions of China Electrotechnical Society*, vol. 38, no. 5, pp. 1287-1298, 2023.

[9] Y. Li, S. P. Li, J. W. Zhou, and L. N. Li, “Vibration and noise reduction method of near-pole slot permanent magnet synchronous motor based on stator tooth cutting,” *Transactions of China Electrotechnical Society*, vol. 30, no. 6, pp. 45-52, 2015.

[10] Q. J. Wang, Y. D. Zheng, and X. Z. Liu, “Research on suppression of motor vibration and noise based on structural parameter optimization,” *Journal of Electrical Engineering*, pp. 1-10, 2023.

[11] T. Bdour and A. Reineix, “Global sensitivity analysis and uncertainty quantification of radiated susceptibility in PCB using nonintrusive polynomial chaos expansions,” *IEEE Transactions on Electromagnetic Compatibility*, vol. 58, no. 3, pp. 939-942, 2016.

[12] D. Torregrossa, F. Peyraut, M. Cirrincione, C. Espanet, A. Cassat, and A. Miraoui, “A new passive methodology for reducing the noise in electrical machines: Impact of some parameters on the modal analysis,” *IEEE Transactions on Industry Applications*, vol. 46, no. 5, pp. 1899-1907, 2010.

[13] J. C. Shi, C. Qian, and Y. Yu, “Evolutionary multi-objective optimization made faster by sequential decomposition,” *2017 IEEE Congress on Evolutionary Computation (CEC)*, Donostia, Spain, pp. 2488-2493, 2017.

[14] S. G. Zuo, C. G. Ma, and R. He, “Analysis and optimization of radial force wave sensitivity of permanent magnet synchronous motor for vehicles,” *Vibration, Testing and Diagnosis*, vol. 33, no. 3, pp. 357-363, 2013.

[15] Y. T. Luo and R. H. Lu, “Electromagnetic noise suppression of motor based on hierarchical optimization of structural parameters,” *Transactions of China Electrotechnical Society*, vol. 36, no. 14, pp. 2957-2970, 2021.

[16] W. Deng and S. Zuo, "Electromagnetic vibration and noise of the permanent-magnet synchronous motors for electric vehicles: An overview," *IEEE Transactions on Transportation Electrification*, vol. 5, no. 1, pp. 59-70, Mar. 2019.

[17] J. Du, Y. Li, Z. Yu, and Z Wang, "Research on radial electromagnetic force and vibration response characteristics of squirrel-cage induction motor fed by PWM inverter," *IEEE Transactions on Applied Superconductivity*, vol. 31, no. 8, pp. 1-4, 2021.

[18] Y. X. Chen, *Analysis and Control of Motor Noise*, Hang Zhou: Zhejiang University Press, 1987.

[19] T. Song, H. Liu, and Q. Zhang, "Multi-physics and multi-objective optimization design of interior permanent magnet synchronous motor for electric vehicles," *IET Electric Power Applications*, vol. 14, no. 11, pp. 2243-2254, 2020.

[20] X. Zhu, J. Huang, L. Quan, Z. Xiang, and B. Shi, "Comprehensive sensitivity analysis and multiobjective optimization research of permanent magnet flux-intensifying motors," *IEEE Transactions on Industrial Electronics*, vol. 66, no. 4, pp. 2613-2627, Apr. 2019.

[21] L. Liu, Y. Huang, M. Zhao, and Y. Ruan, "Parametric Modeling and Optimization of Switched Reluctance Motor for EV," *Applied Computational Electromagnetics Society (ACES) Journal*, vol. 37, no. 9, pp. 948-958, Sep. 2022.

[22] S. G. Zuo, *Noise and Vibration of Vehicle Synchronous Motor*, Bei Jing: Mechanical Industry Press, 2021.

[23] T. F. Song, "Research on electromagnetic vibration and noise suppression of permanent magnet synchronous motor for electric vehicle," Ph.D. thesis, Beijing Jiaotong University, 2022.

Mingwei Zhao was born in Shandong China, in 1975. He received the M.S. degree in power electronics and power drive from Nanjing University of Aeronautics and Astronautics, Nanjing, China, in 2012, and is currently pursuing the Ph.D. degree in control science and control engineering from Shanghai University, Shanghai, China.

Since 2006, he has been an experiment lecturer with the school of Electrical Engineering and Automation, Jiangsu Normal University, Xuzhou, China. He is the author of 10 articles. His research interests include the robot dynamic drive and cooperative control and industrial motion control system.

Xiangyu Wang was born in Jiangsu, China. He received the B.S. degree in electrical engineering from Jinling Institute of Science and Technology, Nanjing, China, in 2019, and is currently pursuing the M.S. degree in Electrical Engineering from Jiangsu Normal University, Xuzhou, China. His research interests include design and optimization of new energy electric drive system.

Lijun Liu was born in Shanxi, China, in 1977. She received the M.S. degree in power electronics and power drive from China University of Mining and Technology, Xuzhou, China, in 2006.

She is currently a lecturer with the school of Electrical Engineering and Automation, Jiangsu Normal University, Xuzhou, China. She has published more than 10 articles. Her research interests include design and optimization of new energy electric drive system and industrial motion control system.

Xiaowei Tu received the Ph.D. degree from University of Technology of Compiegne (UTC), France in 1987. He worked as professor in UTC, and later he became a researcher in French National Research Center (CNRS) in early 1990s. Since 1997, he has been working also as a researcher and R&D project manager in different Canadian research institutes.

He is currently a professor at the School of Mechatronic Engineering and Automation, Shanghai University, China.

Qinghua Yang was born in Shandong, China, in 1981. Ph.D., Associate professor, master supervisor. His research interests include sensor design and development, aviation ground detection and integrated Testing, industrial measurement and control system development and embedded control.

Research on the Prediction Method of Conducted Interference in Flyback Converters based on the High-frequency Transformer Model

Mengxia Zhou[2], Bin Cheng[2], Jianben Liu[1], Yakang Pei[2], Ruining Yao[2], Yan Liu[1], and Feng Li[2]*

[1]State Key Laboratory of Power Grid Environmental Protection
China Electric Power Research Institute, Wuhan 430074, China
liujianben@epri.sgcc.com, 1029358940@qq.com

[2]School of Electrical and Automation Engineering
Nanjing Normal University, Nanjing 210023, China
61239@njnu.edu.cn, 211846067@njnu.edu.cn, eaepyk@nnu.edu.cn,
6598691@qq.com, 61238@njnu.edu.cn
*Corresponding author

Abstract **–** Conducted electromagnetic interference (EMI) has always been a challenge for designers of switched-mode power supplies. Flyback converters are used in various applications. However, as the switching frequency of these converters increases, the issue of electromagnetic interference becomes progressively more severe. In light of this, this paper presents a predictive method for conducted interference in flyback converters, based on a high-frequency transformer model. A high-frequency transformer model topology is proposed, integrating traditional inductance models with a three-capacitor model. Subsequently, a self-organizing migrating algorithm (SOMA) is employed for the extraction of parameters from the high-frequency transformer model, and a high-frequency model is established for a transformer. Finally, the high-frequency model is applied to the prediction of conducted interference in flyback converters. The results demonstrate that the proposed predictive method can effectively forecast the actual conducted interference, thereby providing a reference for suppression of conducted electromagnetic interference.

Index Terms **–** Conducted interference, high-frequency model, interference prediction, self-organizing migrating algorithm (SOMA), transformer.

I. INTRODUCTION

With the continuous development of power electronics technology, the issue of electromagnetic interference (EMI) in flyback converters is becoming increasingly severe. Additionally, transformers in flyback converters have a significant impact on EMI. First, the flyback converter transformer occupies a large volume and weight, and its parameter characteristics have a considerable impact on the performance of the flyback converter and EMI characteristics. In addition, the transformer is mostly designed independently, and their high-frequency characteristics are affected by factors such as design, production process, and installation location [1]. Therefore, a reasonable study and design of transformer can ensure a better parameter fit between components, which can significantly improve the EMI problems of flyback converters.

There have been many studies related to the low-frequency characteristics of transformers, and most of them are relatively mature [2–6]. Although there has been some research into the high-frequency characteristics of transformers, the proposed transformer models were relatively complex in computation [7–11].

In the study of disturbances in flyback converters, Ferber et al. used MATLAB to model the flyback converters, but their flyback converters model is relatively simple and has no feedback circuit, so it is not good at predicting the conducted disturbance waveform of the switching power supply in actual operation [12]. Chen and Liu investigated methods to reduce the conducted interference in flyback converters. The computational model for the equivalent common-mode capacitance in transformers was established. However, the comprehensive high-frequency model for transformers model has not yet been established [13].

In Section II, a high-frequency transformer topology combining the conventional inductor model and the three-capacitor model is proposed. The equivalent circuit topology for each parameter in the high-frequency transformer model is obtained in Section III, and the parameters are extracted using self-organizing migrating algorithm (SOMA). In Section IV, a transformer is selected for high-frequency modeling. In Section V, the

Submitted On: May 8, 2023
Accepted On: February 4, 2024

https://doi.org/10.13052/2024.ACES.J.390110

developed high-frequency model of the transformer is applied to the conducted disturbance prediction of the flyback converter, and the modeling method of the high-frequency model of the transformer is verified.

II. HIGH-FREQUENCY TRANSFORMER MODEL

A. Inductance characteristics

At low frequencies, the primary and secondary sides of the transformer are mainly coupled magnetically, and the primary and secondary inductors are linked by mutual inductance. However, this model can only be used to reflect the principle and basic topology of the transformer and ignores the transformer losses, so it is not suitable for circuit simulation. The model considered in terms of the magnetic field inside the transformer is shown in Fig. 1, where the excitation branch corresponds to the excitation inductance L_m and the leakage path corresponds to the leakage inductances L_{s1} and L_{s2}.

Considering that transformers are inevitably accompanied by iron and copper losses in operation, the effect of adding resistances to equate transformer losses on the basis of Fig. 1 is shown in Fig. 2. As can be seen from Fig. 2, the parallel resistance R_m of the excitation branch of the inductance model is equivalent to the iron loss of the transformer; the series resistances R_{s1} and R_{s2} of the leakage branch are equivalent to the copper losses of the primary and secondary of the transformer, respectively.

Although some improvements have been made to the equivalent model, it still only represents the relevant characteristics of the transformer in the lower frequency range. Because the model does not reflect the effect of transformer distributed parameters at high frequencies, it is not suitable for studying the conducted disturbances in switched-mode power supplies. Therefore, the distributed parameters of the transformer at high frequencies will be analyzed in order to facilitate the subsequent study of conductor disturbances.

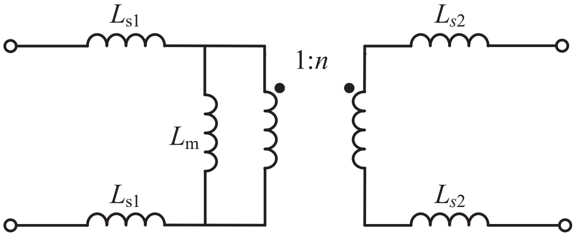

Fig. 1. Transformer excitation inductance and leakage inductance model.

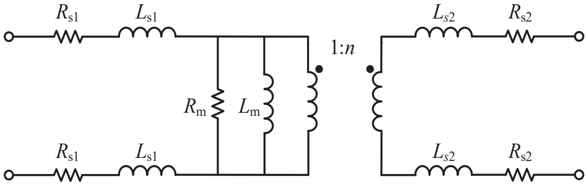

Fig. 2. Transformer low frequency loss inductance equivalent model.

B. Capacitance characteristics

The distributed capacitance of the transformer is generally considered not to change with frequency [14]. The transformer triple capacitance model is shown in Fig. 3 (a) where C_1 represents the equivalent self-capacitance of the primary side of the transformer, C_2 is the equivalent self-capacitance of the secondary side, and C_{12} is the capacitance between the primary and secondary sides. However, in order to facilitate the interference path analysis of conducted disturbances, the equivalent model of the transformer is improved. The improved transformer distributed capacitance model, shown in Fig. 3 (b), adds a capacitor below the transformer, making the model more convenient for the analysis of conducted disturbances in flyback converters.

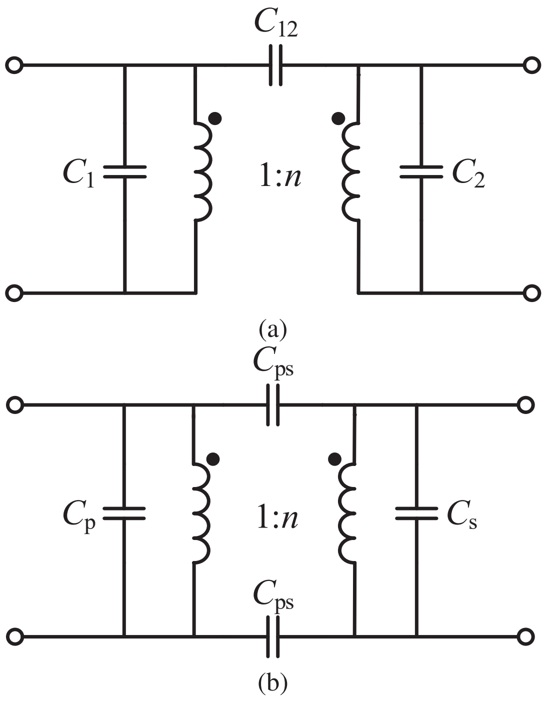

Fig. 3. Transformer (a) three-capacitor model and (b) four-capacitor model.

C. High-frequency equivalent model

Combining the low-frequency loss inductance model of the transformer with the four-capacitance equivalent model, a high-frequency equivalent model of the transformer is obtained, as shown in Fig. 4. Z_{s1} and Z_{s2} are the combined equivalent impedances of the copper loss and leakage inductance of the first and second

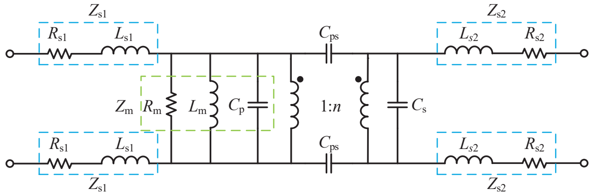

Fig. 4. Transformer high-frequency equivalent model.

sides of the transformer, respectively. Z_m is the combined equivalent impedance of the core iron loss R_m, the excitation inductance L_m, and the primary side winding self-variable capacitance C_p. C_s is the secondary side winding self-capacitance and C_{ps} is a secondary side capacitance between the windings.

III. PARAMETER EXTRACTION FOR THE HIGH-FREQUENCY TRANSFORMER MODEL

In parameter extraction for transformers in this paper, SOMA is used to process the transformer-related impedance data to obtain the *RLC* parameters in the high-frequency model [15]. The high-frequency modeling of transformers is accomplished by using SOMA, which essentially processes the impedance measurement data of transformers in order to solve for the relevant *RLC* parameters in their equivalent circuits in order to obtain the optimal solutions for the above parameters. The steps in SOMA for processing transformer impedance data are as follows [16]:

Step 1: Impedance extraction for high-frequency model parameters of transformers.

In the process of measuring the inter-winding capacitance of a transformer, its primary and secondary sides are short-circuited, respectively. Then, using a vector network analyzer (VNA), the impedance curve is measured, as shown in Fig. 5 (a). To measure the transformer's excitation impedance, Z_m, the secondary side of the transformer is left open-circuited. The impedance of the primary side is then measured with a VNA, as depicted in Fig. 5 (b). For measuring the transformer's leakage inductance impedances, Z_{s1} and Z_{s2}, the secondary side is short-circuited, and the primary side impedance is measured using a VNA, as illustrated in Fig. 5 (c).

Step 2: Equivalent circuit topology and expressions.

After obtaining the measured inter-winding impedance of the transformer, for ease of calculation, the inter-winding capacitance in the transformer's high-frequency model is considered in parallel. The high-frequency model of the capacitance is used for equivalence, with the equivalent circuit topology as shown in Fig. 6 (a). Hence, the expression for inter-winding impedance is:

$$Z_C = \frac{\mathrm{j}\omega RC - \omega^2 LC + 1}{\mathrm{j}\omega C}. \tag{1}$$

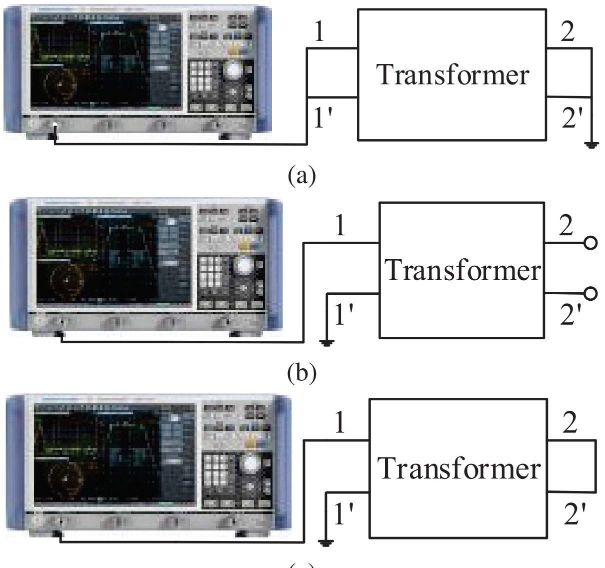

(a)

(b)

(c)

Fig. 5. Measurement methods for transformer high-frequency model parameters: (a) inter-winding impedance, (b) excitation impedance, and (c) leakage inductance impedance.

The transformer's excitation impedance is significantly larger than the leakage magnetic impedance Z_{s1}, thus the effect of leakage magnetic impedance on excitation impedance is neglected. The equivalent circuit topology for excitation impedance is shown in Fig. 6 (b). The derived expression for excitation impedance at this stage is:

$$Z_{\mathrm{m}} = \frac{\mathrm{j}\omega R_{\mathrm{m}} L_{\mathrm{m}}}{R_{\mathrm{m}} + \mathrm{j}\omega L_{\mathrm{m}} - \omega^2 R_{\mathrm{m}} L_{\mathrm{m}} C_{\mathrm{eq}}}. \tag{2}$$

The impedance measured represents the total leakage inductance of the transformer's primary and secondary sides. For ease of analysis, the leakage inductances of the primary and secondary sides are distributed according to the square of the transformation ratio. For the transformer's leakage inductance impedances Z_{s1} and Z_{s2}, considering the frequency-dependent effect of the leakage inductance, R_{s1} and R_{s2} were modified to R_{s1-eq} and R_{s2-eq}, respectively. The right-side inductors L_{s1} and L_{s2} use a high-frequency equivalent model. The final high-frequency equivalent model for leakage inductance is shown in Fig. 6 (c), with its impedance expression as follows:

$$Z_{\mathrm{s \cdot eq}} = R_{\mathrm{s \cdot eq}} + \frac{\mathrm{j}\omega R_{\mathrm{s}} L_{\mathrm{s}}}{R_{\mathrm{s}} + \mathrm{j}\omega L_{\mathrm{s}} - \omega^2 R_{\mathrm{s}} L_{\mathrm{s}} C_{\mathrm{s}}}. \tag{3}$$

Normalization results in the following high-frequency model of the transformer. The high-frequency

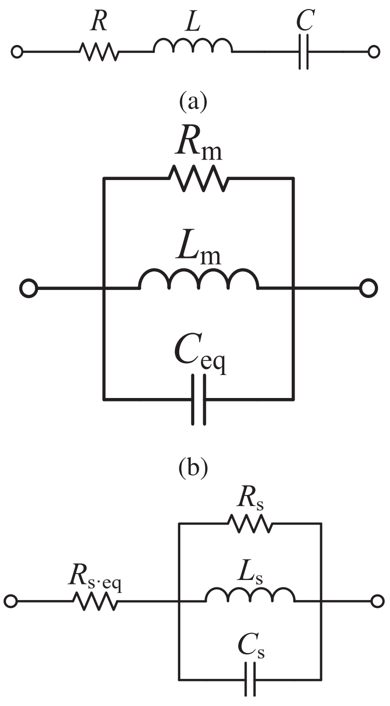

Fig. 6. Equivalent circuit topology of parameters

models for magnetizing and leakage inductance are composed of '*i*' serially connected modules, where '*i*' is the number of segments used during impedance measurement.

Step 3: Transformation of the optimal parameter problem.

The impedance expression obtained from the transformer equivalent circuit topology is transformed into an expression for the impedance amplitude Z_x, and then Z_x is used as the original function of the *RLC* parameters to be optimized, and the measured frequency-dependent impedance data Z_m is the sample. Let the expression of the impedance amplitude Z_x of the transformer-equivalent circuit model be:

$$Z_x = \phi\left(f; x_1, x_2, x_3, \ldots, x_D\right), \tag{4}$$

where *D* represents the number of circuit parameters, *f* is the independent variable (frequency), Z_x is the dependent variable (impedance), and x_1,x_2,x_3,…,x_D are the parameters to be determined, which in this paper correspond to the *RLC* parameters of the impedance equivalent model.

The optimization criterion function can be established based on the least squares sum of the residuals of the system model, as follows:

$$\min Q = \sum_{a=1}^{N} \left|\phi\left(f_i\right) - \phi\left(f_i\right)'\right|^2, \tag{5}$$

where $\varphi(f_i)$ represents the measured impedance magnitude values of the transformer and $\varphi(f_i)$' is the calculated impedance magnitude value of the impedance equivalent circuit. When the variable *Q* is minimized, the corresponding *RLC* parameters are considered as the optimal parameters.

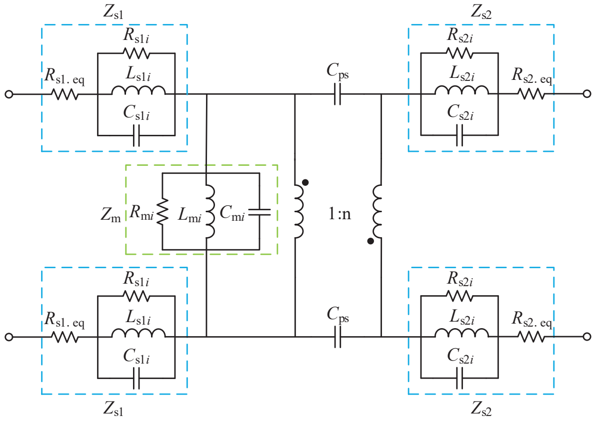

Fig. 7. Transformed high-frequency equivalent model of the transformer.

Step 4: Define the parameters.

Population size, N_P; Step size, Step; Path length, PathLength; Perturbation, PRT; and Migration loop count, ML.

Step 5: Initialization parameters.

Randomly generated for the initial population

$$\left\{x_m(0) \mid x^{L}_{n,m} \le x_{n,m}(0) \le x^{U}_{n,m}, m = 1,2,3,\ldots,N_P; n = 1,2,3,\ldots,D\right\}:$$
$$x_{n,m}(0) = x^{L}_{n,m} + \mathrm{rand}\left(x^{U}_{n,m} - x^{L}_{n,m}\right), \tag{6}$$

where N_P is the population size, $x_m(0)$ refers to the mth individual of the 0th generation in the total, $x_{n,m}(0)$ refers to the nth gene of the mth individual of the 0th generation, and$x^{L}_{n,m}$and$x^{U}_{n,m}$are the minimum and maximum values of the nth gene of the mth individual, respectively. The rand function generates pseudo-random numbers uniformly distributed between 0 and 1.

Step 6: Migration process.

The migration action formula is:

$$x^{\mathrm{ML}+1}_{u,v} = x^{\mathrm{ML}}_{u,v,\mathrm{START}} + \left(x^{\mathrm{ML}}_{\mathrm{L},v} - x^{\mathrm{ML}}_{u,v,\mathrm{START}}\right) \cdot t \cdot \mathrm{PRTVector}_v, \tag{7}$$

where $x^{\mathrm{ML}+1}_{u,v}$ is the value of u individuals after ML+1 migration; $x^{\mathrm{ML}}_{u,v,\mathrm{START}}$ is the position of u individuals at the beginning of migration; $x^{\mathrm{ML}}_{\mathrm{L},v}$ is the leader position at the time of migration; *v* is the dimension; *t*∈(0, PathLength), *t* is the interval length in steps, and the maximum is taken as PathLength; PRTVector is a vector that depends on PRT; if the random number at (0, 1) is smaller than PRT, then PRTVector is set to 1, otherwise it is set to 0.

Step 7: End of algorithm.

The termination criteria are met when the error between particles reaches the set value of MinDiv, or when the number of migration loops reaches the ML.

The end condition is assessed to determine if it has been achieved. If the termination criteria are not met, the process returns to Step 6. If the termination criteria are met, the process concludes. As a result, the optimal values of *RLC* parameters in each impedance formula are obtained.

IV. TRANSFORMER HIGH-FREQUENCY MODEL TEST VERIFICATION

In this paper, the high-frequency characteristics of the transformer in the flyback converter prototype are modeled. The core material is ferrite, the model is EC28/34, the winding method is sandwich winding, and the ratio of primary to secondary turns is 37:3. In the modeling of the transformer, the impedance curve is also divided into frequency bands. In this way, it is possible to process the measured impedance data with SOMA and obtain highly accurate *RLC* values, even without using a professional workstation computer.

The capacitive characteristics of transformers indicate that the distributed capacitance of transformers does not vary with frequency. Therefore, when modeling the inter-winding capacitance, only the impedance curve between transformer windings in the frequency range of 1-50 MHz is measured using VNA for easy processing and saving computational resources. In the process of measuring the inter-winding capacitance of a transformer, its primary and secondary sides are short-circuited, respectively. The impedance data is fitted using SOMA and (1) to obtain the *RLC* parameter in (1). The final obtained parameters are shown in Table 1.

Table 1: *RLC* values for the high-frequency model of inter-winding impedance

R	***L***	***C***
4.13 Ω	0.20 μH	118.96 pF

In modeling the high-frequency characteristics of the excitation impedance, the secondary side of the transformer is open-circuited, and then the excitation impedance curve in the frequency range of 9 kHz-200 MHz on the primary side of the transformer is measured using a VNA. Then the impedance data are divided into three frequency bands based on the number of valleys in the impedance curve obtained from the measurements. Finally, SOMA and (2) are used to fit the impedance data, and then the *RLC* parameters in the excitation impedance high-frequency model are obtained. The *RLC* parameters of the excitation impedance high-frequency model are shown in Table 2.

Table 2: *RLC* values for the high-frequency model of excitation impedance

	***i*=1** (150 kHz-96 MHz)	***i*=2** (96-186 MHz)	***i*=3** (186-200 MHz)
$\boldsymbol{R_{mi}}$	64.14 kΩ	910.16 Ω	346.93 Ω
$\boldsymbol{L_{mi}}$	0.33 mH	0.13 μH	15.02 nH
$\boldsymbol{C_{mi}}$	9.43 pF	13.88 pF	40.96 pF

Table 3: *RLC* values for the high-frequency leakage inductance model

	***i*=1** (150 kHz-96 MHz)	***i*=2** (96-186 MHz)	***i*=3** (186-200 MHz)
$\boldsymbol{R_{si}}$	7.92 kΩ	871.03 Ω	373.64 Ω
$\boldsymbol{L_{si}}$	4.54 μH	0.12 μH	14.36 nH
$\boldsymbol{C_{si}}$	8.84 pF	14.88 pF	42.69 pF

The leakage inductance of the transformer was measured by shorting the secondary side of the transformer and then measuring the impedance data and waveforms in the frequency range of 9 kHz-200 MHz on the primary side of the transformer using a VNA. Then the impedance data was divided into three frequency bands according to the characteristics of the leakage inductance waveform. Finally, the excitation impedance data are processed using SOMA and (3) to obtain the *RLC* parameters, as shown in Table 3, where R_{s-eq} is 10 nΩ, which is obtained by connecting the resistors of the three frequency bands in series.

The transformation of primary and secondary impedances in a transformer is governed by the following relationship:

$$Z_{s1i} = n^2 Z_{s2i}, \tag{8}$$

where Z_{s1i} is the primary impedance of the transformer, Z_{s2i} is the secondary impedance, and *n* is the transformation ratio of the transformer.

For the high-frequency equivalent circuit topology of the leakage inductance, there is:

$$Z_{s1i} + n^2 Z_{s2i} = Z_{si}, \tag{9}$$

where Z_{si} represents the impedance values before applying the transformer's transformation ratio.

Using (8) and (9), the transformed values of the primary and secondary leakage impedances of the transformer can be obtained, as shown in Table 4 [17]. Among them, $R_{s1\cdot eq}$ and $R_{s2\cdot eq}$ are 2.50 nΩ and 16.40 pΩ, respectively.

According to the calculated parameters, the models of inter-winding impedance, excitation impedance, and leakage impedance are built in the simulation software, and then the simulated and measured impedance characteristic curves are compared, respectively. The obtained results are shown in Fig. 8.

Based on the comparison results of simulated and measured impedance in Fig. 9, the established model

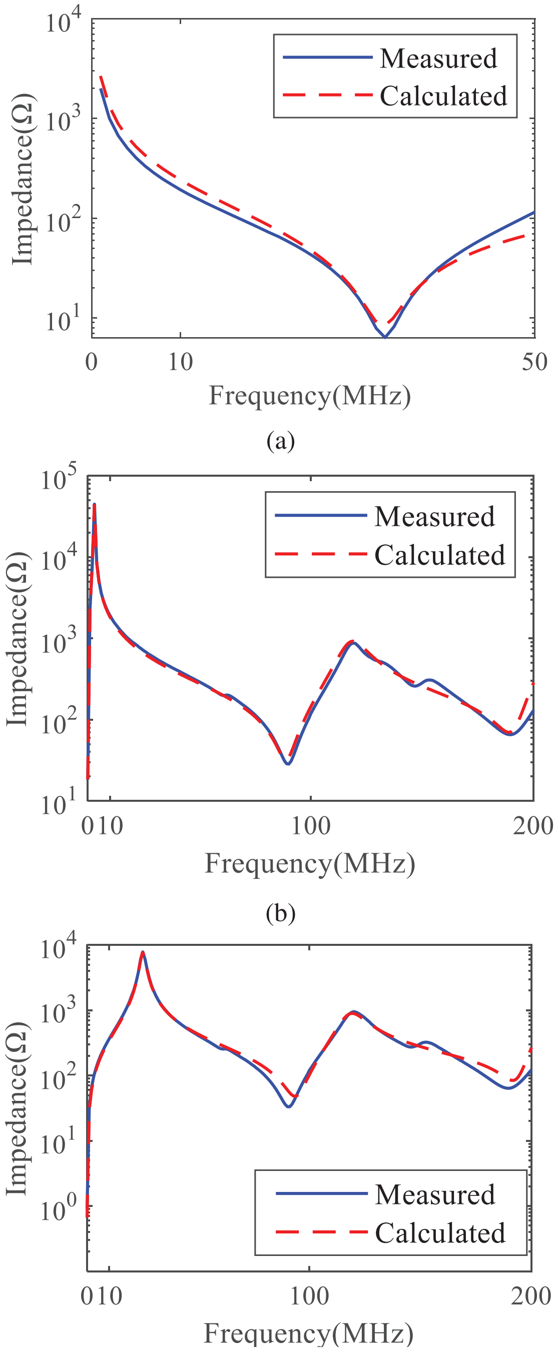

(a)

(b)

(c)

Fig. 8. Comparison between simulated and measured impedance curves of transformer parameters: (a) inter-winding impedance, (b) excitation impedance, and (c) leakage impedance.

adequately reflects the high-frequency characteristics of each parameter. However, due to simplifications and equivalent processing, some errors are inevitably present in the high-frequency model. In Figs. 8 (a-c), the maximum impedance errors are 46 Ω, 178 Ω, and 153 Ω, respectively. If the impedance range measured by the three parameters is taken as the baseline, the maximum errors for the three parameters are 2.3%, 0.37%, and 1.9%, respectively.

Table 4: *RLC* values for the high-frequency model of primary and secondary side leakage inductance

	***i*=1** (150 kHz-96 MHz)	***i*=2** (96-186 MHz)	***i*=3** (186-200 MHz)
R_{s1i}	1.98 kΩ	217.76 Ω	93.41 Ω
L_{s1i}	1.14 μH	0.03 μH	3.59 nH
C_{s1i}	35.36 pF	59.52 pF	170.76 pF
R_{s2i}	13.02 Ω	1.43 Ω	0.61 Ω
L_{s2i}	4.46 nH	0.20 nH	0.02 nH
C_{s2i}	5.38 nF	9.05 pF	2.60 nF

The high-frequency model of this transformer can be obtained by substituting the parameters into the high-frequency model topology shown in Fig. 7. The excitation impedance high-frequency model consists of three R_{mi} L_{mi} C_{mi} parallel modules in series when i=1, 2, 3, corresponding to the corresponding *RLC* values in Table 3. The leakage inductance high-frequency model also consists of R_{s1i}, L_{s1i}, C_{s1i} (R_{s2i}, L_{s2i}, C_{s2i}) parallel modules in series, when i = 1, 2, 3, respectively, corresponding to the corresponding *RLC* values in Table 4. The value of C_{ps} is 118.96 pF.

V. APPLICATION OF THE HIGH-FREQUENCY TRANSFORMER MODEL IN PREDICTING CONDUCTED INTERFERENCE OF FLYBACK CONVERTERS

A. Flyback converters conducted interference analysis

The common mode noise in flyback converters is primarily generated by the switching actions of the switching transistor and the freewheeling diode during operation [18]. When they operate, they will generate a large amount of interference noise because they are always in forward and reverse bias. The loop of common-mode interference generated by the switching transistor is shown as the red line in Fig. 9, while the loop of common-mode interference generated by the reversal diode is shown as the green line in Fig. 9 [19]. The red and green dashed lines in Fig. 9 are the common-mode interference loop and the direction of the interference signal, where V_Q and V_D denote the common-mode interference voltage generated by the switching transistor and the current-continuing diode, respectively. C_{ps} is the capacitance between the transformer windings. C_3 is the capacitance of the secondary side of the transformer to the ground. C_4 and C_5 are the parasitic capacitance

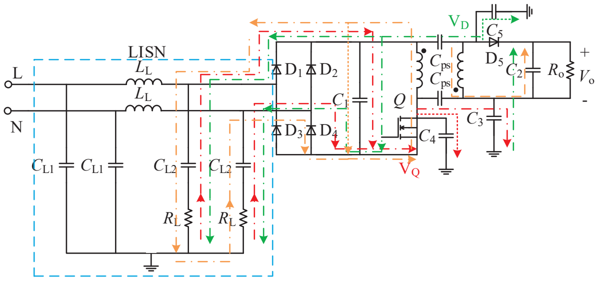

Fig. 9. Schematic diagram of interference loops of different noise sources in flyback converters.

between the switching transistor, the current-continuing diode, and the heat sink, respectively.

The differential mode interference noise is mainly caused by the current ripple in the loop where the switching transistor is located in the flyback converter, which forms a voltage drop on the leakage inductance of the transformer. The differential mode interference circuit of the flyback converter is shown as the orange line in Fig. 9. The orange dashed line in Fig. 9 shows the differential mode interference circuit and the direction of the interference signal.

In the common mode interference loop and differential mode interference loop of the flyback converter, it can be seen that both the path of differential mode interference and the path of common mode interference will flow through the transformer, and the path of common mode interference will flow through the parasitic capacitance between the primary and secondary sides of the transformer, so the high-frequency model of the transformer can be accurately established to effectively predict the conducted interference of the flyback converter.

B. Experimental platform construction

In this paper, a flyback converter is designed using the above-mentioned transformer, and then the simulated noise of the conducted disturbance is compared with the measured noise of the prototype to verify the effectiveness of the proposed transformer high-frequency modeling method and the optimization of the conducted disturbance prediction method for the conventional flyback converter. The topology of the prototype circuit is shown in Fig. 10 (a), which consists of a rectifier, control, and feedback circuits and replaces the transformer model with the high-frequency model established earlier. The fabricated flyback converter prototype is shown in Fig. 10 (b), with an input voltage of 220 V/50 Hz and an output voltage of 12 V. The main component parameters are shown in Table 5.

The flyback converter circuit shown in Fig. 10 (a) is built in the simulation software. After implementing the basic functions of flyback converter simulation, the conducted interference of flyback converters will be simulated next.

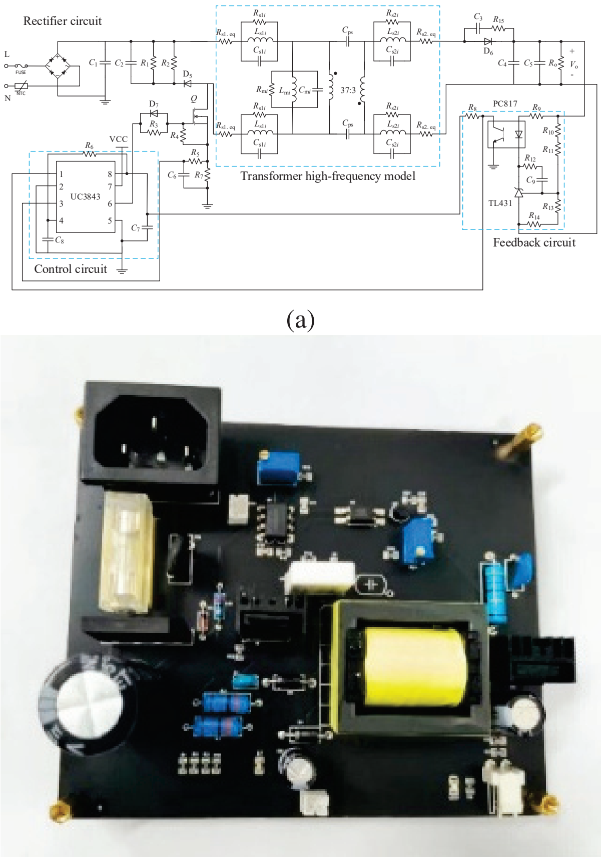

(a)

(b)

Fig. 10. (a) Flyback converter circuit topology and (b) flyback converter prototype.

Table 5: Prototype main components parameters

Component Parameters
Rectifier bridge: GBU808
PWM control chip: UC3843
MOSFET: 10N60
Optocoupler: PC817
Shunt regulator: TL431
Transformer primary inductance: 332 uF
Transformer ratio: 37:3

C. Circuit simulation and interference waveform analysis

In this paper, we designed a flyback converter using the above transformer and then compared the simulated noise of conducted disturbances with the measured noise of the prototype. The test site layout of the conducted interference is shown in Fig. 11, where the signal line of

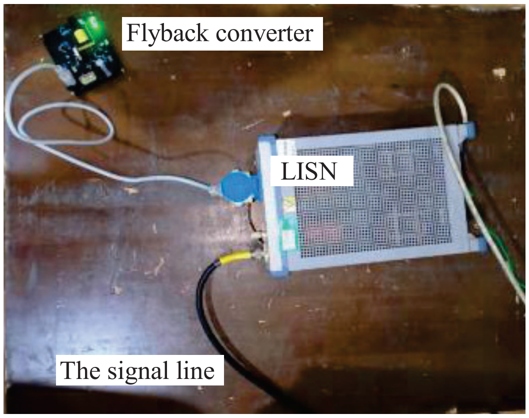

Fig. 11. Conducted interference measurement layout.

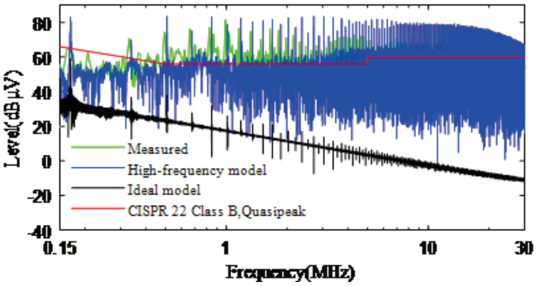

Fig. 12. Comparison of measured and simulated waveforms for conducted interference.

LISN is connected to the spectrum analyzer, the model used for LISN is the R&S ENV216, and the test standard is CISPR 22 Class B. The simulation software employed is PSpice. The simulations are carried out with the ideal model of the transformer and the high-frequency model, and the simulated and measured conducted interference noise waveforms are shown in Fig. 12.

From Fig. 12 it can be seen that the simulation results of the transformer high-frequency model are significantly better than the simulation results of the ideal model in the frequency range of 150 kHz-30 MHz. Although the conducted interference will appear as spikes at the same frequency, the difference in the amplitude of the spikes is large, and this difference will increase with the increase in frequency. The maximum difference is greater than 80 dBuV, and it is obvious that this degree of error in the interference prediction is large. It is obvious that this level of error is not allowed in interference prediction. This shows that the transformer model greatly affects the prediction results of conducted EMI in flyback converters. A comparison between the predicted conducted interference results with the transformer high-frequency model and the prototype shows that the simulated conducted interference waveform in the frequency range of 150 kHz-5 MHz can better reflect the actual interference waveform of the flyback converter with an error within 10 dBuv, while the frequency after 5 MHz has a larger difference in the interference waveform but still reflects the actual interference waveform above the limit value. Since there is no high-frequency modeling of the switching transistor and current-continuing diodes in this paper, and there may also be crosstalk in the circuit, coupled with the limits of the measurement instruments and experimental conditions, this inevitably leads to errors between the measured and simulated conducted interference waveforms. However, the flyback converter simulation circuit using the transformer high-frequency model is better able to predict the actual conducted disturbance waveform over the entire frequency range. Thus, the design and optimization of flyback converters can be facilitated, especially in terms of reducing the amount of labor and resources required for EMI correction.

VI. CONCLUSION

This paper presents a method for predicting conducted disturbances in flyback converters based on the high-frequency transformer model. Through the analysis of the conducted disturbance of the flyback converter, it is known that the transformer model has a great influence on the prediction of conducted disturbance. In order to accurately predict the conduction interference of a flyback converter, this paper proposes a new transformer model topology based on the traditional inductor model and the three-capacitor model and extracts the parameters of the transformer model using SOMA. The high-frequency transformer model is used instead of the ideal model for the optimization of the conduction interference prediction method of flyback converters. The predictions based on the conventional and optimized conduction interference prediction methods are carried out, and the prediction results are compared with the measured results of the prototype to verify the effectiveness of the proposed transformer high-frequency modeling method and the conduction interference prediction method of the flyback converter. The results show that the optimized prediction results are significantly better than the traditional prediction and can accurately reflect the actual interference level of the flyback converter. The proposed method is also applicable to other high-frequency transformer modeling and the interference prediction of flyback converters with transformers.

ACKNOWLEDGMENT

This paper is supported by Open Fund of State Key Laboratory of Power Grid Environmental Protection (GYW51202301426).

REFERENCES

[1] J. Dong, W. Chen, and Z. Lu, "Modeling and analysis of capacitive effects in high-frequency transformer of SMPS," *Proceedings of the Chinese Society of Electrical Engineering*, vol. 27, no. 31, pp. 121-126, 2007.

[2] W. M. Colonel and T. Mclyman, *Transformer and Inductor Design Handbook*, Boca Raton, FL: CRC Press, 2004.

[3] Z. De Grève, O. Deblecker, and J. Lobry, "Fast computation of R L parameters of high frequency multi-winding magnetic components," *COMPEL-The International Journal for Computation and Mathematics in Electrical and Electronic Engineering*, vol. 30, no. 6, pp. 1914-1926, 2011.

[4] G. Antonini, A. Orlandi, and C. R. Paul, "Internal impedance of conductors of rectangular cross section," *IEEE Transactions on Microwave Theory and Techniques*, vol. 47, no. 7, pp. 979-985, July 1999.

[5] H. Y. Lu, J. G. Zhu, and V. S. Ramsden, "Comparison of experimental techniques for determination of stray capacitances in high frequency transformers," *2000 IEEE 31st Annual Power Electronics Specialists Conference. Conference Proceedings*, vol. 3, pp. 1645-1650, 2000.

[6] X. Margueron and J. P. Keradec, "Identifying the magnetic part of the equivalent circuit of n-winding transformer," *2005 IEEE Instrumentation and Measurement Technology Conference Proceedings*, pp. 1064-1069, 2005.

[7] R. C. Degeneff, M. R. Gutierrez, and P. J. McKenny, "A method for constructing reduced order transformer models for system studies from detailed lumped parameter models," *IEEE Transactions on Power Delivery*, vol. 7, no. 2, pp. 649-655, Apr. 1992.

[8] B. Cogitore, J. P. Keradec, and J. Barbaroux, "The two-winding transformer: an experimental method to obtain a wide frequency range equivalent circuit," *IEEE Transactions on Instrumentation and Measurement*, vol. 43, no. 2, pp. 364-371, Apr. 1994.

[9] Hai Yan Lu, Jian Guo Zhu, and S. Y. R. Hui, "Experimental determination of stray capacitances in high frequency transformers," *IEEE Transactions on Power Electronics*, vol. 18, no. 5, pp. 1105-1112, Sep. 2003.

[10] C. Liu, "High voltage high frequency transformer wide-frequency modeling method and its application research," Ph.D. dissertation, Dept. of Electrical Engineering, North China Electric Power University, Beijing, China. 2017.

[11] L. Xie, X. Ruan, and Z. Ye, "Equivalent noise source: An effective method for analyzing common-mode noise in isolated power converters," *IEEE Transactions on Industrial Electronics*, vol. 63, no. 5, pp. 2913-2924, May 2016.

[12] M. Ferber, C. Vollaire, L. Krähenbühl, J.-L. Coulomb, and J. A. Vasconcelos, "Conducted EMI of DC–DC converters with parametric uncertainties," *IEEE Transactions on Electromagnetic Compatibility*, vol. 55, no. 4, pp. 699-706, Aug. 2013.

[13] H. Chen and G. Liu, "Determination of the width of shielding foil in sandwiched winding transformer for minimizing common mode EMI of flyback converters," *IEEE Transactions on Electromagnetic Compatibility*, vol. 62, no. 2, pp. 639-642, Apr. 2020.

[14] J. Liu, L. Zhou, Y. Luo, X. Huang, and G. Wu, "Dielectric frequency response of oil-paper composite insulation with transient moisture distribution," *IEEE Transactions on Dielectrics and Electrical Insulation*, vol. 20, no. 4, pp. 1380-1387, Aug. 2013.

[15] M. Zhou, Y. Zhao, C. Zhang, X. Liu, X. Wu, Y. Sun, and W. Yan, "Predicting the impact of transient voltage suppressor used for ESD protection on the low noise amplifier," *Microelectronics Journal*, vol. 113, July 2021.

[16] Y. Pei, H. Ma, M. Zhou, W. Yan, and C. Zhang, "High-frequency characteristic modeling of common mode chokes based on self-organizing migration algorithm," *Electronic Components and Materials*, vol. 42, no. 02, pp. 200-205, Feb. 2023.

[17] P. R. Wilson and A. D. Brown, "Effective modeling of leakage inductance for use in circuit simulation," *2008 Twenty-Third Annual IEEE Applied Power Electronics Conference and Exposition*, pp. 391-395, 2008.

[18] F. Hubert, P. Dorsch, D. Kuebrich, T. Duerbaum, and S. J. Rupitsch, "Piezoelectric EMI filter for switched-mode power supplies," *IEEE Transactions on Power Electronics*, vol. 36, no. 6, pp. 6624-6643, June 2021.

[19] D. Jiaqi, Y. Ru, L. Zuolian, Y. Hong, and J. Hai, "Modeling and analysis of conducted EMI on flyback converter using power management IC with chaotic suppression EMI," *2020 22nd European Conference on Power Electronics and Applications (EPE'20 ECCE Europe)*, pp. 1-10, 2020.

Mengxia Zhou received the M.S. degree in electrical engineering and the Ph.D. degree in physics and electronics from Nanjing Normal University, in 2018 and 2021, respectively. His main research interests include electromagnetic compatibility, electromagnetic environment effect, and high frequency device modeling.

Bin Cheng was born in Anhui, China. He received his B.E. degree in electrical engineering from Anhui University of Technology in 2021. He is currently pursuing a M.S. degree in electrical engineering at Nanjing Normal University. His current research interests include high frequency device modeling, switched-mode power supplies, and electromagnetic compatibility.

Jianben Liu graduated from Huazhong University of Science and Technology with a Doctor's degree in Electrical engineering in 2013. He is mainly engaged in the research of power electronics technology, power quality and electromagnetic environment of power systems.

Yakang Pei was born in China. He completed his studies in electrical engineering and its automation at the Haibin College of Beijing Jiaotong University in Cangzhou, Hebei, China in 2019, and received his bachelor's degree in engineering. He is a master student at Nanjing Normal University with research interests in electromagnetic compatibility and high frequency device modeling.

Ruining Yao received bachelor's degree in engineering with electrical machine and its control major from Hunan university in 1997. His main research interests include electrical machine, electromagnetic environment effect, electromagnetic compatibility.

Liu Yan is a senior engineer. Her research interests are power grid remote sensing monitoring and line operation and maintenance.

Feng Li obtained his Ph.D. degree from Southeast University, China in 2021. After Ph.D. graduation, he joined school of electrical and automatic engineering, Nanjing Normal University, China. His research areas include power system modelling and simulation, power system stability analysis and control.